UNIVERSITY OF CAPE TOWN
IYUNIVESITHI YASEKAPA • UNIVERSITEIT VAN KAAPSTAD

The effect of boundary conditions and architecture on the response of cancellous bone

Kelsey Hilton

Supervisor: Mr Trevor Cloete

Blast Impact and Survivability Research Unit
Department of Mechanical Engineering
University of Cape Town

October 18, 2018

This work is submitted in partial fulfilment of the requirements of the degree of Master of Science in Engineering specialising in Mechanical Engineering

Declaration

1. I know the meaning of plagiarism and declare that all the work in the document, save for that which is properly acknowledged, is my own.
2. This thesis/dissertation has been submitted to the Turnitin module (or equivalent similarity and originality checking software) and I confirm that my supervisor has seen my report and any concerns revealed by such have been resolved with my supervisor.
3. I have used the IEEE convention for citation and referencing. Each significant contribution to, and quotation in, this report from work(s) of other people has been attributed, and has been cited and referenced.
4. I have not allowed, and will not allow anyone to copy my work with the intention of passing it off as his or her own work.

Signature: Signed by candidate

Kelsey Hilton (HLTKEL002)

Abstract

The investigation presented herein was performed to determine the effect of boundary conditions and architectural parameters on the mechanical properties of bovine cancellous bone. 124 cylindrical cancellous samples (7.5 mm height) were harvested from a total of 9 bovine humeri. Mechanical properties of these samples were determined using compression tests performed at three, quasi-static strain rates, namely: 10^{-3} , 10^{-2} and 10^{-1} s^{-1}.The specimen conditions investigated were standard specimens (with marrow, 10 mm diameter), defatted specimens (without marrow, 10 mm diameter), structurally confined specimens (with marrow and a confining collar, 10 mm diameter) and bone confined specimens (with marrow, 20 mm and 28 mm diameters).

Each specimen was scanned using a μCT scanner (Phoenix, voxel size 80 μm, 70 kV, 350 μA, acquisition time of 500 ms per image). The images were used to determine the architectural parameters for each specimen, which were calculated using algorithms developed during the study. These algorithms were validated against existing software (BoneJ) which is available to calculate cancellous bone architectural parameters.

The results of the compression testing showed little dependence of mechanical properties on strain rate. The results of the defatted and structurally confined specimens showed a decrease in scatter with the elimination and reduction, respectively, of flow of the marrow within the trabecular network. This suggests that although marrow does not strengthen bone at quasi-static strain rates, the flow of marrow disrupts the trabecular network.

The bone confinement results showed significantly increased mechanical strength of the inner 10 mm core compared to the whole sample. Apparent modulus was found to be 58% and 60% higher in the central core of the sample for 20 mm and 28 mm samples respectively. This suggests that doubling the diameter effectively removes the edge effects, with any additional diameter increase having no effect. Inner core yield strength was 58% higher in the 20 mm samples, and roughly 96% higher in the 28 mm samples compared to full specimen yield strength. This suggested that post-yield behaviour requires a further increase in overall diameter to sufficiently remove the edge effects due to the boundary condition.

The results of the architectural parameters suggested a linear correlation between the mechanical properties and parameters bone volume versus total volume and trabecular number. An exponential relationship was found to exist between the mechanical properties and mean trabecular separation. No correlation was found between mechanical properties and mean trabecular thickness. It was also concluded that specimen condition affects the relationship between mechanical properties and architectural parameters. Therefore, to effectively predict the response of cancellous bone, specimen condition should be used in conjunction with at least two architectural parameters, preferably bone volume versus total volume and mean trabecular separation.

Acknowledgements

I would like to thank my supervisor, Mr Trevor Cloete, for all his guidance and knowledge during the course of this project. The random inspirations after many months of going down a different path would not have been possible without him and I am grateful for everything he had done to help me through my research. Thank you for your encouragement Trevor, I appreciate it.

I am particularly grateful to Professor Nurick, who encouraged me with kind words, found papers he thought may be interesting for me, and kept me positive in my own abilities. Thank you, Prof., I will never forget the kindness you treated me with.

I would like to acknowledge the contributions of Dr Guillaume du Bois, Dr Marianne Prot and Dr Sébastien Laporte for their help and guidance. Especially to Dr Guillaume du Bois, for teaching me and allowing me to complete experimentation alongside him, as well as all his help with processing data and finding credible, relevant papers to read. Thank you, Guillaume, it was wonderful working with you.

To Richard Curry, Richard Whittemore, Julian Meyer and Dr Reuben Govender, I would like to acknowledge all the help and hours put in to helping me with my experimental set up.

A sincere thank you to Mr Charles Harris, who spent hours with me, mostly over weekends and after work, machining specimens for my experiments. I could not have done it without you, Charles. Thank you.

I would like to thank Pierre Smith and the UCT Mechanical Engineering workshop for their skilled workmanship and constant willingness to help. I asked for rushed jobs many times and they were happy to help wherever they could. Thank you all so much.

I would like to acknowledge the contributions of Sack's Butchery and the Stellenbosch CT scanning facility. The help of these organisations was invaluable in making my project viable and relevant.

I am sincerely grateful to the Center for Materials Engineering at UCT for the use of their equipment for my experimentation. Especially, I would like to thank Mrs Penny Louw for her willingness to help me work after hours while I was completing my masters and working concurrently.

To all the BISRU postgrad students, especially Dustin Fischer, Sherlyn Gabriel, Alessandro Scribani, Matthew Weyer, Christopher Long, Lee-Anne Welgemoed, Andrew Roginsky and Ismail Ghoor, I would like to say thank you for keeping my spirits high. Your humour carried me through some tough days and I will always consider you friends.

I would also like to thank Dr Steeve Chung Kim Yuen and Dr Genevieve Langdon for their concern and guidance while I was a part of BISRU.

The financial assistance of the National Research Foundation (NRF) towards this research is hereby acknowledged. Opinions expressed and conclusions arrived at, are those of the author and are not necessarily to be attributed to the NRF.

To Dale Warncke I would like to say a very special thank you. Thank you for your constant support, for spending hours at the lab with me, for putting a smile on my face and for believing in me to the ends of the earth. I could not have done it without you, and your confidence in me is something that has definitely changed the way I see myself. Thank you, from the bottom of my heart.

Finally, to my mom, dad and sister (blister) - thank you for you support and encouragement throughout this journey. Thank you for keeping me sane and for believing in me no matter what.

Table of Contents

List of Tables

List of Figures

Acronyms

BV/TV	bone volume versus total volume
CTH	Circular Hough Transform
FE	finite element
HRCT	high-resolution computed tomogrophy
ID	inner diameter
MLE	maximum likelihood estimation
SEM	scanning electron microscope
SHPB	split Hopkinson pressure bar
Tb.N	trabecular number
Tb.Sp	mean trabecular separation
Tb.Th	mean trabecular thickness
US	ultimate strength
VOI	volume of interest

Nomenclature

$A_{specimen}$	area of compressive specimen
ϵ_H	hoop strain
A_{lc}	area of loadcell
σ	stress
$\sigma_{specimen}$	specimen stress
σ_u	ultimate stress
σ_H	hoop stress
σ_R	radial stress
σ_y	yield strength
ν	Poisson's ratio
ϵ	strain
E	Young's modulus
E_{app}	apparent modulus
ϵ_m	strain due to machine take-up
$F_{measured}$	measured force
$Gain$	gain set by strain gauge amplifier
K_f	loadecell calibration factor
K_{gf}	gauge factor
N	number of active gauges
R	radius
V_{BV}	bridge voltage
V_{out}	output voltage

Chapter 1

Introduction

1.1 Background

Bone is a complex, biological, connective tissue. Bone is classified macroscopically as either cortical ("dense") or cancellous ("spongy") bone. Cancellous bone has a hierarchical microstructure which allows for marrow to be present within a network of trabeculae, and this causes strengths of the overall structure which far exceed the strengths of the individual components. Cancellous bone microstructure, in particular, is remodelled under strain - caused by running, lifting weights, or other day to day activities - and is therefore highly irregular and unique to each individual [1].

Macroscopic fracture of bone can occur during events such as falling, vehicle collisions, projectile or blunt force trauma. The mechanical response of bone is an important factor to consider when studying these macroscopic fracture events, and as such, has been under investigation for many years. Multiple studies have conducted investigations, both numerical and experimental, into the way in which bone behaves in various confinement and boundary conditions [2–10]. However, few studies have successfully replicated the true *in vivo* response of cancellous bone, as most whole bone studies are purely numerical [6–8] and therefore do not have experimental data to validate the results.

Results of an investigation of this kind could serve to better inform vehicle accident or landmine blast simulations. There are between 20 and 50 million injuries sustained per year due to car accidents [11]. Currently, the risk of injury during these events is based on quantified tests involving Post Mortem Human Surrogates (PMHS). While PMHS tests are useful in a broad sense, they do not provide an accurate representation of the way in which the human body reacts to these events.

The scarcity of confinement data suggests a need to experimentally investigate the effect of a confinement condition on cancellous bone in order to represent *in vivo* conditions.

In addition, the inter-individual variation of cancellous bone gives rise to the need to accurately reconstruct specific bone samples when simulating fracture events. One way to perform this reconstruction is by using microstructural (or architectural) parameters specific to individual bone samples.

1.2 Scope of Investigation

The investigation herein was performed to determine the effect of boundary conditions and architectural parameters on the mechanical properties of bovine cancellous bone. Mechanical properties were calculated from experimental results, and were analysed across five specimen boundary conditions. Specimens were compressed at 10^{-3}, 10^{-2} and 10^{-1} s^{-1}. The specimen conditions investigated were:

1. 10 mm diameter Standard specimens
2. 10 mm diameter Defatted specimens
3. 10 mm diameter Structurally Confined specimens
4. 20 mm Bone Confined specimens
5. 28 mm Bone Confined specimens

Each of these specimens was scanned using a μCT scanner (Phoenix, voxel size 80 μm, 70 kV, 350 μA, acquisition time of 500 ms per image). The images were used to determine the architectural parameters for each specimen, which were calculated using algorithms developed during the study. These algorithms were validated against existing software (BoneJ) which is available to calculate cancellous bone architectural parameters.

Based on the five specimen conditions, the objectives of the study were:

1. Perform a set of experiments which investigate the effect of the following parameters on the mechanical response of bovine cancellous bone:
    - Strain rate
    - Presence of marrow
    - Confinement condition
    - Architectural parameters

2. Develop algorithms to calculate the architectural parameters of individually μCT scanned samples
3. Validate the developed algorithm using BoneJ
4. Develop an experimental confinement technique that more accurately represents an *in vivo* response
5. Draw conclusions and make recommendations based on the findings of the investigation

1.3 Outline

Chapter 2 presents a review of relevant literature. The physiology of cancellous bone is described, following which architectural parameters are defined. A brief review of image acquisition and processing methods is given, after which the intrinsic and extrinsic factors which influence the mechanical response of bone are presented. This includes a review of various studies which have conducted both numerical and experimental studies.

Chapter 3 decribes the details of the specimen preparation process for the investigation. This includes machining, defatting and storing of individual specimens.

The method for obtaining architectural parameters is presented in chapter 4. This includes the methods used to scan and process the images for each sample, as well as binarising images to be used in calculations. The validation of the developed algorithms is also described in this chapter.

Chapter 5 presents the experimental configurations for the various tests and specimen configurations. A detailed discussion on the design and calibration of the confinement platform, used for bone confinement tests, is presented, following which the experimental test series are summarised. Descriptions of the methods used to determine mechanical properties as well as to statistically analyse the data are given.

The results of and discussion about the investigation are presented in chapter 6, following which conclusions are drawn and recommendations are made in chapters 7 and 8 respectively.

Chapter 2

Literature Review

Bone is a complex material which has been studied extensively over the years. Various studies have aimed to quantify the response of bone, and have investigated many different aspects of this material in order to do so. This literature review reports on the results of these studies to inform the investigation herein, and focusses on studies specific to cancellous bone.

The chapter begins with a description of the physiology of cancellous bone, followed by definitions of the architectural parameters which define the geometry of cancellous bone. Image processing methods relating specifically to cancellous bone are investigated and presented. Finally, factors affecting the mechanical response of bone - such as architectural parameters, anatomical site and orientation, apparent density, strain rate, boundary conditions, presence of marrow and specimen preparation and storage - are presented.

The outcomes of this review will serve to provide insights into the decisions and assumptions made throughout this study.

2.1 Bone Physiology

Bone is a complex, biological, connective tissue which forms majority of the skeleton in vertebrates. Bone is responsible for major organ protection, nutrient storage and production, blood production and movement facilitation through its load-bearing capabilities as well as muscle attachment sites. In order for bone to perform its functions, it is stiff, rigid, and has an adapted architectural structure depending on anatomical site. There are two types of bone; cancellous - also called trabecular or "spongy" bone - and cortical bone. This investigation will focus on cancellous bone in particular.

2.1.1 Cancellous Bone

Cancellous bone is typically found at the ends of long bones, as well as at the core of vertebrae and flat bones such as the skull and scapula [1]. It is less dense than cortical bone - having porosities ranging from 30 to over 90 % [9] - and is made up of trabeculae which are interconnected and surrounded by red bone marrow [1]. The trabeculae have thicknesses between 100-640 μm [3].

Figure 2.1 shows this structure. The canaliculi present on the trabecular surfaces make cancellous bone highly porous. At a microstructural level, cancellous bone is made of lamellae, which are organised into concentric lamella packets [12], as seen in figure 2.1.

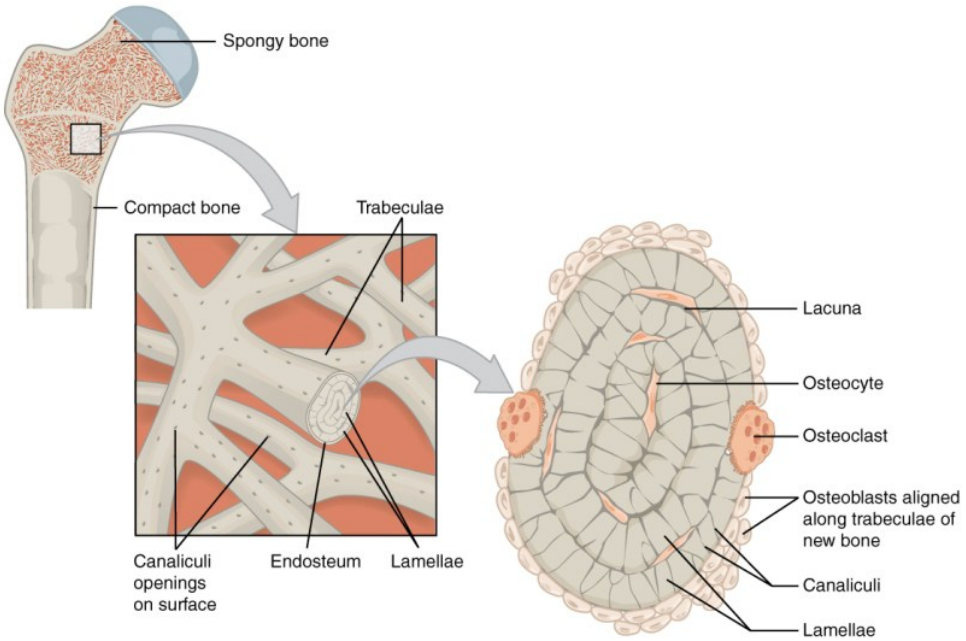

Figure 2.1: Cancellous bone physiology [1]

Lamella packets are deposited onto the trabecular surfaces as bone remodelling occurs, changing the orientation and shape of each trabecula [12]. Figure 2.2 shows newly deposited lamella packets in contrast to older packets. It is evident that the newest or outermost packet (indicated with white solid parallel lines) are aligned with the current trabecular orientation, while the older packets (indicated with black dotted and black dashed parallel lines) are no longer aligned with the trabecular axis.

Remodelling of this form causes a gradual change in the entire trabecular surface of the bone, eventually reshaping the trabecular network as a whole. This leads to a randomised and unpredictable network structure. This network of randomly organised trabeculae forms the architectural level of cancellous bone. An example of this trabecular network is shown in figure 2.3. The architectural level of cancellous bone is the focus of this investigation.

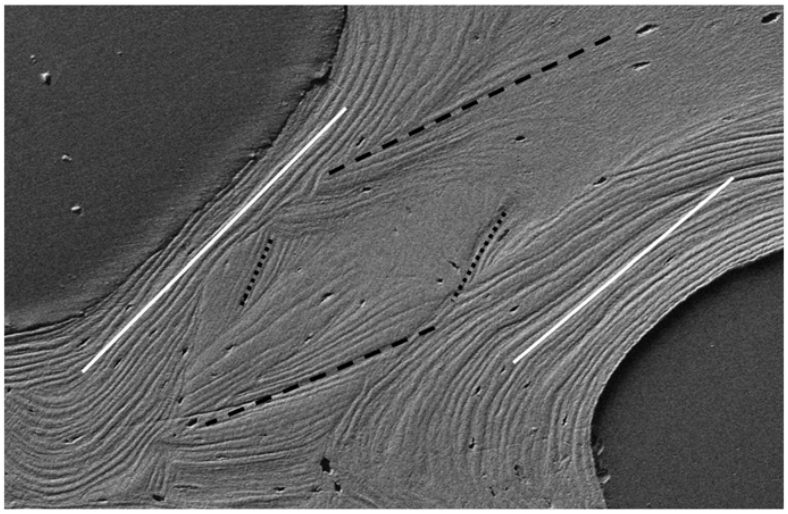

Figure 2.2: A photograph acquired using a scanning electron microscope of a dissected trabecula. Pairs of parallel lines show lamellar packets [12]

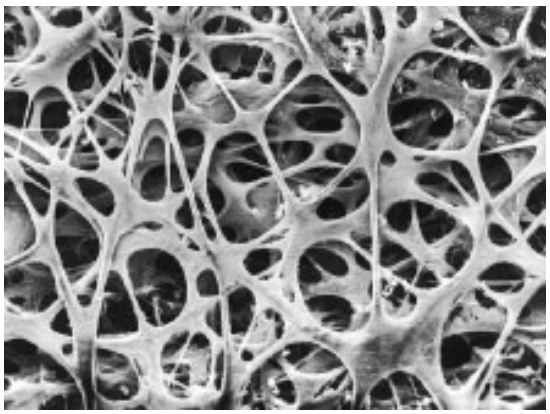

Figure 2.3: Scanning electron microscope photograph of a trabecular network [13]

2.1.2 Cancellous Architectural Parameter Description

Over recent years, the use of micro-computed tomography (μCT) to assess the architectural morphology of cancellous bone has grown exponentially. There are, however, many different parameters which can be assessed, and these parameters are often quantified inconsistently [14]. These inconsistencies arise from differences in image acquisition methods between μCT systems as well as differences evaluating and reporting the results [14].

In order to account for inconsistencies, Bouxsein et al. (2010) [14] suggest that any study that uses μCT-based data acquisition include information on the following in the methods section:

- Image Acquisition
  - scanning medium
  - X-ray tube potential
  - voxel size
  - volume of interest
- Image Processing
  - image filtration algorithms
  - image segmentation approach

Based on multiple studies [14–26], cancellous bone architecture is conventionally described using the architectural parameters defined in table 2.1. This is, however, a non-exhaustive list. The architectural parameters in bold are considered the minimum set of parameters to be reported when quantifying cancellous bone architecture [14].

In order to quantify these parameters, either a 2-dimensional or 3-dimensional approach must be taken [16, 26, 27].

In the case of the 2D approach, either a "rodlike" or a "platelike" model must be assumed for the trabecular network of cancellous bone. Examples of these network types are shown in figure 2.4. Equations 2.1-2.5 show algorithms used by Hipp et al. (1996) [16] in order to calculate the geometric and morphological parameters mentioned in table 2.1 using 2D methods. While the authors do not specify whether a rodlike or a platelike model was assumed, these equations are consistent with those used by Hildebrand et al. (1999) [27] and Silva et al. (2014) [26] for rodlike trabeculae. Figure 2.5a shows an explanation for calculating mean trabecular number (Tb.N) as described in equation 2.2. Mean trabecular separation (Tb.Sp) can also be calculated using a 2D test line method. Figure 2.5b gives a graphical explanation of this method. The average space (in mm) between trabeculae is calculated for each test line.

$$\mathrm{BV/TV} = \frac{\text{No. of bone pixels}}{\text{Total pixels}} \tag{2.1}$$

$$\mathrm{Tb.N} = \frac{\text{No. of test line intersections with bone-marrow interface}}{\text{Unit test line length}} \tag{2.2}$$

Table 2.1: A table showing a summary of conventional architectural parameters [14–26]

Family	Parameter	Description	Unit
Geometry and Morphology	BV	Bone Volume	mm^3
	TV	Total Volume	mm^3
	BV/TV	**Bone Volume Fraction**	**%**
	BS	Bone Surface	mm^2
	BS/BV	Specific Bone Surface	mm^2/mm^3
	BS/TV	Bone Surface Density	mm^2/mm^3
	Tb.N	**Trabecular Number**	$1/mm$
	Tb.Th	**Mean Trabecular Thickness**	mm
	Tb.Sp	**Mean Trabecular Separation**	mm
	Tb.Sp.SD	Trabecular Separation Standard Deviation	mm
	Tb.Sp.SD	Trabecular Separation Standard Deviation	mm
Topology	FD	Fractal Dimension	
	SMI	Structural Model Index	
	Conn.D	Connectivity Density	
Connectivity	N.Nd	Number of Junctions	$1/mm^3$
	N.Tp	Number of Triple Point	$1/mm^3$
	N.Qp	Number of Quadruple Point	$1/mm^3$
Anisotropy	DA	Normalised Degree of Anisotropy	mm
	MIL	Mean Intercept Length	mm

$$\text{Tb.Th} = \frac{\text{BV/TV}}{\text{Tb.N}} \tag{2.3}$$

$$\text{Tb.Sp} = \frac{\text{1 - BV/TV}}{\text{Tb.N}} \tag{2.4}$$

OR

$$\text{Tb.Sp} = \text{average length between bone-marrow interfaces} \tag{2.5}$$

While parameters such as BV/TV and BS/TV show no significant sensitivity to either the 2D or 3D approach, other parameters such as Tb.N, Tb.Sp and Tb.Th have been found to exhibit unpredictable errors when using the 2D rather than the 3D approach [14]. This is largely due to the fact that the 2D approach requires an assumption of the underlying structure of the bone (either rodlike or platelike), when in reality the trabecular network may consist of a combination of these types [14, 16, 26, 27]. In order

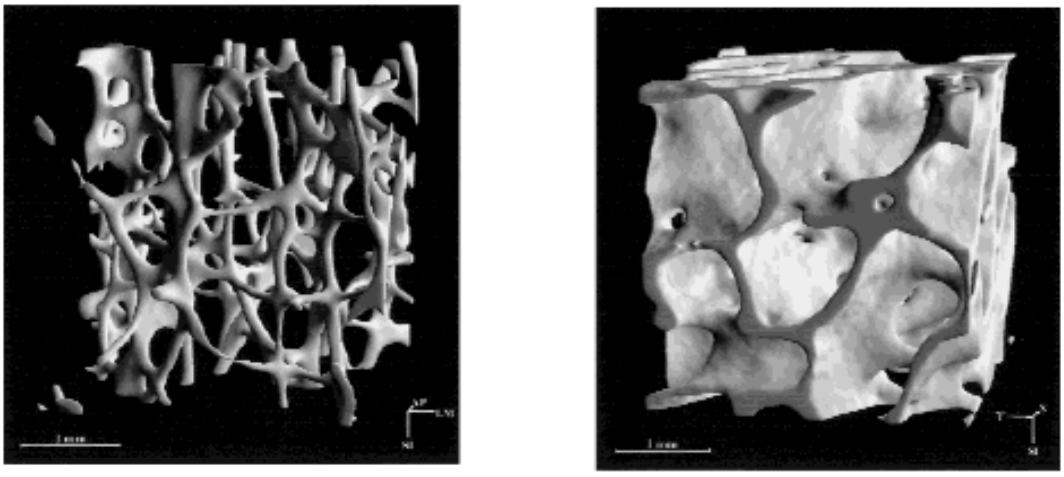

(a) Rodlike network (b) Platelike network

Figure 2.4: A 3D model comparison of rodlike and platelike trabecular networks [27]

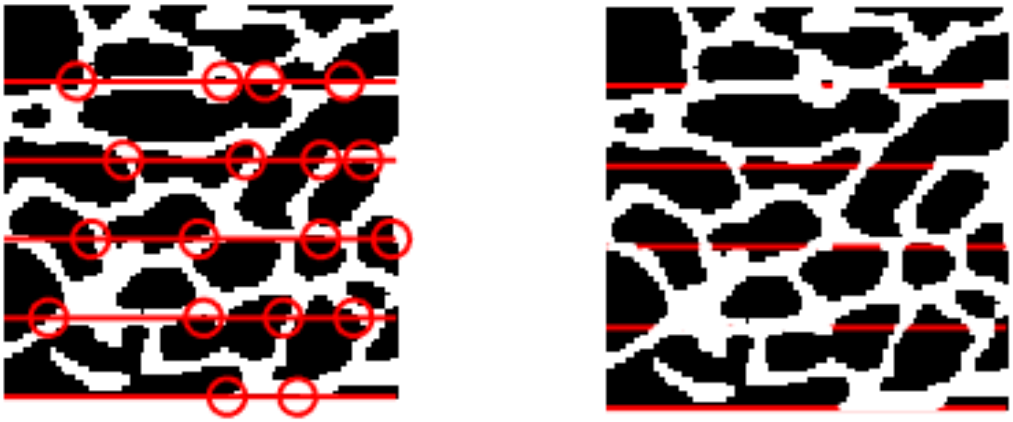

(a) Tb.N graphical explanation (b) Tb.Sp graphical explanation

Figure 2.5: Illustrations showing graphical explanations for the test line method of calculating Tb.N and Tb.Sp [27]

to obtain these parameters without assuming an underlying model for the trabecular network, as recommended by Bouxsein et al. (2010) [14], 3D methods must be used. 3D methods use a sphere fitting method in order to calculate Tb.Sp as well as Tb.Th. The sphere fitting method is shown in figure 2.6. Tb.N is then calculated as the inverse of the mean distance between trabeculae mid-axes (in mm^{-1}) [14], as shown in figure 2.7.

Tb.N is calculated in one of two ways - either directly, as in figure 2.7, or indirectly using the inverse of Tb.Sp. Although this method will be slightly less accurate than computing the mean distances between trabeculae directly, it can dramatically reduce computation time if the algorithms are implemented directly rather than through dedicated software.

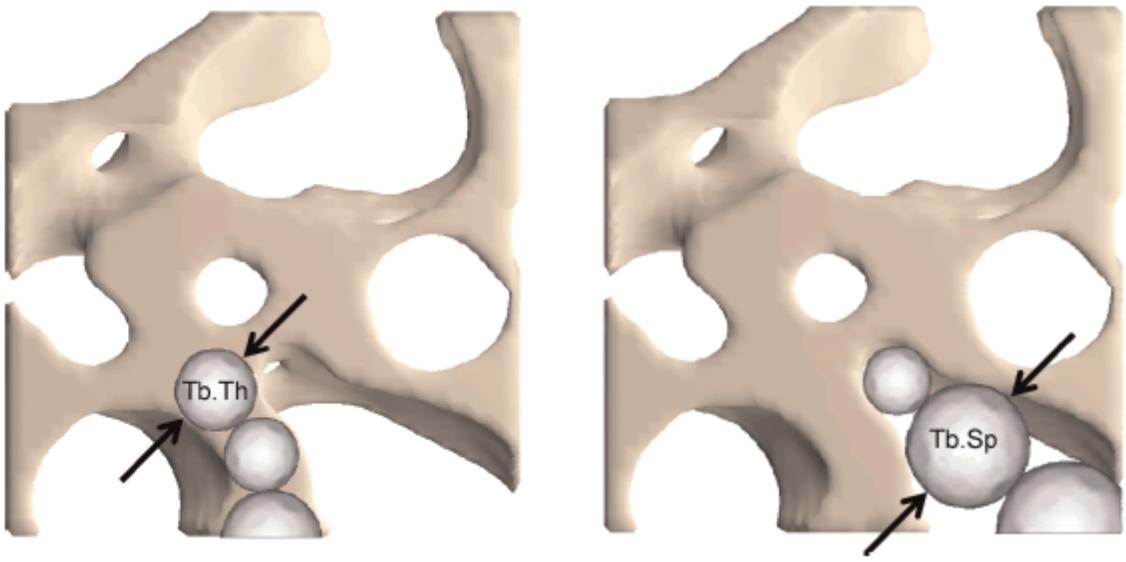

(a) Tb.Th sphere fitting (b) Tb.Sp sphere fitting

Figure 2.6: A 3D model showing the sphere fitting method for calculating Tb.Th and Tb.Sp using the 3D approach [14]

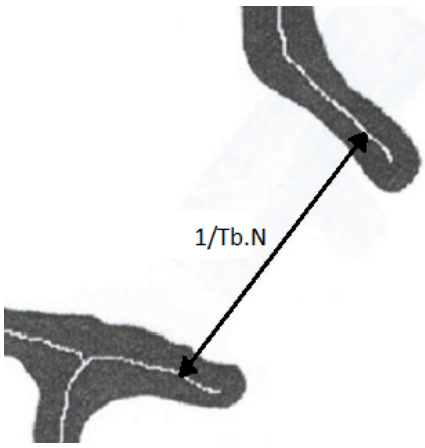

Figure 2.7: An illustration of the Tb.N mid-axis distance [26]

2.2 Architecture acquisition

As outlined in section 2.1.2, there are variables which should be included as a minimum in a study which uses μCT scanning to quantify cancellous bone architecture. The following sections demonstrate the effect of variables such as scanning equipment, scanning medium and image segmentation methods, on the outcome of the reported architectural parameters.

2.2.1 Image Acquisition Equipment

High-resolution μCT scanners are highly specialised imaging tools. Each machine has different specifications, and these specifications can affect the accuracy of the scanned images as well as the architectural parameters inferred from these images.

While μCT images provide an accurate, non-destructive method for determining architectural parameters of bone, prolonged exposure to high intensity X-rays is dangerous for living patients. As such, Teo *et al.* [28] conducted a study in which clinical-CT scans (150 μm resolution) were compared with μCT images (14 μm resolution). It was determined that parameters such as BV/TV correlated well between clinical- and μCT, but that others such as Tb.N and Tb.Sp only correlated moderately [28]. This is likely due to lower resolution images making it difficult to discern between bone and non-bone structures. As such, resolutions higher than 100 μm should be used when assessing the architectural parameters of cancellous bone [28].

Christiansen [29] studied the effect of voxel size on determining the microstructural parameters for cancellous bone in mice. The study compared images taken of the same structures at various voxel sizes, and found that lower resolution images became difficult to distinguish between bone and non-bone regions of the scan, causing inaccuracies and variability in the determined architectural parameters. Figures 2.8a and 2.8b show scans of the same structures at various voxel sizes. The images suggest that voxel sizes of 15 μm or less are required for accurate imaging on the bone samples.

Although the findings of Teo *et al.* [28] and Christiansen [29] do not agree with one another, the latter study was performed on mice while the first was performed on pigs. The larger animal has larger bones, which implies significantly larger trabeculae. This would therefore suggest that voxel sizes of 100 μm or less would be sufficient for any samples harvested from animals as large or larger than pigs.

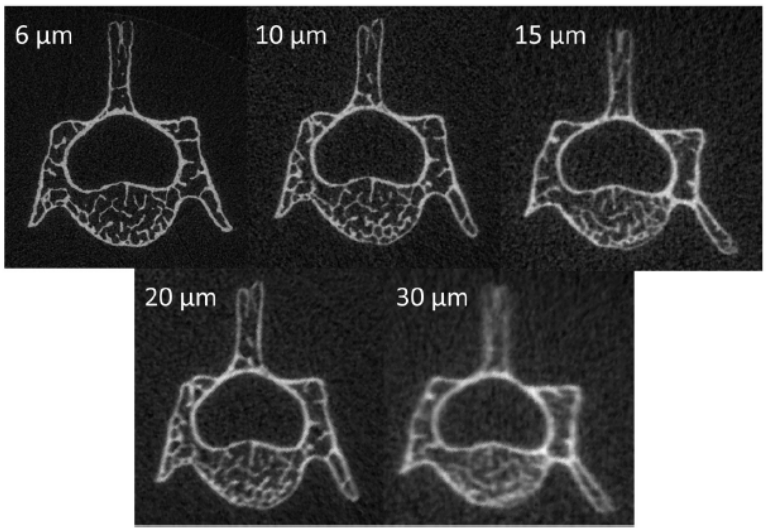

(a) μCT scanned 2D raw images of a mouse lumbar vertebra

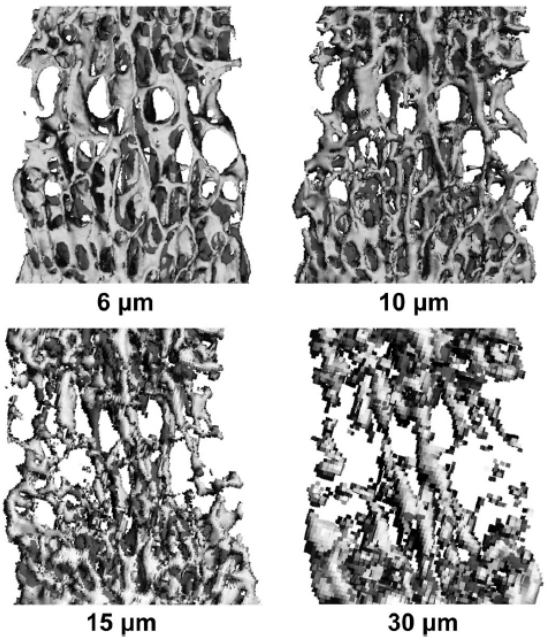

(b) 3D reconstruction of a cancellous bone sample shown in figure 2.8a

Figure 2.8: Images presented by Christiansen [29] depicting the differences between scans using varying voxel sizes - from 6 to 30 μm

2.2.2 Image processing

Image processing is required once μCT scans have been completed. This allows for the separation of cortical bone from cancellous bone, as well as other non-bone structures - such as marrow or other inclusions. Bone can have a complex structural organisation, and it is therefore important to ensure that any analysis is performed on the correct structures. This section describes the ways in which μCT images are segmented in order to yield the most accurate analysis of the structures.

2.2.2.1 Segmentation methods

Segmentation is process to achieve differentiation between bone types, as well as between bone and non-bone structures within a bone specimen. These structures include marrow or blood vessles, among others. For the purposes of this study, segmentation was limited to differentiating between bone and non-bone structures, or bone and bone marrow in the case of cancellous bone.

Segmentation of cancellous bone relies on binarising 2D scanned images, essentially classifying each voxel as either "bone" or "non-bone". Methods of segmentation range from manual to fully-automated [30].

Rathnayaka *et al.* [30] investigated the effects of different segmentation methods on the accuracy of long bone reconstructions from CT scans. It was concluded that although manual methods are simplest to implement, they allow for intra- or inter-personal variability of the data. Semi- or fully-automated segmentation methods rely on either edge detection techniques or image thresholding [30]. Canny edge detection was used in the study, shown in figure 2.9. As is seen in figure 2.9, some post processing was required by the user to correct for gaps within the image.

Rathnayaka *et al.* [30] performed image thresholding using a histogram approach on grayscale images. The histogram showed intensities of grayscale voxels, such as in figure 2.10.

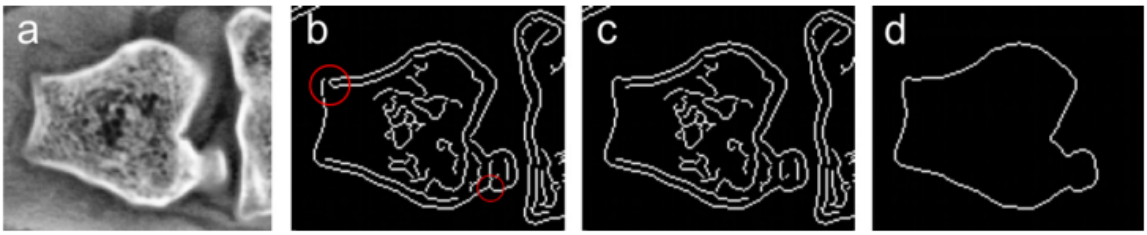

Figure 2.9: A graphical representation of Canny edge detection used to differentiate bone volume from the background of an image [30].

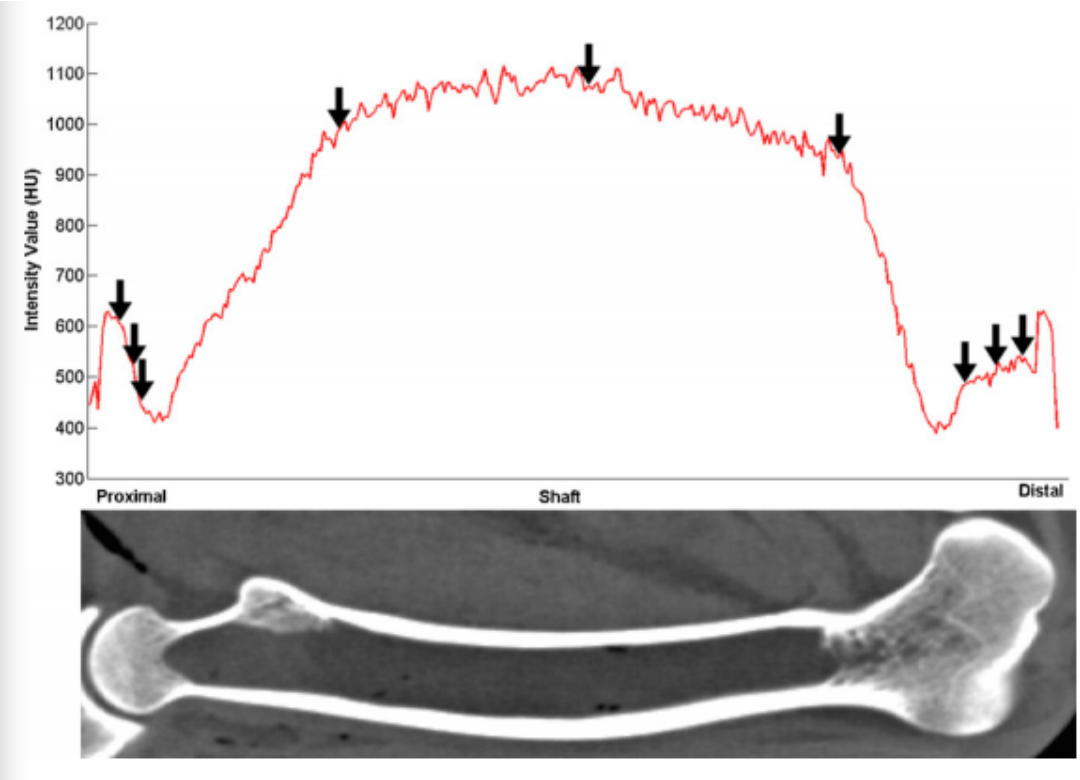

Figure 2.10: Grayscale intensity histogram of a femur, as presented by Rathnayaka *et al.* [30].

As seen in the image, the thicker regions of bone have higher voxel intensities, which correlate to the thick outer layer of cortical bone along the shaft of the femur. Lower intensities correspond to areas of cancellous bone, or thinner walled cortical bone. Histograms such as these were used to calculate multiple thresholding values, by using the values demarcated with arrows in figure 2.10 to segment each region of the femur [30]. A single threshold value was also applied to the same images based on an average intensity value for each 2D image. It was concluded that multi-threshold techniques produced the lowest errors for whole bones, followed by Canny filtering and single thresholding techniques [30]. Due to the labour intensive nature of manual thresholding and its tendency to produce user dependent variability, multi-thresholding techniques were deemed the most accurate measure of long bone reconstructions.

Christiansen [29] performed a study in which scanned images were segmented either manually by a skilled operator, or using the histogram method described previously. The segmented images were used to determine microstructural organisation of each of the bone samples. The study found that at higher resolutions (or smaller voxel sizes), both segmentation methods yielded similar results. However, at larger voxel sizes, the results diverged, as seen in figures 2.11a - 2.11d. The results suggest that the histogram method of segmentation is effective for voxel sizes of up to 10 μm.

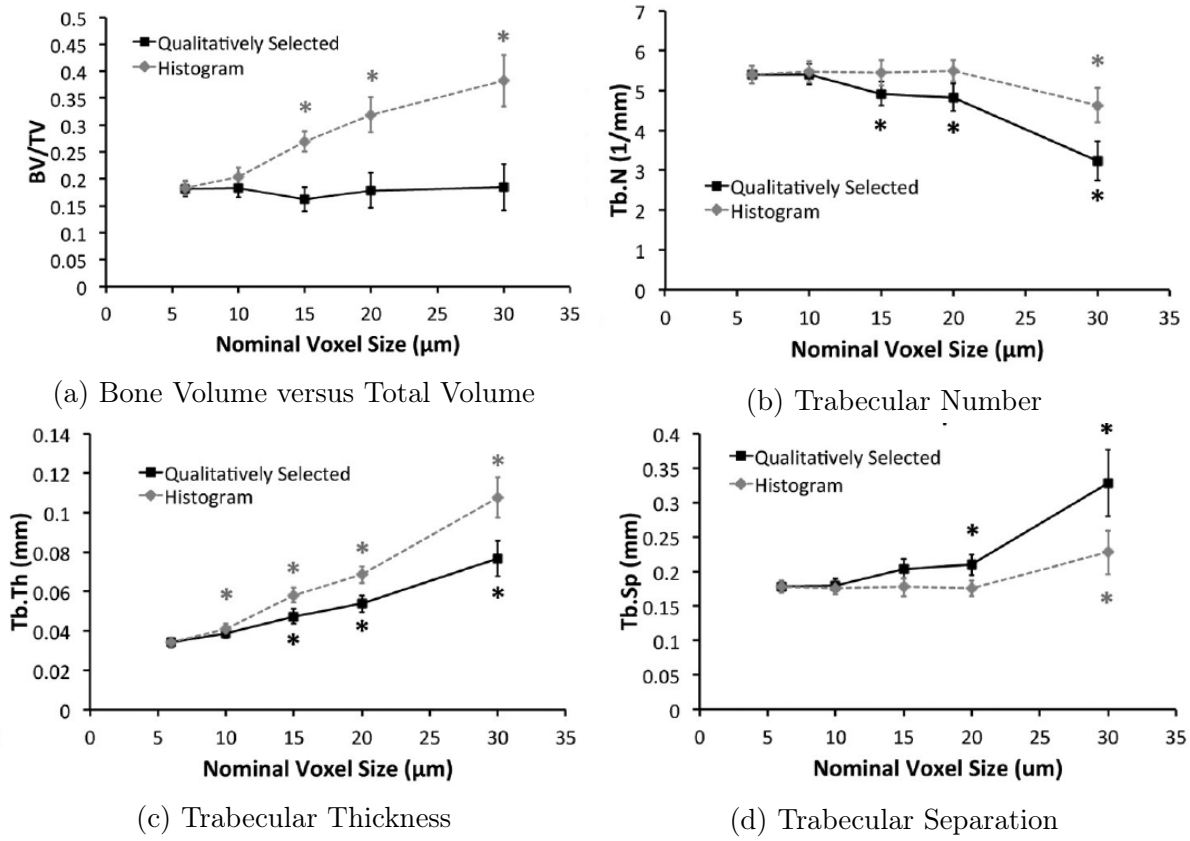

(a) Bone Volume versus Total Volume

(b) Trabecular Number

(c) Trabecular Thickness

(d) Trabecular Separation

Figure 2.11: Graphs showing the manually (qualitatively) selected segmentation method in comparison to the histogram segmentation method at different voxel sizes [29]

There are several multi-thresholding techniques which can be applied to CT images. One such method is Otsu's method, which is used in many commercial image processing programmes. A built-in function in MATLAB, *im2bw*, uses Otsu's method of thresholding. Otsu's method assumes that images have two pixel "classes", and uses intensity histograms to minimise the intra-class variance [31]. This method has the same effect as maximising the inter-class variance, therefore creating distinct differences between "bone" and "non-bone" regions, as shown in figure 2.12.

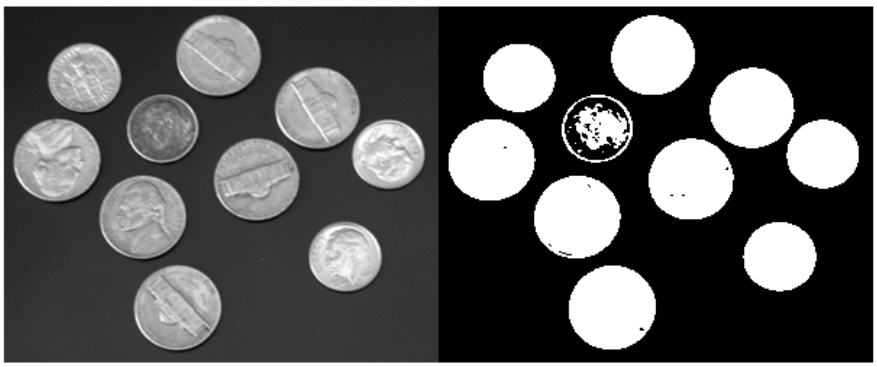

Figure 2.12: Grayscale image converted to binary using Otsu's method of thresholding [32].

2.3 Factors influencing mechanical response

When characterising the mechanical response of cancellous bone, it is important to note the factors which may influence this response. As discussed previously, bone is a complex, biological structure and as such, there are many factors which affect the strength of cancellous bone.

The following sections discuss both intrinsic and extrinsic factors which influence the response of cancellous bone to mechanical loading, and therefore its mechanical properties such as Apparent Modulus and Ultimate Stress.

2.3.1 Intrinsic factors

2.3.1.1 Architectural parameters

Section 2.1.2 detailed architectural parameters for cancellous bone as well as the way in which these parameters are computed. Multiple studies have investigated the effect that these parameters have on the response of cancellous bone [3, 18, 20–25, 28, 28, 33–46]. Many of these studies have found that mechanical properties are far better predicted when taking architectural parameters into consideration along with other factors.

Cendre *et al.* [33] performed compression testing at quasi-static strain rates on cubed cancellous specimens. Specimens from the same bones were extracted and analysed using histomorphometry and high-resolution computed tomography (HRCT) to find the architectural parameters. A significant correlation between compressive strength and architectural parameters determined using these imaging methods was observed, however, it should be noted that the same specimens which were compressed were not tested for architecture. Although specimens were taken from the same bone, slightly adjacent specimens could have differing architectural parameters, and it would therefore be more beneficial to perform imaging methods on specimens which are tested directly.

Charlebois [3] noted a significant improvement in the prediction of ultimate strain as well as yield strain when more than one architectural parameter was accounted for in samples. Prot *et al.* [20, 43] agreed with this finding, concluding that architectural parameters are strong predictors of mechanical response of trabecular bone.

Nazarian *et al.* [42] performed step-wise micro-compression testing on human lumbar vertebral specimens. μCT imaging was completed in combination with these compression tests in order to capture the failure behaviour of the specimens. Figure 2.13 shows the scanned images of a specimen after each compression step.

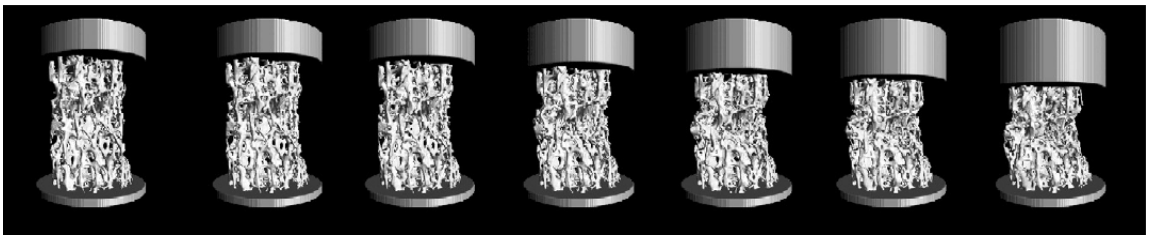

Figure 2.13: 3D reconstructions of the compression steps of a single cancellous bone specimen, adapted from Nazarian *et al.* [42]. Steps (from left to right) are 0, 2, 4, 8, 12, 16 and 20% strain.

These scanned images were analysed for architectural parameters such as BV/TV, Tb.Th and Tb.N, amongst others. Each specimen was divided into subregions, as shown in figure 2.14, and was examined for failure in each of these regions. The failure regions were then compared to the architectural parameters for each region, and a maximum likelihood estimation (MLE) used to predict failure based on each of the architectural parameters measured.

Figure 2.15 shows the way in which probability of failure varies with a change in architectural parameters such as BV/TV, Conn.D and H_1 in each subregion. H_1 is the tertiary eigenvector for the bone sample, which indicates a magnitude and direction in which the least amount of bone is orientated [47]. It is clear that across all varying architectural parameters, the probability of failure decreases as BV/TV increases. This suggests that a bone will break at its weakest link, regardless of the whole bone structure.

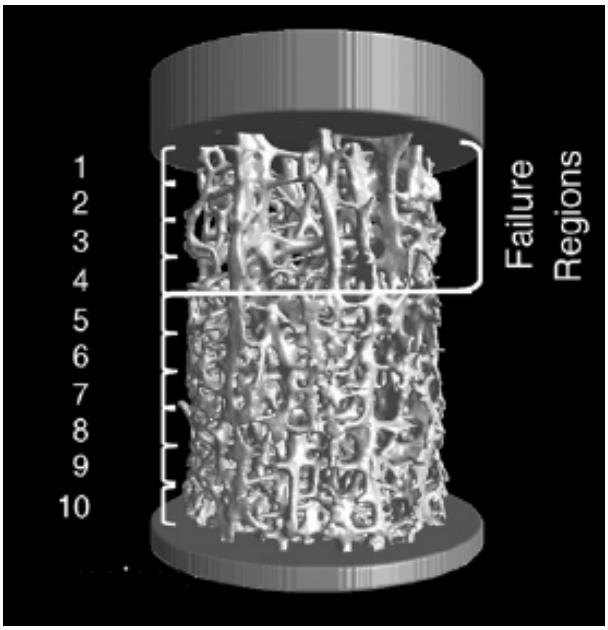

Figure 2.14: AN image of the subregions assigned to compressive specimens, adapted from Nazarian *et al.* [42].

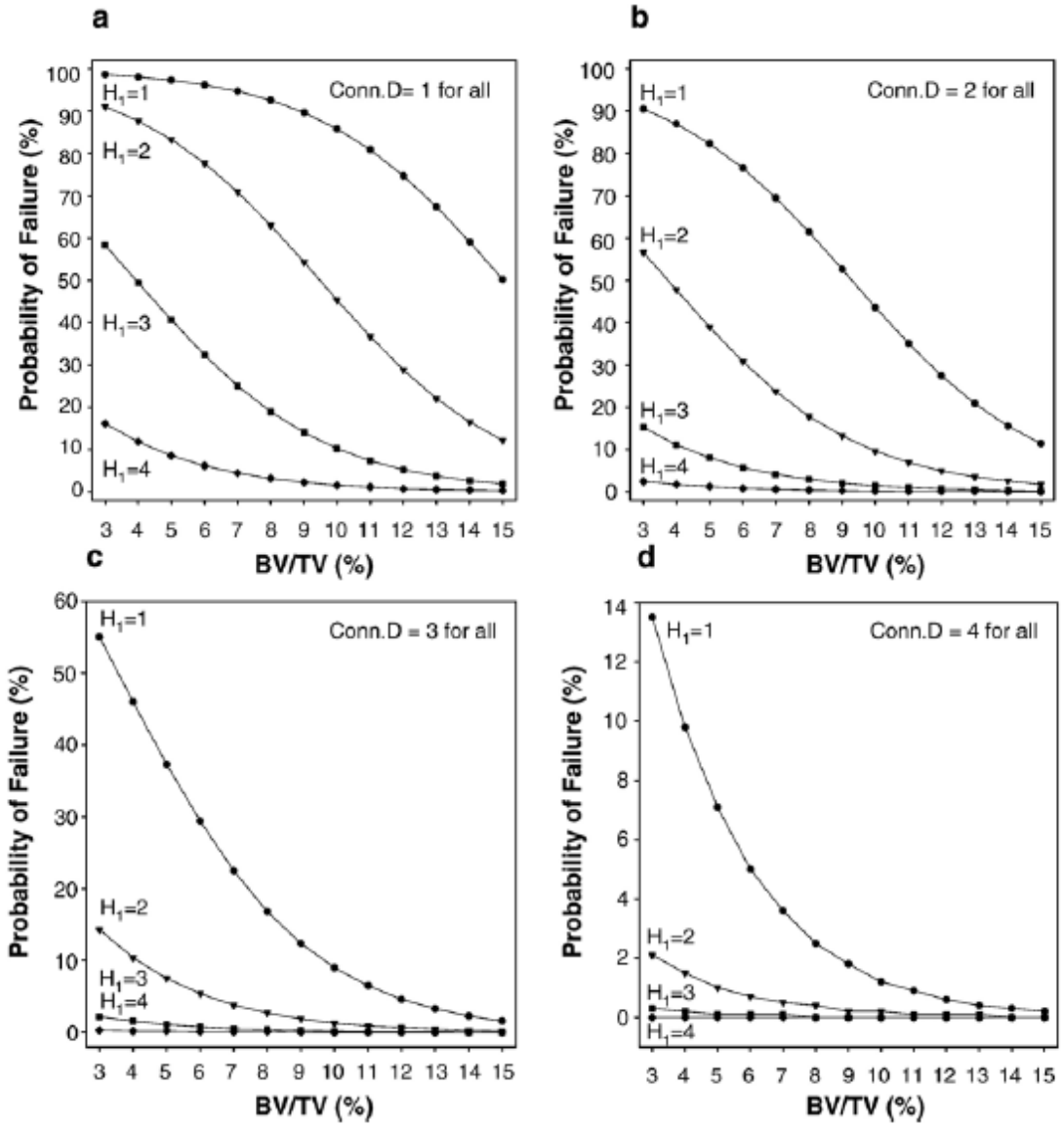

Figure 2.15: Graphs showing the dependence of probability of failure on various architectural parameters [42].

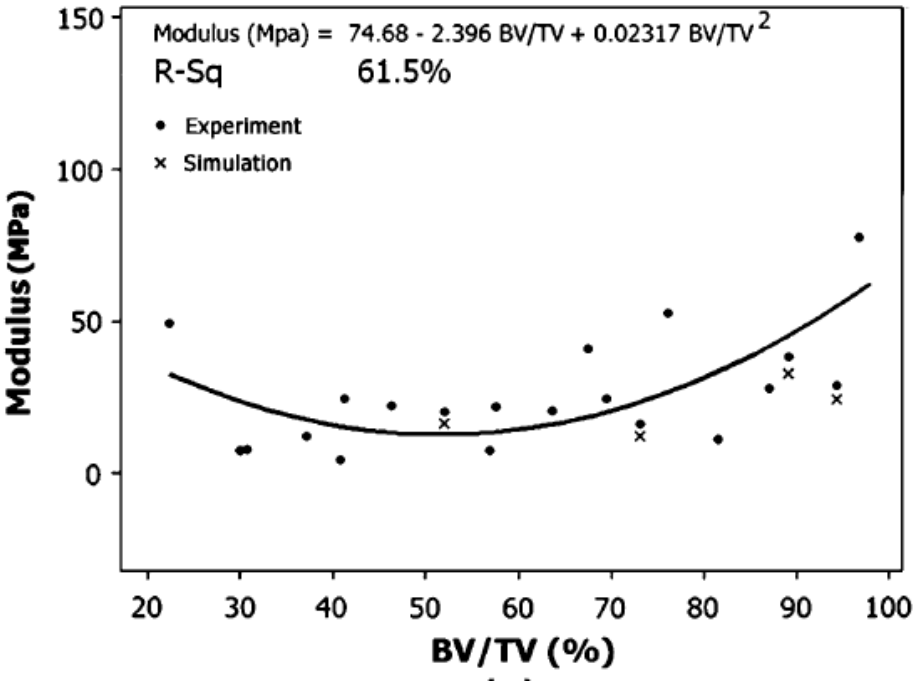

Figure 2.16: A graph showing the experimental versus numerical results by Syahrom *et al.* [22] showing the dependence of cancellous bone modulus on BV/TV.

Syahrom *et al.* [22] investigated the effects of architectural parameters on trabecular bone using both experimental and simulation studies. Compression tests were performed on cylindrical, defatted specimens at a constant strain rate of 0.001 s^{-1}. A subset of the specimens were scanned using μCT, from which 3D models and finite element (FE) simulations were created. Three distinct types of failure mechanism were reported during mechanical compression; namely oblique, global and local fracture [22], however, no correlation was found between the architectural parameters and the type of failure. The numerical results seemed to correspond with the experimental data collected, as shown in figure 2.16, however, the simulation data set was small compared to the overall sample size (4 numerical versus 24 experimental).

2.3.1.2 Anatomical site and orientation

Different bones in the skeleton perform different functions, and as such, have structural differences which influence the mechanical response. The dependence of the mechanical response of trabecular bone on anatomical site has been studied by various authors [3, 24, 27, 38, 42, 48].

Morgan and Keaveny [48] investigated the effect of anatomical site on the strength of cancellous bone by performing compressive and tensile tests on cylindrical specimens from various anatomical sites. Various mechanical properties were found to be dependent on anatomical site, with 20% variance for yield strain, and a factor of 8 and 10 for yield

stress and modulus respectively between anatomical sites. Morgan and Keaveny also observed little *intra*-site variance in these properties, despite specimens being harvested from multiple age categories and from both men and women [48].

Charlebois [3] conducted an experimental and numerical investigation on human cancellous bone from different anatomical sites. After CT scanning each specimen, architectural parameters were plotted against one another for each site, as shown in figure 2.17a. This image shows distinct regions for each anatomical site, and as discussed previously, architectural parameters of bone specimens have significant influence on the mechanical response of each specimen. Visually, figure 2.17b shows the difference in architectural organisation between cancellous samples taken from different anatomical sites. The difference in organisation depending on anatomical site suggests that each of these sites would exhibit similar grouping when mechanical response to compressive stresses was compared. This was observed in the experimental results, as shown in comparison to the results of the numerical model for modulus as yield stress, presented in figure 2.18. As seen in the results, distinct groups are apparent for each anatomical site - with the distal radius and femoral head showing the greatest strength results.

Nazarian *et al.* [42] and Hildebrand *et al.* [27] both concluded that the lumbar spine has the lowest average BV/TV when compared to other anatomical sites.

2.3.1.3 Apparent density

Apparent density refers to the mass of a sample divided by the total volume, including all pores and voids which are inherent to the structure [49]. For bone samples, especially cancellous bone, apparent density is much simpler to determine than true density. True density requires submersion of samples due to the complex nature of the trabecular network, whereas apparent density requires only overall dimensions and weight of a sample. Apparent density has been found to have an effect on the mechanical response of cancellous bone, and is therefore an important variable to consider when performing experiments.

Cendre *et al.* [33] and Garrison *et al.* [35] observed a significant correlation between maximum compressive strength and apparent density. Kasra and Grynpas [50] observed a proportional relationship between the shear strength of cancellous bone and apparent density raised to the power of 1.02. Similarly, shear modulus was found to be proportional to apparent density raised to the power of 1.08. Correlations between apparent density and the mechanical properties measured were found across all strain rates, as shown in figure 2.19.

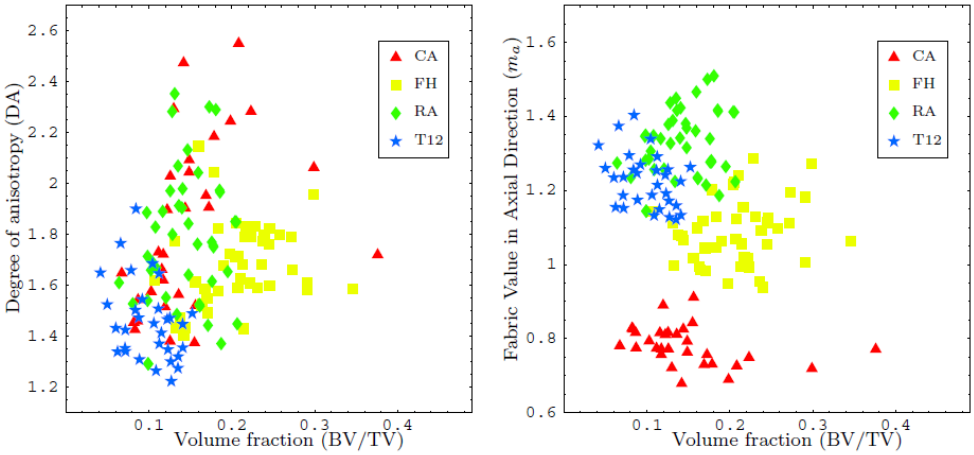

(a) Graphs showing the relation between volume fraction and degree of anisotropy (left) and axial fabric (right) [3]. CA: Calcaneous, FH: Femoral Head, RA: Distal Radius, T12: 12th Thoracic Vertebra

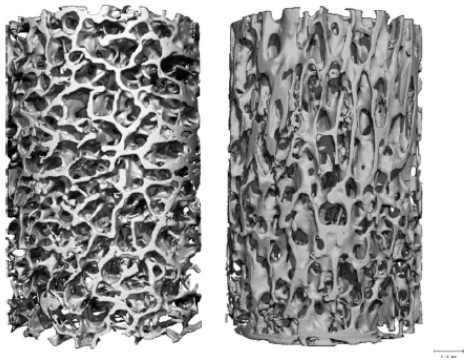

(b) 3D reconstruction of cancellous bone samples taken from two anatomical sites - left: calcaneous, right: distal radius [3]

Figure 2.17: Differences in architecture observed for different anatomical sites [3]

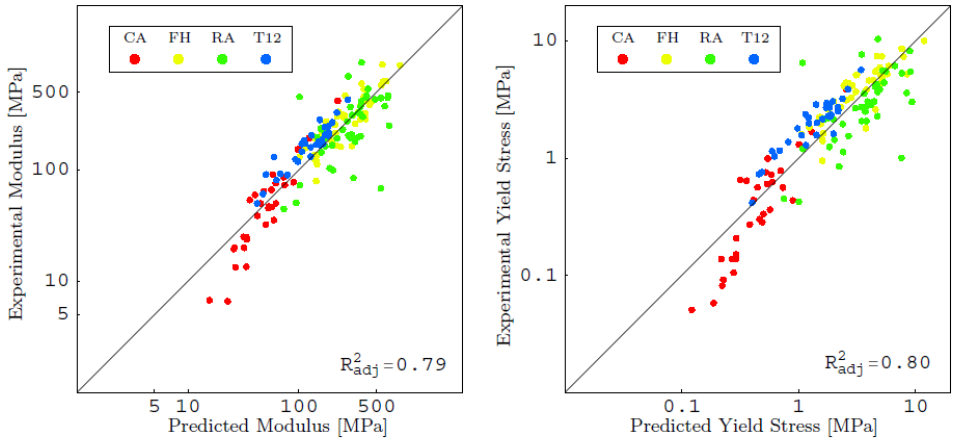

Figure 2.18: Graphs showing the experimental versus numerical results by Charlebois [3] showing distinct differences in mechanical response over different anatomical sites.

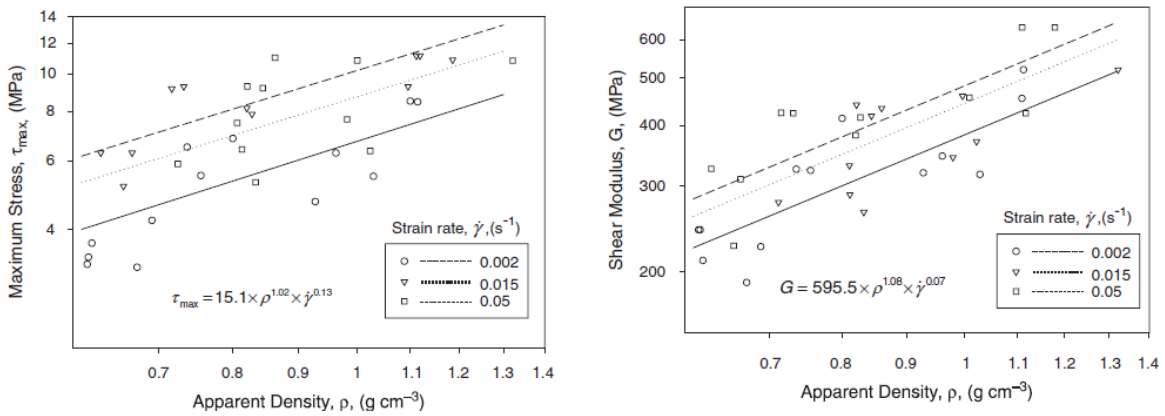

Figure 2.19: Graphs showing the results of apparent density versus maximum torsional stress and Shear Modulus as presented by Kasra and Grynpas [50]

Kopperdahl and Keaveny [51] investigated the hypothesis that apparent density has no influence on the yield strain of cancellous bone subjected to on-axis loading. The study consisted of 22 tensile and 22 compressive tests performed at a strain rate of 0.005 s^{-1} on 8 mm diameter human cancellous bone specimens cut from T10-L4 vertebrae. The cylindrical specimens were nominally 25 mm long, with the end 5 mm of each end glued into a brass end cap to eliminate end artefacts. The relevant measurements are highly sensitive to end artefacts, and therefore achieving accurate results without securing the specimen ends would be difficult [52]. The data collected from the human cancellous bone samples was compared to bovine data collected previously. The study disproved the hypothesis, with findings showing a linear correlation between apparent density and yield strain for both human and bovine cancellous bone. However, as shown in figure 2.20, the tensile tests showed no dependence on apparent density.

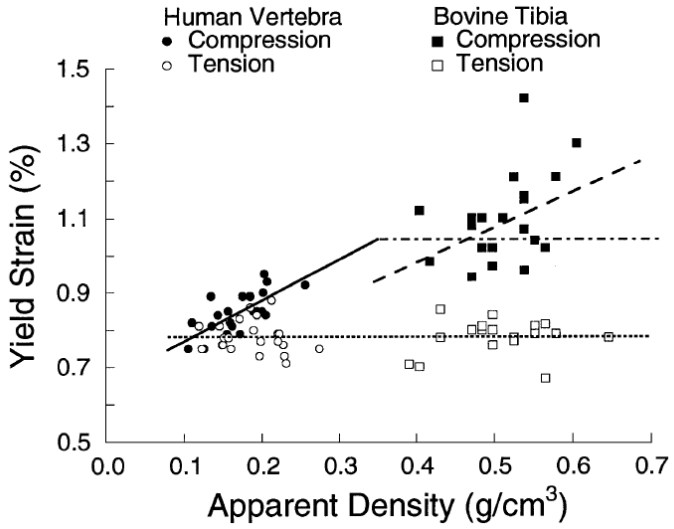

Figure 2.20: A graph showing apparent density versus yield strain results from the study conducted by Kopperdahl and Keaveny [51].

2.3.2 Extrinsic factors

2.3.2.1 Strain rate

Strain rate dependency is an important factor when considering the strength of bone, as it has often been described as a visco-elastic material. There are two distinct strain rate regimes, namely quasi-static and dynamic strain rates. Quasi-static strain rates are less than 1 s^{-1}, while dynamic strain rates are split into the intermediate range, 1-100 s^{-1}, and the high strain rate range, greater than 100 s^{1}. Numerous studies have investigated the effect of strain rate on the mechanical response of bone [9,37,50,53–56]. For the purposes of this study, the quasi-static regime will be considered. These strain rates correspond to those experienced while walking, running, and even some impact fractures [9].

Kasra and Grynpas [50] performed an experimental torsion study using cylindrical specimens of sheep cancellous bone. Three quasi-static strain rates were investigated, namely 0.002 s^{-1}, 0.015 s^{-1} and 0.05 s^{-1}. The results of the investigation showed a significant increase in shear modulus and shear strength with an increase of strain rate.

Cloete *et al.* [57] investigated the strain rate dependence of bovine cortical bone. The study spanned a range of strain rates from quasi-static through to dynamic, including an intermediate range which was previously lacking data in the literature. The results of the investigation showed an increase in Young's modulus as the strain increased, showing a distinct transition in the mechanical properties between the quasi-static and intermediate strain rate ranges. Figure 2.21 shows this trend, with the intermediate strain rate range highlighted in the red box.

Prot *et al.* [54, 55] investigated the strain rate dependence of cancellous bone, focussing on the intermediate strain rate range. Experimental testing was performed using two techniques developed by Cloete *et al.* [57], namely the split Hopkinson pressure bar (SHPB) and the Wedge-Bar. The data collected in the studies was consistent with similar data in the literature, with the dynamic strain rates showing non-linear response of cancellous bone. However, the intermediate strain rate ranges have been under-represented in the literature. Therefore, the data collected could not be compared. Figure 2.22 shows the results presented by Prot *et al.* [55]. The graph indicates a clear strain rate dependence of ultimate stress (σ_u).

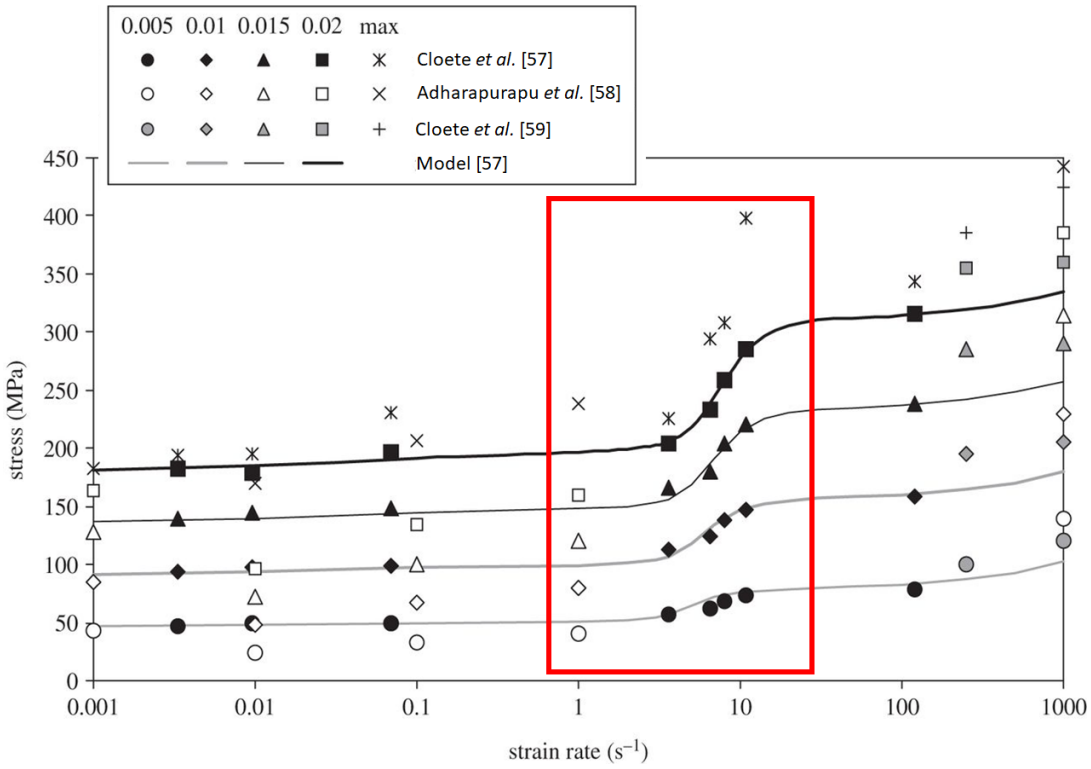

Figure 2.21: Data presented by Cloete *et al.* [57], including data from references [58, 59], showing the strain rate dependence of the Young's modulus of bovine cortical bone. Red box indicates intermediate strain rate range.

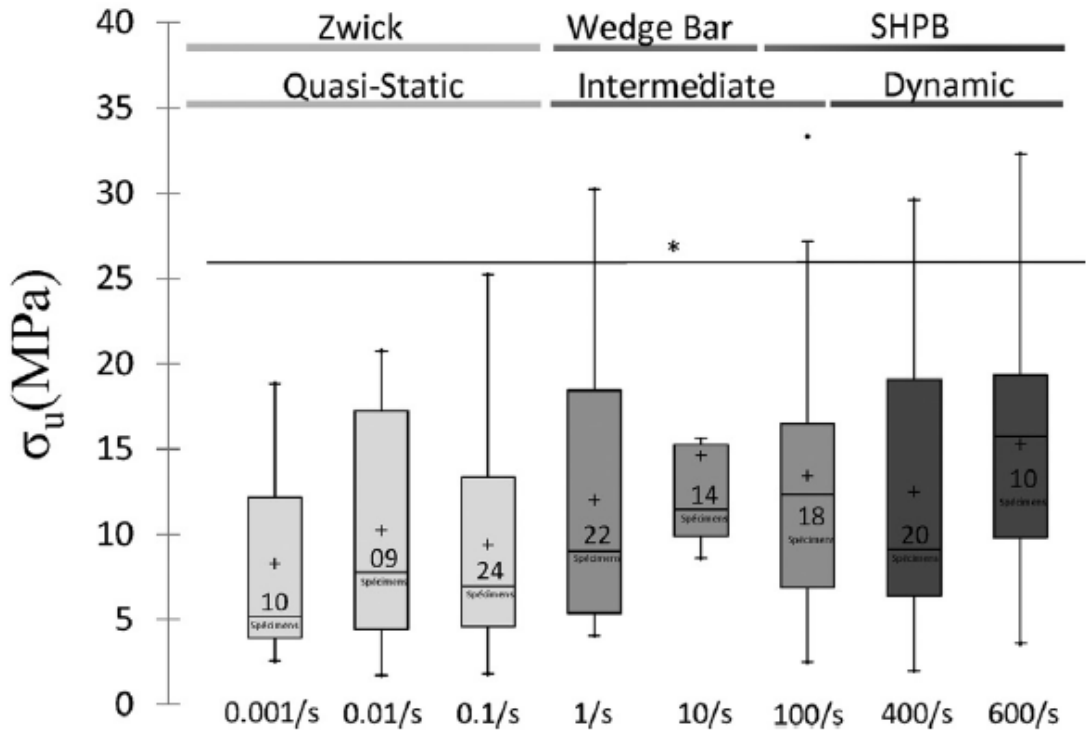

Figure 2.22: A box and whisker plot showing ultimate stress of specimens compressed at different strain rates, from Quasi-Static to Dynamic, adapted from Prot *et al.* [55].

2.3.2.2 Boundary conditions

Boundary conditions of a bone sample affect the way in which the sample reacts to loading. Certain boundary conditions, such as confinement, may help the sample resist fracture and contain the bone marrow within the sample, which could better represent the *in vivo* conditions of whole bones. Other boundary conditions, such as edge effects, could cause stress concentrations in certain bone sample geometries. It is therefore important to consider the boundary conditions of bone samples, both when performing experimental tests and when undertaking numerical simulations.

Chaari *et al.* [2] investigated compression of trabecular samples using both open cell (unconfined) and closed cell (confined) testing methods, experimentally and using FE models. Specimens were cut from from bovine rib bones. The unconfined configuration allowed marrow to escape from within the specimen during compression without changing the specimens response, while the confined configuration aimed to mimic *in vivo* boundary conditions by preventing marrow and other fluid from being expelled from the sample during compression. During sample compression, three distinct loading stages were observed, as shown in figure 2.23.

It was concluded that the effect of the boundary condition had little significance during the initial loading stage for the specimen. However, a comparison of the confined and unconfined methods over the entire loading of the specimen showed a significant decrease in stress in the specimen for unconfined compared to confined specimens. Figure 2.24 shows the similarity between both methods during the initial loading stage, as well as the difference in stress during the rest of the compression.

The numerical investigation was performed using μCT scanning to acquire the

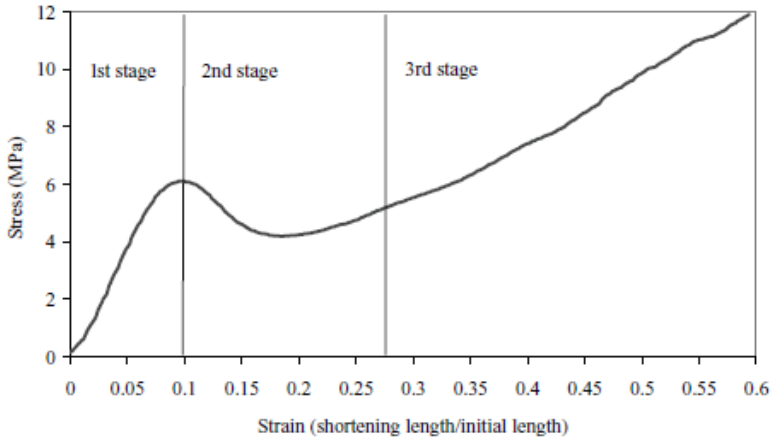

Figure 2.23: A graph showing the compression stages of cancellous bone as presented by Chaari *et al.* [2]

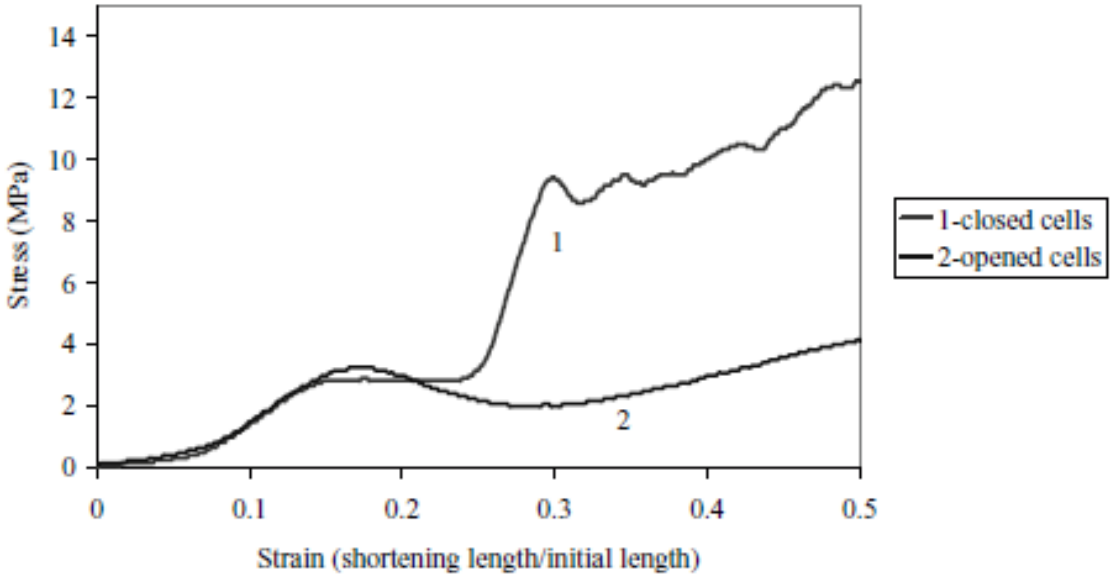

Figure 2.24: A graph showing Stress-Strain curves for compression tests of cancellous bone presented by Chaari *et al.* [2]

architectural organisation of each specimen. The finding that there was no significance between boundary conditions in the initial loading stage of the specimens led the authors to neglect the effect of the boundary condition and fluid interaction on the behaviour of the specimen in the FE models. An example of the results from this model is shown in figure 2.25.

Although the study showed good correlation between boundary condition and mechanical response, the specimens used were a combination of both cancellous and cortical bone. Therefore, the authors' claim that the compression tests performed represent the response of cancellous bone alone is questionable. The FE models were only performed using the architecture of the cancellous bone, and therefore do not accurately represent the

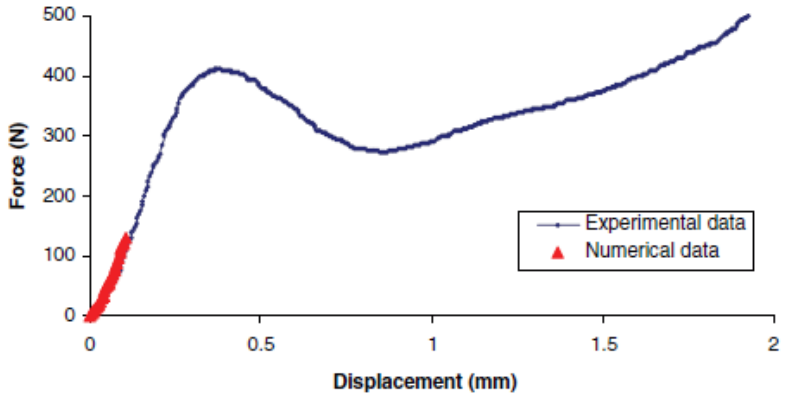

Figure 2.25: A graph showing the numerical results in comparison to the experimental force-displacement curve [2]

compression tests performed.

Charlebois [3] tested human cancellous bone in compression both with and without confinement, as described in section 2.3.1.2. Confinement was achieved using simple stainless steel confinement tubes, where each specimen was fitted into several confinement tubes with varying inner diameters until the "best fit" for each specimen was found. The specimens were glued to metal rods which were fixed to the testing machine using hydraulic grips, as shown in figure 2.26. During this investigation, it was observed that there was no statistical difference between samples which were confined versus those which were unconfined, with both datasets showing large variability.

Kelly and McGarry [4] investigated the confinement effect experimentally, using a setup as shown in figure 2.27. Specimens used in the study were not bone, but were rather made from polyurethane foam which is commercially available and used as a cancellous bone analogue. The study was augmented with a material model and simulations, and it was concluded that confinement has a significant effect on the mechanical properties due to high confinement pressures during compression. While the experimental results contradict those of Charlebois [3], it must be noted that the experiments in the study performed by Kelly and McGarry [4] were not performed on cancellous bone. The analogue material is more uniform than cancellous bone and this likely caused a significant reduction in variability when compared to that seen by Charlebois.

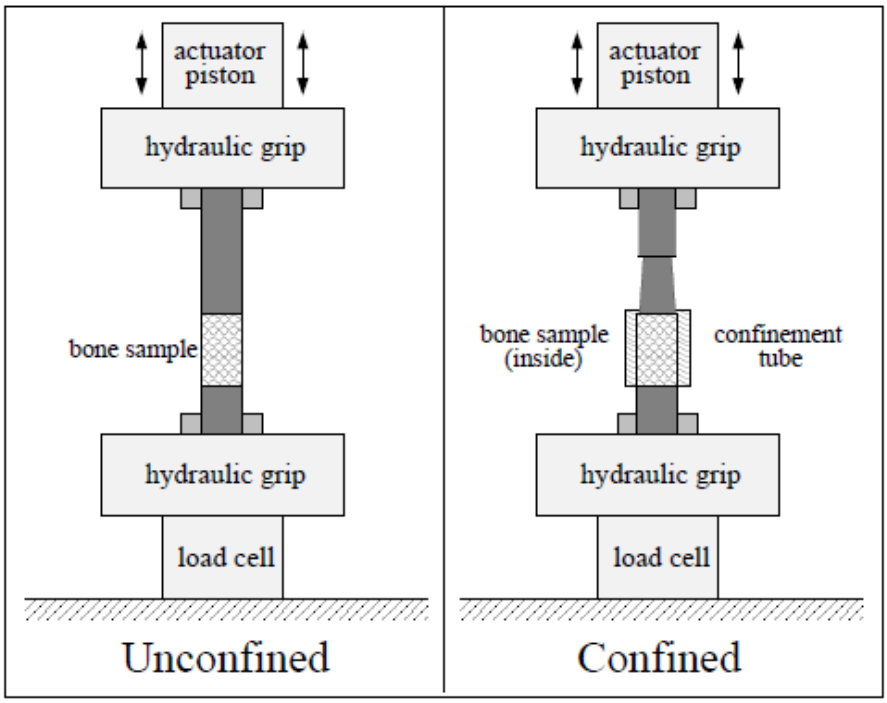

Figure 2.26: A schematic of the experimental setup used by Charlebois [3] to compress unconfined and confined specimens

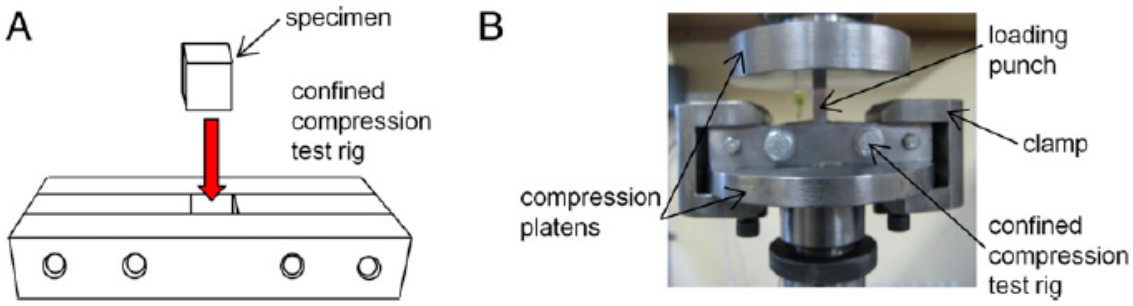

Figure 2.27: A schematic an photographs of the experimental confinement setup used by Kelly and McGarry [4]

Harrison and McHugh [5] modelled bone as cored samples as well as part of a whole bone. Figure 2.28 shows the distribution of minimum principal strain throughout an independent sample as well as a sample within a whole bone. As clearly seen in the image, deformation was concentrated around the circumference of the core in the independent specimen (shown by the black arrow). The box and circle also highlight the difference in loaded trabeculae, with the whole bone sample showing larger deformations throughout the specimen when compared to the minimally loaded struts seen in the independent sample. It was therefore concluded that edge effects played a significant role on the response of cancellous bone, with the results showing a 17.4-20.4% increase in apparent modulus of samples within whole bones as compared to individual samples.

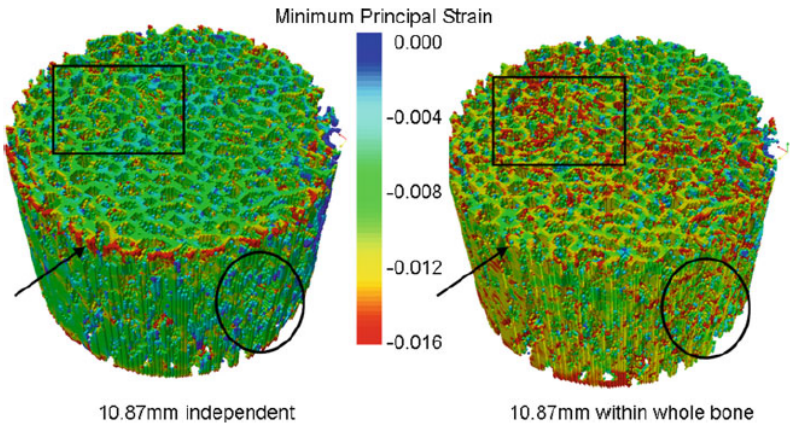

Figure 2.28: An image showing a comparison of simulation results for an independently cored sample and a sample within a whole bone as presented by Harrison and McHugh [5]

2.3.2.3 Presence of marrow

Various studies have investigated the effect of marrow on the mechanical properties of cancellous bone [6, 7, 9, 10, 60]. Many of these have been simulation studies. However, without experimental data to validate these simulations, the results of the studies cannot be proven to be valid.

In one such simulation study, Chen *et al.* [6] investigated the effect of marrow on the mechanical response of cancellous bone. The results of the study showed that the presence of marrow in specimens contributed to a maximum stress of 3-9% lower than those without marrow, while the average stress of specimens containing marrow was found to be 9-56% larger than those without marrow present. Chen *et al.* [6] therefore concluded that the presence of marrow cannot be neglected in simulation studies.

Ma *et al.* [7] also performed a simulation study to investigate the effect of marrow. Ma *et al.* concluded the opposite result to Halgrin *et al.*. The simulation study assumed that both bone and marrow were linear elastic materials - uni-axial compression simulations were performed at constant strain rates. This assumption likely caused inaccurate results as neither bone nor marrow has been proven to be linear elastic under compression. Figure 2.29 shows a comparison of the simulations with and without marrow. As seen in the image, the specimen without marrow experienced "unbalanced" stress distribution within its trabeculae, meaning that the trabeculae were more likely to fracture [7]. It was concluded that cancellous bone with marrow had a 7.56% - 18.81% higher maximum stress and that the presence of marrow may decrease the risk of bone fracture.

Metzger *et al.* [39] conducted a similar simulation study, in which the interaction between the bone-marrow interface was investigated. Cubic samples of porcine trabecular bone were harvested and scanned using μCT, from which numerical models were built. It was found that during compression, the shear stress at the interface between bone and

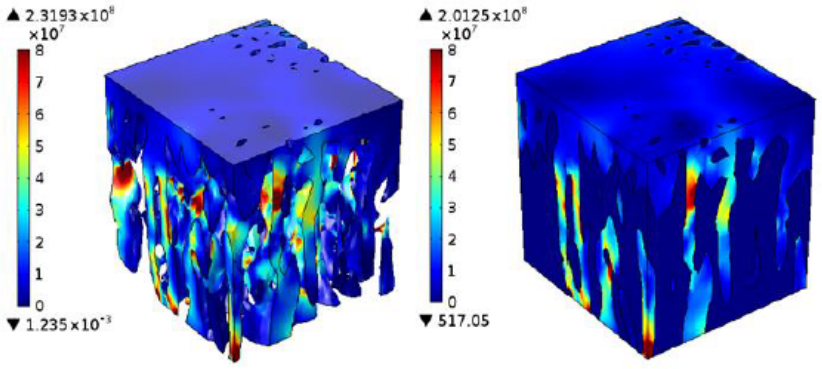

Figure 2.29: Simulation images of the von Mises stress distribution for a specimen without marrow (left) and with marrow (right) as presented by Ma *et al.* [7]

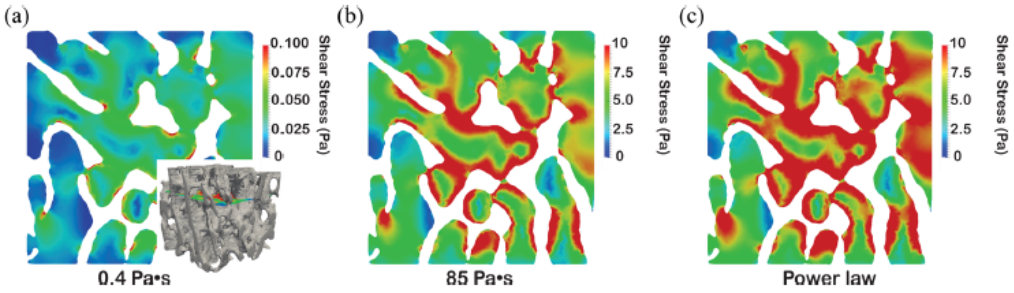

Figure 2.30: Images of results of the simulation performed by Metzger *et al.* [39] showing the interaction between marrow and bone in a trabeular bone network

marrow was highest, with the stress decreasing further away from this interface, as shown in figure 2.30. The white spaces in the image indicate trabecular bone, while the marrow is presented showing a shear stress distribution at various modelled viscosities. As seen in the image, the shear stress is dependent on viscosity, but the same pattern exists across all viscosities - shear stress decreases further away from the bone-marrow interface.

A number of studies have performed mechanical testing in order to investigate the effect of marrow on the mechanical properties of cancellous bone. Some were conducted to augment simulation studies.

Carter and Hayes [9] conducted an experimental study on human and bovine bone in which specimens were compressed both with and without marrow at various strain rates. The study concluded that the presence of marrow did not affect the strength, modulus or energy absorption of the specimens at lower (quasi-static and intermediate) strain rates. However, the presence of marrow showed a marked increase in these properties for the dynamic strain rate of 10 /s - compressive strength increased by approximately 350%, compressive modulus increased by approximately 390%, and energy absorbed at 50% strain increased by 290%.

Halgrin *et al.* [10] conducted a study to investigate the effect of marrow on the response of cancellous bone. 48 cubic samples (8.7 mm^3) were extracted from bovine ribs and were compressed immediately after specimen preparation. All 48 specimens were compressed at a strain rate of 0.1 s^{-1}. 24 of these specimens had their marrow removed prior to testing. The specimens were compressed between two pieces of steel, which the authors claimed simulated the confinement of cancellous bone within cortical layers. However, specimens were left unconfined on all other faces. The results showed that the effects of marrow could not be ignored as the two groups showed statistically significant differences - cancellous bone was significantly stronger in terms of maximum compressive stress, elastic modulus and other mechanical parameters when marrow was extracted from the specimen.

2.4 Specimen preparation and treatment

2.4.1 Pre-testing storage

There are a variety of methods for storage of bone samples, both with and without marrow. However, this range of techniques have led to inconsistencies in data reported and collected in the literature [8]. To reduce these inconsistencies, it is necessary to store specimens using physiologically relevant methods which preserve the natural interactions between cells, the extracellular matrix and the intercellular fluid.

It is common practice in bone studies to either wrap bone samples in gauze soaked with physiological saline solution (0.9% NaCl), or to completely submerge the samples in the same solution before freezing [19]. This is thought to mimic the *in vivo* conditions of the bone, while preventing the samples from decaying prior to testing. This is especially helpful if μCT scanning needs to be undertaken between specimen harvesting and testing. Freezing is typically set to -20°C as this temperature maintains the mechanical properties of bone [22, 28].

Metzger *et al.* [8] investigated the effects of storage and post-mortem time on bone marrow. A total of 18 porcine femurs were used for the study, 12 of which had fresh marrow specimens harvested 8 hours post-mortem. The remaining 6 femurs were frozen at -30°C for 5 days, before being thawed for 3 hours at room temperature in order to collect marrow samples. Both sample sets were tested for mechanical properties, viscosity and for the effect of freezing on the cells by staining and examining them under a microscope. It was concluded that the viscosity of the fresh marrow was an order of magnitude greater than that which had been frozen and thawed. This was found over a range of shear rates, as shown in figure 2.31

It was also found that the adipocyte (fat cells) membranes were disrupted. In figure 2.32, the differences between fresh and frozen cells stained and examined using two different stain types are observed. The image shows a higher lipid content in the fresh, Oil Red O stained cells, indicating the disruption of the adipocyte membrane in the previously frozen sample. The Trypan Blue stained previously frozen sample also shows that the adipocytes have absorbed the stain, which indicates disruptions in the cell membrane - whereas the fresh cells show almost no stain absorption within the cell.

While the study performed by Metzger *et al.* [8] proves that freezing specimens affects the properties of marrow, no attempt was made during the study to store the frozen bones in any sort of fluid medium to prevent cells from drying out. This is likely the reason for the disruptions in the adipocyte membranes, as fluid may have leached out of the cells during freezing and thawing which could not be replenished as it would be *in vivo*.

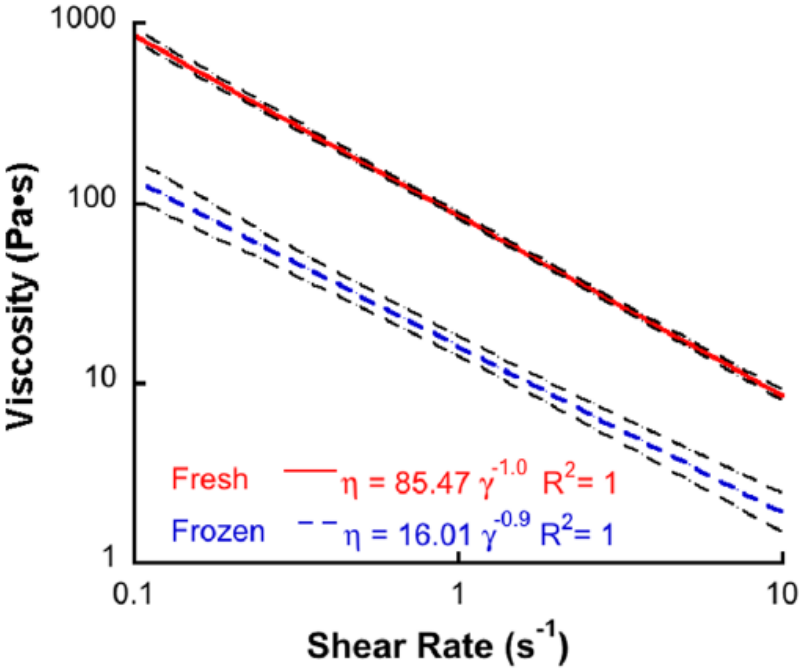

Figure 2.31: A graph showing a comparison the viscosity of fresh and previously frozen marrow over a range of shear rates as presented by Metzger *et al.* [8]

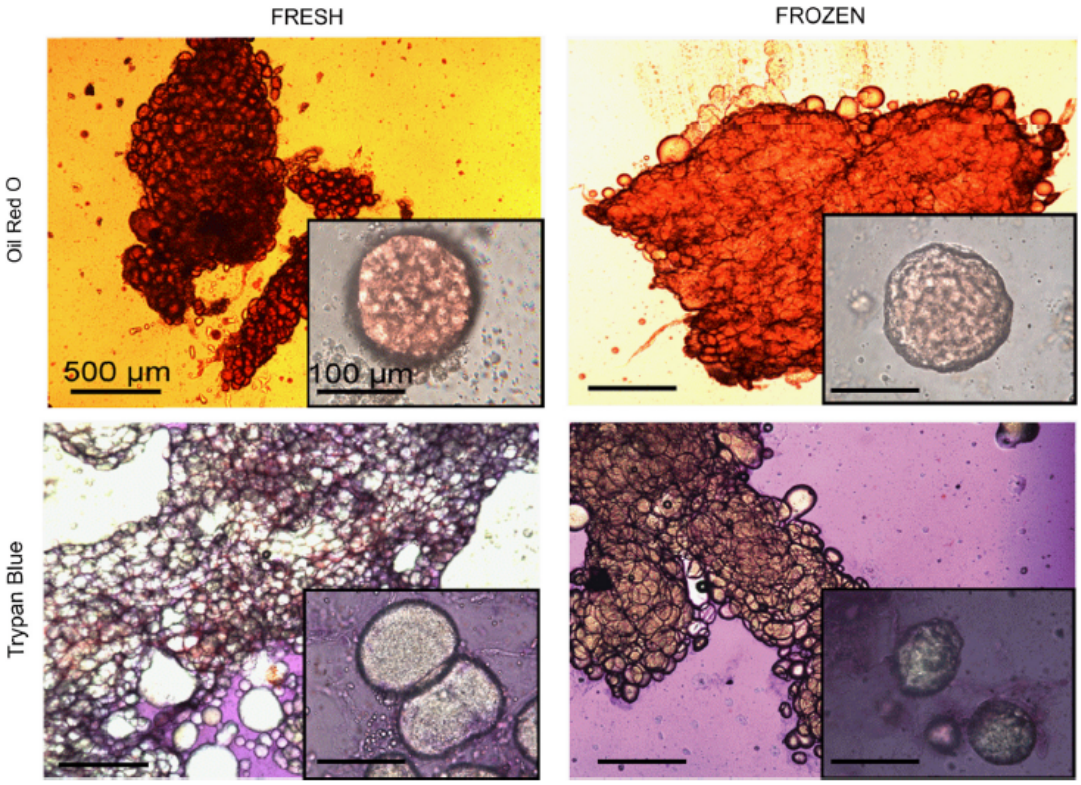

Figure 2.32: Microscope images of Oil Red O and Trypan Blue stained fresh and frozen marrow samples [8]

2.4.2 Testing temperature

Testing temperature is important to consider if mechanical tests on cancellous bone are to represent the *in vivo* properties of the complex material. Both bone and marrow may have temperature dependencies which need to be considered when investigating the mechanical properties of cancellous bone.

Metzger *et al.* [8] investigated the effect of temperature on the viscosity of porcine bone marrow. Figure 2.33 shows the dependence of marrow viscosity with variation in temperature. As is evident from the results, viscosity decreases significantly with an increase in temperature. Therefore, to accurately represent the way in which marrow behaves *in vivo*, tests should ideally be conducted at the body temperature of the specimen donor (i.e. 37°C for humans).

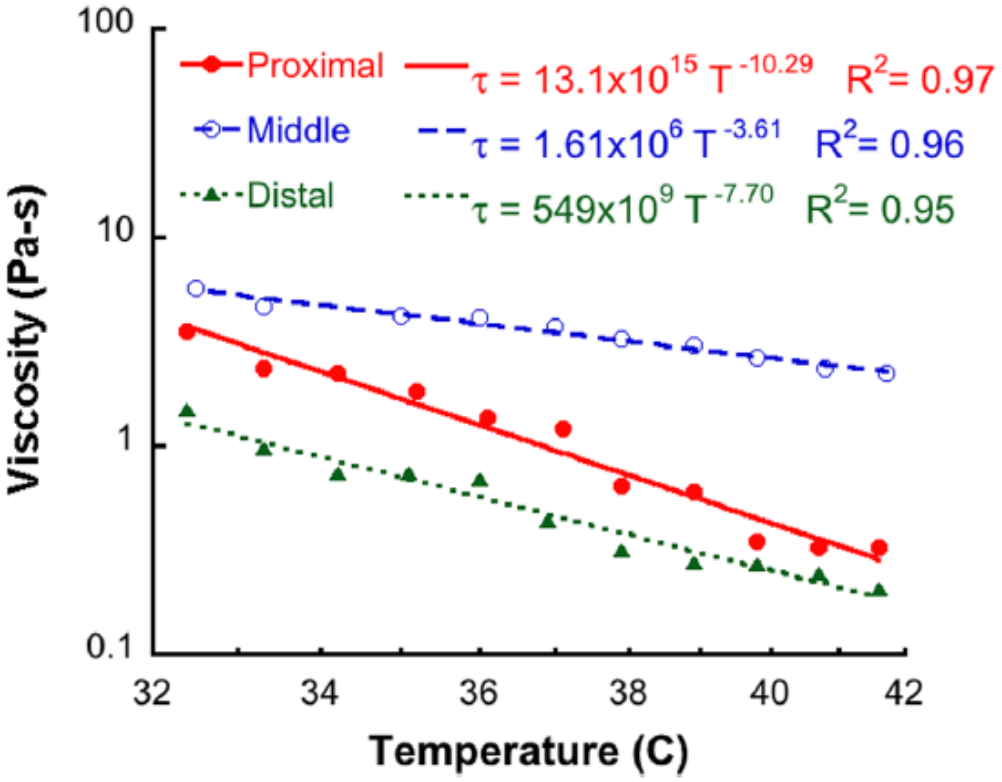

Figure 2.33: A graph showing the results of the change in viscosity of bone marrow as temperature increases, as presented by Metzger *et al.* [8]

Chapter 3

Specimen Preparation

To test the effect of strain rate, architectural parameters and boundary conditions, various specimen types were required for the investigation. These specimens include:

- 10 mm diameter cylinders - standard
- 10 mm diameter defatted cylinders - marrow removed to assess the effect of marrow
- 20 mm diameter cylinders - for boundary condition comparison
- 28 mm diameter cylinders - for boundary condition comparison

This chapter describes the general method for machining cylindrical specimens, the way in which specimens were stored, and the process of defatting specimens.

3.1 Material

Nine whole bovine humeri were sourced from Sacks Butchery in Westlake, Cape Town. The bones were cleaned of most meat and fibrous tissue, as shown in figure 3.1, before being frozen and transported from the butchery (roughly 15 km). The bones were stored in a freezer at -32°C before and after specimen preparation. The age at slaughter and slaughter date of the cows were not known. It was also unclear how many individuals were represented in the batch. However, the bones were all sourced together and are assumed to be from the same population and age group.

The bovine humerus bears a large majority of the weight of a cow, making it ideal for comparison to the human femur in terms of load bearing properties. Bovine humeri are long bones and therefore contain cancellous bone in both the distal and proximal epiphyses, making them suitable bones for the manufacture of cancellous bone specimens.

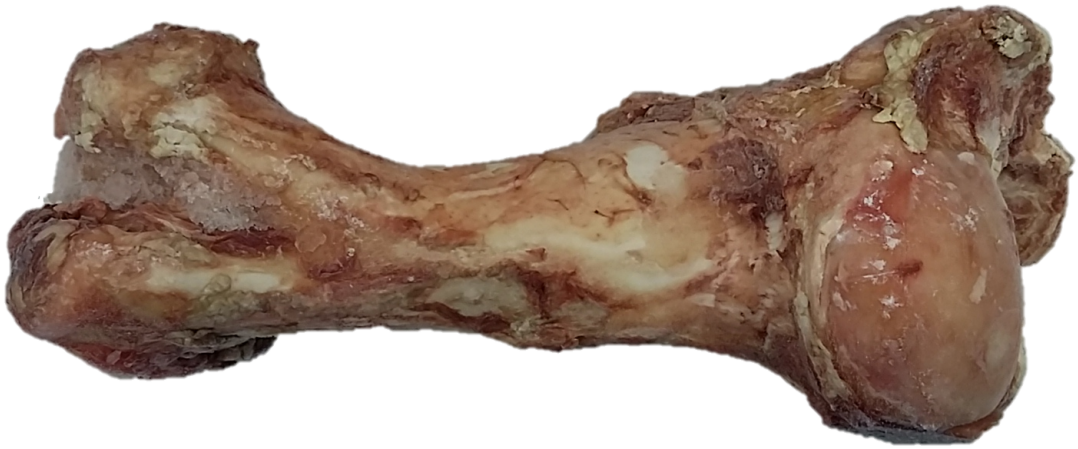

Figure 3.1: Photograph of a single bovine humerus - cleaned of meat and fibrous tissue.

3.2 Specimen Machining

To investigate the effects of strain rate, architectural parameters and confinement conditions, cancellous bone specimens were machined from the proximal epiphysis of each bovine humerus. The proximal epiphysis is thick and contains a large amount of cancellous material, making it easy to obtain multiple samples from a single bone. This allowed for fewer bones to be used, resulting in decreased probability that differences in response were due to individual variation rather than experimental variation.

3.2.1 Bone Slicing

The bones were thawed overnight before machining. Once thawed, slices were cut from the proximal epiphyses of the humeral heads using a band saw, as shown in figure 3.2a. The resulting slices are shown in figure 3.2b. Each slice was roughly 10 mm thick, to allow for post-machining of specimens to the desired height of 7.5 mm. Slices were cut in three principle directions, namely transverse, sagittal and frontal. A representation of these directions is shown in figure 3.3.

(a) Bovine humeral head being sliced on a band saw.

(b) Sliced sections of bovine humerus.

Figure 3.2: Photographs of bovine humeral head slicing

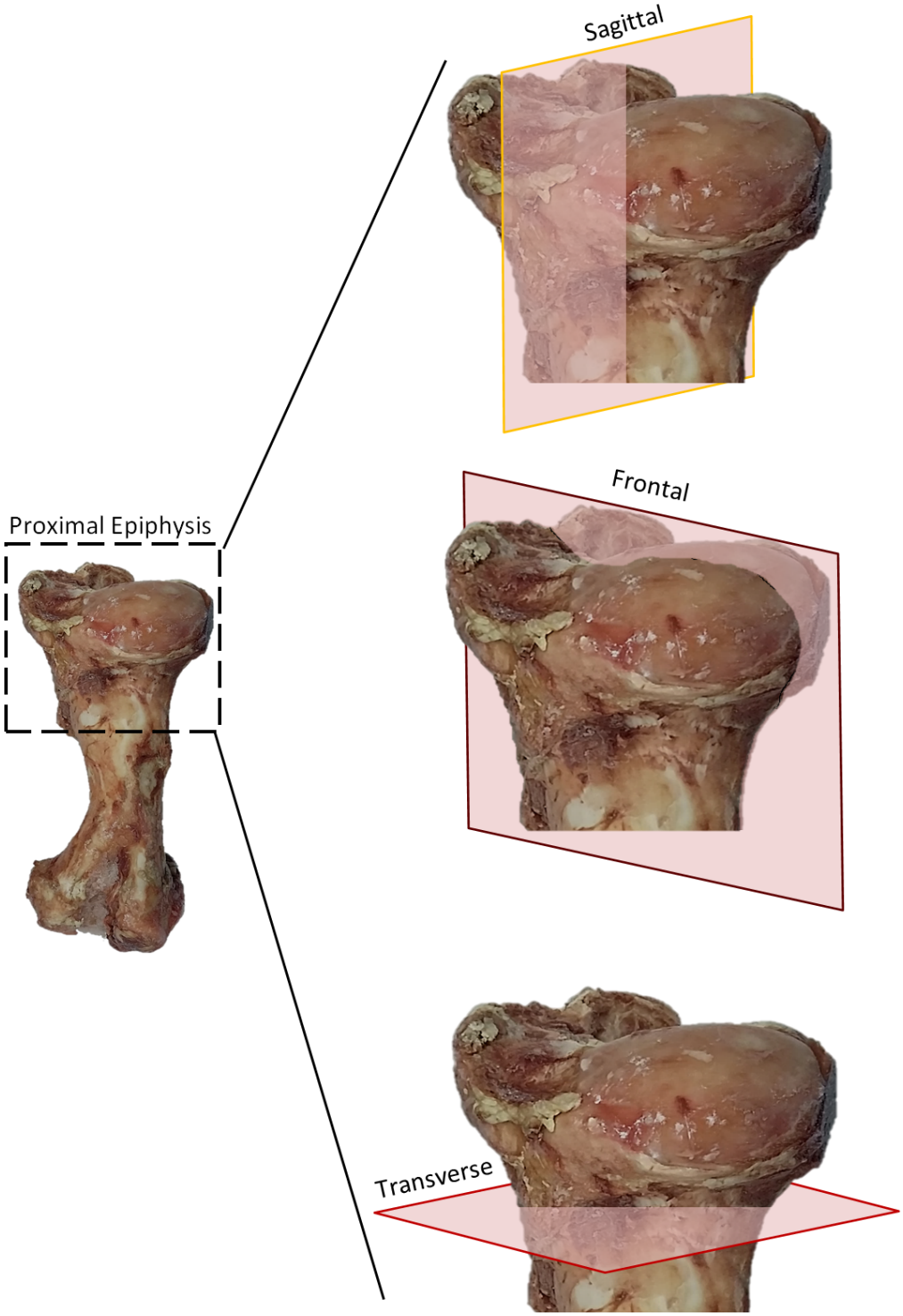

Figure 3.3: A diagram showing the three principle directions in which bovine humerus slices were cut.

3.2.2 Specimen Coring

From the pre-cut slices, cylindrical specimens were cored out of the cancellous bone section. The distinction between the cancellous and cortical bone is shown in figure 3.4. Cylinders were cored using three different corers, custom manufactured with inner diameters (IDs) of 10 mm, 20 mm and 28 mm respectively. Figure 3.5 shows a photograph of a custom manufactured corer used to cut the cylindrical specimens.

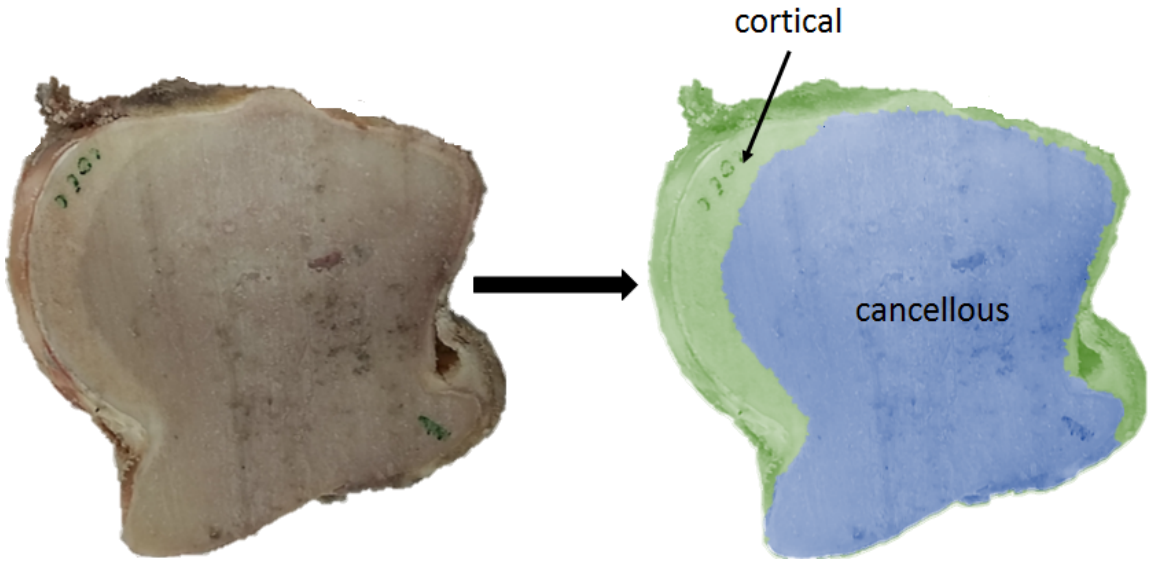

Figure 3.4: An illustration showing the distinction between cortical and cancellous bone seen on each humerus slice.

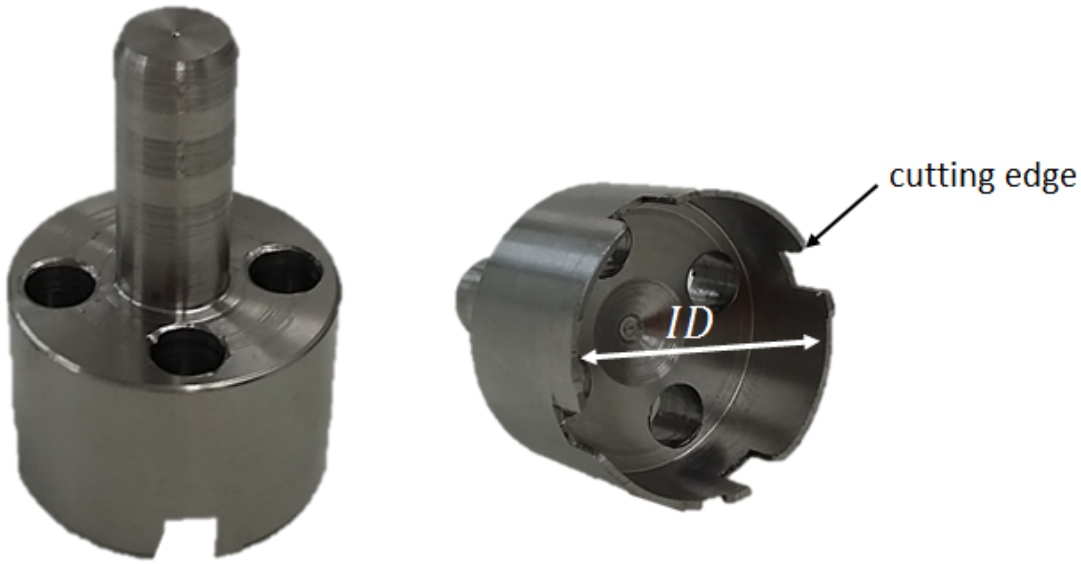

Figure 3.5: Photographs of the custom manufactured corer used to core out 28 mm diameter cylindrical cancellous bone specimens.

The corers were fitted to a drill press perpendicular to the sliced section as shown in figure 3.6. The coring process left behind cored out specimens of the same diameter as the ID of the corer. Care was taken to ensure that each specimen was cut from a sliced section that did not contain fatty deposits, as shown in figure 3.7.

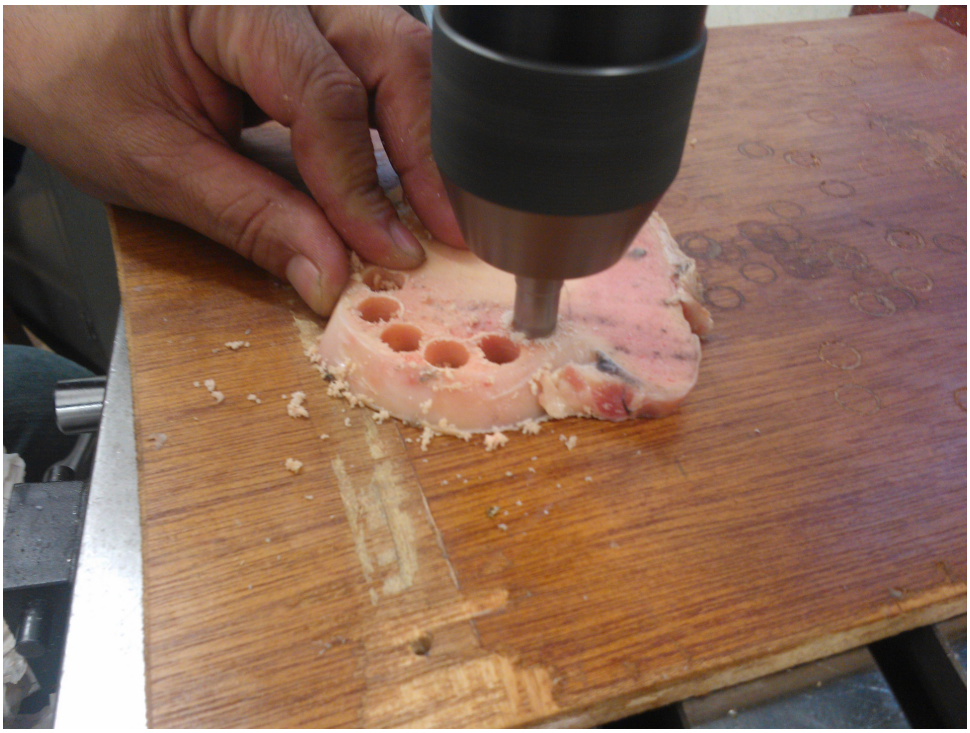

Figure 3.6: Photograph of a custom corer being used to core out cylindrical specimens.

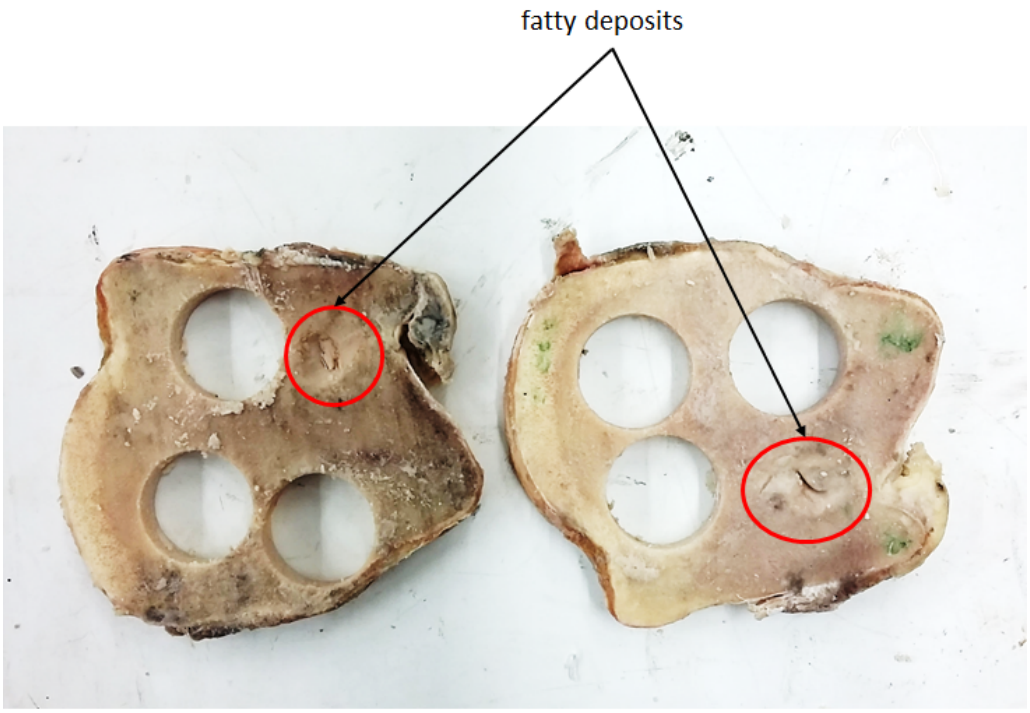

Figure 3.7: Photograph indicating fatty deposits within cancellous bone.

Figure 3.8: A photograph of a 28 mm cored specimen being measured for accuracy of cored diameter.

During the coring process, every second specimen diameter was measured using a digital vernier calliper as shown in figure 3.8 to ensure that the coring process consistently yielded specimens with diameters within 0.1 mm of the desired diameter, depending on which corer was used.

3.2.3 Specimen Facing

Once specimens had been sliced and cored, facing was performed on a lathe to obtain specimens with a uniform height of 7.5 mm. Aluminium collars of three diameters were manufactured with a height of 7.5 mm each. Each specimen was placed inside the relevant collar and gripped inside the lathe chuck, after which it was faced such that the bone surface was parallel to the end of the aluminium sleeve. The same process was repeated on the opposite face of the specimen using the same collar.

During the facing process, every second specimen was measured using a digital vernier calliper as shown in figure 3.9 to ensure that the process was yielding specimens which were 7.5 $\pm$ 0.1 mm in height.

3.3 Specimen Storage

Once cored, each specimen was given a unique number for identification purposes. For each specimen, the bone number, slice number and location within the slice was recorded. A container was marked with the specimen number and filled with physiological saline (0.9% NaCl, 99.1% water) which covered the specimen completely. Physiological saline mimics the fluid conditions inside the body, therefore storing specimens inside this solution causes minimal leaching of minerals from the bone [19].

Once the specimens had undergone the facing phase of manufacture, they were returned to their respective containers filled with saline solution and stored in a freezer at -32°C before experimentation. Figure 3.10 shows finished specimens, ready to be frozen before experimentation.

3.4 Defatting

A subset of specimens were defatted prior to experimentation. These defatted samples were used to investigate the effect of marrow on the mechanical response of cancellous bone. Defatting involves removal of the marrow from the trabecular network of the bone.

Defatting of the specimens was performed using a water bath, set to 38 ± 1°C as shown in figure 3.11. Each specimen was placed inside the water bath, suspended using string while still in individual containers and physiological saline. Suspension of the container ensured that it was never completely submerged, and therefore any leaks which may

Figure 3.9: Photograph of a faced specimen being measured for accuracy of faced height.

Figure 3.10: Photograph if the finished specimens, stored in individual containers.

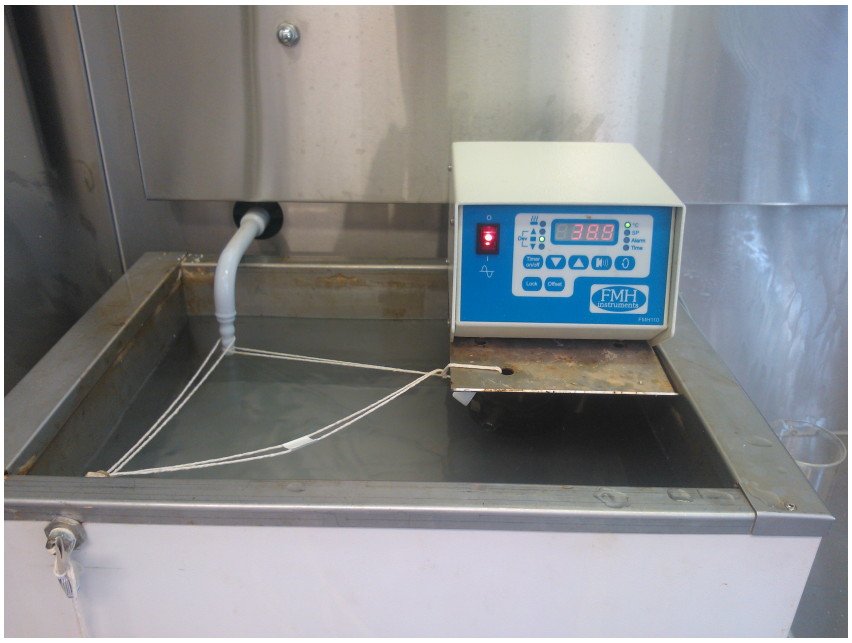

Figure 3.11: Photograph of the water bath with temperature control.

have been present did not affect the concentration of the saline solution. The saline was allowed sufficient time to thaw and to reach the same temperature as the water bath, after which the specimen was removed for defatting.

Body temperature is roughly 37°C, therefore the water bath ensured that specimen temperature was above body temperature. The elevated temperature softened the marrow, making it easy to expel from the trabecular network using a compressed air gun. A typical example of an as-machined, defatted specimen seen in figure 3.12. After defatting, specimens were returned to their respective containers filled with saline solution and refrozen before experimentation.

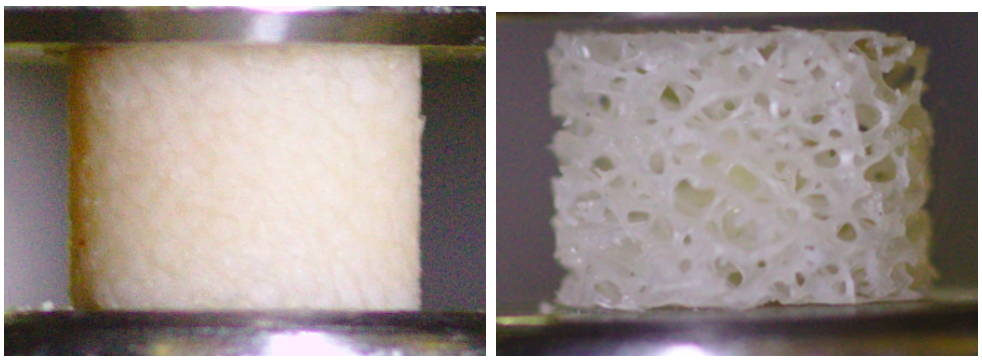

(a) Before defatting. (b) After defatting.

Figure 3.12: Photographs of a specimen before and after defatting. Note: photographs depict two different specimens.

Chapter 4

Architectural Parameter Acquisition

To determine the architectural parameters of each specimen, μCT scans were performed. The scans were processed using the Image Processing toolbox in MATLAB and various algorithms were applied to extract the relevant architectural parameters as described in section 2.1.2. The following sections describe the scanning and image processing techniques used and developed during the investigation.

4.1 Specimen scanning

A μCT scanner (Phoenix, voxel size 80 μm, 70 kV, 350 μA, acquisition time of 500 ms per image) was used to scan specimens. The scanning medium used for all specimens was air, and scans were performed using a polystyrene sleeve filled with discs as shown in figure 4.1. Polystyrene was chosen as the radiopacity is low and it would therefore not disrupt the view of bone samples in the scan. The polystyrene sleeve allowed for specimen separation within one disc, as well as between discs. This was achieved by inserting empty discs of polystyrene between discs filled with specimens. This configuration allowed for multiple samples to be scanned at once, making scanning cost and time effective. Small pieces of wood were pressed into the polystyrene at each level in order to orientate and identify individual discs within the larger polystyrene sleeve. For example, figure 4.2a shows a schematic of specimen placement within a disc. Figure 4.2b shows the scanned image of the same disc, with wooden pieces circled in red. In this way, the individual specimens were identified from each batch scan, bearing in mind that scanned images were mirror images of their schematic counterparts.

The result of each batch scan was a series of roughly 2000 TIFF images, each representing a slice of the entire scan. Using various image processing methods, described in detail in section 4.2, these images were used to isolate individual specimens

and retrieve architectural parameters. The images were also collated and rendered as a 3D depiction of the full scan, as shown in figure 4.3. This image was created using ImageJ, an open source image processing software.

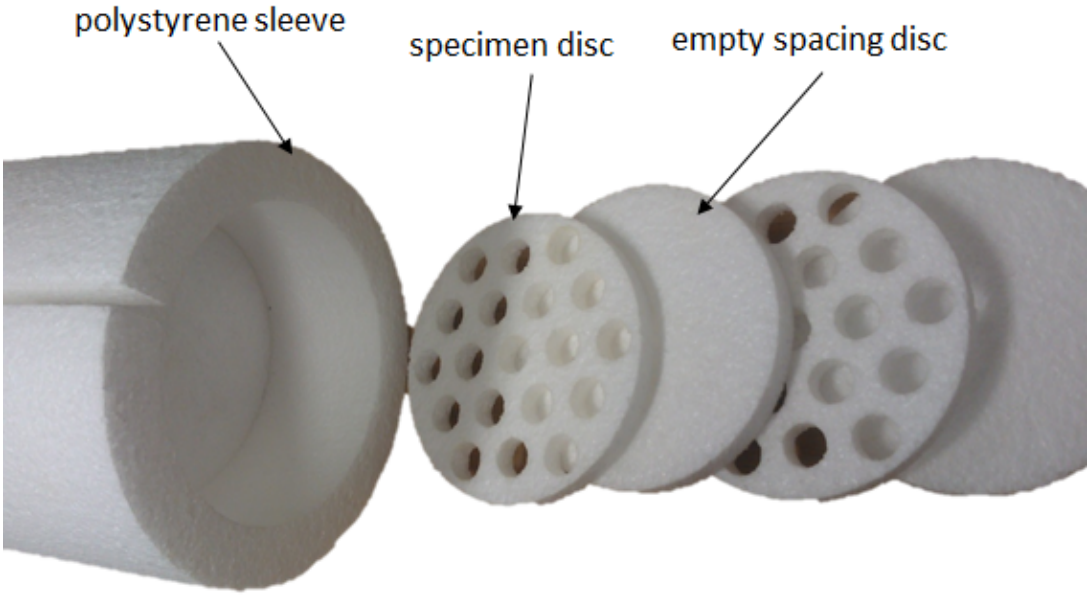

Figure 4.1: Photograph of the polystyrene sleeve for specimen scanning with empty polystyrene spacers between specimen-filled discs

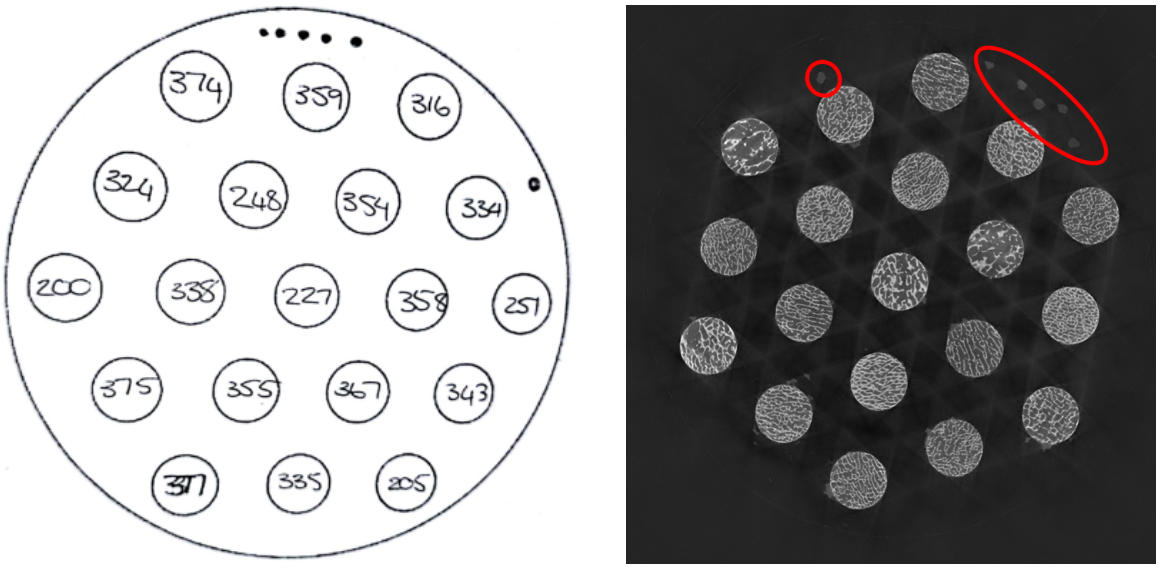

(a) Pre-scan schematic (b) Scanned image

Figure 4.2: An example of a pre-scan schematic and its corresponding scanned TIFF image with wooden pieces for disc identification and orientation

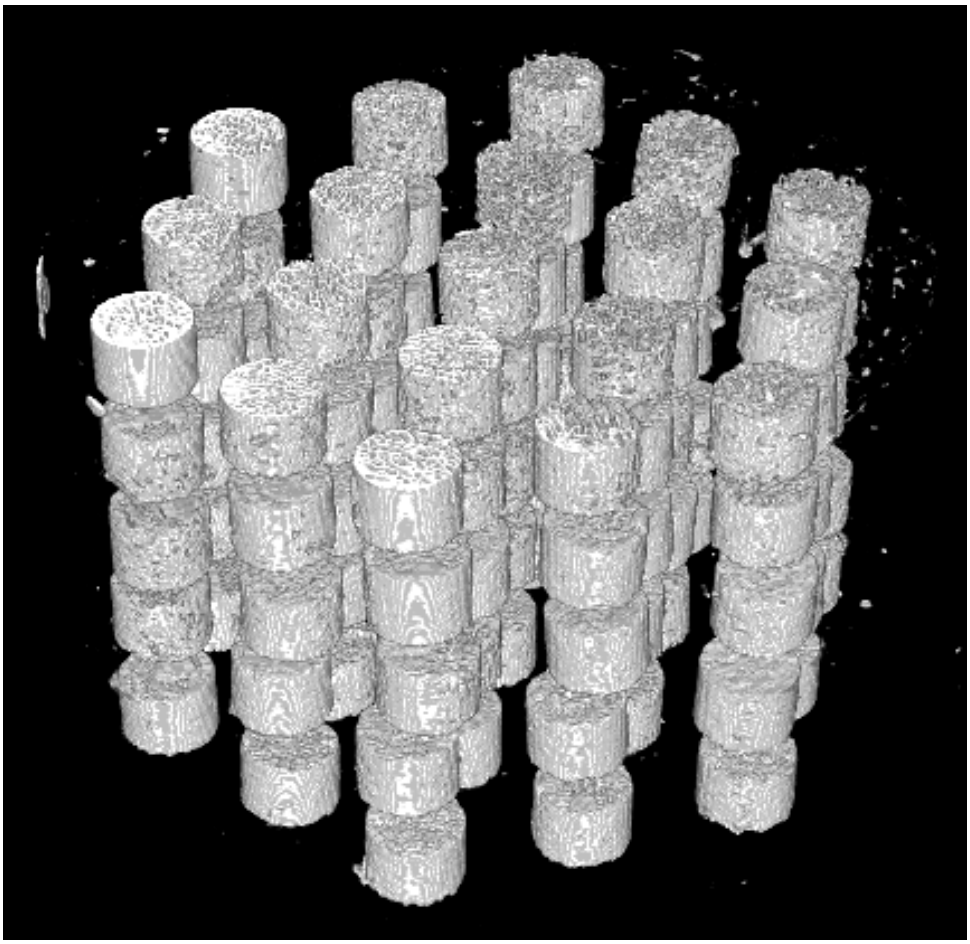

Figure 4.3: A 3-dimensional full batch scan, generated using ImageJ

4.2 Image Processing

As mentioned in section 2.1.2, either a 2D or 3D approach can be taken to quantify the architectural parameters of cancellous bone. An open source software called ImageJ is applicable for 3D methods. This software supports a plugin called BoneJ, which allows for bone image analysis. While a 3D approach may be more reliable for the calculation of some architectural parameters, BoneJ is difficult to automate as it requires manual input of individual specimen stacks to calculate parameters for each specimen. Therefore, for the scope of this investigation, a 2D method was developed using the Image Processing Toolbox in MATLAB. This method could be easily automated to run through multiple specimens, determining the architectural parameters of each specimen using one script. BoneJ was still used, however, on a sample set of specimens, in order to validate the accuracy of the developed 2D technique. The details of this validation are discussed in section 4.2.6.

Before the scanned images were processed, scans were manually separated into specimen-filled layers. This was accomplished using empty images as a reference for the tops and bottoms of each specimen-filled disc. Each layer was saved into separate folders of multiple images and given a name corresponding to the batch and disc number, as recorded using the pre-scan schematic mentioned in section 4.1. Once separated into layers, the scan was processed in order to determine the architectural parameters of individual specimens. In order to do this, various image processing techniques were required. These techniques included specimen detection, image cropping and binarising of images, as well as applying algorithms in order to determine the architectural parameters discussed in section 2.1.2.

4.2.1 Specimen Detection

The first step taken to determine architectural parameters was to separate individual specimens from a layer within each scan. In order to do this, multiple images containing specimens from one layer were overlaid on one another using MATLAB. This created distinct white circles where each specimen was, as shown in figure 4.4a. A Circular Hough Transform (CTH) was used on each consecutive image, or "slice", of a scan. The algorithm was used to detect circles based on specimen radius, and the sensitivity of the CTH was changed until the correct number of specimens was detected within each slice. The detected circles, shown as red rings in figure 4.4b, were each identified by x and y centre coordinates. Using these centre coordinates, along with the schematics filled in before each scan which were orientated using the pieces of wood, individual specimen numbers were identified as shown in figure 4.4c.

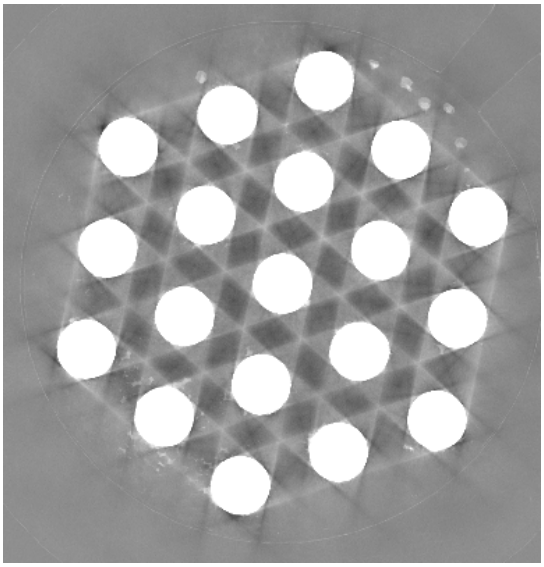

(a) Overlaid images creating distinct circles

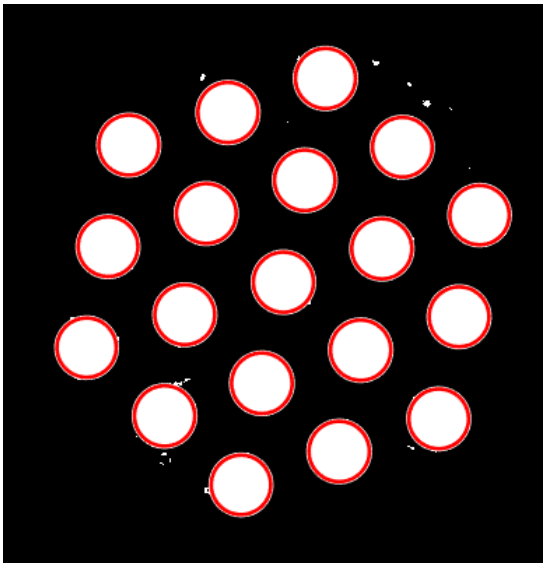

(b) Circles detected using CTH

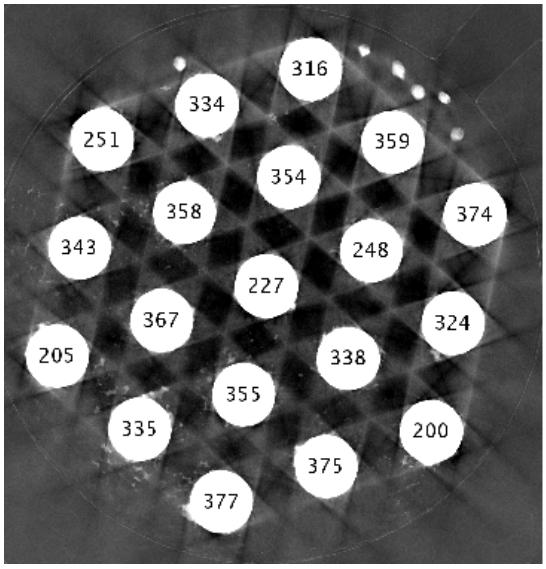

(c) Identified specimen numbers

Figure 4.4: Images of the specimen detection and identification techniques used

4.2.2 Individual Specimen Cropping

After individual specimens were identified by number, the images required cropping in order to isolate each specimen. Using the detected specimen centre along with the radius of the specimen, a square surrounding each specimen, which was 10% larger than the specimen diameter, was cropped from within a slice. This was repeated for the same centre (i.e. the same specimen) throughout the layer, resulting in multiple images of one specimen. Each cropped image represented a thin slice of a specimen, and when stacked together with other slices of the same specimen, these images created a full scan of an individual specimen, as shown in figure 4.5. The images were saved in folders according to specimen number, sequentially from the top to the bottom slice. Figure 4.6 shows a 3-dimensional image of an individual scanned specimen, separated from within a layer of the scanned specimens.

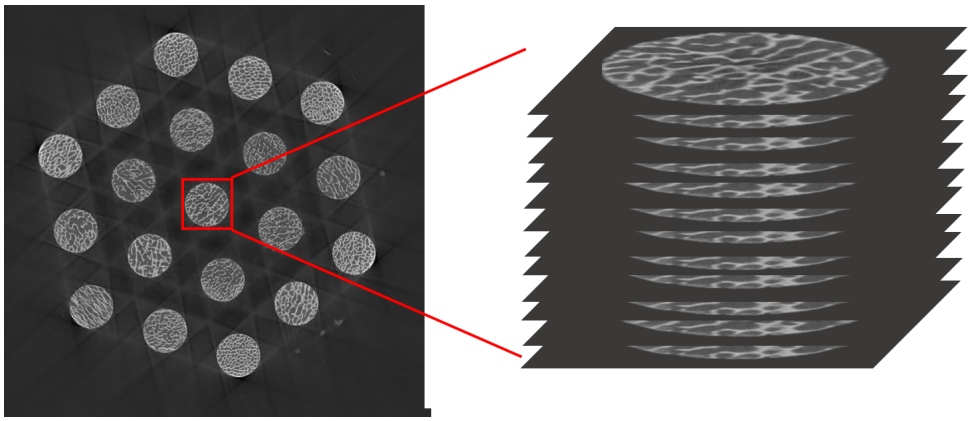

Figure 4.5: An image representing the placement of each square surrounding a specimen slice and the layering of these slices to create a full specimen scan.

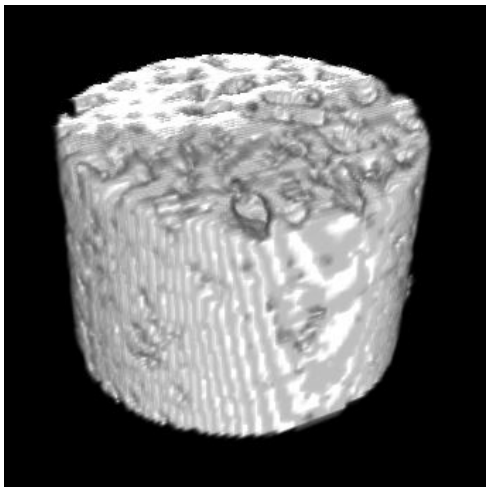

Figure 4.6: ImageJ created 3-dimensional image of an individual specimen

4.2.3 Volume of Interest

For ease of cropping using MATLAB, it was decided that the volume of interest (VOI) used would be a rectangular prism. Due to the nature of the machining, as described in section 3.2, bone on the boundary surfaces of each specimen was likely damaged and would not represent the correct architectural parameters. An example of this boundary damage is shown in figure 4.7, which shows images of a specimen taken using a scanning electron microscope (SEM).

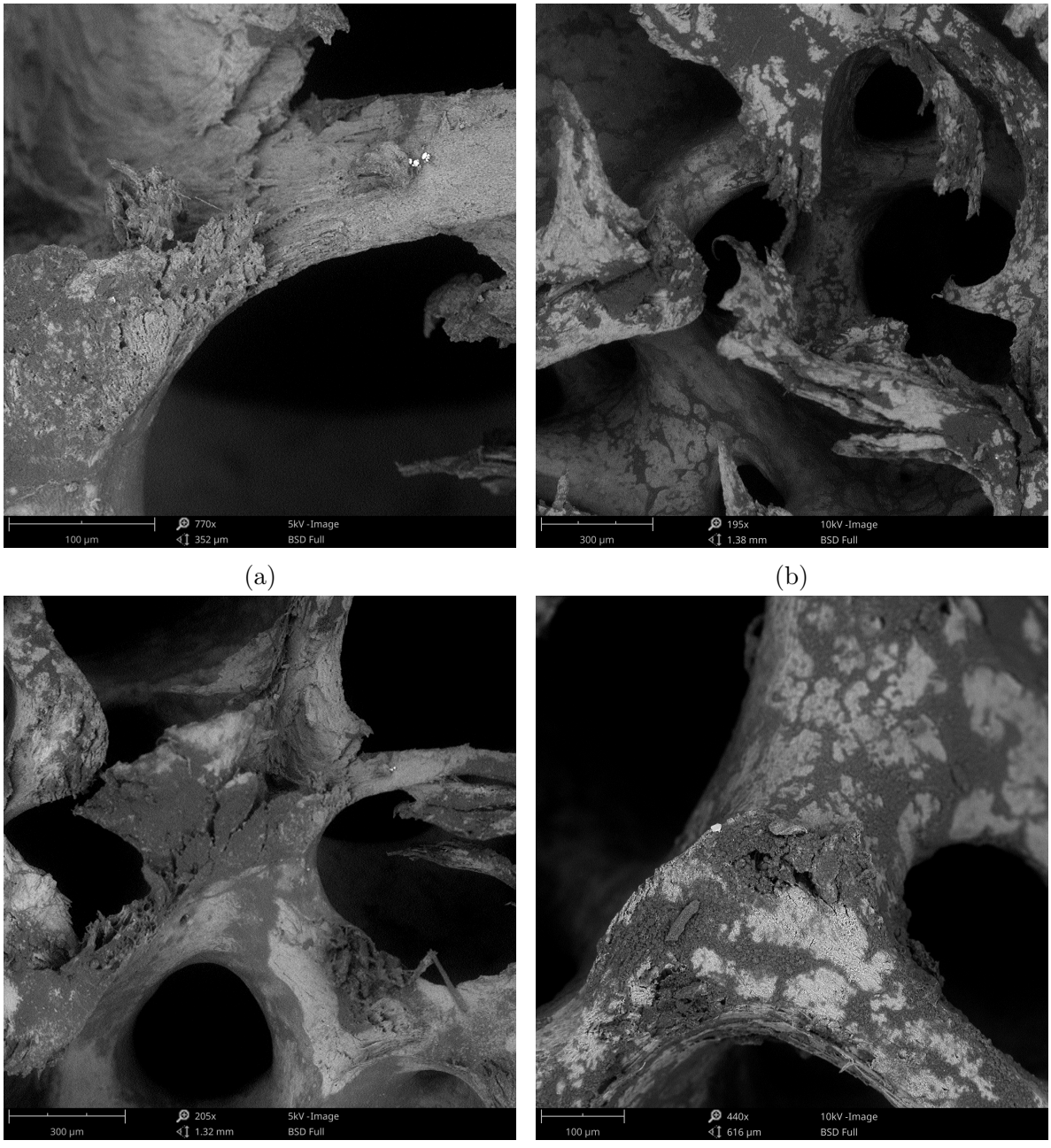

(a) (b)

(c) (d)

Figure 4.7: SEM images showing boundary damage on specimens caused by machining.

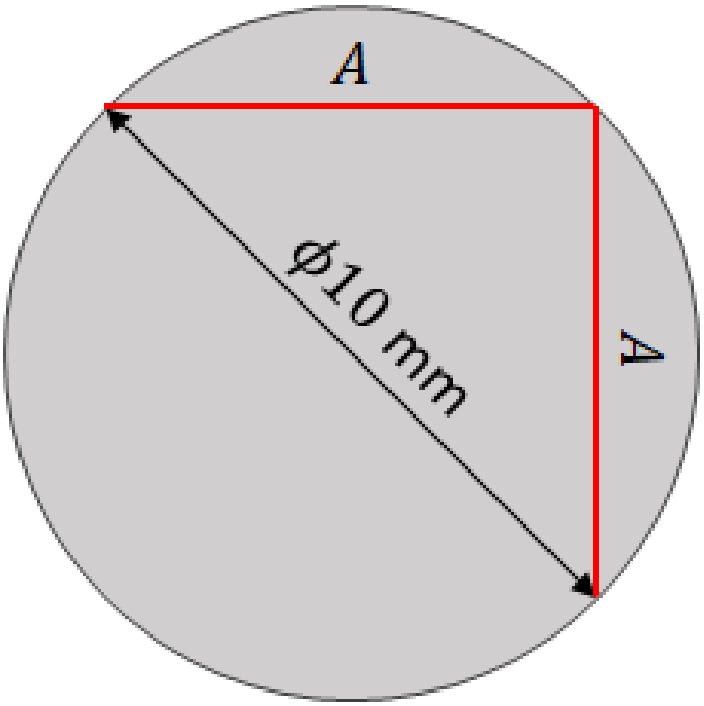

Figure 4.8: Schematic top view of smallest specimen

For the purposes of this investigation, the VOI needed to correspond to the largest prism which could be wholly contained within the smallest specimen. The first face of the prism corresponds to a square within the smallest specimen, which is 10 mm in diameter, as shown in figure 4.8. The largest lengths of the sides of the square are derived as follows:

$$10^2 = 2A^2 \tag{4.1}$$

$$\therefore A = 7.071mm^2 \tag{4.2}$$

To ensure that the entire square fits inside every specimen, a side length of 6.5 mm was chosen for the VOI. The height of the prism was chosen to be 6.5 mm. As the height of each specimen was machined to be 7.5 $\pm$ 0.1 mm, this ensured that the full height of the VOI was contained within each specimen. The total VOI was therefore 674.625 mm^3. This volume needed to remain constant for all scanned specimens, and is shown in relation to each specimen diameter in figure 4.9.

Cropping the VOI from within each sample was similar to cropping individual specimens from a full layer scan. First, the centres of the individually cropped specimens were found and matched with their corresponding specimen number. To determine the number of pixels corresponding to a 6.5 mm internal square, the known radius of 5 mm for all of the

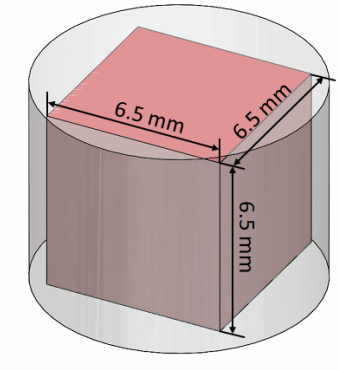

(a) 10 mm specimen

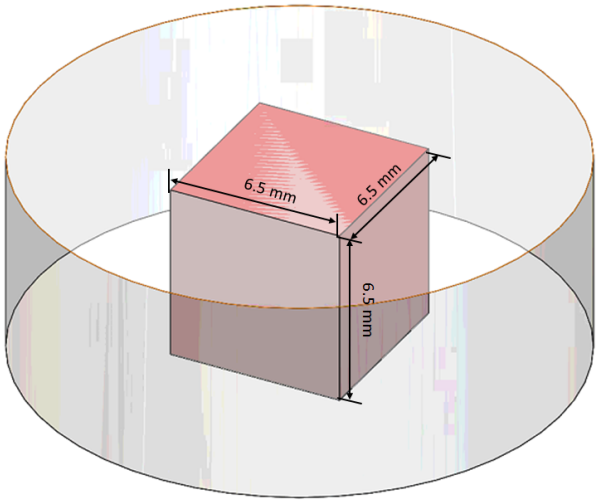

(b) 20 mm specimen

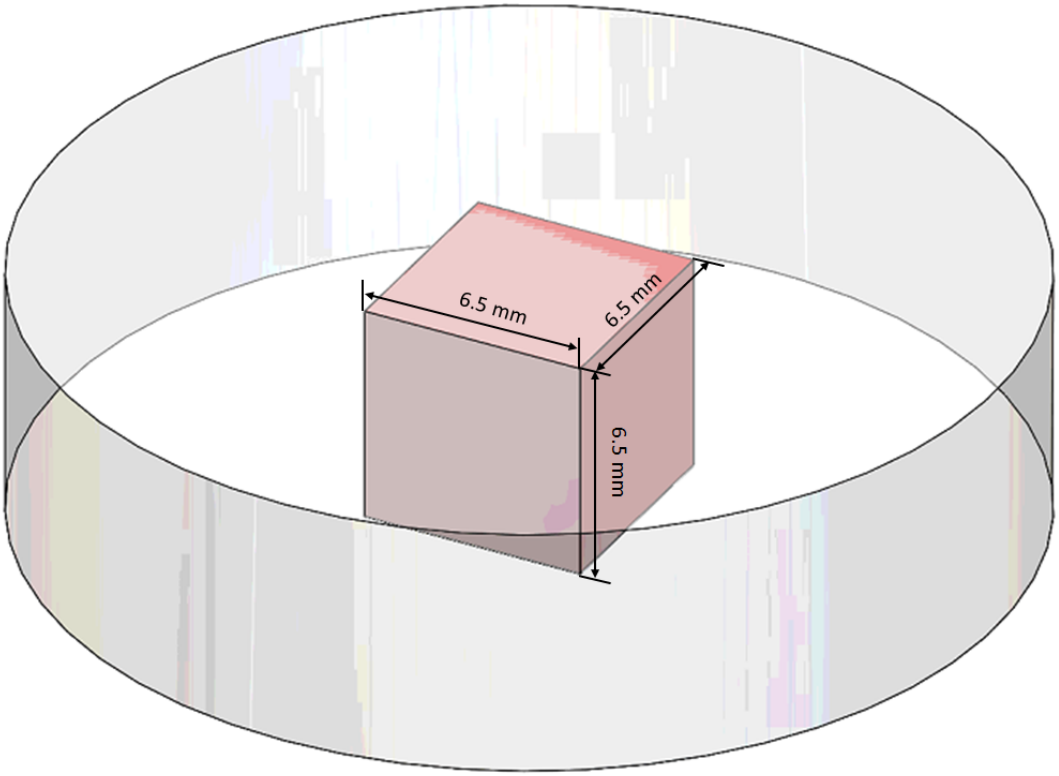

(c) 28 mm specimen

Figure 4.9: Schematics of the total Volume of Interest in relation to specimen diameter

smallest specimens was compared to the detected radius of these specimens, which was given in number of pixels as an output of the CTH. This allowed for a ratio of pixels to millimetres to be determined, which was applied to each layer of the individual samples of each size to crop out the central 6.5 mm square. A height of 6.5 mm for each internal sample corresponded to 86% of the total specimen height. Therefore, the height of the internal sample was simply determined using a ratio of image numbers for one specimen to the height of the specimen. For example, if one specimen contained 140 images, 121 central images were stacked for the internal sample. Each internally cropped image was saved to a folder named after the specimen number to uniquely identify the sample during further processing.

4.2.4 Binarisation

Binarisation of images is the process of reducing an image with many levels of colour to one with only black and white. This is required to determine the architectural parameters of cancellous bone.

As discussed in section 2.2.2.1, many image segmentation and thresholding methods can be used to binarise images of bone. The most commonly used method is Otsu's method. The Image Processing Toolbox in MATLAB has a built in Otsu's method function, *im2bw*, which was used for each image of the cropped internal samples to create a binary version of the same cropped sample. The binarised image was used in algorithms which determined architectural parameters using 2D techniques. Figure 4.10 shows a grayscale scanned image, having undergone Otsu's method of thresholding, and the resulting binary image. The bone is seen in white, while black pixels represent non-bone areas within the scan.

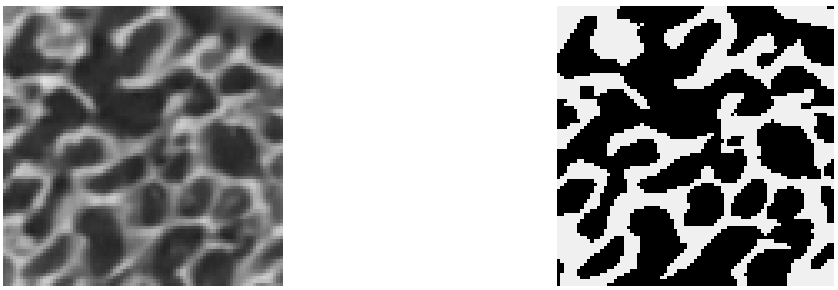

(a) Grayscale image (b) Binary image

Figure 4.10: A grayscale image and its resulting binary image after undergoing Otsu's method of thresholding.

4.2.5 Architectural Parameters

The following sections describe the algorithms developed during the investigation to determine the architectural parameters of cancellous bone specimens. The algorithms all made use of the Image Processing Toolbox in MATLAB, modelled after 2D techniques. A subset of samples were used to validate the developed algorithms using ImageJ. This validation is described in section 4.2.6.

4.2.5.1 Determining Trabecular Network Model

As described in section 2.1.2, either a rodlike or a platelike trabecular network model must be assumed to calculate architectural parameters using 2D methods. The nature of the trabecular network (rodlike or platelike) was determined by examining microscopic images of the samples. Figure 4.11 shows a series of images taken under a microscope of two defatted samples, each from different bones and different locations within the bone. This was to obtain a view of a range of different specimens used during the investigation.

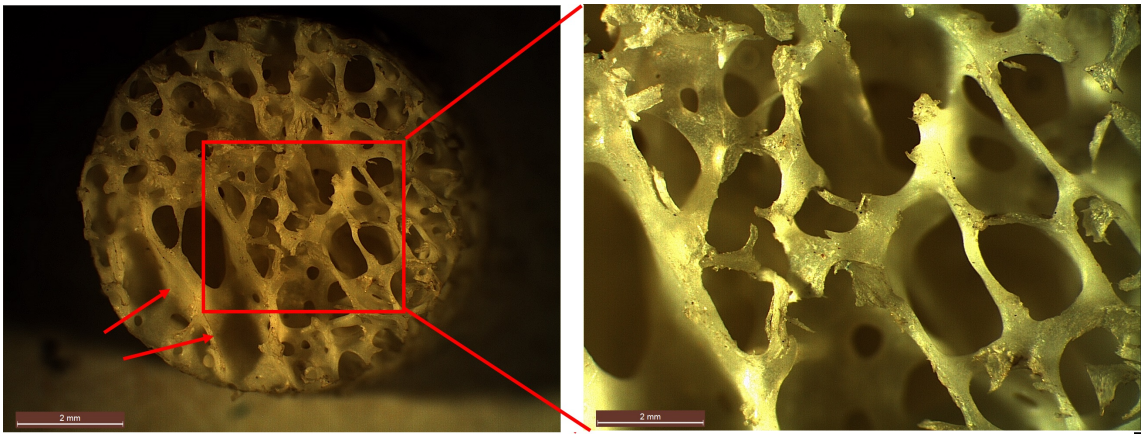

(a) Sample 436

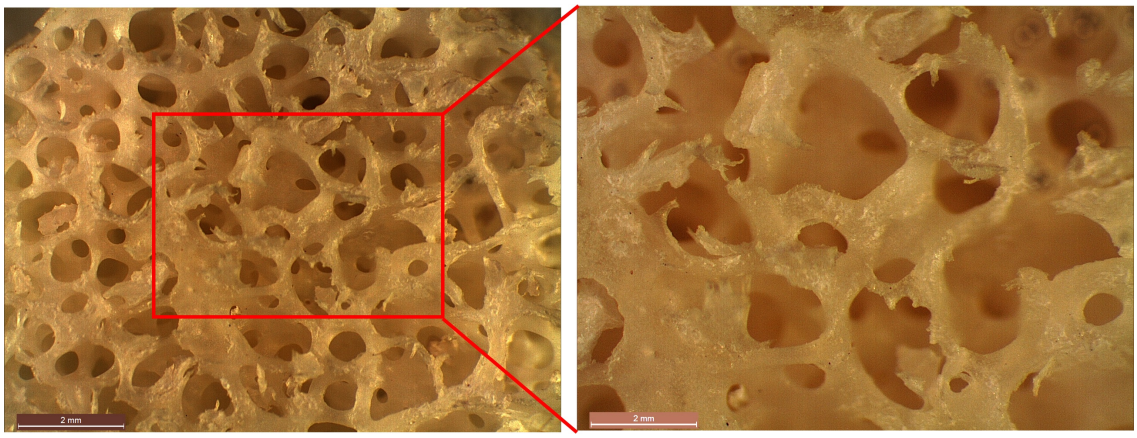

(b) Sample 421

Figure 4.11: Microscope images of two defatted bone samples - red arrows indicate platelike structures.

While there are some regions of platelike structures within the network - indicated by the red arrows in figure 4.11a - a rodlike model was chosen as the majority of the network was observed to be rodlike.

4.2.5.2 Parameter Algorithms

Algorithms for four architectural parameters were developed during the investigation, namely bone volume versus total volume (BV/TV), trabecular number (Tb.N), mean trabecular thickness (Tb.Th) and mean trabecular separation (Tb.Sp).

To determine BV/TV of the VOI, described in section 4.2.3, both the total volume and the bone volume of each VOI was calculated. For each slice of a sample, the sum of the number of black and white pixels in the image corresponded to the total area, and the number of white pixels in the image corresponded to area of bone in the image. The number of total pixels and the number of white pixels were calculated for each image within an internal sample, and these numbers were summed to determine the total number of pixels as well as the total number of white pixels throughout the sample volume. BV/TV was calculated for each samples as described by equation 2.1, repeated here for convenience.

$$\text{BV/TV} = \frac{\text{No. of bone pixels}}{\text{Total pixels}}$$

Tb.N is a measure of the number of trabeculae per unit length. As described in section 2.1.2, this is calculated using the test line method in 2D. For the algorithm developed for the investigation, eight test lines were used on the binarised images of internal samples. The number of bone-marrow intersections were counted for each test line. This was achieved by counting each instance along the line in which the binary image went from white to black, or 1 to 0. This number was divided by 6.5 mm - the length of the image as described previously in section 4.2.3. Once this was calculated for each test line, an average was determined per image and was stored in a number array. After each image was processed, the average Tb.N value for each image was used to determine an overall average throughout the internal sample volume.

Mean trabecular thickness was determined using a simple calculation, as described in section 2.1.2. Once the BV/TV and Tb.N were determined, Tb.Th was determined as follows:

$$\text{Tb.Th} = \frac{\text{BV/TV}}{\text{Tb.N}}$$

Mean trabecular spacing was calculated in two ways. The first was a simple calculation as described in section 2.1.2, in which Tb.Sp is assumed to be the leftover proportion of the whole sample after Tb.Th is calculated. This portion was calculated using the following equation:

$$\text{Tb.Sp} = \frac{1 - \text{BV/TV}}{\text{Tb.N}}$$

The second method was to use the test line method, in which eight test lines were used in each binary image, similar to the method used to calculate Tb.N. The line was cut over regions of white pixels, leaving the test line present only over regions between bone, as described previously and shown in figure 2.5b. The length of the non-bone space was calculated and averaged in the same way as for Tb.N.

The first method was found to accumulate errors from calculations of both BV/TV and Tb.N, should any errors arise using the developed algorithms. However, the test line method was less likely to incur cumulative errors and it was therefore was used to calculate Tb.Sp for the purposes of this investigation.

4.2.6 Validation of Developed Technique

Validation of the developed algorithms was required to ensure that the architectural parameters determined were accurate. To do this, a subset of 20 samples were chosen and their architectural parameters were determined using ImageJ. ImageJ uses 3D techniques, and is therefore more accurate as it does not assume a rodlike or a platelike trabecular structure. The results of the ImageJ processing were compared to the results calculated using the algorithms developed during the investigation.

Figure 4.12 shows the results of the comparison. The solid black lines shown in the graphs represent where the ImageJ and developed algorithms agree. The dotted black lines show a 10% error band. Figure 4.12a shows good correlation between the methods for BV/TV, however, figures 4.12b - 4.12d for Tb.N, Tb.Sp and Tb.Th respectively, do not. This is likely due to the fact that the developed algorithms assume a rodlike trabecular network structure, whereas the true structure is more likely a combination of rodlike and platelike. This agrees with findings in the literature [14] as discussed in section 2.1.2.

Correcting for the error was achieved by assuming that data points determined by the developed algorithm differed from the ImageJ values by a factor of the calculated value. A series of factors were then checked, iteratively changing the error factor a number of times between -1 and 1. Each correction factor was fitted to a straight line graph passing through the origin, and once these graphs were populated for each error, the factor which

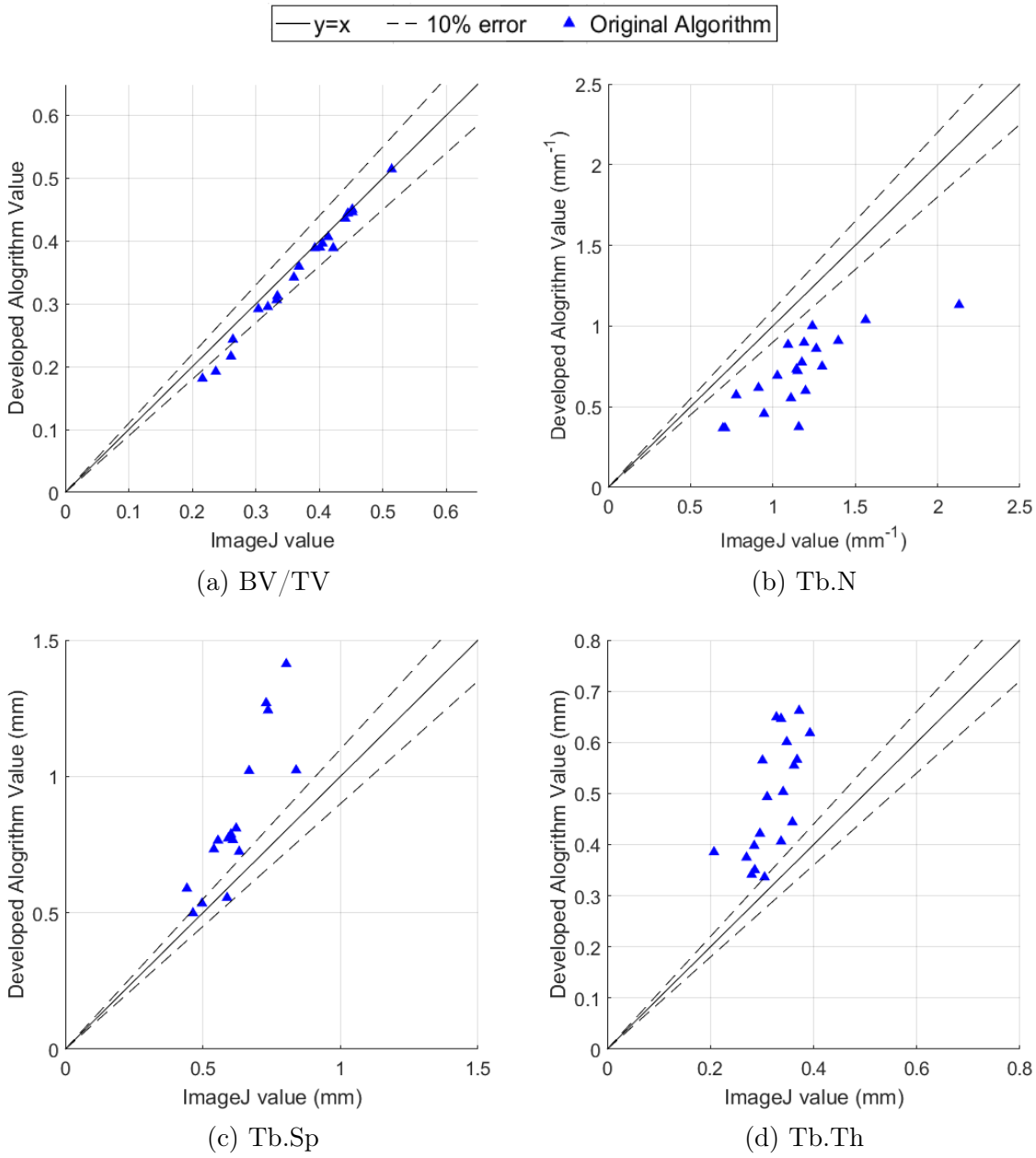

(a) BV/TV (b) Tb.N

(c) Tb.Sp (d) Tb.Th

Figure 4.12: Graohs showing a comparison of the architectural parameters determined by ImageJ versus those determined by the developed algorithm

had a fitted line gradient closest to 1 (i.e. y = x) was determined to be the best choice for the correction factor. This correction was performed for the variables BV/TV, Tb.N and Tb.Sp, and each was assigned a unique correction factor based on this method. The corrected values were used in calculations for Tb.Th. Below is an example of the described error correction, as performed for the parameter BV/TV.

First, the original data was plotted, as seen in figure 4.12a. Each original data point was then altered by a correction factor according to the following equation:

$$\mathrm{BV/TV'} = \mathrm{BV/TV} \times (1+\text{correction factor}) \tag{4.3}$$

where the apostrophe (') signifies the corrected value.

Five hundred correction factors were tested between -1 and 1 to ensure that an accurate factor was found. For each correction factor, the altered data points versus the ImageJ values were fitted to a straight line passing through the origin using the *fit* function in MATLAB. This function outputs the gradient of the line which best fits the given data.

Once the number array was fully populated, the index within the number array at which the gradient was closest to 1 was found. In the case of BV/TV, this index was 260 and the corresponding gradient was 0.9985. Finally, the 260th entry in the correction factor number array was found to be 0.0381. This factor was used to correct the original algorithm using equation 4.3 in order to plot figure 4.13a.

The same process was followed for both Tb.N and Tb.Sp. The results of the correction for BV/TV and Tb.N were used to calculate Tb.Th using the equation:

$$\mathrm{Tb.Th'} = \frac{\mathrm{BV/TV'}}{\mathrm{Tb.N'}} \tag{4.4}$$

Once this calculation was complete, the altered data points for Tb.Th were fitted to a straight line to determine the fitted gradient achieved.

Figure 4.13 shows the results of the corrections for each architectural parameter. Table 4.1 shows the correction factors and their corresponding achieved gradients for each of the corrected parameters. These correction factors were used in conjunction with the developed algorithms throughout the investigation.

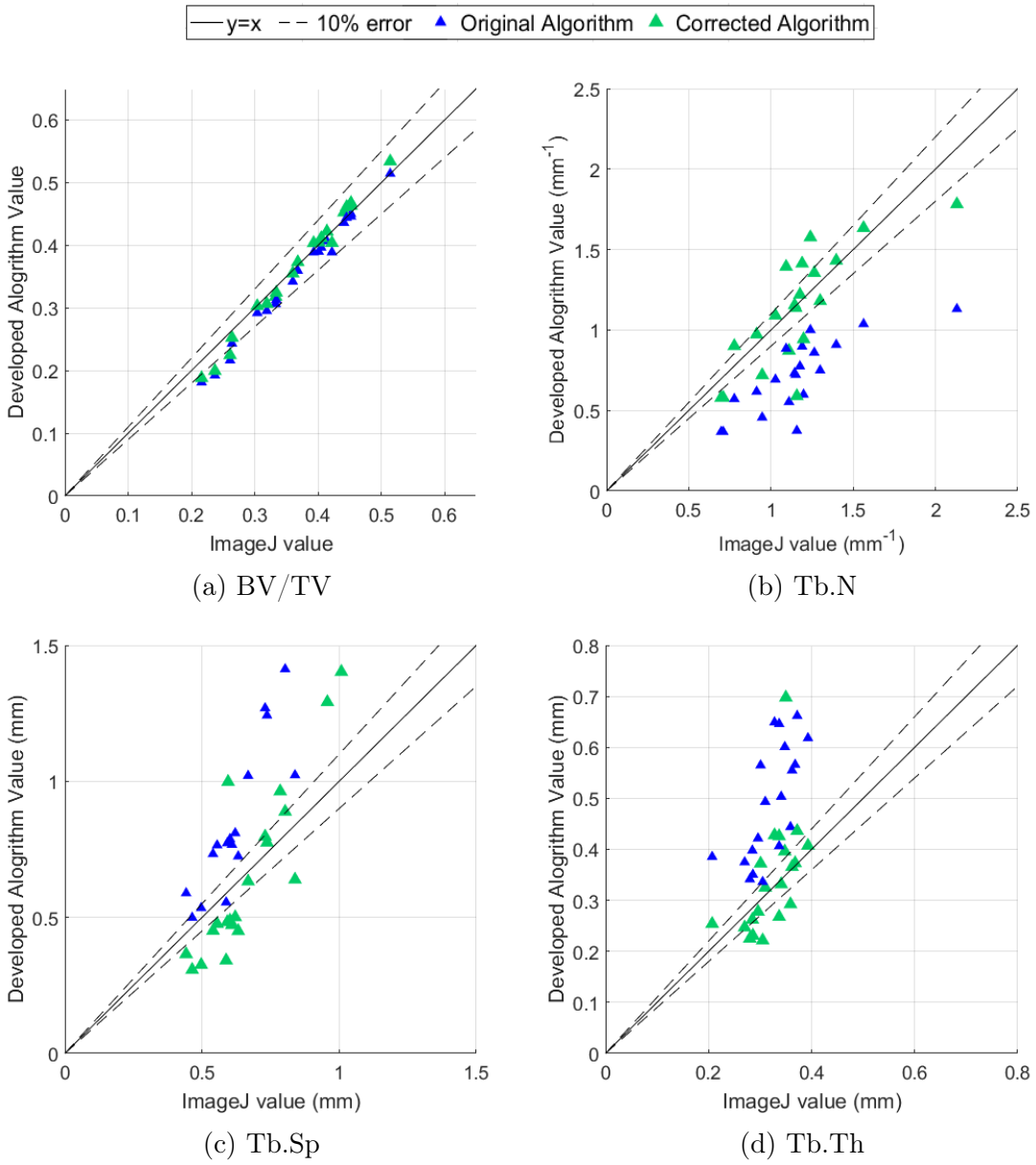

(a) BV/TV (b) Tb.N

(c) Tb.Sp (d) Tb.Th

Figure 4.13: Graphs showing a comparison of ImageJ versus developed algorithm, including value after correction

Table 4.1: A table showing the correction factors and gradients achieved during the validation of architectural parameter algorithms

Architecrural Parameter	**Correction Factor**	**Gradient Achieved**
BV/TV	0.0381	0.9985
Tb.N	0.5752	1.0002
Tb.Sp	-0.4309	0.9973
Tb.Th	N/A	0.8752

Chapter 5

Experimental Design

To complete experimental testing, specimens were subjected to compressive strain at quasi-static strain rates in various experimental configurations. This chapter describes these configurations, giving insights into design of each configuration. The chapter also describes the ways in which data collected from each test was analysed.

5.1 Specimen Dimensions

As mentioned in section 3, three different specimen dimensions were machined for use during the study; namely 10 mm, 20 mm and 28 mm diameter cylinders, all 7.5 mm in height. The diameter of the specimens were therefore all larger than their height, which is contrary to compression test protocols used during similar bone compression studies [22, 35, 42, 48, 51, 61]. These studies make use of specimens which are taller than they are wide, normally in order to minimize the effect of friction on flow stress in dense materials. This, however, is not a concern for porous materials such as cancellous bone.

The dimensions of the specimens used in this study were chosen so that the effect of confinement could be investigated. Using tall, thin specimens would not produce the desired confinement effect. It is possible that compressing specimens which are wider than they are tall could lead to anomalies in the results, such as crushing failure where shear or cracking failure may normally occur. However, many studies make use of specimens which are either short, wide specimens [2, 5, 9] or cubic specimens [10, 33]. The studies investigated cancellous bone or other porous structures, analogous to the specimens used during this investigation.

Another factor which was considered was buckling. Specimens which are taller than they are wide often require additional support in the experimental setup in order to prevent buckling. For the purposes of this study, additional support was undesirable as it could

add unwanted edge effects on the perimeter of the cylindrical specimen. It has been recommended that for repeatability of mechanical testing, specimen dimensions greater than 6.5 mm be used [10]. No specimens used during this study had dimensions less than 6.5 mm, and the use of the stated specimen dimensions was therefore deemed acceptable.

5.2 Compression Testing

Compression testing for this study was performed at quasi-static strain rates only, using a Zwick 1484 Universal Tester. Three strain rates, namely 10^{-3} s^{-1}, 10^{-2} s^{-1} and 10^{-1} s^{-1} were used to compress the cylindrical specimens. The displacement and force histories, along with test time, for each specimen were captured during the compression test, and were later used to determine mechanical properties such as apparent modulus (E_{app}), ultimate strength (US) and yield strength (σ_y). Prior to testing, specimens were thawed overnight at room temperature to ensure that they were no longer frozen. Before each test, the specimen was dabbed dry using tissue paper, weighed and measured for both diameter and height.

Compression tests were performed using three loading scenarios; unconfined, defatted and confined. Unconfined specimens were used as a measure of the standard specimen geometry (Φ 10mm $\times$ 7.5 mm) from which to draw comparisons. Defatted specimens were manufactured from the same size specimens and used to assess the effect of marrow on the response of cancellous bone - by comparing their response to that of the unconfined group. The defatted specimens used were prepared as described in section 3.4. Finally, confined specimens were used to determine the effect of a confinement boundary condition on the mechanical response of cancellous bone. Confinement aimed to mimic *in vivo* conditions and was achieved using two distinct methods:

1. structural confinement
2. bone confinement

Structural confinement was achieved using aluminium collars surrounding specimens. The collars aimed to confine and support the trabeculae on circumferential face of the specimen. The details of this confinement technique are presented in section 5.3.1. Bone confinement was realised by compressing larger specimens (20 mm and 28 mm diameters) while measuring the response of the inner 10 mm cylindrical region of each specimen. This was achieved using a specially designed confinement platform, described in detail in section 5.3.4.1. Figure 5.1 shows an example of the test set up used during the study, with an unconfined, standard specimen in the testing position.

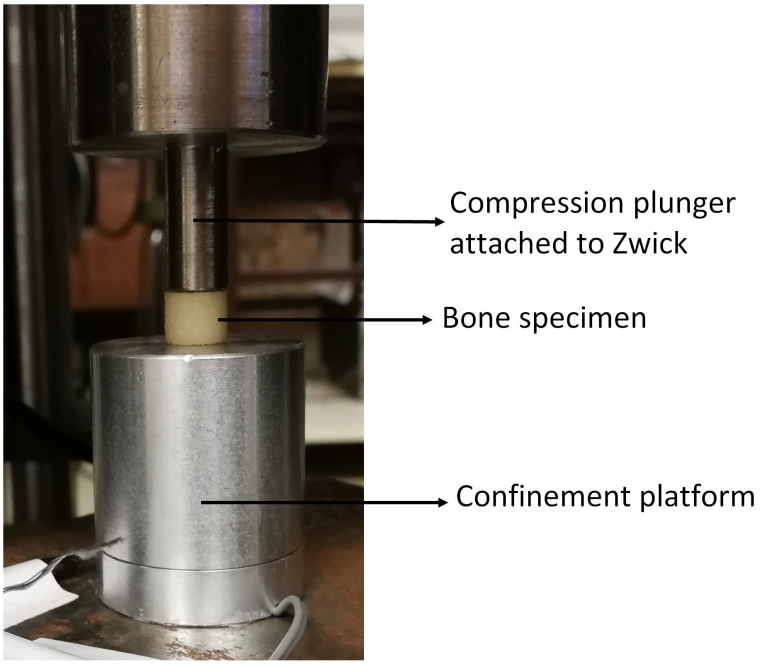

Figure 5.1: Photograph of the compression test set up using the Zwick 1484.

5.3 Confinement Design

Coring cylindrical specimens of bone from within a larger bone removes the structural integrity and support surrounding the specimen. In an *in vivo* environment, the specimen may have been supported by surrounding trabeculae, marrow and possibly cortical bone. When the cylinder is removed from the whole bone, it is no longer in contact with the aforementioned support, allowing marrow to escape from the inter-trabecular spaces and potentially causing weaker trabecular response to crushing forces.

In an attempt to replicate the *in vivo* response, confinement techniques were developed during the investigation. The following sections describe different methods of confinement aimed at both supporting the trabeculae and at preventing marrow from being forced out of the inter-trabecular spaces within each specimen.

5.3.1 Structural confinement

Structural confinement of specimens involved creating a physical boundary for the trabeculae on the external circumferential face of the specimen. Structural confinement in the investigation also aimed to contain the marrow within the trabecular network.

An attempt at structural confinement was made using a 10 mm inner diameter collar and plunger system made of aluminium. This system was a modified version of the quasi-oedometric compression test set up used by Forquin *et al.* [62]. The system is shown

in a photograph in figure 5.2a. Figure 5.2b shows a schematic of the placement of each specimen during testing. An air release hole was drilled into the aluminium to allow air to escape the confinement when setting the specimen position, while an o-ring was placed over the outer diameter of the plunger in order to stop marrow from being expelled through gaps in the system. Figure 5.3 indicates the order in which the specimen was placed in the collar and plunger system in order to eliminate air bubbles from the system. First, the bone specimen was placed inside the end of the collar, on the opposite side to the air release hole as shown in step 1. The specimen was then advanced into the collar using the aluminium stopper as shown in step 2, until the first face of the specimen was in line with the air release hole. When in position, as shown in step 3, the plunger was pushed into the collar until in contact with the exposed face of the specimen. The air release hole allowed air to escape while the plunger was being positioned. Finally, the specimen and aluminium stopper were pressed down together, until the aluminium stopper was aligned with the bottom of the collar as shown in step 4. These steps were completed by hand to ensure that no substantial compressive force was applied to the specimen during loading.

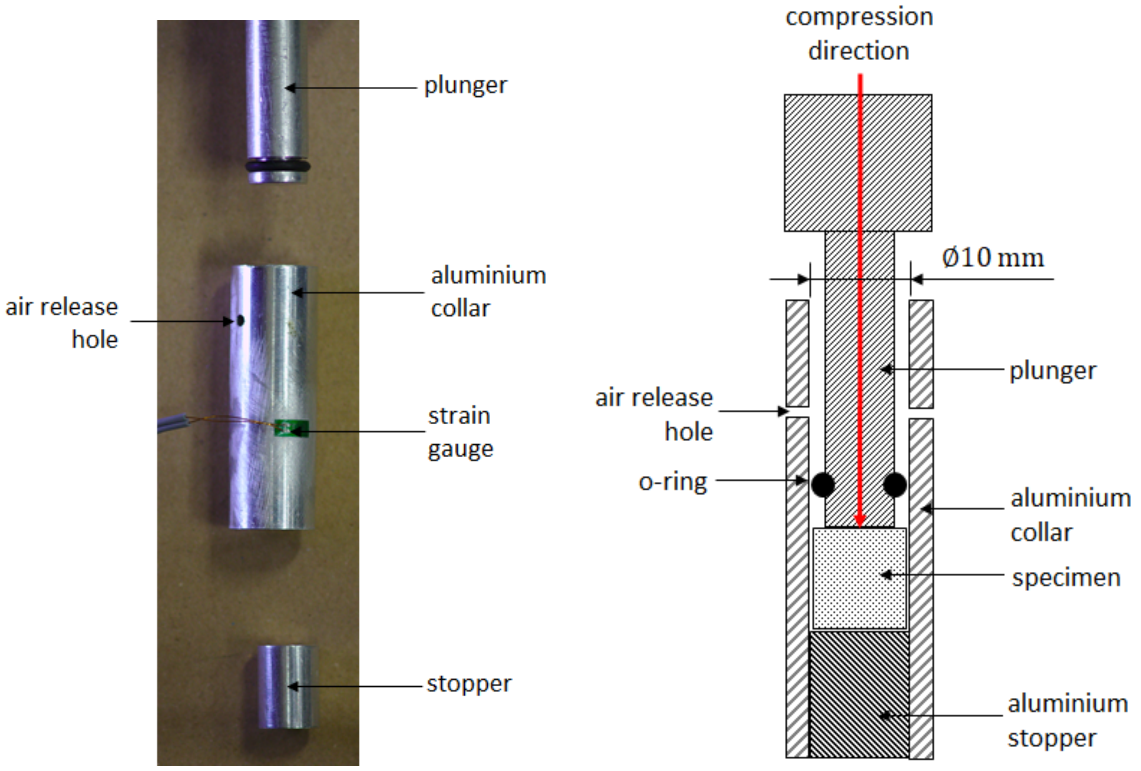

(a) Photograph (b) Schematic including specimen

Figure 5.2: A photograph and schematic of the first attempt at confinement (structural) - a collar and plunger system.

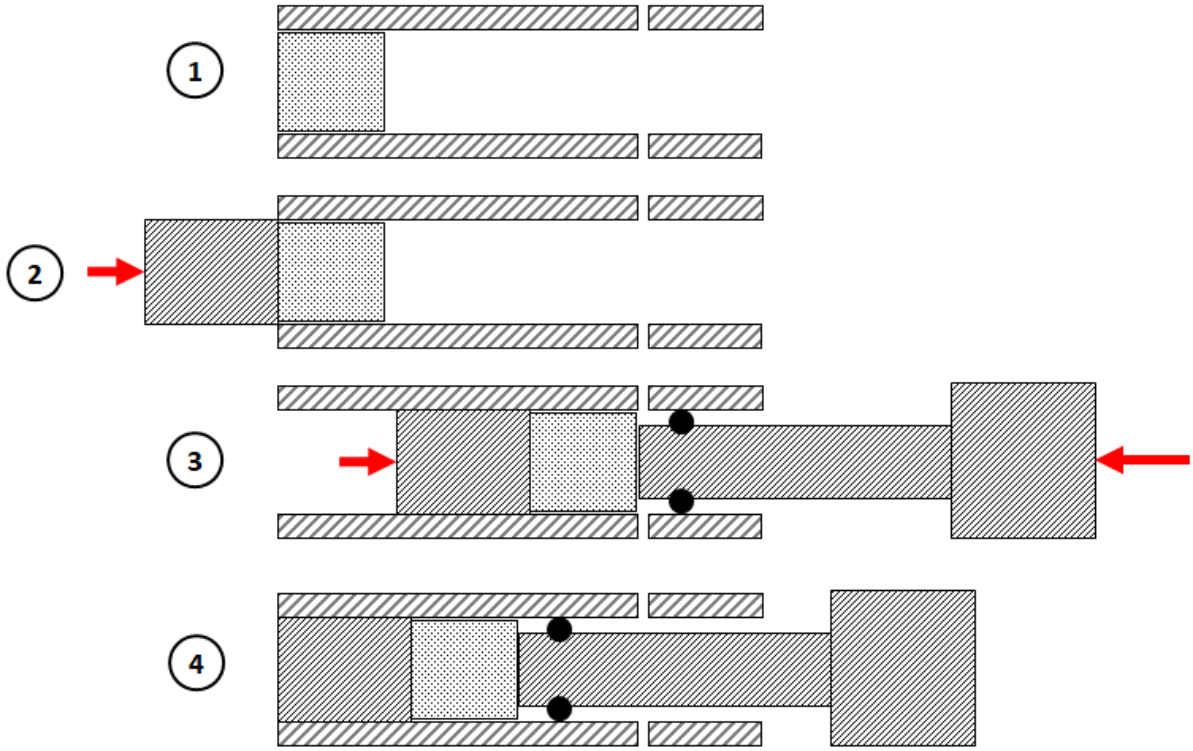

Figure 5.3: A schematic showing the sequence for specimen placement in collar and plunger system to eliminate air bubbles.

This system was designed for use on 10 mm diameter specimens, and aimed to measure the response of specimens when radially confined while being axially compressed. The collar was fitted with a circumferential strain gauge to measure the collar hoop strain during compression of the specimen. For thick-walled cylinders with an applied internal pressure, as shown in figure 5.4, the external hoop strain (ϵ_H^{ext}) is related to the internal pressure (P_{int}) of the cylinder using thick-walled cylinder theory as shown in equation 5.1. The derivation of equation 5.1 is shown in Appendix A.

$$\epsilon_H^{ext} = \frac{2P_{int}}{E} \frac{R_{int}^2}{R_{ext}^2 - R_{int}^2} \tag{5.1}$$

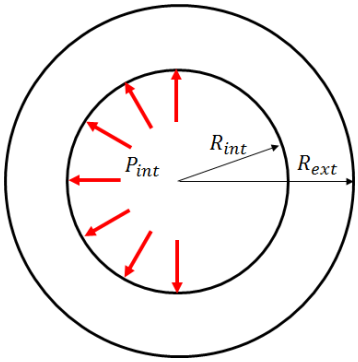

Figure 5.4: A schematic of a thick-walled cylinder

By measuring the hoop strain on the outer surface of the collar surrounding each confined specimen, the internal radial pressure caused by axially compressing the specimen is inferred. Although Forquin *et al.* [62] achieved success using a similar confinement method, the investigation used an "interface product" between the confinement and the specimen which filled any internal gaps. The investigation did not rely on pre-machined samples fitting uniformly into a "one-size-fits-all" confinement collar. Therefore, from this investigation it was determined that further refinement of the confinement design is required, as specimen size variation made it difficult for one collar to provide the same fit for every specimen.

5.3.2 Bone Confinement

Confining specimens using surrounding bone was achieved by machining larger diameter specimens to be compressed. Diameters of 20 mm and 28 mm were machined using custom manufactured corers. Plungers were manufactured to match the diameter of each specimen, which allowed the entire specimen to be compressed uniformly.

The response of the inner 10 mm of each specimen was measured during compression. This allowed for a comparison to the mechanical properties of the standard specimen group of 10 mm diameter, and required specialised equipment and instrumentation, namely a confinement platform - discussed further in section 5.3.4.1. Figure 5.5 shows a schematic of the confinement platform and specimen setup.

Figure 5.6 shows photographs of the larger specimens, in place on the confinement platform with specially manufactured plungers in place.

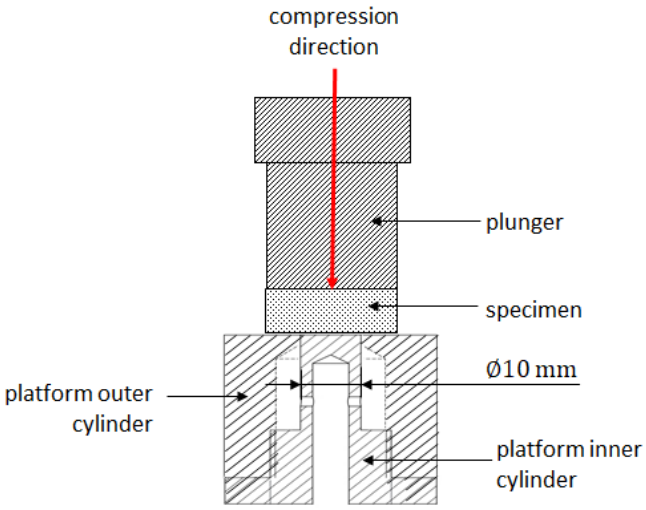

Figure 5.5: A schematic of the second attempt at confinement (bone) - a confinement platform and plunger system.

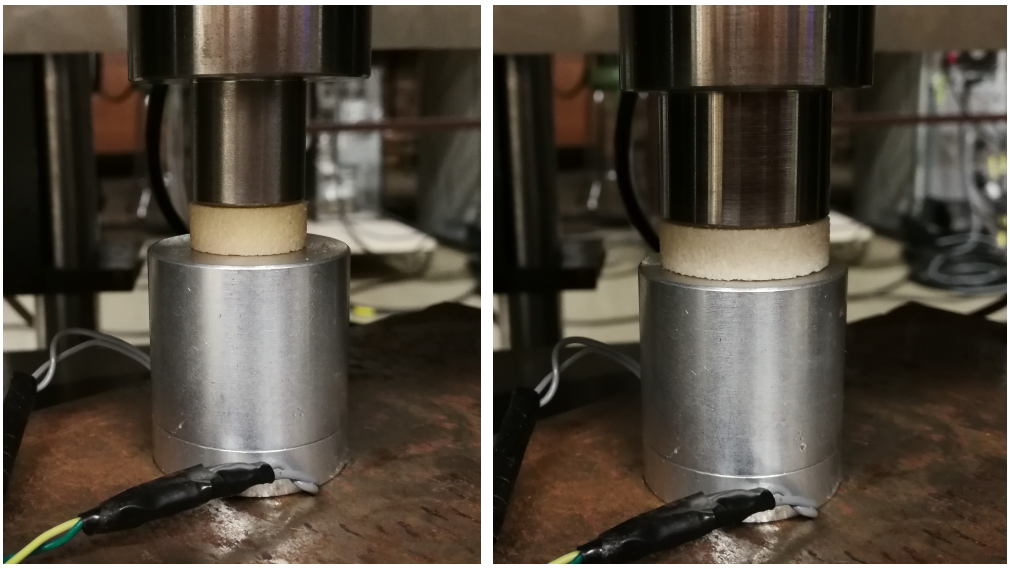

(a) 20 mm specimen (b) 28 mm specimen

Figure 5.6: Photographs of the bone confinement specimen setup

5.3.3 Confinement Setup Summary

The two confinement techniques developed during the study were structural confinement and bone confinement. The schematics in figure 5.7 summarise each technique visually.

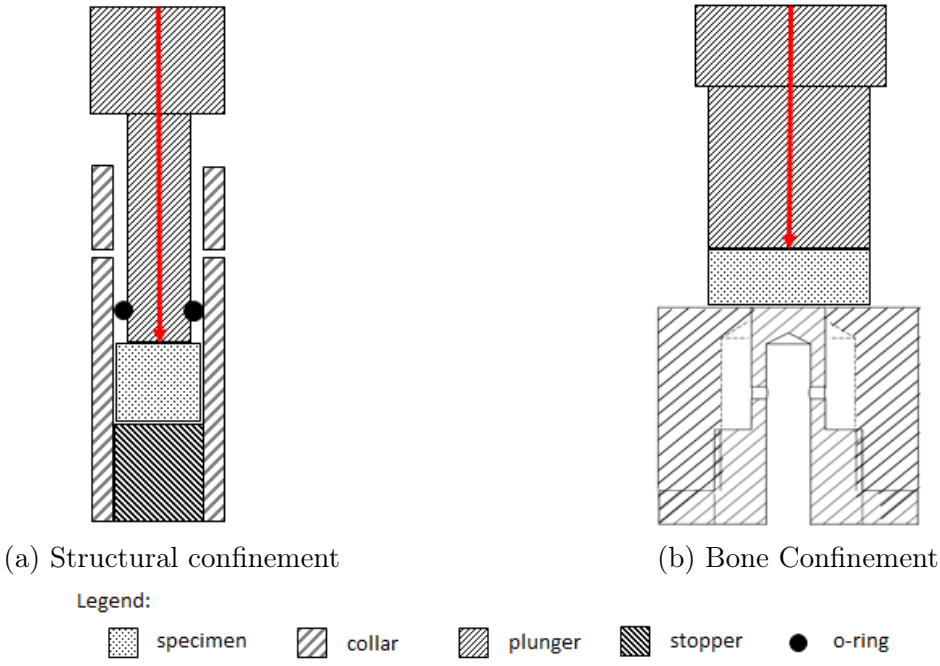

(a) Structural confinement (b) Bone Confinement

Figure 5.7: Schematics showing the confinement setup summary

5.3.4 Confinement Platform

5.3.4.1 Design

In order to measure the response of the inner cylinder of larger specimens, a confinement platform was designed and manufactured. The platform aimed to mimic a loadcell by measuring the force on the inner 10 mm cylinder of bone while the entire bone specimen was compressed. The entire specimen was compressed rather than only the central section in order for the bone confinement to remain aligned with the inner cylinder throughout the compression.

This uniform specimen compression was achieved using a large diameter flat surface on which to compress the specimens consisting of two pieces - an inner central cylinder of 10 mm diameter and an outer cylinder surrounding the 10 mm cylinder which allows for the entire specimen to be compressed at once. Figure 5.8 shows a schematic of the platform design. Figure 5.9 show photographs of the platform, as-machined and strain gauged. Detailed machine and assembly drawings are presented in Appendix C.

The inner cylinder was hollowed out to allow for larger deformation of the section during compression. The circumferential face of the cylinder was then fitted with strain gauges, in order for the cylinder to act as a loadcell. The use of strain gauges aimed to measure the axial strain of the inner cylinder of the confinement platform. The force on the inner 10 mm diameter of the specimen was inferred from this strain measurement.

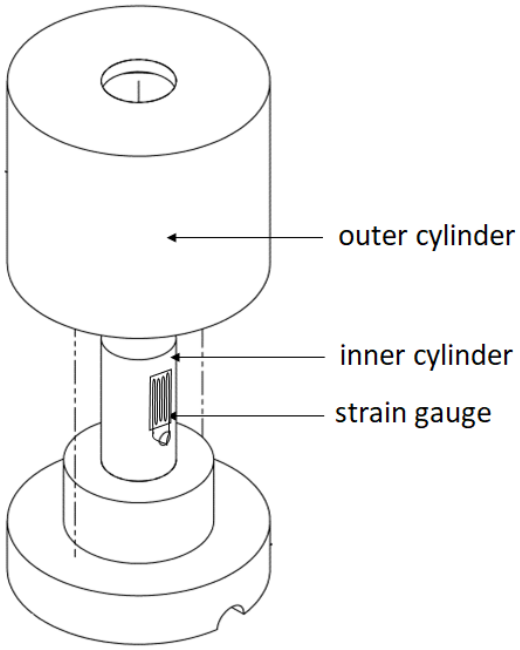

Figure 5.8: Schematic of the assembled confinement platform design.

(a) Inner cylinder

(b) Platform underside

(c) Assembled

Figure 5.9: Photographs of the as-machined and strain gauged confinement platform. (a) shows the strain gauged, pasted on the circumferential face of the inner cylinder. (b) shows in hole bored out of the centre of the inner cylinder for larger deformations. Note the groove machined for strain gauge leads. (c) shows the full confinement platform, assembled with strain gauge leads in place.

Two strain gauges were placed axially along the length of the inner cylinder, diametrically opposite to one another. The gauge outputs were connected to a strain gauge amplifier in a Wheatstone bridge in half bridge configuration. The amplifier was manufactured in house at BISRU. In order to capture the data output, a PicoScope® 12 bit PC oscilloscope was connected to the output of the strain gauge amplifier. The force, and hence stress in the specimen, was related to the voltage output using strain gauge theory, as shown in equations 5.2 - 5.4. Equations sourced from Stander [63].

$$K_f = \frac{4 \times E_{lc} \times A_{lc}}{Gain \times K_{gf} \times N \times V_{BV}} \tag{5.2}$$

$$F_{measured} = K_f \times V_{out} \tag{5.3}$$

$$\sigma_{specimen} = \frac{F_{measured}}{A_{specimen}} \tag{5.4}$$

where:

- A_{lc} is the area of the loadcell - the cross sectional area of the strain gauged section of the inner cylinder
- E_{lc} is the Young's modulus of the loadcell material
- K_f is the loadcell calibration factor
- K_{gf} is the gauge factor of the strain gauges, provided by the manufacturer

- N is the number of active gauges in the Wheatstone bridge
- V_{BV} is the applied bridge voltage
- $Gain$ is the gain of the system set by the amplifier
- $F_{measured}$ is force measured by the loadcell
- V_{out} is voltage output of the bridge
- $\sigma_{specimen}$ is stress in the compressive specimen
- $A_{specimen}$ is the area of the compressive specimen

The loadcell material was chosen to be aluminium, as it is easy to machine and has a relatively low Young's modulus. This allowed for larger deformation during compression, making it possible to obtain strain readings from strain gauges. A metal was chosen rather than a softer material, such as a polymer, to ensure that the loadcell was sufficiently stronger than the specimen being compressed. The outer diameter of the loadcell was set at 10 mm in order to measure the response of the inner 10 mm of each specimen for comparison to the standard specimen group. Therefore, in order to determine the optimal inner diameter of the loadcell, the theoretical output voltage needed to be determined as a function of the inner diameter. The parameters in table 5.1 were used as constants to determine the theoretical measured force, and based on the parameters the graph in figure 5.10 was generated.

Table 5.1: A table presenting the parameters used to determine theoretical measured force

Parameter	**Set Value**
$Gain$	1000
V_{BV}	3 V
E_{lc}	69 GPa
K_{gf}	2.12
N	2

The excitation voltage of the strain gauges (and hence output voltage of the bridge configuration) may not exceed 4 V, as per the manufacturers specifications. Additionally, literature has reported compressive stresses in cancellous bone of up to 50 MPa [22, 55]. The graph in figure 5.10 depicts a greyed out area above the 4 V output voltage, indicating that any geometry which results in voltages within this range may not be considered for

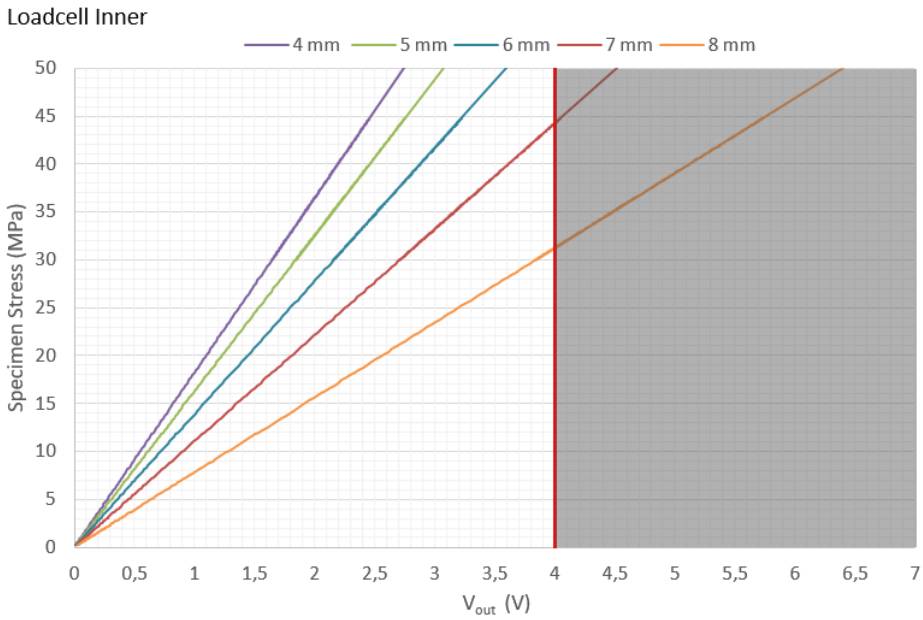

Figure 5.10: A graph showing the theoretical output voltage of the loadcell with respect to the specimen stress based on varying loadcell inner diameters.

the loadcell design. As is evident, the 6 mm inner diameter is the geometry resulting in the largest allowable voltage range for the given configuration, and the loadcell was therefore manufactured with a 10 mm outer diameter and a 6 mm inner diameter.

The outer cylinder of the confinement platform aimed to provide support for larger diameter specimens during compression. In order for this to be effective, the top circular faces of both the inner and outer cylinders needed to be well-aligned and have no significant gaps or surface differences between them. The outer cylinder was therefore fixed to the inner loadcell cylinder using a threaded section below the strain gauged cylinder, which mated with a larger diameter section of the inner cylinder as shown in figure 5.8. This allowed for correct alignment once the outer platform was completely screwed into the threaded section. The diameter of the outer cylinder was set to 35 mm in order to comfortably accommodate larger bone specimens and their various confinement collars.

The two parts of the platform were required to deform at relatively similar rates when compressed. This was to ensure that the entire surface of the specimen was compressed uniformly, eliminating any edges effects. A simple deflection simulation was therefore performed using Autodesk Inventor. A 5 kN force was applied to a 28 mm diameter specimen over the top of the entire platform. This simulated the largest specimen diameter and the estimated largest force expected during compression experiments. The bottom face of the platform was fixed during the simulation.

The wall thickness of the outer platform was varied until the resulting geometry yielded

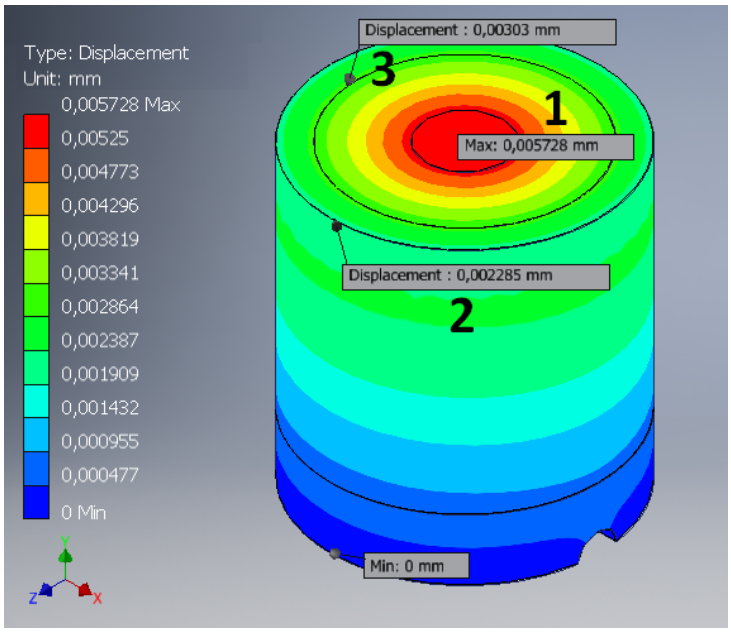

Figure 5.11: Depiction of the deflection simulation of the confinement platform assembly performed using Autodesk Inventor.

minimal differences in the maximum deflections of each part. The final simulation is depicted in figure 5.11 and shows that the difference in the deformation over the entire platform top face is theoretically only 0,00344 mm. This is shown by the displacement at the centre of the platform (probe 1, 0.00573 mm) versus the displacement at the outside edge of the top face (probe 2, 0.00229 mm). Over the entire specimen surface, the difference in displacement between the centre (probe 1) and the outside edge of the specimen (probe 3, 0.00303 mm) would be 0,00270 mm. This result was considered significantly small for the purposes of this study.

5.3.4.2 Specimen Alignment

To ensure that specimens were centrally located on the confinement platform, special care was taken to align the specimens. Alignment was achieved by attaching the 10 mm plunger to the Zwick and placing the confinement platform underneath the plunger. The platform was fixed to a large steel block using double-sided tape. The plunger was brought down slowly until almost in contact with the platform, and the platform was aligned by moving the steel plate so that the inner cylinder was concentric with the 10 mm plunger, as shown in figure 5.12. Once the alignment was complete, the steel plate was not moved again until all tests were complete. This allowed for the plungers to be inter-changed without interfering with the specimen alignment between series.

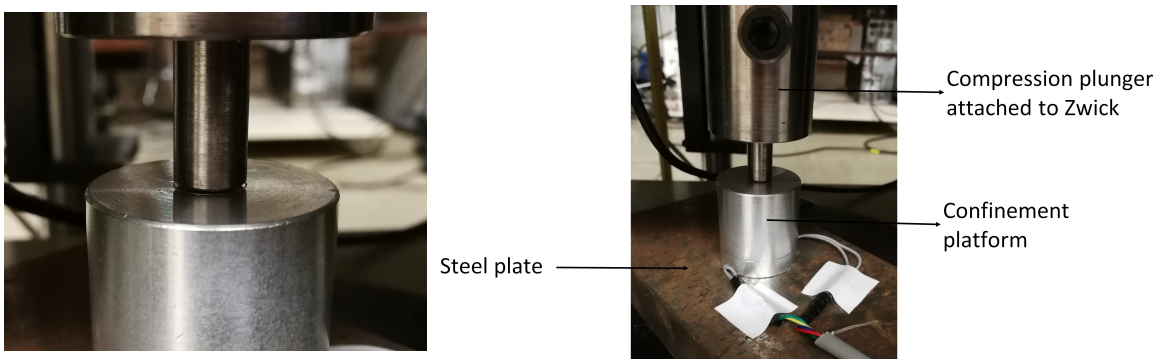

(a) Concentric alignment.

(b) Steel plate positioning.

Figure 5.12: Photographs of technique for aligning the confinement platform with the plunger attached to the Zwick.

5.3.4.3 Calibration

Calibration of the confinement platform was required for accurate force measurements while using the platform during experimentation. To perform this calibration, a 10 mm plunger was attached to the Zwick and aligned with the platform as described in section 5.3.4.2. Eighteen (18) standard specimens were tested on top of the platform, and data from both the platform strain gauges (captured using the Picoscope®) and the Zwick were collected. During the investigation, the parameters in table 5.2 were used.

Table 5.2: A table presenting the confinement platform setup parameters used during the investigation

Parameter	**Set Value**
$Gain$	1000
V_{BV}	15 V
E_{lc}	69 GPa
K_{gf}	2.12
N	2

A bridge voltage of 15 V was used for better sensitivity to a change in force. The remaining parameters were used as described in section 5.3.4.1. Based on equations 5.2-5.4, given in section 5.3.4.1, the theoretical calibration factor based on the parameters used was 218.13.

In order to determine the actual calibration factor, both the Zwick and Picoscope® data were processed using the method described in section 5.5.1. This method smoothed and shifted both sets of data to pass through the origin. The maximum strain gauge voltage output for each of the 18 specimens was then compared to the maximum force output

read by the Zwick loadcell for each loaded specimen. The calibration factor for each specimen was determined using equation 5.5.

$$\text{Calibration factor} = \frac{\text{Zwick Force}_{max}}{\text{Strain Gauge Voltage Output}_{max}} \tag{5.5}$$

Figure 5.13 shows examples of force-displacement graphs for two specimens which were used during the aforementioned calibration. As seen in figure 5.13, the shape and magnitude of the force measured by the platform agrees well with that measured by the Zwick loadcell.

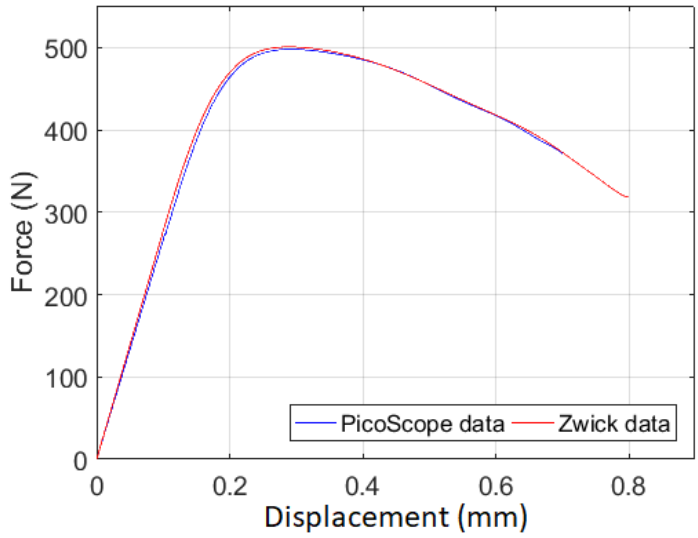

(a) Specimen 455

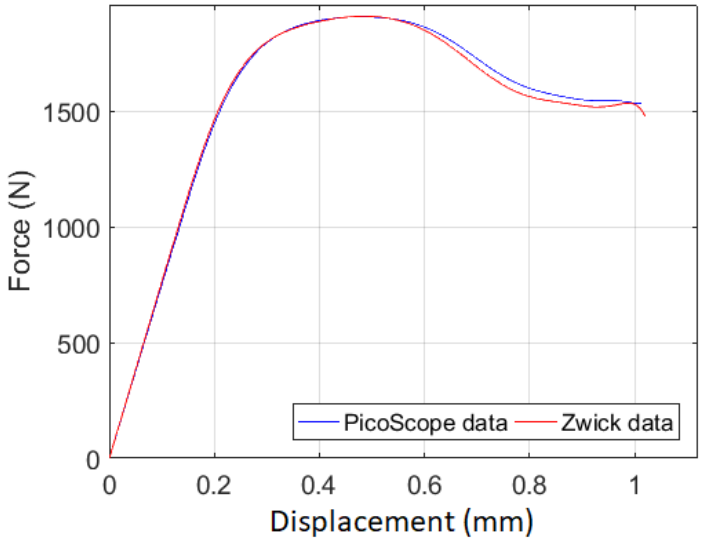

(b) Specimen 462

Figure 5.13: Graphs showing examples of force-displacement curves for specimen tests used to calibrate the confinement platform.

The average calibration factor for all 19 specimens was determined to be 252.88. This value was used throughout the remainder of the investigation. The actual calibration factor was 13.74% greater than the theoretical calibration factor for the parameters used. This may be attributed to a number of factors, such as inaccuracies during machining of the platform (inner and/or outer diameters), actual Young's Modulus of the Aluminium used or unforeseen movement between the platform, specimen and base during the testing. Although there was an error between theoretical and actual calibration factor values, this was deemed acceptable because of the consistent calibration results.

5.4 Experimental Test Series

The experimental investigation was performed using three main specimen conditions, namely:

1. Unconfined with marrow (standard)
2. Defatted
3. Confined

Confined specimens were further divided into 2 types of confinement, as described previously, namely:

1. Structural confinement
2. Bone confinement

For each specimen condition, three strain rate experiments were performed, namely 10^{-3} s^{-1}, 10^{-2} s^{-1} and 10^{-1} s^{-1}. However, bone confinement was only performed at strain rates of 10^{-3} s^{-1} and 10^{-1} s^{-1}. This resulted in a total of 6 loading scenarios and 13 test series. A summary of these scenarios is shown in table 5.3.

Table 5.3: A table showing a summary of the experimental test series.

Series	**Specimen Condition**	**Confinement Type**	**Specimen Diameter (mm)**	**Strain Rate (s^{-1})**	**Number of tests**
1	Standard	None	10	10^{-3}	15
2				10^{-2}	8
3				10^{-1}	18
4	Defatted	None	10	10^{-3}	9
5				10^{-2}	10
6				10^{-1}	14
7	Confined	Structural	10	10^{-3}	8
8				10^{-2}	10
9				10^{-1}	15
10	Confined	Bone	20	10^{-3}	4
11				10^{-1}	5
12	Confined	Bone	28	10^{-3}	5
13				10^{-1}	3
Total number of tests					**124**

5.5 Compression Data Analysis

The compression data obtained during the investigation was in the form of force and displacement data, outputted by the Zwick Universal Tester. Additional strain data was obtained using the strain gauge and PicoScope® combination described in section 5.3.4.1. MATLAB was used to convert the raw data into stress and strain data in order to determine the mechanical properties of each specimen. The following sections describe the way in which data was processed and analysed.

5.5.1 Determining Mechanical Properties

In order to determine the mechanical properties of each specimen, the raw force and displacement data from the Zwick, as shown in figure 5.14a, was converted to stress (σ) versus strain (ϵ) curves for each test performed, using the equations:

$$\sigma = \frac{F}{A_{specimen}} \tag{5.6}$$

$$\epsilon = \frac{Displacement}{H_{specimen}} \tag{5.7}$$

Where $A_{specimen}$ and $H_{specimen}$ are the original specimen area and height respectively. For accurate results, each specimen diameter and height was measured using a digital vernier calliper prior to compression testing. The converted data is shown in figure 5.14b. The red square shown in the figure indicates a portion of "take-up" or "settling" of the setup, present in each compression test due to compliance in the test set up as the specimen loading begins.

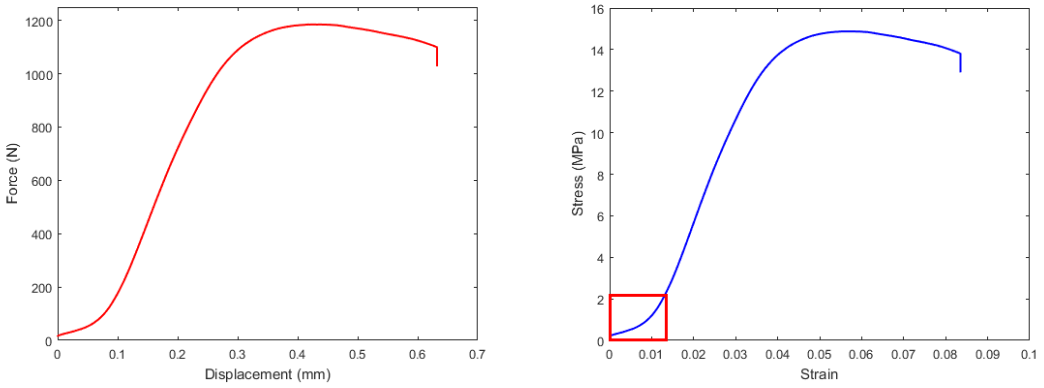

(a) Force-displacement (b) Stress-strain

Figure 5.14: Plots of raw force-displacement and converted stress-strain curves for an example compressed specimen.

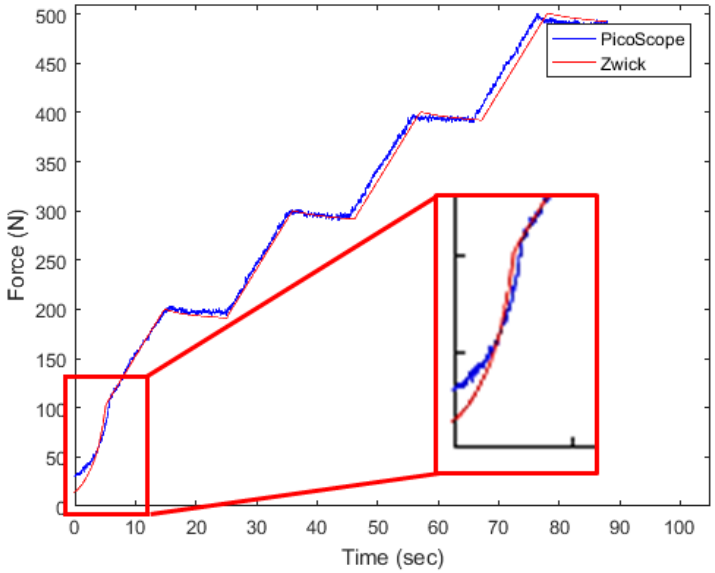

Figure 5.15: A graph showing an example of the experimental setup calibration data

The non-linear portion of the graph shown in figure 5.14 was identified as "take-up" or "settling" during calibration of the test set up. The graph shown in figure 5.15 is an example of the data collected during the calibration of the experimental setup. Calibration was performed using the experimentation equipment as shown previously in the photograph in figure 5.12 - with no specimen present. The data from this calibration all indicated a varying region of take-up, and it was therefore determined that this portion of the graph was due, at least in part, to machine compliance. Data in the literature is consistent with bone acting linearly under small strain, and the variation in the take-up portion seen during calibration is consistent with a settling behaviour of the setup.

In order for the curve to represent the true loading scenario, the take-up portion of the curve was removed. This was accomplished by first fitting a 6th order polynomial to the stress-strain data using MATLAB. The maximum gradient of the fitted polynomial within the elastic region of the curve was calculated, and the point at which this gradient occurred was found. A line with a gradient equal to the maximum gradient was fitted to the data, passing through the point at which this gradient occurred. The resulting graph is shown in figure 5.16a. A close up of the section within the red square is shown in figure 5.16b. As seen in figure 5.16b, the fitted straight line does not pass through the origin. In order for the curve to represent the true specimen loading, the entire graph was shifted by a strain (ϵ_m) equal to the strain in the entire system due to machine take-up. The shifted graph is shown in figure 5.16c.

The drop-off portion at the end of the curve, indicated with a red oval in figure 5.16c, was due to the termination of the experiment, or the rapid unloading of the specimen. This

portion of the data was removed by finding the point at which the gradient of the graph was most rapidly decreasing within the yielding portion of the data. Mathematically, this point was found by equating the second derivative of the curve to zero.

Finally, the portion of the graph indicating machine take-up was replaced with the fitted straight line graph. The resulting curve is shown in figure 5.16d. The point marked with a black square in figure 5.16d indicates the yield strength (σ_y) of the specimen. The yield strength was determined in MATLAB using the intersection between the stress-strain curve and the straight line, with gradient equal to the maximum gradient of the elastic region, passing through a strain of 0.002. This corresponds to the 0.2% offset yield point, shown as the red dotted line in figure 5.16d. Similarly, the point marked x on the graph represents the US of the material, which was found using MATLAB by determining the largest stress value on the curve. Mathematically, the shifted strain data was calculated using equation 5.8.

$$\epsilon_m = \epsilon_{max.grad} - \frac{\sigma_{max.grad}}{m} \tag{5.8}$$

where $\sigma_{max.grad}$ and $\epsilon_{max.grad}$ are the stress and strain at the point corresponding to the maximum gradient respectively and m is the value of the maximum gradient.

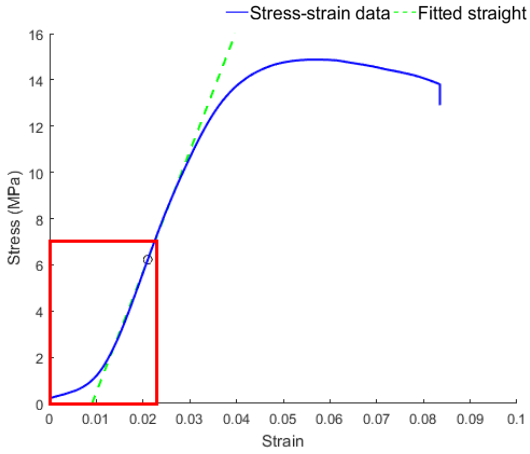

(a) Straight line fitted through point of maximum gradient.

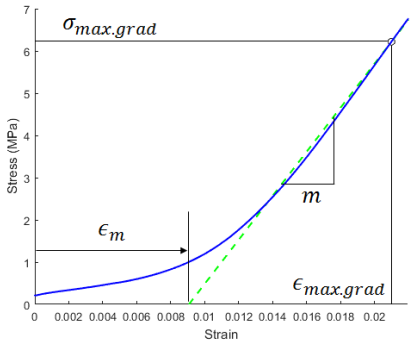

(b) Close up of fitted straight line.

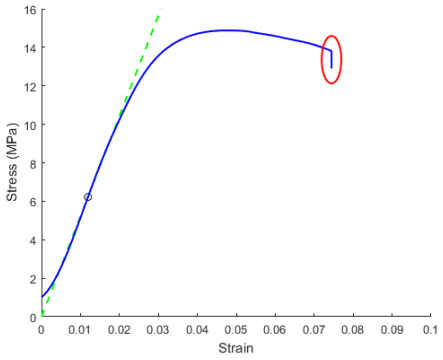

(c) Graph shifted by ϵ_m.

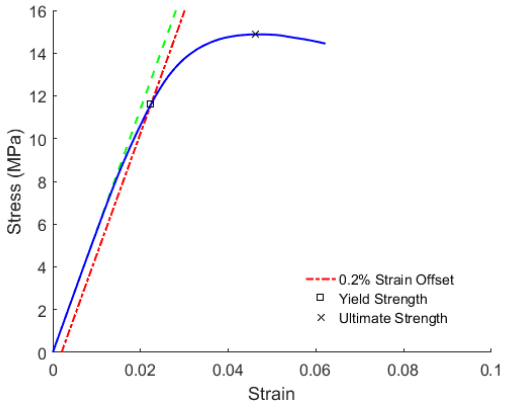

(d) Final corrected graph

Figure 5.16: Graphs showing the removal of the effects of machine take-up and specimen unloading on a stress-strain curve.

The strain data obtained from the PicoScope® and confinement platform setup was processed in a similar way. First, the output voltage curve was smoothed using a low pass RC filter, with a cut-off frequency of 2 Hz. The filtered voltage was converted to force using the method described in section 5.3.4.3. The force data was coupled with the Zwick displacement data, and was converted to stress versus strain data, as described above. For the data obtained from the confinement platform, stress was calculated using the outer diameter of the inner cylinder of the platform (10 mm).

5.5.2 Statistical Analysis of Data

Statistical analysis of the results was performed by assuming a modified Log-normal distribution for each data set. The aim of this analysis was to determine relevant mode and standard deviations for the data sets, and to compare these to one another.

A Log-normal distribution is typically used to fit data sets which comprise of positive, real values and which are suspected to be skewed [64]. In the case of the mechanical properties of cancellous bone, it was suspected that these values would be skewed, or have outlying data which could affect the average values of the results, making a Log-normal distribution an appropriate choice for analysing the results of the investigation.

A variable, X, is said to be Log-normally distributed if $Y = ln(X)$ is normally distributed. Normally distributed data has the advantage of being easy to analyse - average and mode occur at the same point, and three standard deviations on either side of the mode will encompass 99.7% of the data within the set. For these reasons, it was desirable to model the data obtained during this investigation using a normal distribution.

For the data obtained during this investigation, it was not clear whether or not the natural log of the data was normally distributed. Therefore, the first step in the analysis was to transform the data into Log-normally distributed data, using steps 1-4 below.

1. A random variable was added to each point in the data set according to equation 5.9.

$$X = XX + a; \tag{5.9}$$

   Where:

   - XX is the original data
   - a is a random variable

2. The natural log of the new data set (X) was calculated as in equation 5.10

$$Y = ln(X) \tag{5.10}$$

3. The skewness of the distribution of Y was determined.

4. The random variable, a, was iteratively changed until the skewness of Y was zero (or minimised)

Once these steps were complete, the data set $Y = ln(X)$ was normally distributed. Figures 5.17 and 5.18 show an example of this transformation. As seen in figure 5.18, the modified data is now normally distributed.

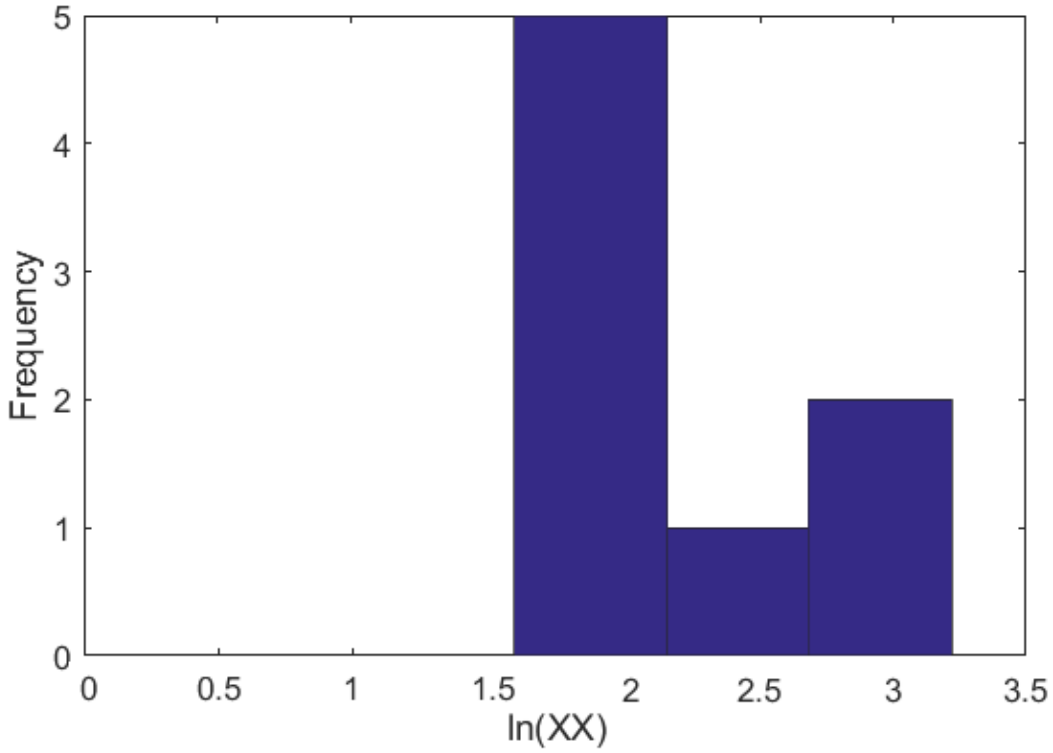

Figure 5.17: Histogram showing the distribution of the natural log of the original data set.

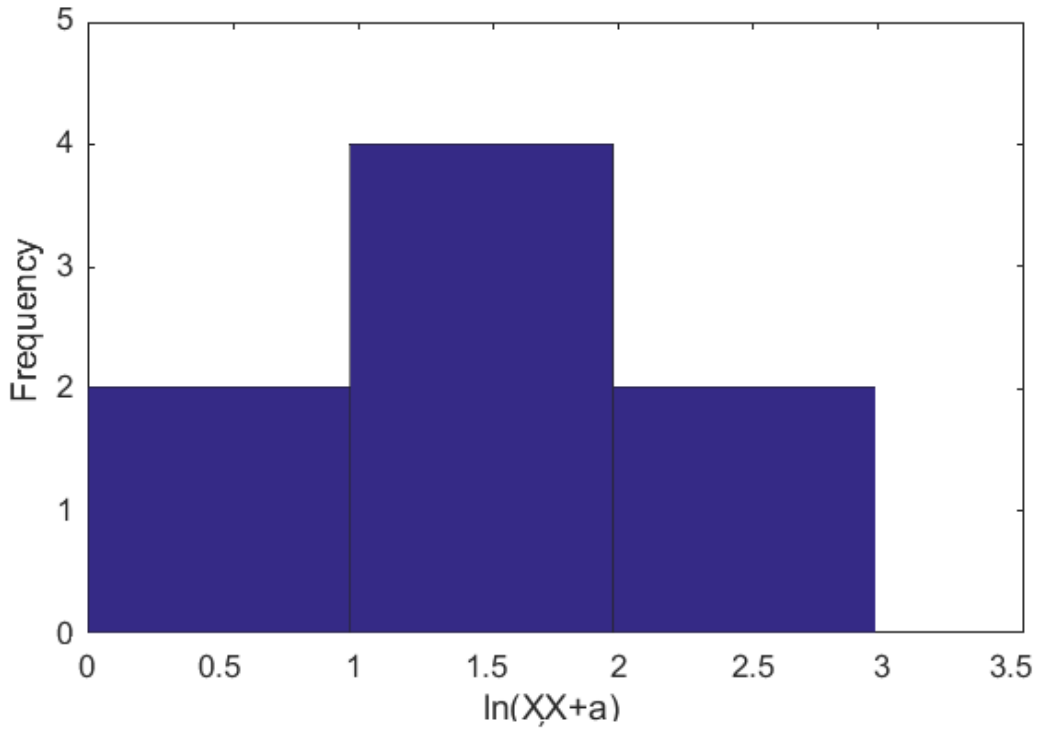

Figure 5.18: Histogram showing distribution of the natural log of the modified data set, with optimal variable, a, included.

The transformed data was analysed to obtain the mode and standard deviation values. These values were used to determine the upper and lower bounds of the probability density function - i.e. mode $\pm$ 3 $\times$ standard deviation. Figure 5.19 shows the modified data, with probability density function overlaid. The mode and both upper and lower bounds of the graph are indicated in the image as a black circle and black crosses respectively. The maximum value of the overlaid curve is an indication of the tightness of the grouping of the data in the set. This value, shown as a black square in figure 5.19, was used in the analysis as a "tightness factor" to compare data sets to one another. The greater the value, the more tightly grouped the data set.

The calculated values for mode and upper and lower bounds were transformed back to the original data space, using a reverse of the Log transformation. This was transformation was performed using equation 5.11.

$$XX = e^{X} - a \tag{5.11}$$

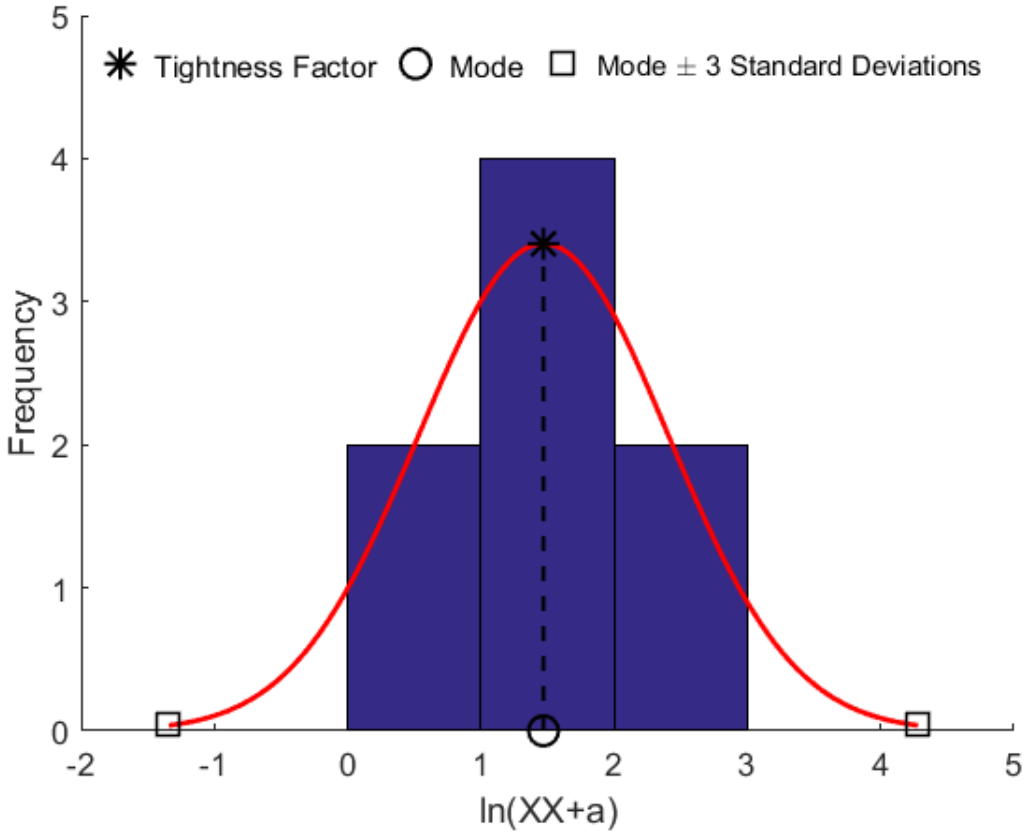

Figure 5.19: A graph showing the modified data set with overlaid, normally distributed, probability density function.

When converting the lower bound value back to the original data space, values were limited to zero, as no data obtained during the investigation could be negative. The converted values for the mode and upper and lower bounds, along with the unconverted tightness factor and the average value of the unmodified data set, were used to plot a graph for each data set such as that shown in figure 5.20. These graphs give a visual representation of a full data set, making analysis and comparison of data sets simpler.

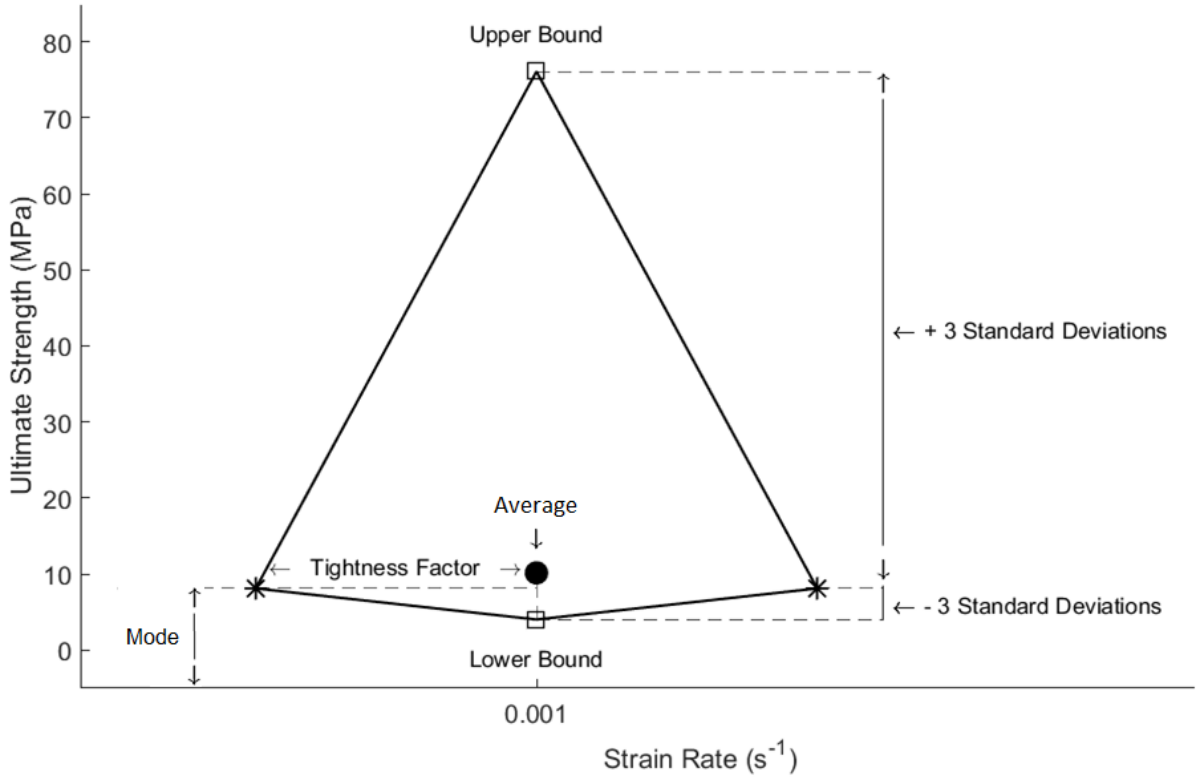

Figure 5.20: A graph with annotations showing an example of graphs used for data analysis, constructed using the statistical analysis method described previously.

Chapter 6

Results and Discussion

This chapter presents the results of experimental tests as well as image processing performed to determine architectural parameters. The influence of factors such as strain rate, presence of marrow, confinement condition and architectural parameters are analysed and compared both to one another, and also to the literature.

6.1 Compression Test Results

Stress-strain curves for each test were obtained and analysed using the method described in section 5.5.1. Figure 6.1 shows an example of these curves. The full set of stress-strain curves for the tested samples are presented in Appendix B.

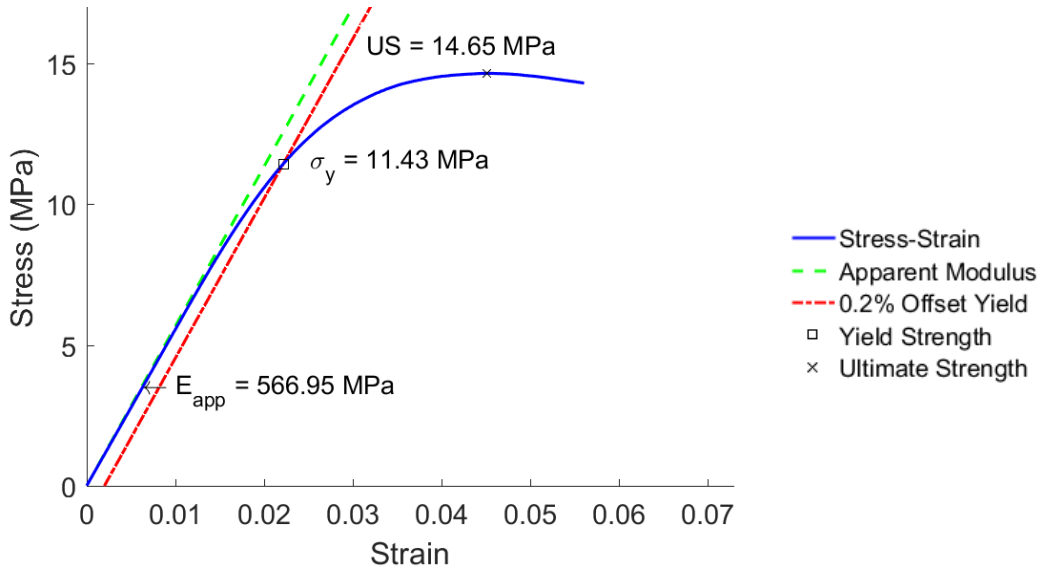

Figure 6.1: A graph showing an example of a Stress-Strain curve obtained during this investigation

6.1.1 Apparent Modulus

Figures 6.2a - 6.2e show the apparent modulus results for various testing conditions at the tested strain rates (10^{-3}, 10^{-2} and 10^{-1} s^{-1}).

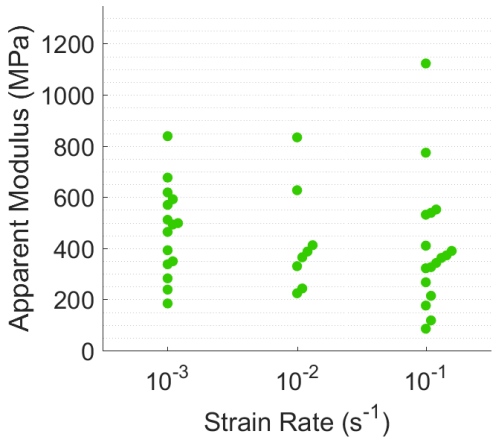

(a) Standard Specimen

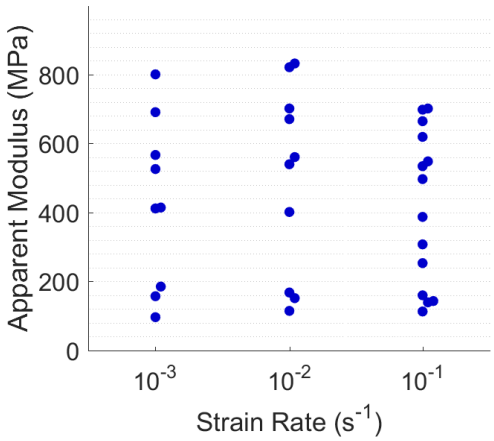

(b) Defatted Specimen

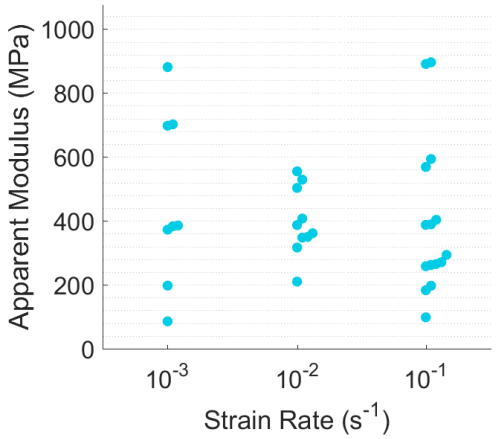

(c) Confined Specimen

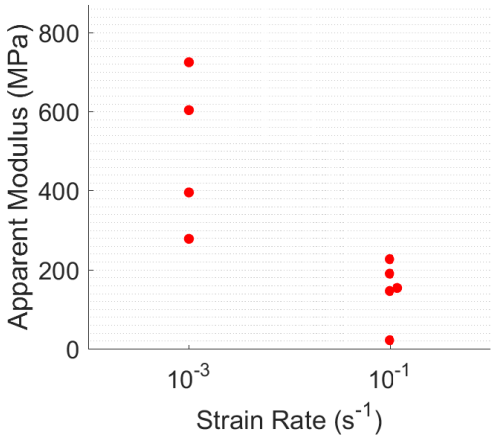

(d) 20 mm Bone Confined Specimen

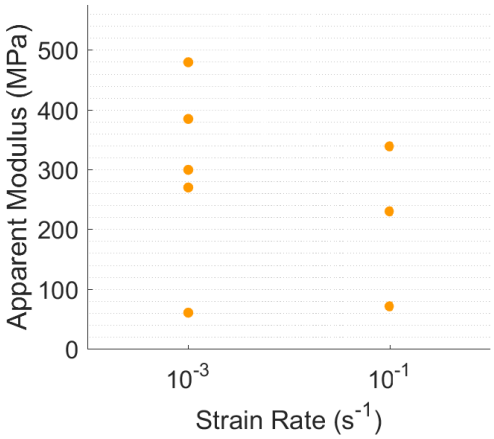

(e) 28 mm Bone Confined Specimen

Figure 6.2: Graphs showing the Apparent Modulus Results

6.1.2 Yield Strength

Figures 6.3a - 6.3e show the yield strength results for various testing conditions at the tested strain rates (10^{-3}, 10^{-2} and 10^{1} s^{-1}).

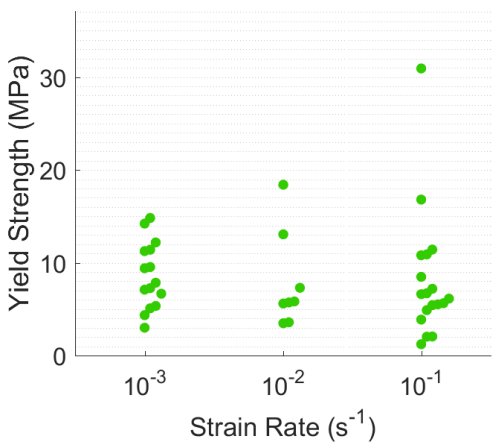

(a) Standard Specimen

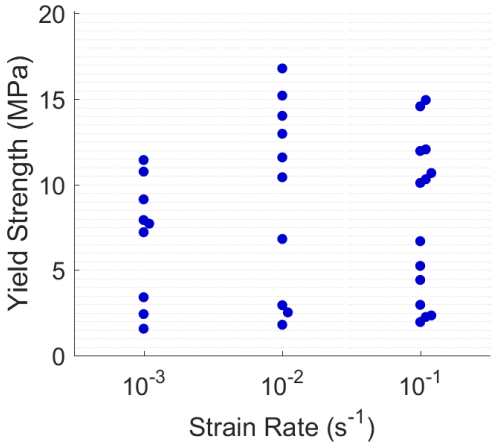

(b) Defatted Specimen

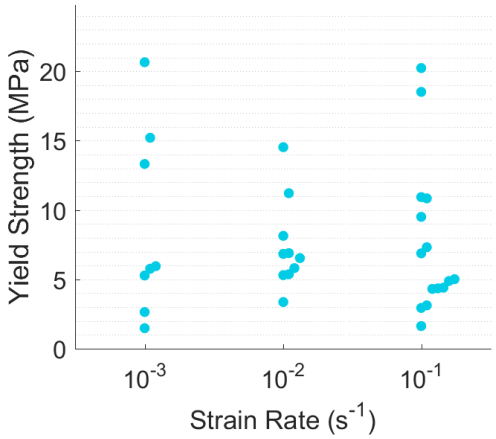

(c) Confined Specimen

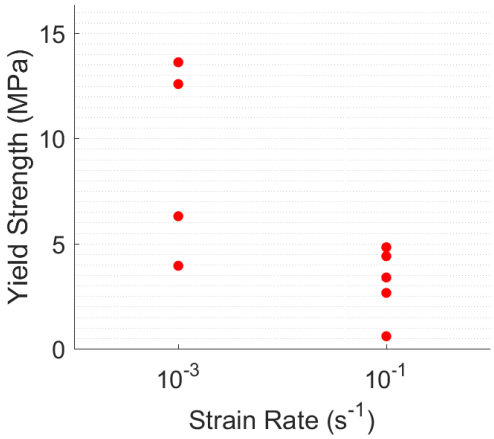

(d) 20 mm Bone Confined Specimen

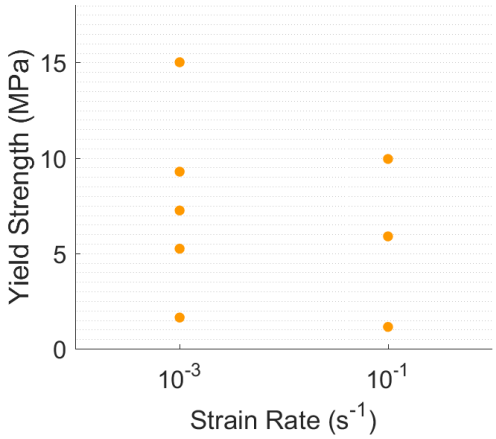

(e) 28 mm Bone Confined Specimen

Figure 6.3: Graphs showing the Yield Strength Results

6.1.3 Ultimate Strength

Figures 6.4a - 6.4e show the ultimate strength results for various testing conditions at the tested strain rates (10^{-3}, 10^{-2} and 10^{-1} s^{-1}).

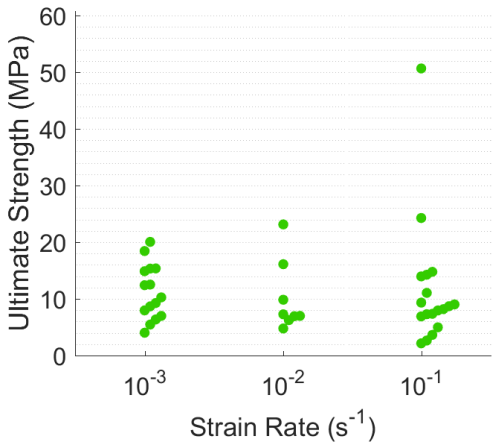

(a) Standard Specimen

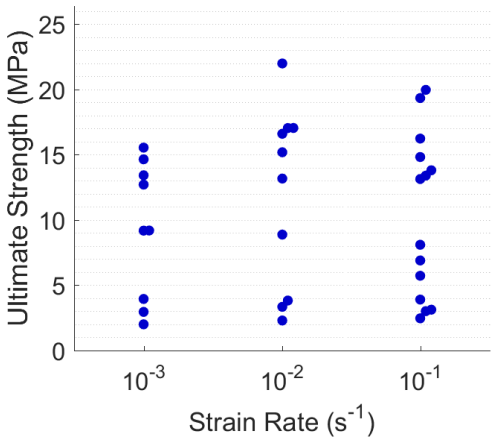

(b) Defatted Specimen

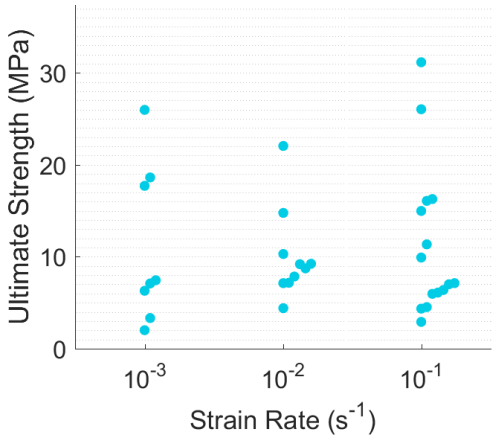

(c) Confined Specimen

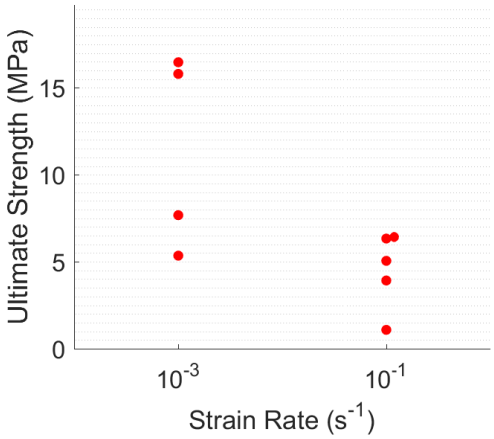

(d) 20 mm Bone Confined Specimen

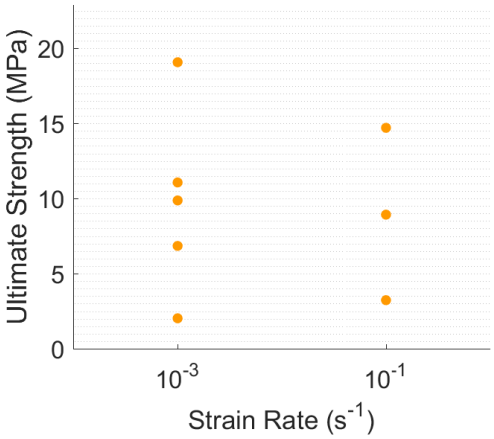

(e) 28 mm Bone Confined Specimen

Figure 6.4: Graphs showing the Ultimate Strength Results

6.2 General Discussion

The results showed a large range of variability over the test types, as well as scatter within test types. This is consistent with what has been reported in the literature [20, 24, 33, 35, 42, 50, 51, 61, 65] as trabecular bone has been seen to exhibit a range of mechanical properties depending on numerous factors, such as apparent density, anatomical site, architectural parameters and testing conditions. In table 6.1, the results for each test series as shown in table 5.3 are presented. The results are presented as averages for apparent modulus (E_{app}), yield strength (σ_y) and ultimate strength (US) for each test series.

Table 6.1: A table showing the average experimental test results.

Series	**Test Type**	**Strain Rate (s^{-1})**	**Average (MPa)**		
			E_{app}	σ_y	**US**
1	Standard	10^{-3} (N=15)	453.84	8.20	10.68
2		10^{-2} (N=8)	427.52	7.87	10.17
3		10^{-1} (N=18)	406.20	8.14	11.51
4	Defatted	10^{-3} (N=9)	427.85	6.84	9.29
5		10^{-2} (N=10)	496.33	9.51	11.94
6		10^{-1} (N=14)	412.05	7.89	10.29
7	Structurally Confined	10^{-3} (N=8)	462.99	8.79	11.06
8		10^{-2} (N=10)	396.57	7.40	10.09
9		10^{-1} (N=15)	397.05	7.66	11.35
10	20 mm Bone Confined	10^{-3} (N=4)	500.38	9.11	11.32
11		10^{-1} (N=5)	147.53	3.17	4.56
12	28 mm Bone Confined	10^{-3} (N=5)	298.65	7.68	9.77
13		10^{-1} (N=3)	213.13	5.66	8.95

The average results show variability between values for series 1-9. There was a large range of scatter within each test series, which suggests that average values may have been skewed by outliers in the data and this may result in overall averages exhibiting similar trends. The data in table 6.1 also suggests that the bone confined specimens have a weaker mechanical response in terms of apparent modulus. However, due to bone availability and large specimen sizes, fewer specimens were available for testing for series 12-15 - with only 4-5 specimens per series. This smaller sample set could be the cause of the lower average moduli, yield strength and ultimate strength values. In addition, the variation may be attributed to the fact that all the specimens of larger diameters were manufactured markedly later than the original specimens. Although sourced from

the same initial set of whole bones, the bone confined specimens were machined after the whole bones had been frozen (without physiological saline) for a year. To more accurately assess the effects of test type on mechanical response, the following sections present details of multiple tests, comparing strain rate, boundary conditions and architectural parameters.

6.3 Strain Rate Comparison

The literature suggests that trabecular bone exhibits visco-elastic properties [53–56, 65]. Strain rate is therefore an important parameter to consider when determining the mechanical properties of bone. As stated previously, only quasi-static strain rates (10^{-3}-10^{-1} s^{-1}) were investigated during this study. The results of this investigation are shown using graphs and discussion in the following sections. For all graphs in these sections, refer to figure 5.20 for an explanation of the data points.

6.3.1 Standard Specimens

Figure 6.5 shows the results for standard specimens across three quasi-static strain rates. It is observed in the figure that there is little to no significant difference between average and mode values across the strain rates. However, when tests were performed at the lowest strain rate, 10^{-3} s^{-1}, the data appeared to be less scattered. This is evident by the wide tightness factor. The tighter grouping of the upper and lower bounds when compared to the other two strain rates also validates this finding.

The 10^{-1} s^{-1} data set has the widest tightness factor, however, the upper bound is noticeably higher than the 10^{-3} s^{-1} data set. This suggests a greater standard deviation, considering both data sets have similar mode values.

While the specimens tested at a strain rate of 10^{-2} s^{-1} appear to be most scattered - smallest tightness factor and largest upper bound - the data set also has the smallest sample size of the three groups. This suggests that outliers would have a greater effect on the overall data for this particular data set.

The data in figure 6.5 suggests that while strain rate has no significant effect on the average apparent modulus of data sets, increasing the strain rate introduces increased scatter to the data. This observation is mirrored in figures 6.6 and 6.7. In each case, the average and mode of the data sets remain similar, while the upper bounds of each of the higher strain rate tests is significantly larger than that of the specimens tested at the lowest strain rate.

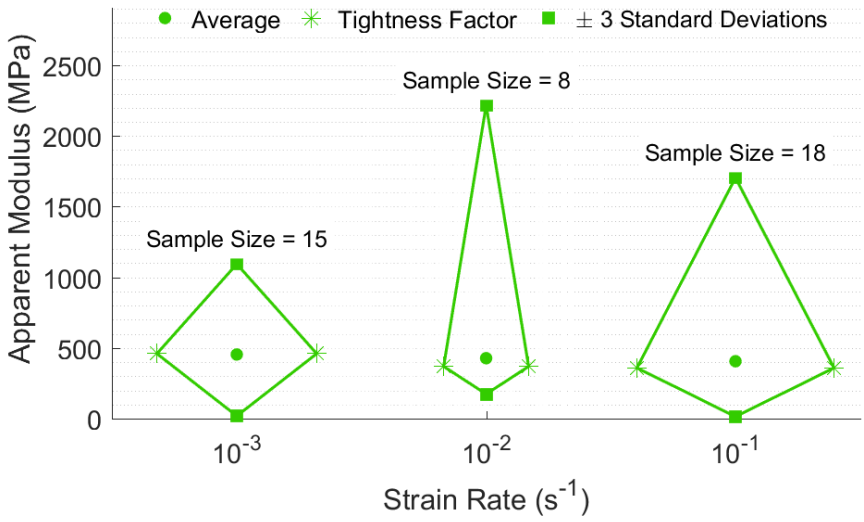

Figure 6.5: A graph of Apparent Modulus versus Strain Rate for standard specimens

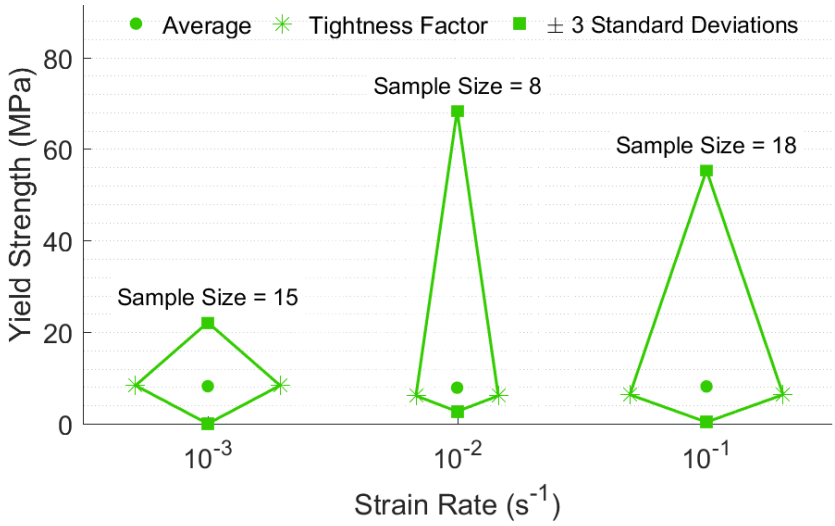

Figure 6.6: A graph of Yield Strength versus Strain Rate for standard specimens

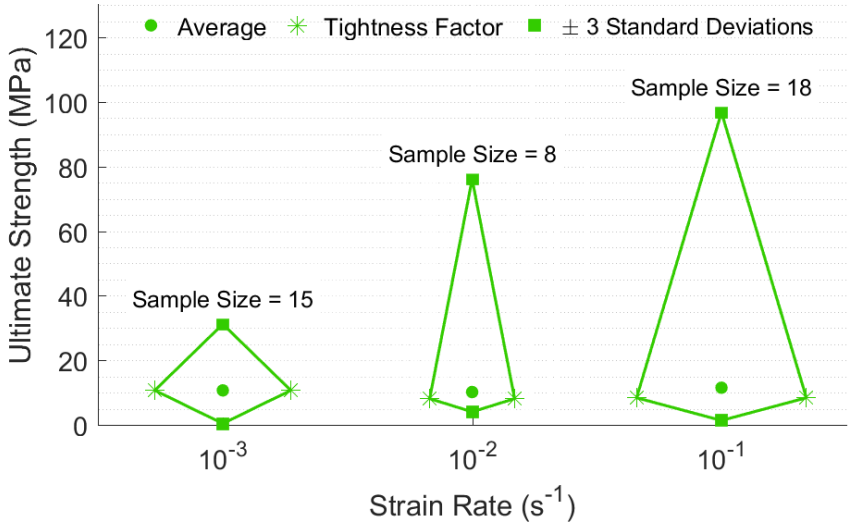

Figure 6.7: A graph of Ultimate Strength versus Strain Rate for standard specimens

6.3.2 Defatted Specimens

Figures 6.8-6.7 show the results for apparent modulus, yield strength and ultimate strength of defatted, 10 mm cylinderical trabecular bone samples over the three strain rates investigated.

The graphs show no correlation between the average or mode of these data sets and strain rate, and little correlation between scatter over varying strain rates. The literature suggests that marrow plays an important role in the mechanical response of trabecular bone [6, 7, 39], and the removal of the marrow may therefore be the cause of this insignificant correlation.

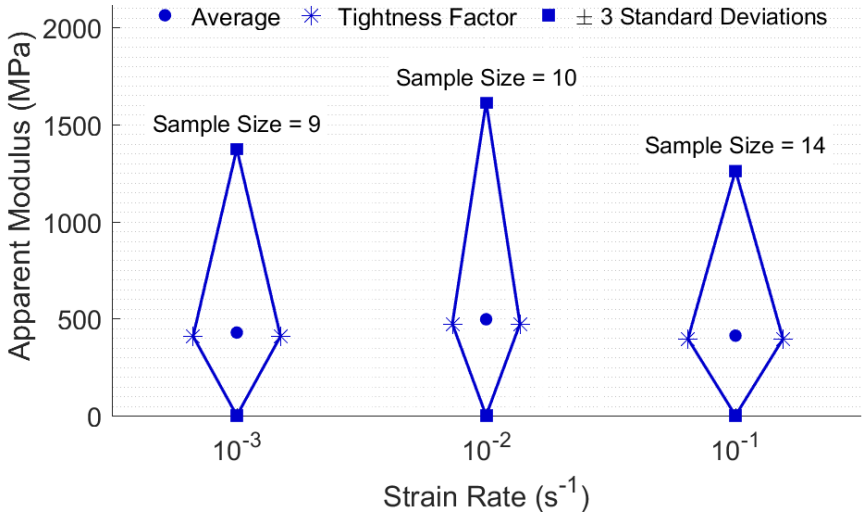

Figure 6.8: A graph of Apparent Modulus versus Strain Rate for defatted specimens

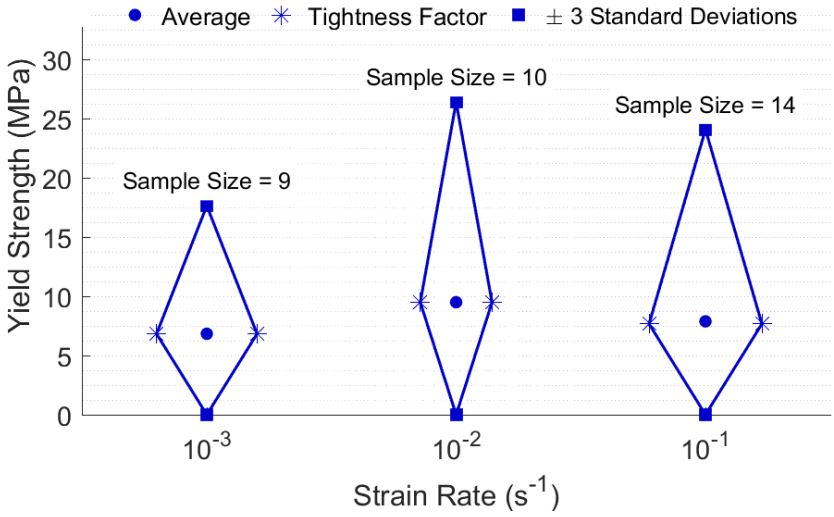

Figure 6.9: A graph of Yield Strength versus Strain Rate for defatted specimens

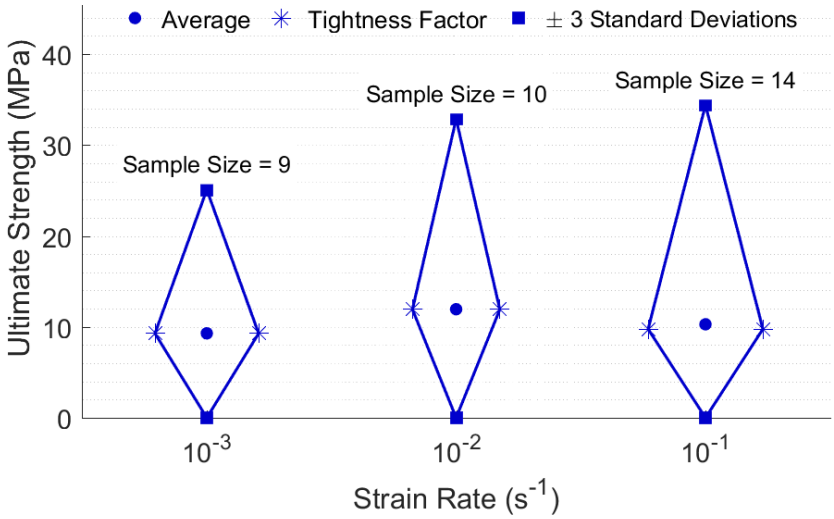

Figure 6.10: A graph of Ultimate Strength versus Strain Rate for defatted specimens

6.3.3 Structurally Confined Specimens

The graphs in figures 6.11-6.13 show the results of the effect of strain rate on apparent modulus for the three confinement techniques used during the investigation.

The data in figure 6.11 shows results for apparent modulus versus strain rate for specimens tested using the collar and plunger confinement described in section 5.3.1. The strain rate appears to have no effect on the average mechanical response, with average, mode and tightness factor values remaining relatively constant across data sets. The data set tested at a strain rate of 10^{-2} s^{-1} appears to be the least scattered of all the data sets. The yield and ultimate strength results for confinement data sets show similar trends to those of the apparent modulus graphs, as seen in figures 6.12 and 6.13.

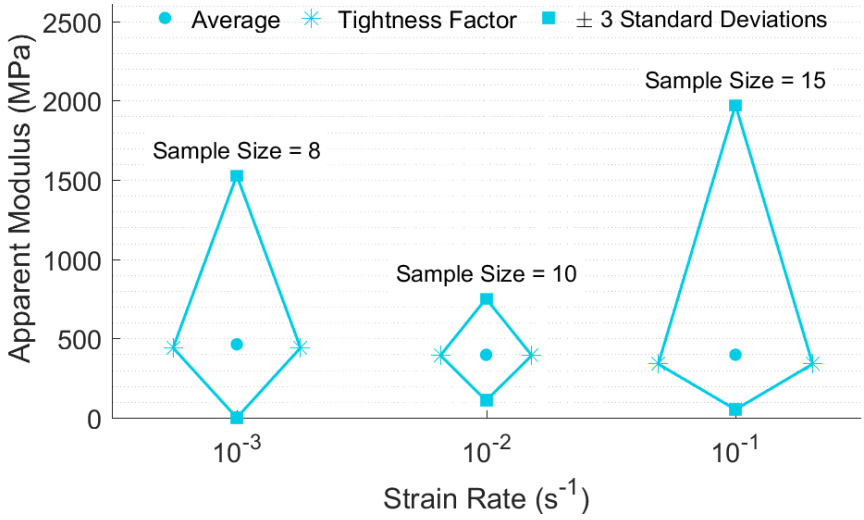

Figure 6.11: A graph of Apparent Modulus versus Strain Rate for confined specimens

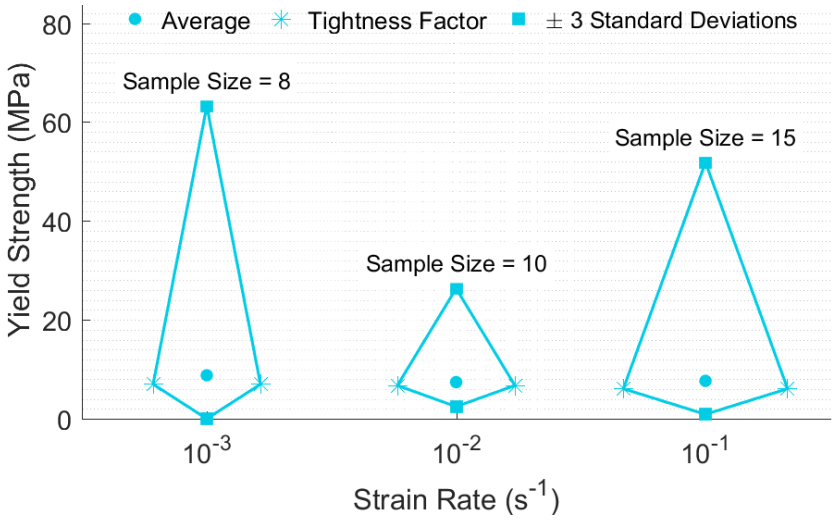

Figure 6.12: A graph of Yield Strength versus Strain Rate for confined specimens

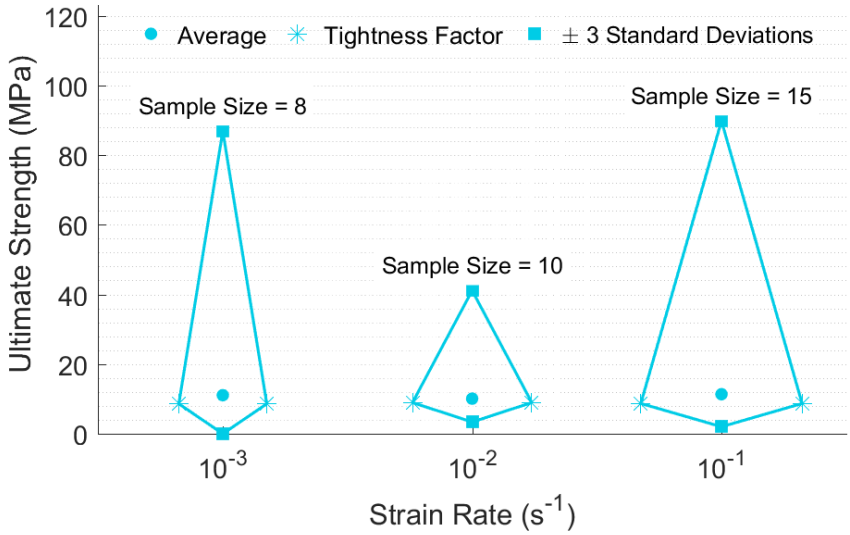

Figure 6.13: A graph of Ultimate Strength versus Strain Rate for confined specimens

6.3.4 20 mm Bone Confined Specimens

Figures 6.14-6.16 present the results of the strain rate comparison for bone confined, 20 mm cylindrical specimens. The presented results show the response of the inner 10 mm cylinder only. These graphs show significantly lower average mechanical properties for the specimens tested at 10^{-1} s^{-1}. While the upper bound of this data set is also noticeably lower, this is likely due to the lower average rather than a smaller standard deviation, as both data sets for each property have similar tightness factors. During experimental test series 10 - 20 mm specimens compressed at 10^{-3} s^{-1} - one set of results was incorrectly recorded using the confinement platform set up and could therefore not be used. The sample size for series 10 was therefore smaller than the already small set for series 11.

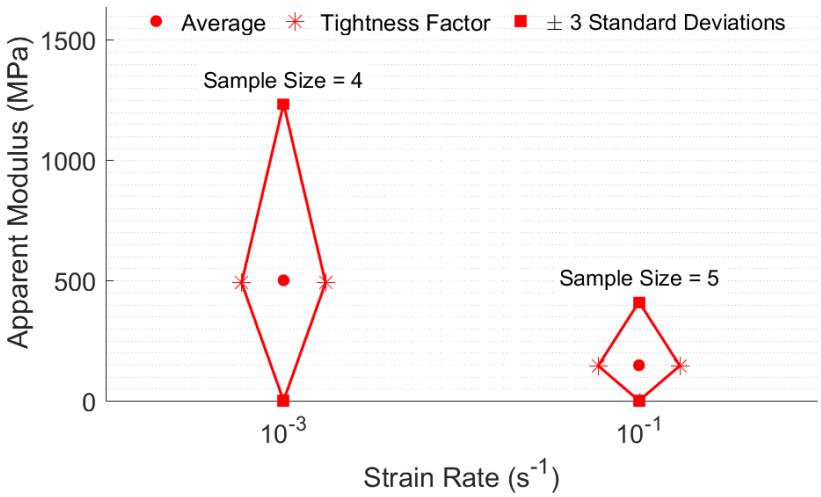

Figure 6.14: A graph of Apparent Modulus versus Strain Rate for 20 mm bone confined specimens

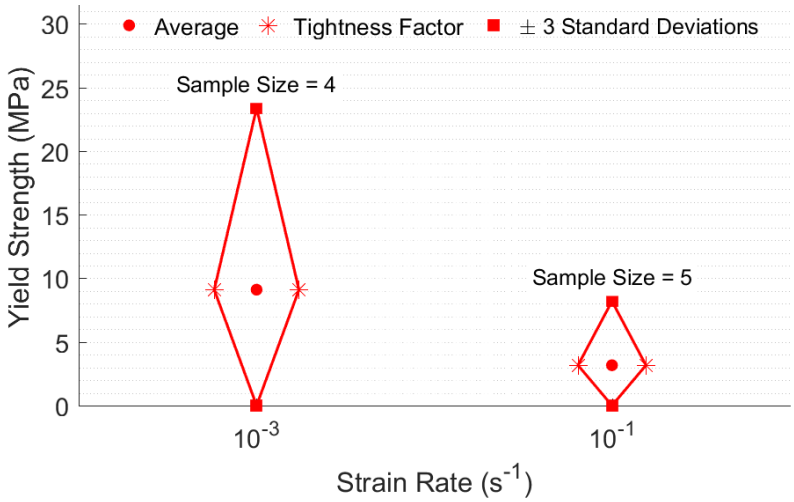

Figure 6.15: A graph of Yield Strength versus Strain Rate for 20 mm bone confined specimens

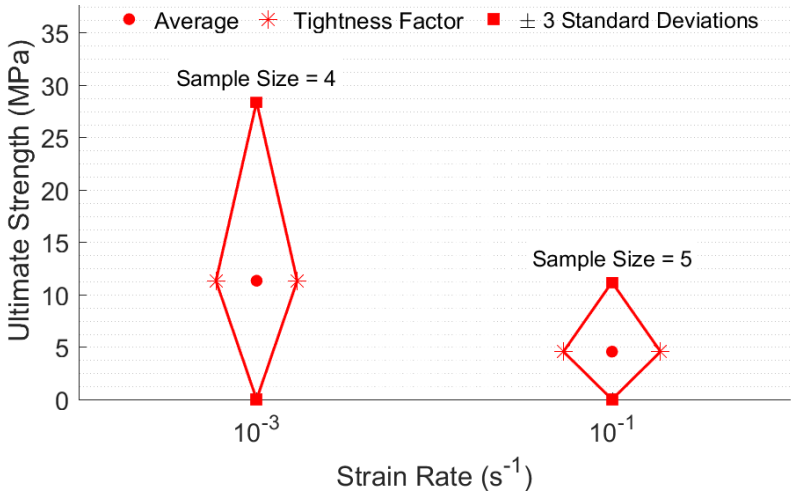

Figure 6.16: A graph of Ultimate Strength versus Strain Rate for 20 mm bone confined specimens

6.3.5 28 mm Bone Confined Specimens

Figures 6.17-6.19 present the results for the 28 mm bone confinement series. During the experimentation, the data for two specimens in the 10^{-1} s^{-1} series was incorrectly captured, making it unusable. The subsequent sample size was therefore only 3 specimens.

The data in figure 6.17 indicates a slightly decreased apparent modulus and scatter for the higher strain rate, although not as significantly decreased as in figures 6.14-6.16. Figures 6.18 and 6.19 show similar trends to those observed in figure 6.17.

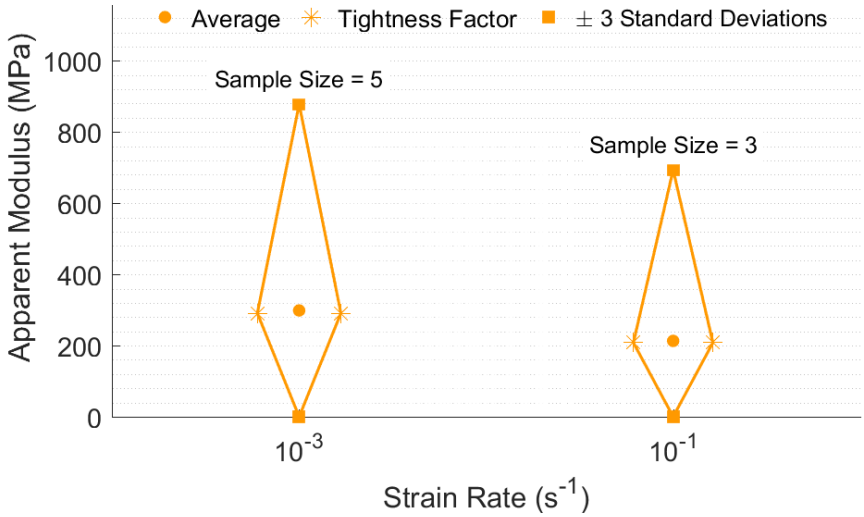

Figure 6.17: A graph of Apparent Modulus versus Strain Rate for 28 mm bone confined specimens

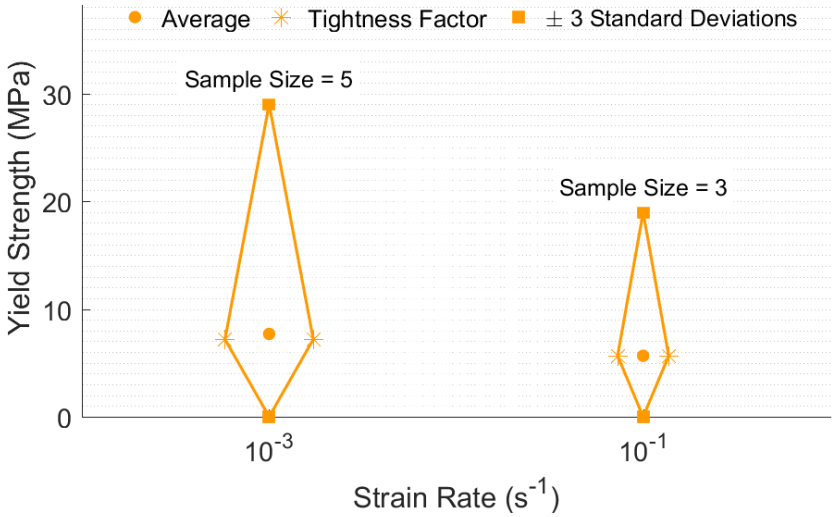

Figure 6.18: A graph of Yield Strength versus Strain Rate for 28 mm bone confined specimens

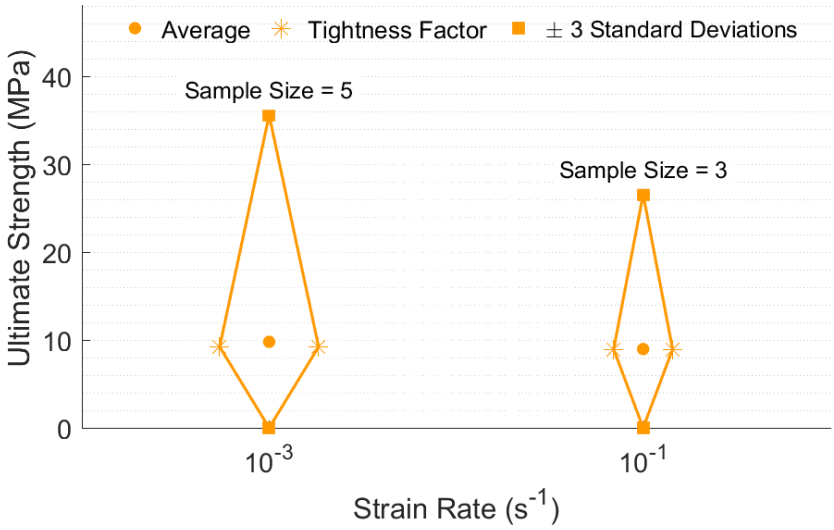

Figure 6.19: A graph of Ultimate Strength versus Strain Rate for 28 mm bone confined specimens

The results presented for the bone confined tests, figures 6.14-6.18, suggest varying responses of the trabecular bone specimens over the two strain rates tested in these series. These results were not considered statistically relevant as the sample sizes in each group were so small.

6.4 Boundary Condition Comparison

To assess the effect of boundary conditions on the mechanical response of trabecular bone, various specimen boundary conditions were tested during the investigation. The following sections present and compare the results for the standard, defatted and confined specimen boundary conditions.

6.4.1 Standard Versus Defatted

Figures 6.20-6.22 show a comparison of the results for apparent modulus, yield strength and ultimate strength respectively, for standard and defatted specimens.

The graphs all exhibit similar trends - the average mechanical properties seem insignificantly affected by boundary condition, while majority of the data sets show decreased scatter for the defatted group of specimens. This suggests that at quasi-static strain rates, although the bone marrow may not affect the strength of the trabecular bone, it does play a role in introducing scatter to the data. It may also suggest that the presence of marrow introduced experimental results with much stronger mechanical properties when compared to the defatted samples, as the upper bounds are significantly higher for most of the standard data sets. This agrees with the findings of Ma *et al.* [7]. The scatter apparent in the mechanical properties of the standard specimens may be a result of the fact that the marrow was not confined to within the trabecular network during compression.

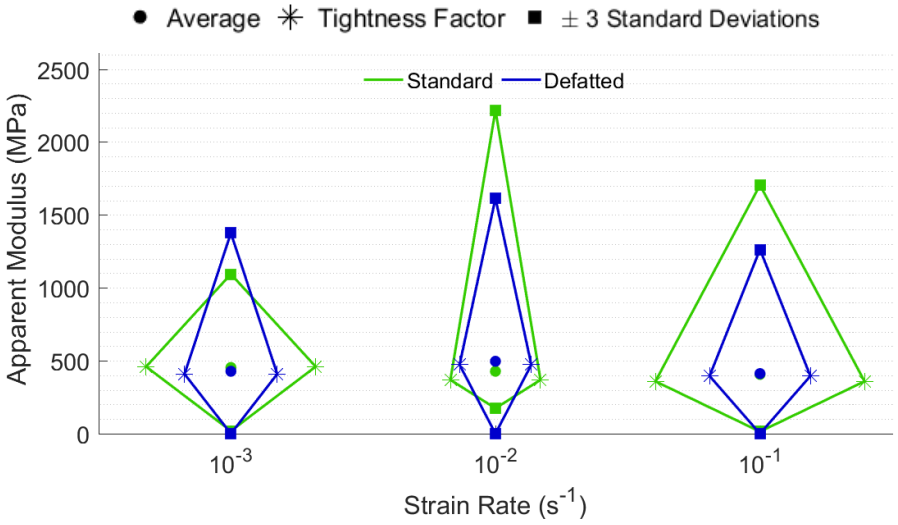

Figure 6.20: A graph showing Apparent Modulus Results for Standard and Defatted specimens

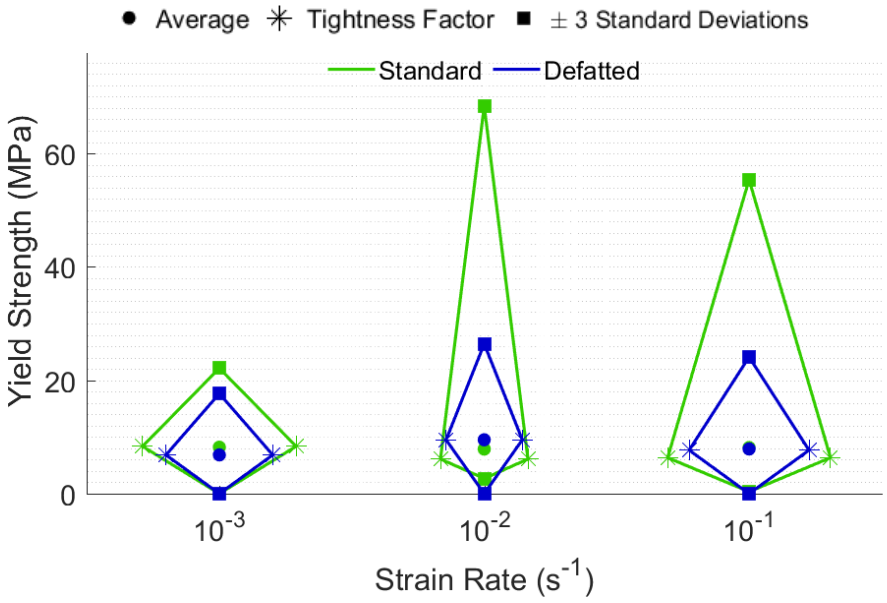

Figure 6.21: A graph showing Yield Strength Results for Standard and Defatted specimens

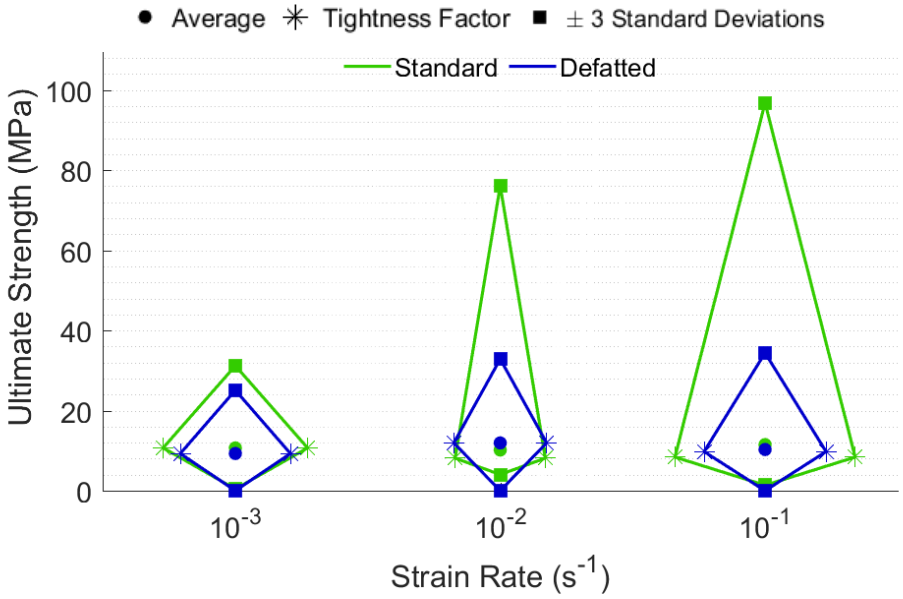

Figure 6.22: A graph showing Ultimate Strength Results for Standard and Defatted specimens

Figure 6.23 shows a comparison of the way in which marrow was forced out of two different specimens. These specimens were machined from the same bone, and both were tested at the same strain rate. However, as is evident, the sites at and manner in which the marrow exits the trabecular network are considerably different. This may be attributed to the highly anisotropic and randomised nature of the trabecular network.

Figure 6.23: Photographs showing a comparison of marrow forced out of two different compressed specimens. Both specimens were compressed at the same strain rate.

The results also show that the presence of marrow yielded an ultimate strength 4.92-60.57% higher than defatted specimens. This results contradicts the findings of Chen *et al.* [6]. Figure 6.24 shows the results of the maximum ultimate strengths for each strain rate of both standard and defatted samples. This result is mirrored by the results for apparent modulus and yield strength, which show an increase of 8.76-51.69% and 0.16-37.50% respectively for specimens with marrow versus those without.

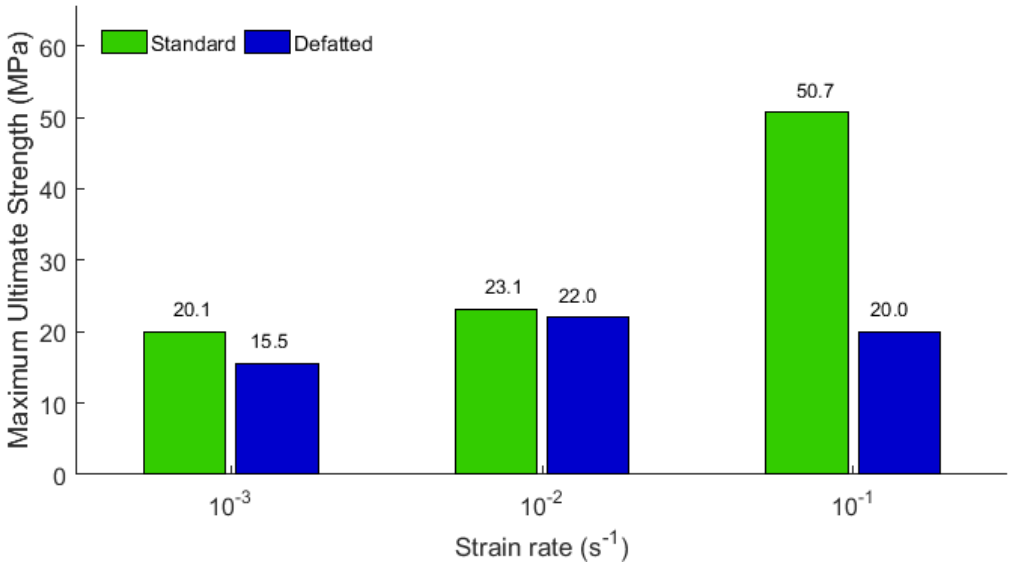

Figure 6.24: A graph showing a comparison of the Maximum Ultimate Strength for Standard and Defatted samples

6.4.2 Standard Versus Structurally Confined

Figures 6.25-6.27 present the results for the 10 mm specimens, confined using a collar and plunger confinement (series 7-9) in comparison to the standard set of specimens.

As was evident in previous data sets, this confinement technique does not significantly affect the average mechanical properties of the tested specimens. Across all the mechanical properties (E_{app}, σ_y and US), the reduced scatter in the confined data set compressed at 10^{-2} s^{-1} appears to disagree with the overall trends. In general, the confined specimens exhibit similar or more scatter when compared to the standard specimen results.

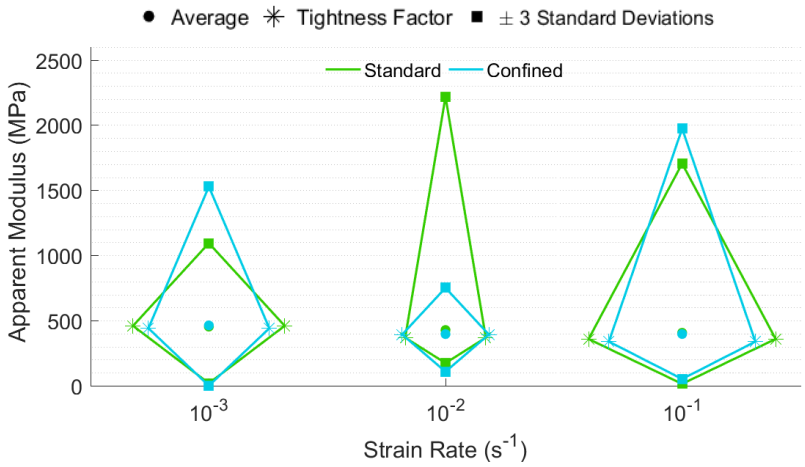

Figure 6.25: A graph showing Apparent Modulus Results for Standard and Confined specimens

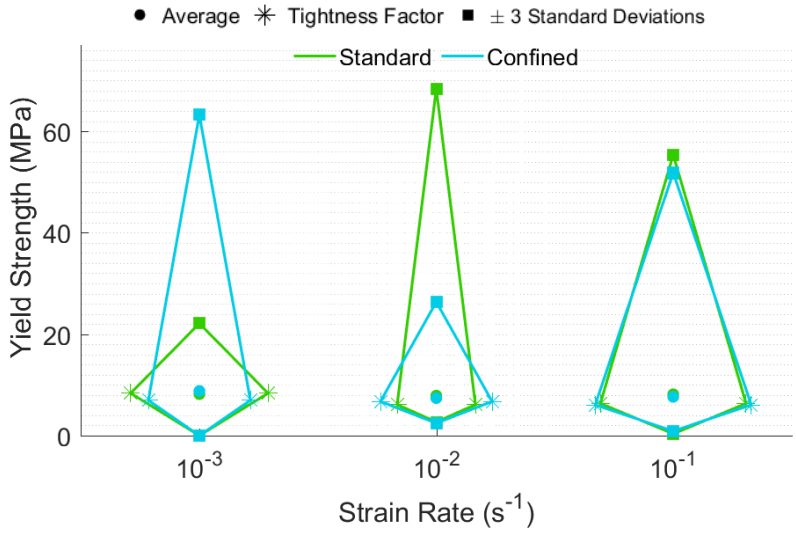

Figure 6.26: A graph showing Yield Strength Results for Standard and Confined specimens

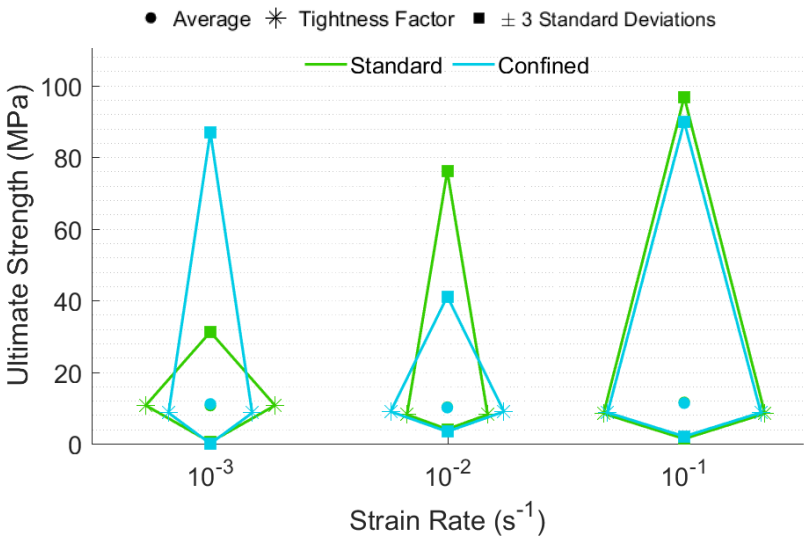

Figure 6.27: A graph showing Ultimate Strength Results for Standard and Confined specimens

The differences in scatter may be a result of the fit of each specimen inside the aluminium collar. Table 6.2 presents the average, minimum and maximum diameters for series 7-9. The data in the table shows that the specimens in series 8 all had diameters of 10 mm or more, while the series 7 and 9 contained specimens with measured diameters less than 10 mm, both having average diameters under 10 mm. This suggests that specimens which fit more tightly inside the collar confinement will perform more consistently. This also implies that looser fitting specimens may not experience a sufficient support force from the collar boundary condition. While forcing specimens with larger diameters into the confinement collar was sometimes required, this was only achieved using the force a hand is able to deliver. The trabecular bone cylinders were not able to be compressed by hand, and therefore any force applied by hand to fit the sample into the collar was not able to damage the specimen. This result, along with the results presented in section 6.4.1, suggest that the presence of marrow does not significantly increase the strength of the bone as quasi-static strain rates, but that the flow of marrow may have a disruptive effect on the trabecular network.

Table 6.2: A table showing average, minimum and maximum diameters of the structurally confined specimens. Series 7, 8 and 9 correspond to the confined specimen data in figures 6.25-6.27

Series	**Average diameter (mm)**	**Minimum diameter (mm)**	**Maximum diameter (mm)**
7	9.98	9.91	10.02
8	10.02	10.00	10.07
9	9.98	9.90	10.07

6.4.3 Bone Confinement

The following sections present the results for the bone confinement test series. These results compare standard specimens to bone confined specimens, specifically the inner 10 mm diameter. Further comparison is made between the response of the inner 10 mm and whole specimens, both 20 mm and 28 mm diameters.

6.4.3.1 Standard Versus 20 mm Bone Confined

Figures 6.28-6.30 show the mechanical properties for the 20 mm bone confinement series. The apparent modulus, yield and ultimate strength results all show the same trends - average values are unaffected by the confinement at 10^{-3} s^{-1}, while the 20 mm bone confined specimens tested at 10^{-1} s^{-1} exhibit decreased mechanical properties in comparison to the standard specimens. The confined specimens show narrower tightness factors than the standard specimens, but this is likely a direct result of the smaller sample size for the 20 mm confined specimen data sets.

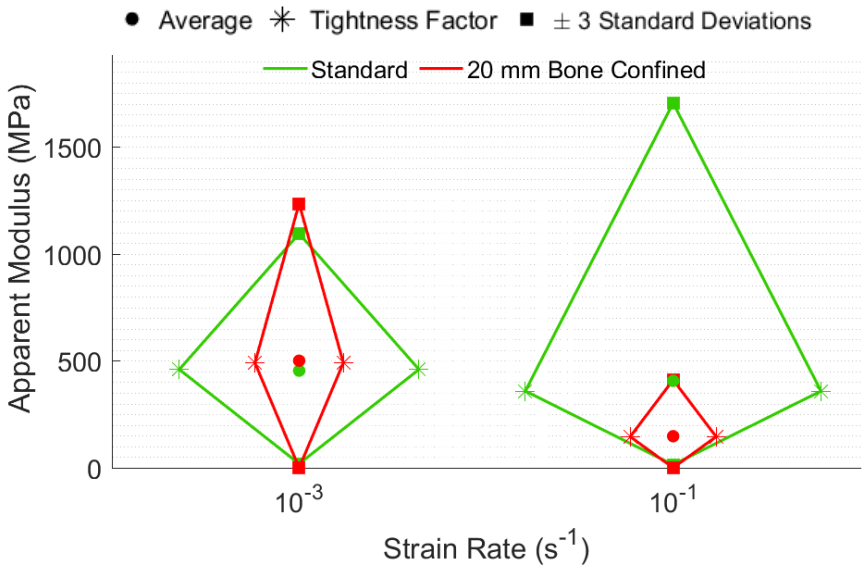

Figure 6.28: A graph showing Apparent Modulus Results for Standard and 20 mm Bone Confined specimens

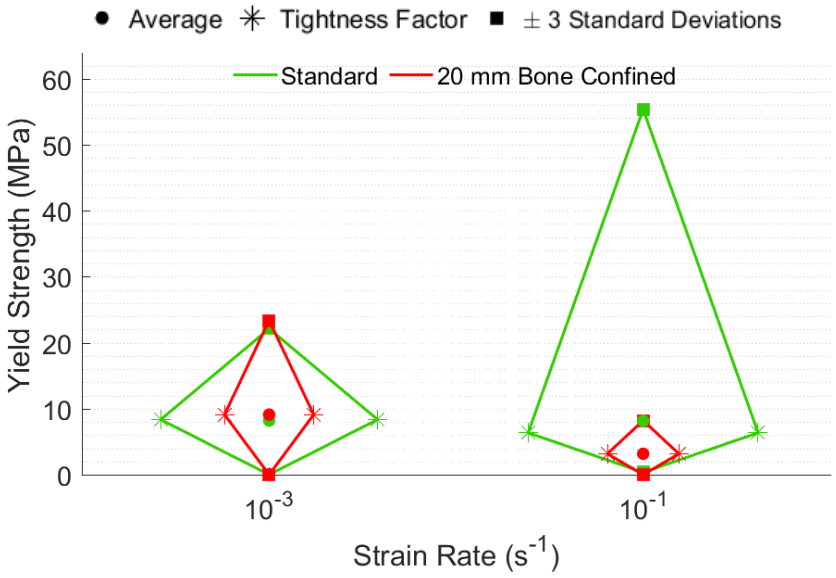

Figure 6.29: A graph showing Yield Strength Results for Standard and 20 mm Bone Confined specimens

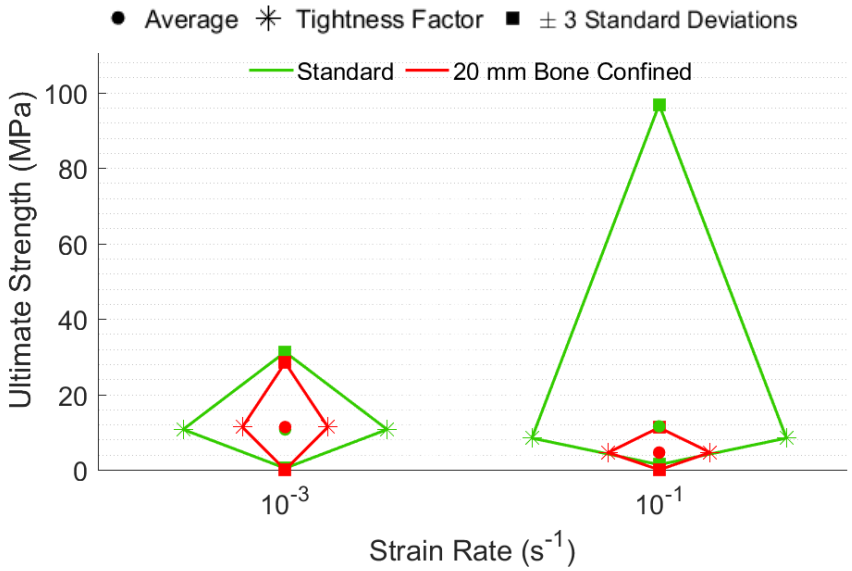

Figure 6.30: A graph showing Ultimate Strength Results for Standard and 20 mm Bone Confined specimens

6.4.3.2 Standard Versus 28 mm Bone Confined

Figures 6.31-6.33 present the results for the 28 mm bone confinement series. The results show similar trends to those presented for the 20 mm bone confinement series, except that a decrease in mechanical properties is observed across both strain rates tested. Apparent modulus also exhibits a larger decrease when compared to the other two mechanical properties, suggesting the apparent modulus has a greater sensitivity to confinement than yield and ultimate strength.

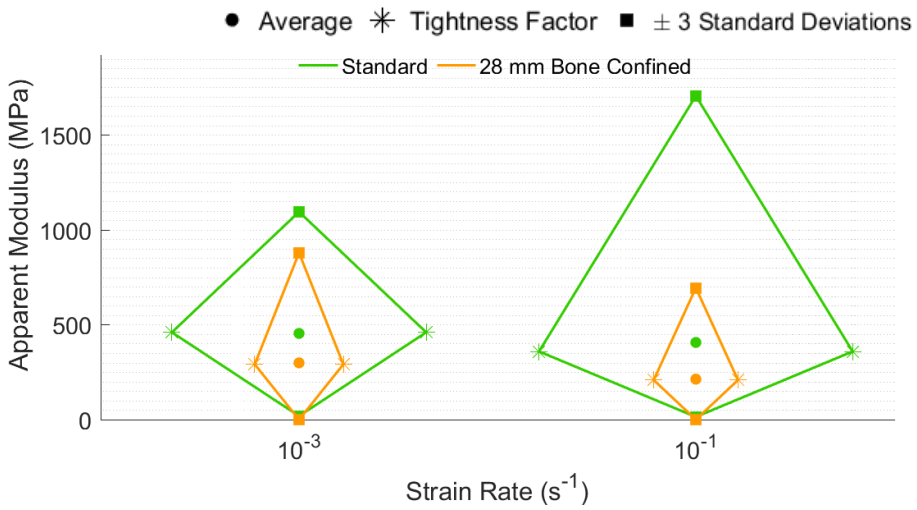

Figure 6.31: A graph showing Apparent Modulus Results for Standard and 28 mm Bone Confined specimens

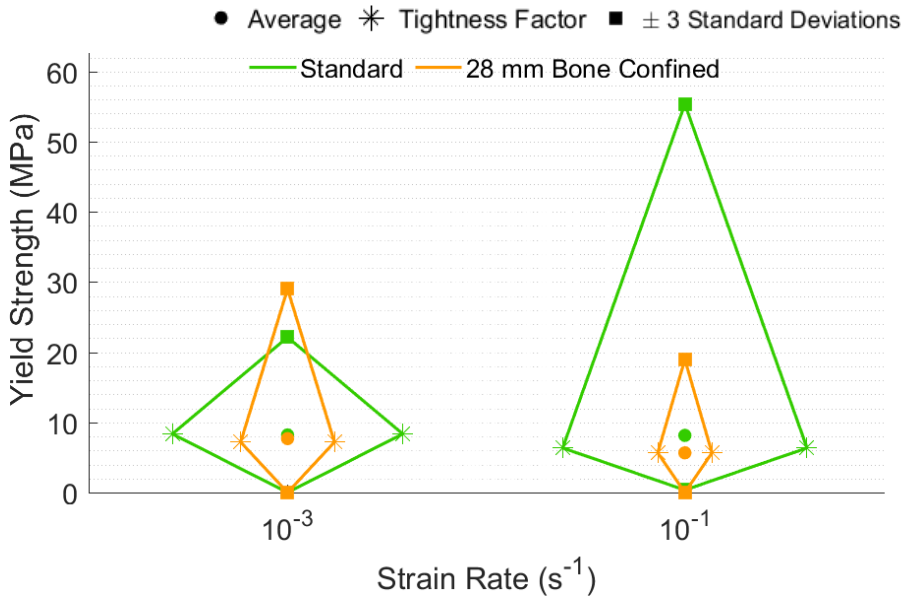

Figure 6.32: A graph showing Yield Strength Results for Standard and 28 mm Bone Confined specimens

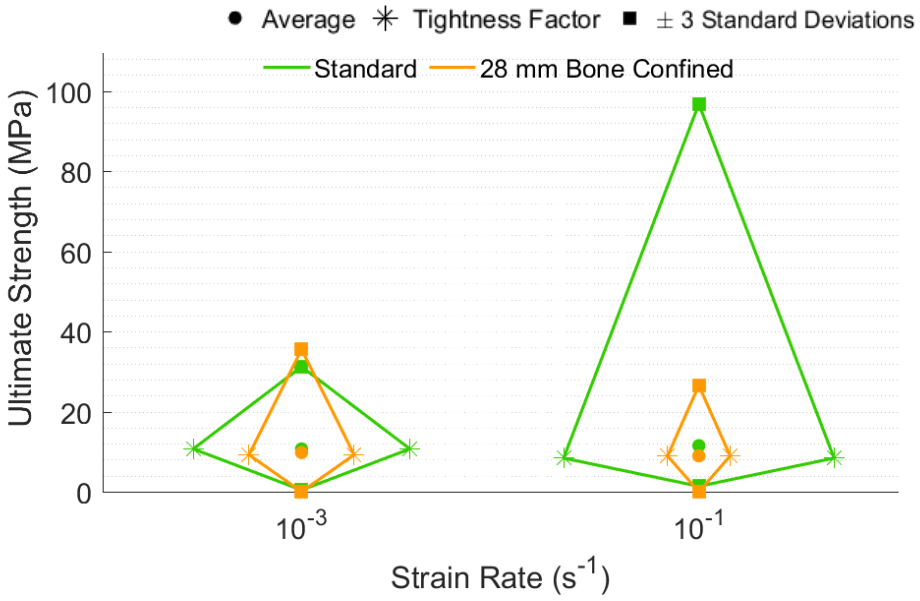

Figure 6.33: A graph showing Ultimate Strength Results for Standard and 28 mm Bone Confined specimens

While the results presented in figures 6.28-6.33 suggest that bone confinement results in a decrease in mechanical properties, the sample sizes for the bone confinement series were much smaller than those for the standard series. Four or five specimens in a data set is likely not enough to draw any relevant statistical analysis, therefore, these results should be extended to comparable sample sizes before any conclusions can be drawn.

Figure 6.34 shows a comparison of the results for the maximum apparent modulus for each confinement technique. The graphs suggest that none of the confinement techniques investigated during the study achieved results which mimicked *in vivo* conditions. Chaari *et al.* [2] suggested that confinement boundary conditions only affect samples after the initial loading phase of the specimens. This could not be verified during this study as the specimens were not loaded past the first stage. This type of loading would be an insightful extension to the current investigation.

While the data in the graph in figure 6.34 suggests a clear decrease in strength of confined specimens, both the 20 mm and 28 mm specimens were machined from humerus 8 and 9 respectively. Due to an unforeseen need for further samples, these two bones in particular were stored and frozen as whole bones (without physiological saline) for over a year before machining. There was also no overlap between these specimens across different bones, as there was in other datasets. This suggests that these two humeri in particular may have been weaker than the rest. Without samples spanning more than one bone for the bone confinement datasets, it is difficult to draw meaningful conclusions as the decreased mechanical strength may be a result of specimens originating from different humeri or having different storage conditions, rather than being a result of the confinement.

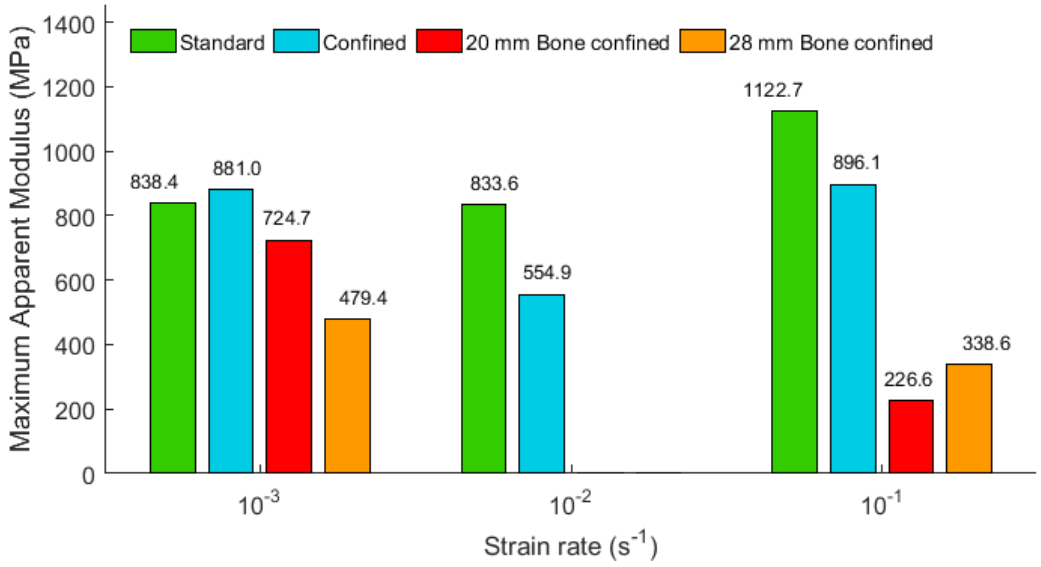

Figure 6.34: A graph showing a comparison of the Maximum Apparent Modulus for Standard specimens and all Confinement techniques

In general, the confinement results therefore suggest that the strength of cancellous bone is unaffected by the testing condition, and provided enough samples are tested, the scatter can be mostly ignored.

6.4.3.3 Inner 10 mm Versus Whole 20 mm Specimen

While the previous section suggested a decrease in mechanical strength with bone confinement, individual specimens results contradict show an increase in mechanical properties for the confined section of bone. The following section presents results of individual, bone confined specimens by comparing the inner 10 mm specimen to the overall strength of the larger bone specimen.

Figures 6.35a and 6.35b show examples of the stress-strain results for individual, 20 mm specimens. The red curve indicates the stress-strain curve obtained from the Zwick, and therefore represents the overall stress in the large specimen. The blue curve indicates the stress measured by the confinement platform and therefore represents the stress in the inner 10 mm cylinder of the specimen. The graphs show a clear increase in mechanical strength of the inner 10 mm cylinder when compared to the overall specimen.

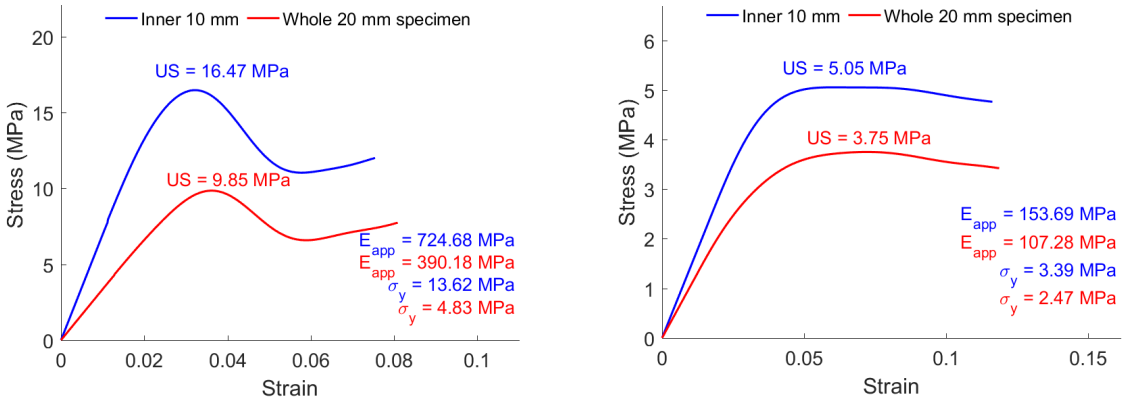

(a) Sample number 503 (b) Sample number 512

Figure 6.35: Example graphs of the stress-strain curves for 20 mm bone confinement specimens

This result is reiterated in figures 6.36 - 6.38. The graphs show a comparison of the results for apparent modulus, yield and ultimate strength respective, for both the inner 10 mm and the whole 20 mm specimen. An increase in the mechanical properties of the confined specimens across both strain rates was evident. This suggests that the confinement had a significant affect, and that the decrease in mechanical properties observed between the standard and bone confined specimens in section 6.4.3.1 was due to the bone storage conditions rather than the confinement conditions of the specimens. The data in table 6.3 presents a ratio of the inner versus outer diameters for each mechanical property as determined during the experimentation. The results show that the inner 10 mm have strength properties 41-58% greater than those of the whole 20 mm specimens. This shows a clear confinement effect.

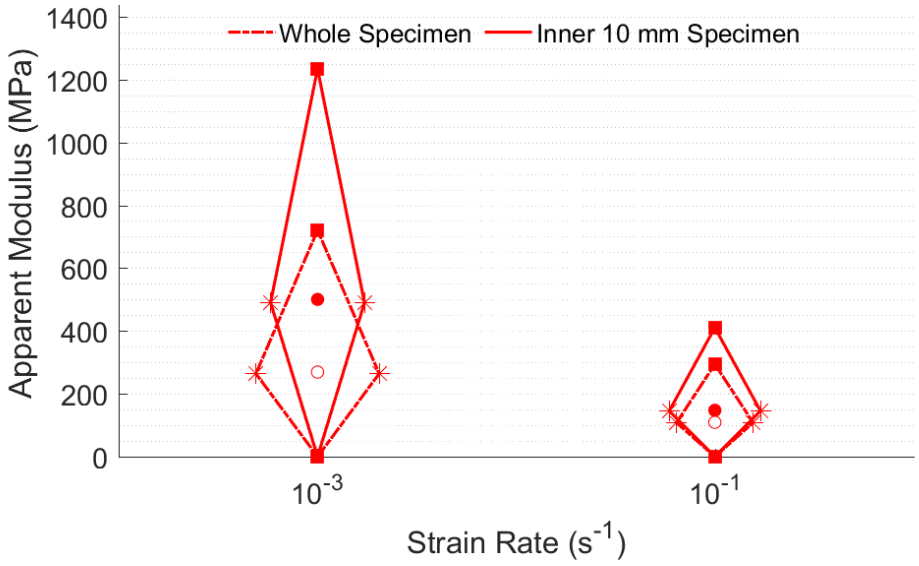

Figure 6.36: A graph showing a comparison of apparent modulus of the whole 20 mm specimen versus the inner 10 mm diameter

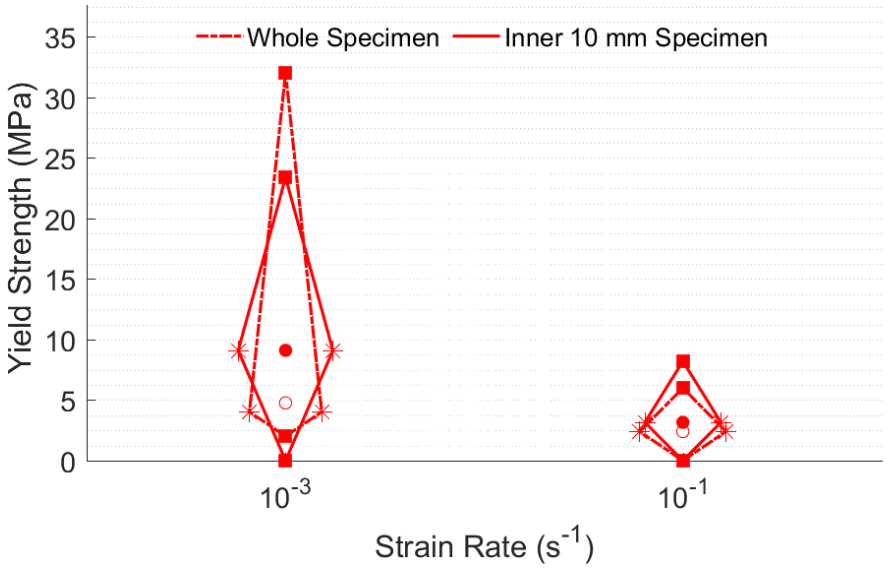

Figure 6.37: A graph showing a comparison of yield strength of the whole 20 mm specimen versus the inner 10 mm diameter

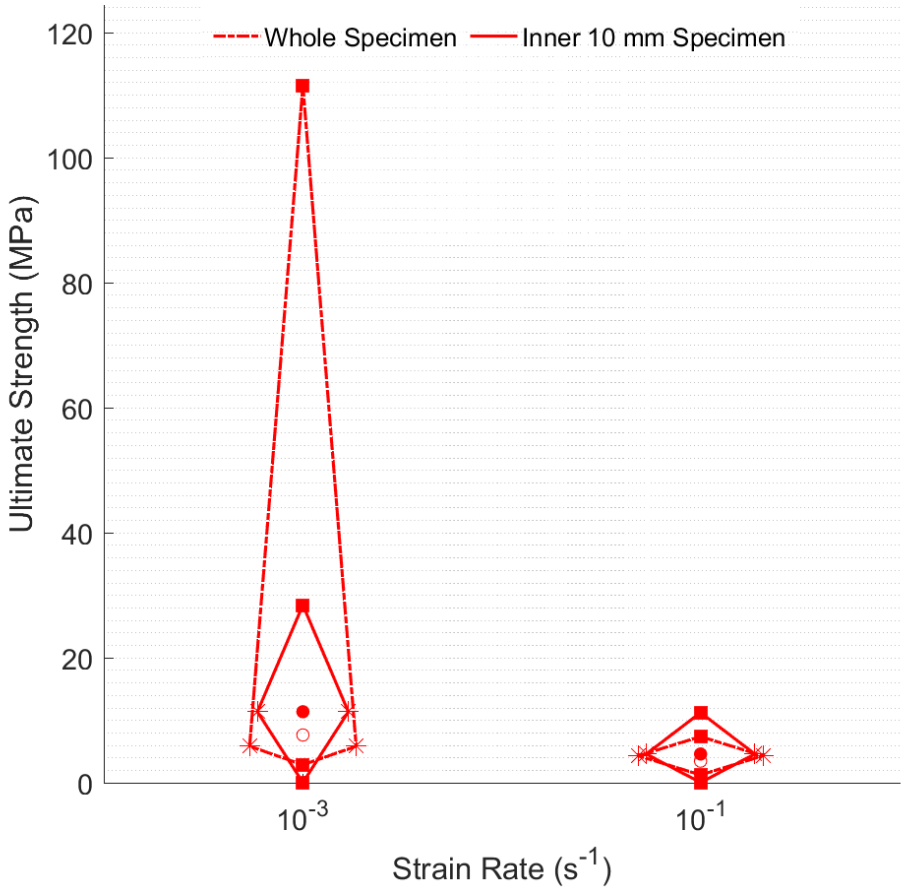

Figure 6.38: A graph showing a comparison of ultimate strength of the whole 20 mm specimen versus the inner 10 mm diameter

Table 6.3: A table presenting the mechanical properties of the inner 10 mm cylinder compared to the overall 20 mm bone specimen.

Sample Number	**Apparent Modulus (MPa)**			**Yield Strength (MPa)**			**Ultimate Strength (MPa)**		
	Inner	**Whole**	**Ratio**	**Inner**	**Whole**	**Ratio**	**Inner**	**Whole**	**Ratio**
498	603.58	372.02	1.62	12.58	8.37	1.50	15.80	12.88	1.23
503	724.68	390.18	1.86	13.62	4.83	2.82	16.47	9.85	1.67
504	277.95	142.58	1.95	3.94	2.86	1.38	5.35	3.75	1.43
506	395.31	171.78	2.30	6.30	3.01	2.09	7.68	3.96	1.94
508	21.55	21.19	1.02	0.59	0.49	1.21	1.08	0.78	1.38
510	226.59	173.49	1.31	4.82	3.36	1.44	6.42	5.04	1.27
512	153.69	107.28	1.43	3.39	2.47	1.37	5.05	3.75	1.35
513	189.83	138.78	1.37	4.40	3.47	1.27	6.33	5.22	1.21
514	145.97	106.08	1.38	2.65	2.24	1.18	3.92	3.10	1.26
	Average Ratio		1.58	**Average Ratio**		1.58	**Average Ratio**		1.41

6.4.3.4 Inner 10 mm Versus Whole 28 mm Specimen

Figures 6.39 and 6.40 present the apparent modulus and yield strength results for the 28 mm bone confined specimens. These graphs compare the inner 10 mm specimens to the whole bone specimens, and show that bone confinement significantly strengthens the mechanical properties of the specimen.

The ultimate strength data was not presented as multiple tests in this series were not able to reach completion due to force limitations of the Zwick. Figure 6.41 shows examples of tests which were deemed incomplete, as compression was stopped before a true ultimate strength was reached.

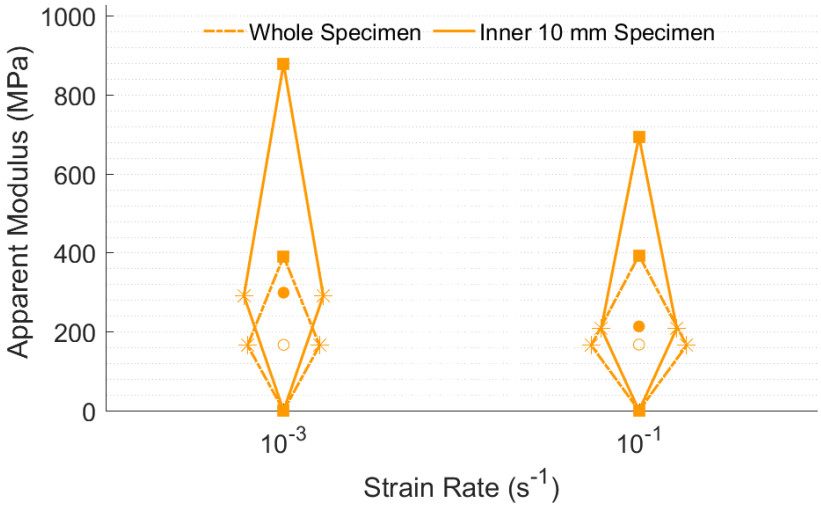

Figure 6.39: A graph showing a comparison of apparent modulus of the whole 28 mm specimen versus the inner 10 mm diameter

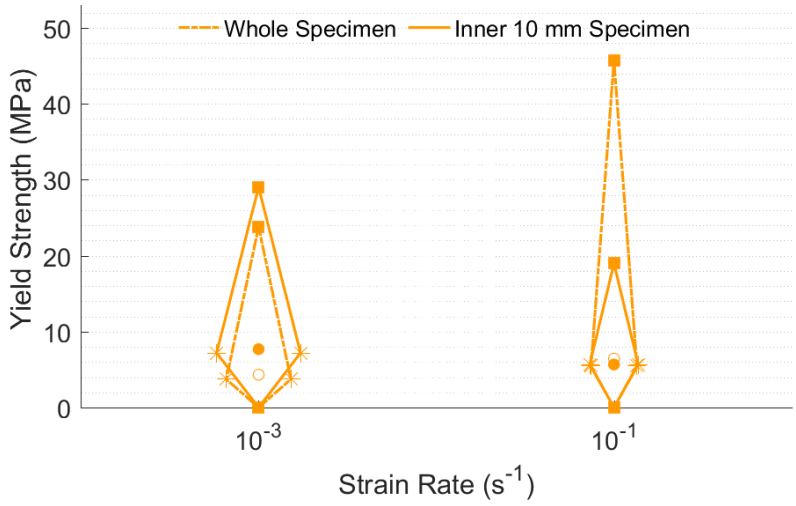

Figure 6.40: A graph showing a comparison of yield strength of the whole 28 mm specimen versus the inner 10 mm diameter

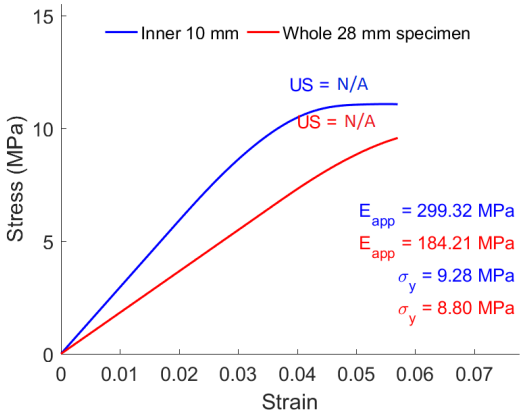

(a) Sample Number 530

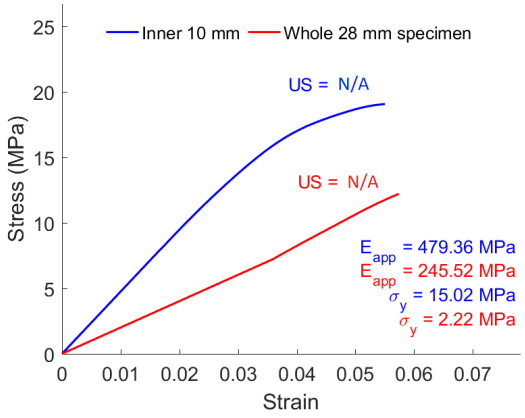

(b) Sample Number 532

Figure 6.41: Graphs showing Stress-Strain curves of incompletely compressed specimens

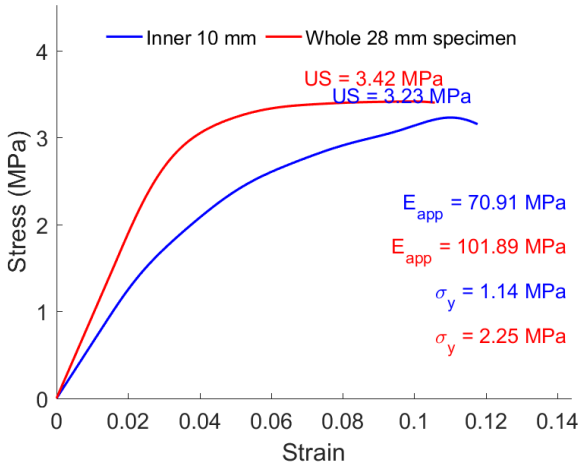

Figure 6.42: A graph showing the results for sample number 535 presenting unexpected results

One test in the series, shown in figure 6.42, presented unexpected results when compared to the rest in the dataset, with the whole bone specimen appearing to have higher strength than the inner 10 mm specimen (red curve appears above the blue curve). This specimen data was likely captured incorrectly from the confinement platform, although no obvious reason for this was found.

Table 6.4 presents the results of the ratio of the inner versus outer diameters for each mechanical property. The data presented in figure 6.42 is highlighted in grey in table 6.4. The results show that the inner 10 mm have strength properties 22-78% greater than those of the whole 20 mm specimens, if sample 535 is included. However, if specimen 535 is excluded, the results show a 31%-96% increase in mechanical strength. In all cases, ultimate strength exhibits the smallest increase in mechanical properties, while yield strength appears to have the greatest sensitivity to confinement.

Table 6.4: A table showing the mechanical properties of the inner 10 mm cylinder compared to the overall 28 mm bone specimen.

Sample Number	**Apparent Modulus (MPa)**			**Yield Strength (MPa)**			**Ultimate Strength (MPa)**		
	Inner	**Whole**	**Ratio**	**Inner**	**Whole**	**Ratio**	**Inner**	**Whole**	**Ratio**
529	269.76	162.85	1.66	5.24	4.47	1.17	6.84	5.69	1.20
530	299.32	184.21	1.62	9.28	8.80	1.05	-	-	-
532	479.36	245.52	1.95	15.02	2.22	6.77	-	-	-
533	60.26	59.37	1.02	1.63	1.32	1.24	-	-	-
534	384.53	180.66	2.13	7.25	4.77	1.52	9.87	6.43	1.53
535	70.91	101.89	0.70	1.14	2.25	0.51	3.23	3.42	0.95
537	229.86	165.28	1.39	5.89	5.45	1.08	8.92	7.42	1.20
538	338.62	234.58	1.44	9.95	11.58	0.86	-	-	-
	Average Ratio (including sample 535)								
	1.48			1.78			1.22		
	Average Ratio (excluding sample 535)								
	1.60			1.96			1.31		

6.4.3.5 Summary of Bone Confinement

The results have shown that bone confinement significantly increases the mechanical strength of the specimen. Inner 10 mm versus whole specimens apparent modulus increased by 58% in 20 mm specimens, and by 60% in 28 mm specimens. This suggests that any further increase in the specimen diameter would not affect the ratio of inner to whole specimen apparent modulus any further. This result implies that edge effects on apparent modulus have been effectively removed by doubling the specimen diameter. These results do not agree with the assertion by Chaari *et al.* [2] that boundary condition has little to no significance on specimen response during the initial loading phase.

Yield strength, however, does not appear to exhibit similar removal of edge effects. The ratio of inner to whole bone yield strength increases from 58% to 96% between the 20 mm and 28 mm specimens. This suggests that a further increase in specimen diameter would be required to reflect a loading scenario closer to the *in vivo* environment. This further implies that while cancellous bone is deforming, before it has reached the fracture point, it can be more effectively tested for *in vivo* conditions with smaller specimens, but that post-fracture behaviour requires larger distances between the test specimen and its boundary to effectively eliminate edge effects.

No meaningful conclusions were drawn between the ultimate strengths of the 20 mm and 28 mm specimens as too few usable samples were left within the 28 mm specimen datasets.

Bone confinement is a unique method of attempting to replicate the *in vivo* response of bone. The investigation yielded promising results which show a significant effect of boundary conditions on the overall mechanical response of the specimens. The results of this study contradict other confinement studies in the literature [2–4] which reported no significant confinement effect. Harrison and McHugh [5] observed an increase in apparent modulus of between 17.4% and 20.4% for samples within whole bones versus individual samples. The results of the current investigation find an increase in apparent modulus of 58-60% in bone confined samples, suggesting that the numerical simulations performed by Harrison and McHugh [5] underpredict the increase in mechanical strength in the *in vivo* environment.

6.5 Influence of Architectural Parameters

The effect of architectural parameters on the mechanical response of cancellous bone has been well documented in the literature [3, 18, 20–25, 28, 28, 33–46]. Almost all the studies conducted have concluded that the mechanical properties of trabecular bone are better predicted through the use of architectural parameters. The following sections present the results of the investigation for each mechanical property in relation to four architectural parameters, namely Bone Volume versus Total Volume (BV/TV), Trabecular Number (Tb.N), Trabecular Separation (Tb.Sp) and Trabecular Thickness (Tb.Th). Each of the parameters were calculated using the techniques and equations presented in section 4.2.6.

6.5.1 Bone Volume versus Total Volume

Figure 6.43 shows the apparent modulus of all tested specimens as a function of BV/TV for each specimen. The black line in the graph shows the best fit straight line for the full dataset. As seen in figure 6.43, the apparent modulus of each specimen is well predicted by its BV/TV, and an overall trend exists according to the equation $E_{app} = 1511.51\text{BV/TV} - 100.88$.

The value for BV/TV of any sample is limited to a maximum of 1 - where the entire sample is bone, without space for marrow in the trabecular network. While this is impractical in real life specimens, the equivalent scenario would be testing a single trabecula rod. This trendline suggests that the apparent modulus for cancellous bone, or a single trabecula rod, is 1410.63 MPa.

Figures 6.45 and 6.46 show similar trends for yield and ultimate strength respectively. The yield strength versus BV/TV data is well predicted by a linear function with the equation $\sigma_y = 33.81\text{BV/TV} - 3.58$. Using the same reasoning as with apparent modulus, this suggests a trabecula yield strength of 30.23 MPa. For ultimate strength, the fitted linear curve equation is $\text{US} = 47.13\text{BV/TV} - 5.39$. This suggests a single trabecula has an ultimate strength of 41.74 MPa.

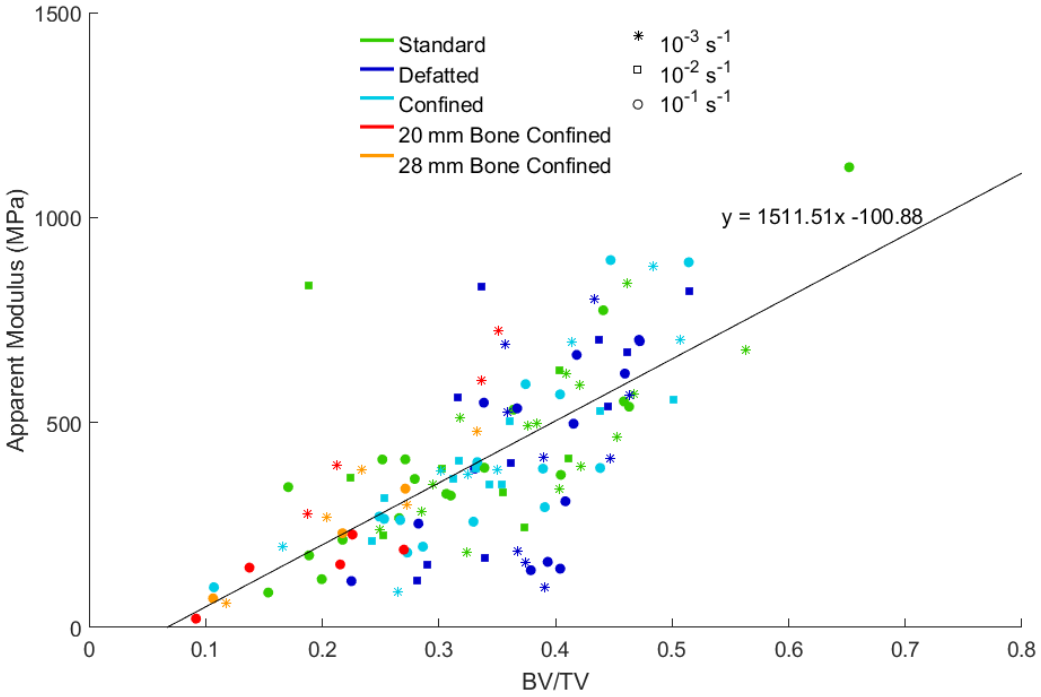

Figure 6.43: A graph of Apparent Modulus versus BV/TV for all test series performed in this study

Figures 6.44a-6.44e show the results as shown in figure 6.43, separated into specimen conditions. The specimen condition specific fitted curves, shown as dotted lines, differ slightly to the overall fitted curve in each case. This result suggests that while the overall trend for each of these condition graphs shows a positive, linear correlation, each specimen condition has a slightly different relationship between apparent modulus and BV/TV. This further suggests that the architectural parameter BV/TV alone may not accurately predict the response of cancellous bone, and that the parameter must be coupled with test type and loading condition in order to fully predict the mechanical response. This result is mirrored across all mechanical properties for BV/TV, and the remaining graphs - for both yield and ultimate strength - are shown in Appendix B.

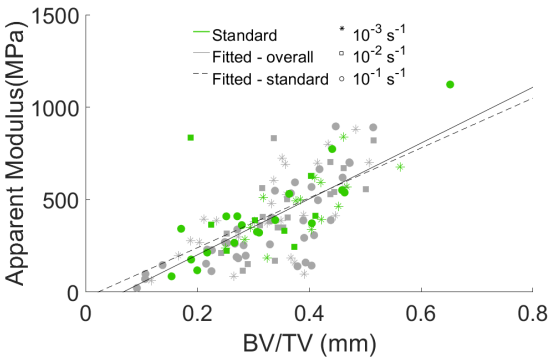

(a) Standard

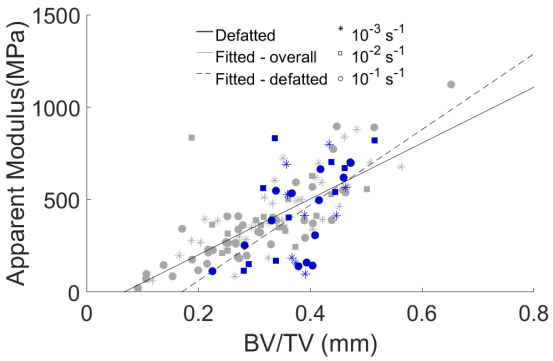

(b) Defatted

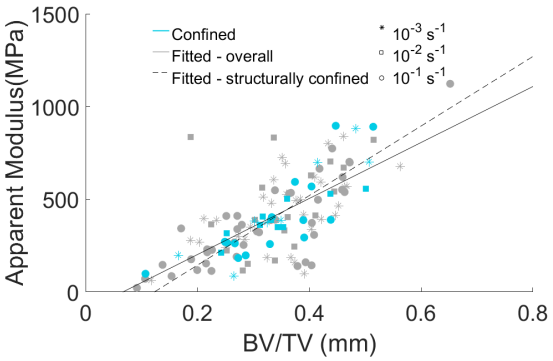

(c) Structurally Confined

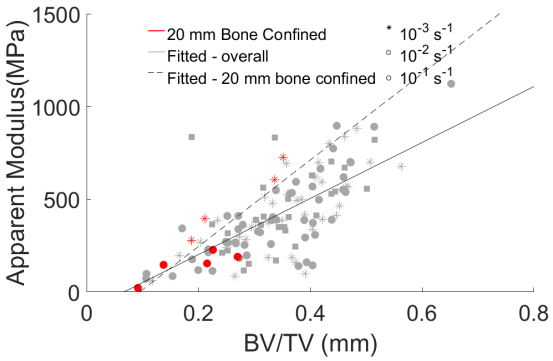

(d) 20 mm Bone Confined

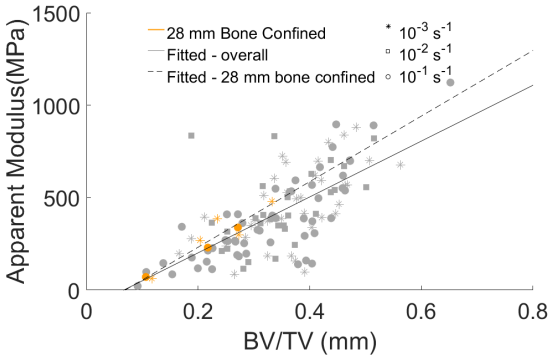

(e) 28 mm Bone Confined

Figure 6.44: Graphs showing Apparent Modulus versus BV/TV for each specimen condition

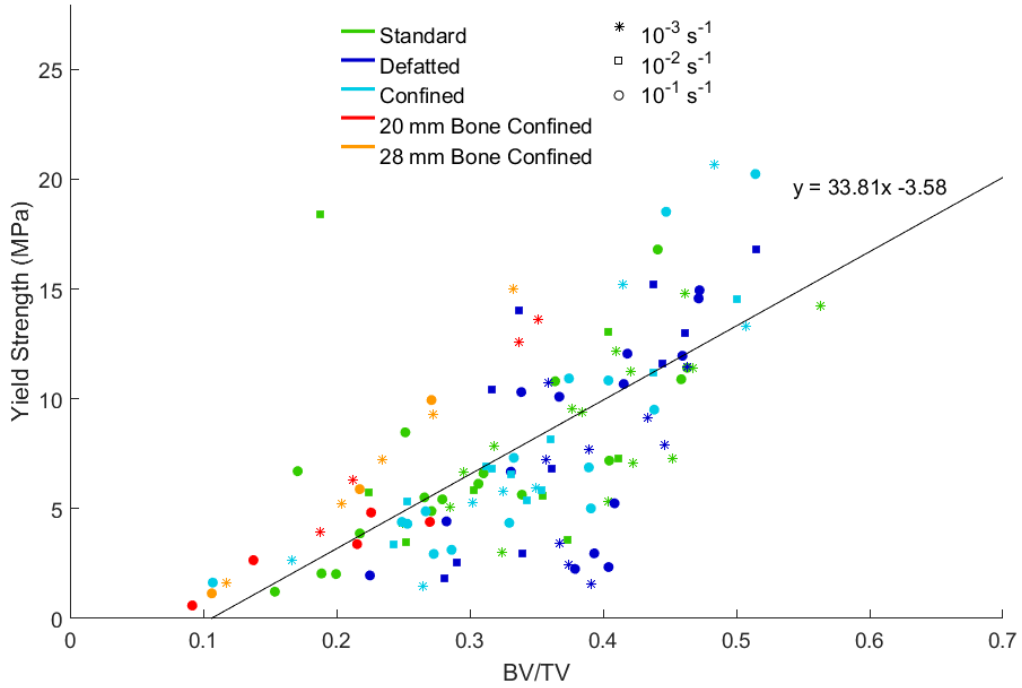

Figure 6.45: A graph of Yield Strength versus BV/TV for all test series performed in this study

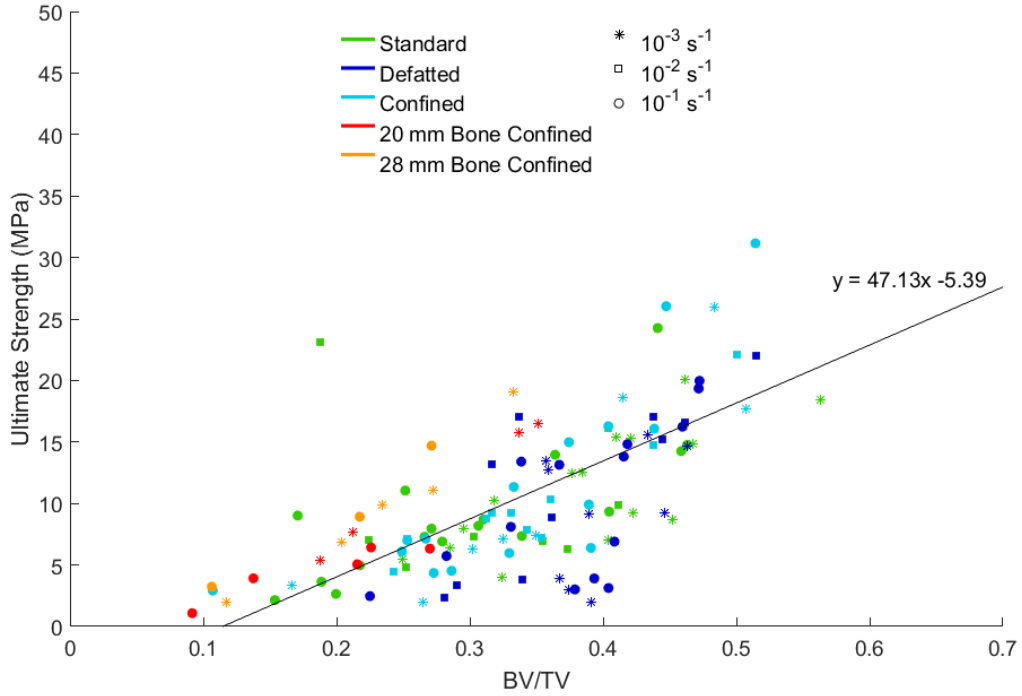

Figure 6.46: A graph of Ultimate Strength versus BV/TV for all test series performed in this study

6.5.2 Trabecular Number

Trabecular number is a measurement of the number of trabeculae present per unit length in a cancellous bone sample. As this number increases, it suggests an increase in the number of trabeculae in the sample, which, in turn, suggests a larger percentage of bone volume. Therefore, it would be expected that the trends seen in section 6.5.1 would be mirrored by those seen for Tb.N.

Figure 6.47 shows a similar positive, linear trend as seen previously in figure 6.43. While a direct correlation between Tb.N and apparent modulus of a single trabecula rod cannot be drawn, the trend suggests that an increase in Tb.N causes an increase in E_{app} given by the equation $E_{app} = 391.07\text{Tb.N} - 26.19$.

Both yield and ultimate strength show similar trends as that for apparent modulus, as seen in figures 6.49 and 6.50. Yield strength is predicted by the equation $\sigma_y = 7.66\text{Tb.N} - 0.70$ while ultimate strength is predicted by $\text{US} = 10.42\text{Tb.N} - 1.09$.

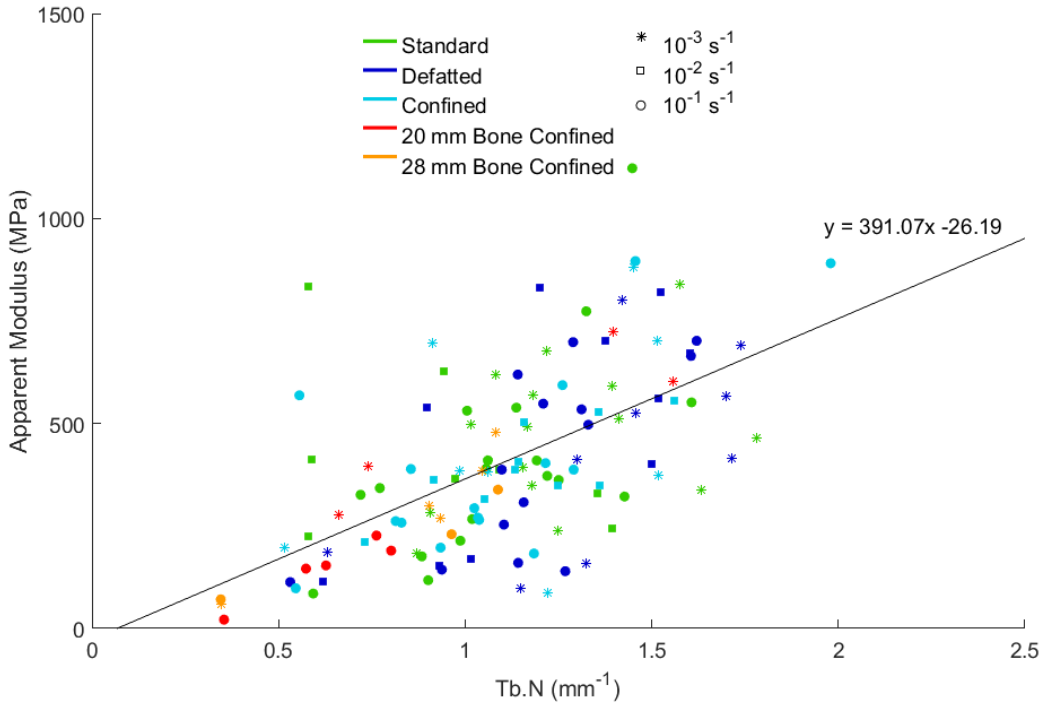

Figure 6.47: A graph of Apparent Modulus versus Tb.N for all test series performed in this study

Figures 6.48a-6.48e show the results as shown in figure 6.47, separated into specimen conditions. As in the case of BV/TV, each specimen condition exhibits a different relationship to that of the overall data. The condition specific graphs for yield and strength are presented in Appendix B.

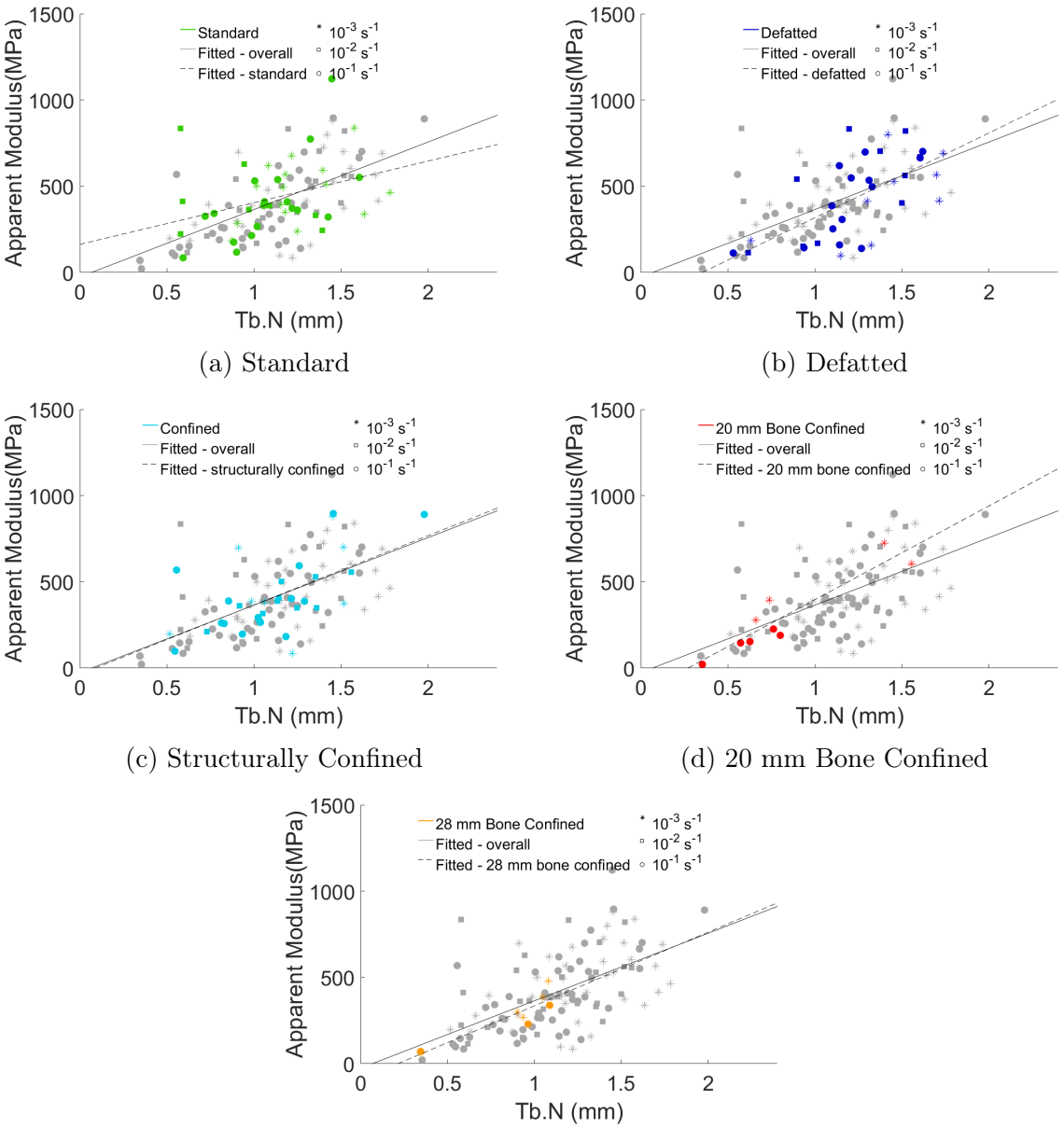

Figure 6.48: Graphs showing Apparent Modulus versus Tb.N for each specimen condition

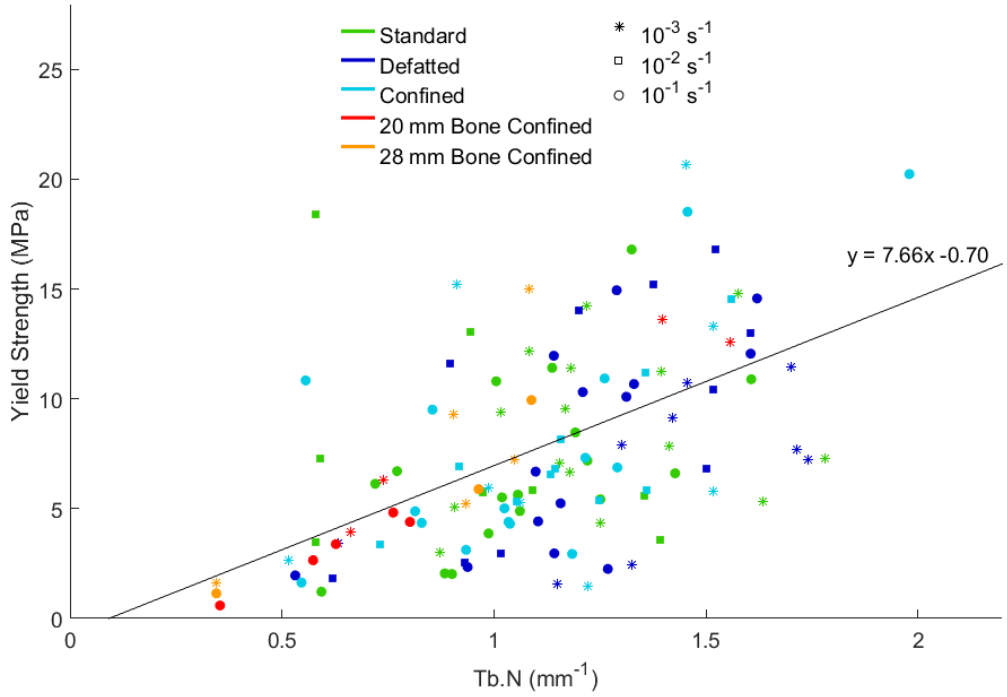

Figure 6.49: A graph of Yield Strength versus Tb.N for all test series performed in this study

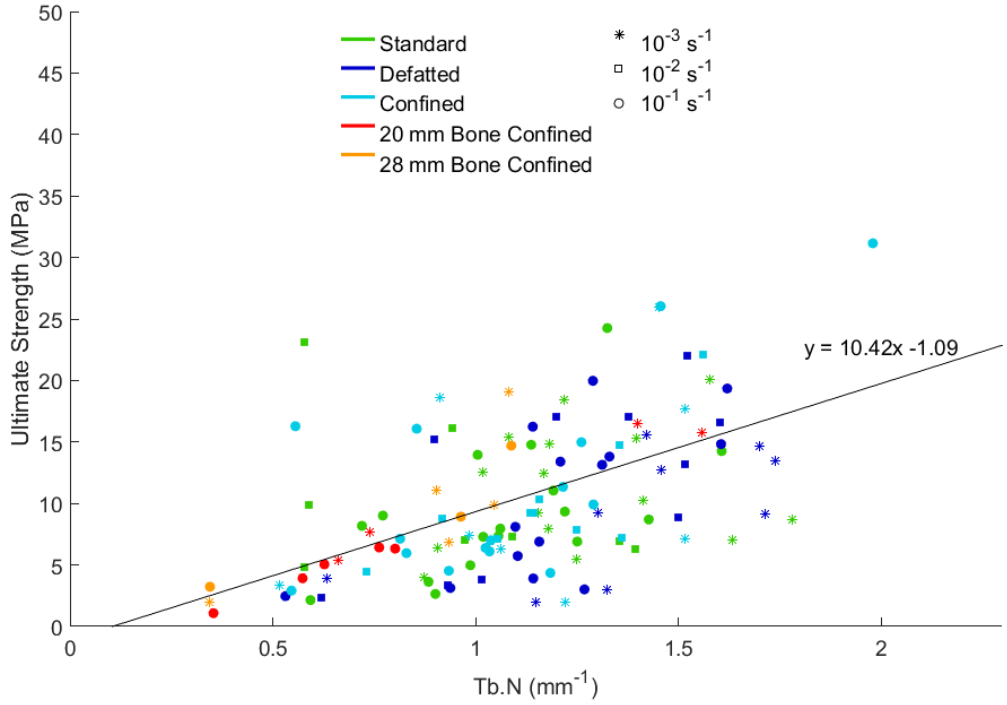

Figure 6.50: A graph of Ultimate Strength versus Tb.N for all test series performed in this study

6.5.3 Trabecular Separation

Trabecular separation is a measure of the space between trabeculae in a sample. In contrast to Tb.N, an increase in this architectural parameter suggests a decrease in bone volume. If the Tb.Sp value approaches zero, this implies that the bone is tending towards having no space between trabeculae, and is therefore tending towards being solid cancellous bone. Conversely, as the value of Tb.Sp tends towards infinity, the sample tends towards infinitely thin rods of trabeculae. These theoretical assumptions suggest that mechanical properties should depend on Tb.Sp in an exponentially decreasing manner, where the mechanical property approaches zero asymptotically as the value of Tb.Sp approaches infinity. Figures 6.51-6.54 agree well with this hypothesis.

The data in figure 6.51 suggests that apparent modulus depends on Tb.Sp according to $E_{app} = 1105.67e^{-1.66Tb.Sp}$. This trend suggests a single trabecula apparent modulus of 1105.67 MPa (when Tb.Sp is zero). This value is only 21% lower than the value predicted by BV/TV for the same mechanical property.

Figures 6.52a-6.52e show the results as shown in figure 6.51, presented per specimen conditions. As in the case of both BV/TV and Tb.N, each specimen condition exhibits a different relationship to that of the overall data. The condition specific graphs for yield and strength are presented in Appendix B.

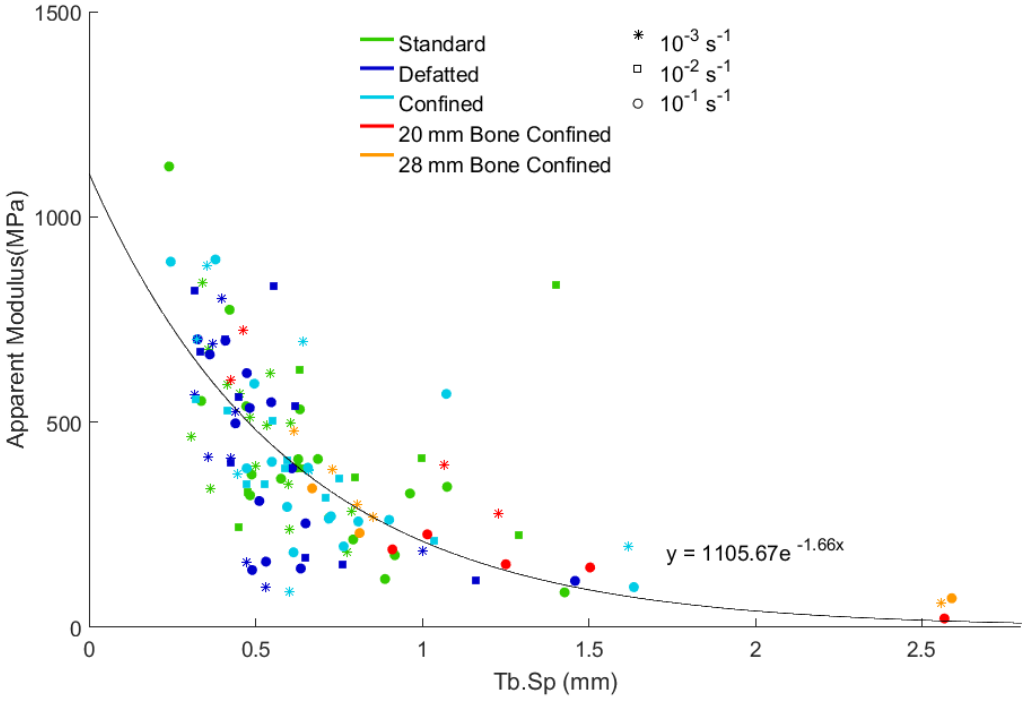

Figure 6.51: A graph of Apparent Modulus versus Tb.Sp for all test series performed in this study

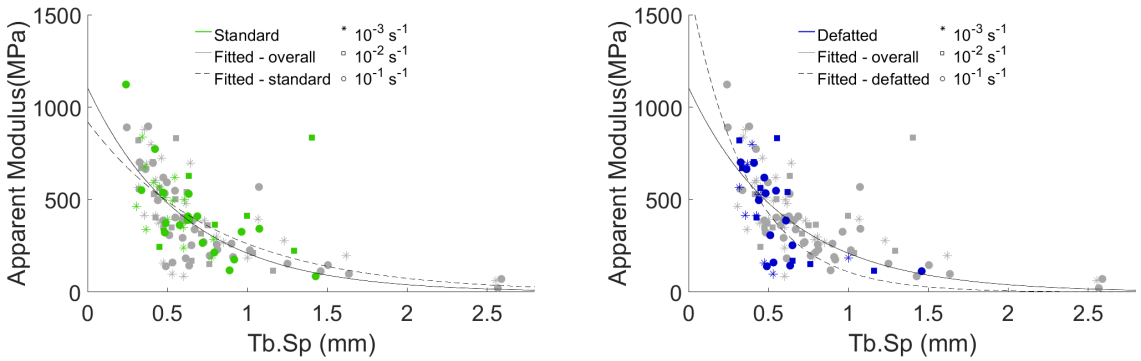

(a) Standard

(b) Defatted

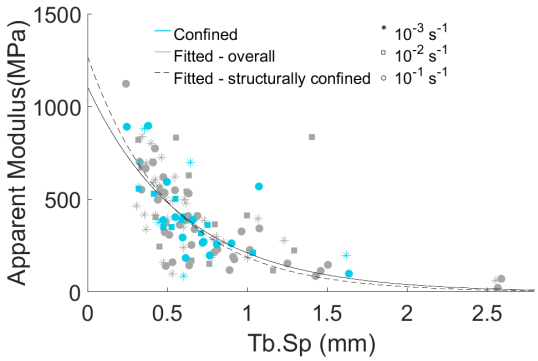

(c) Structurally Confined

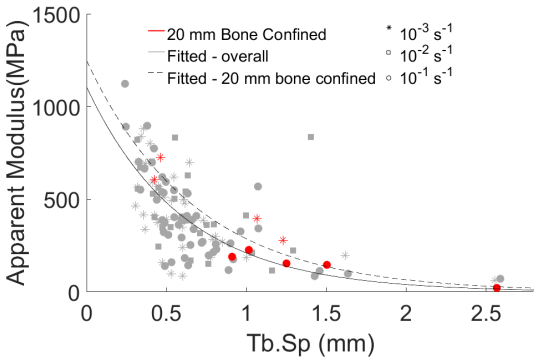

(d) 20 mm Bone Confined

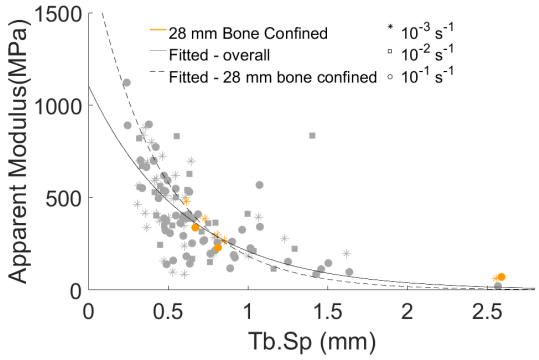

(e) 28 mm Bone Confined

Figure 6.52: Graphs showing Apparent Modulus versus Tb.Sp for each specimen condition

Figures 6.53 and 6.54 present the results for yield and ultimate strengths, represented by the equations $\sigma_y = 25.99e^{-2.07Tb.Sp}$ and US $= 39.96e^{-2.35Tb.Sp}$ respectively. These equations predict single trabecula yield and ultimate strengths of 25.99 MPa and 39.96 MPa respectively. The yield strength predicted by Tb.Sp agrees to within 14% of that predicted by BV/TV, while ultimate strength agrees to within 4%. These trends suggest that a combination of BV/TV and Tb.Sp is a good predictor of the mechanical response of cancellous bone, and that simulations aiming to mimic the response of cancellous bone should, at a minimum, include BV/TV and Tb.Sp. The observed relationship differences between test types suggest a combination of both the specimen condition and architectural parameters be used when modelling cancellous bone.

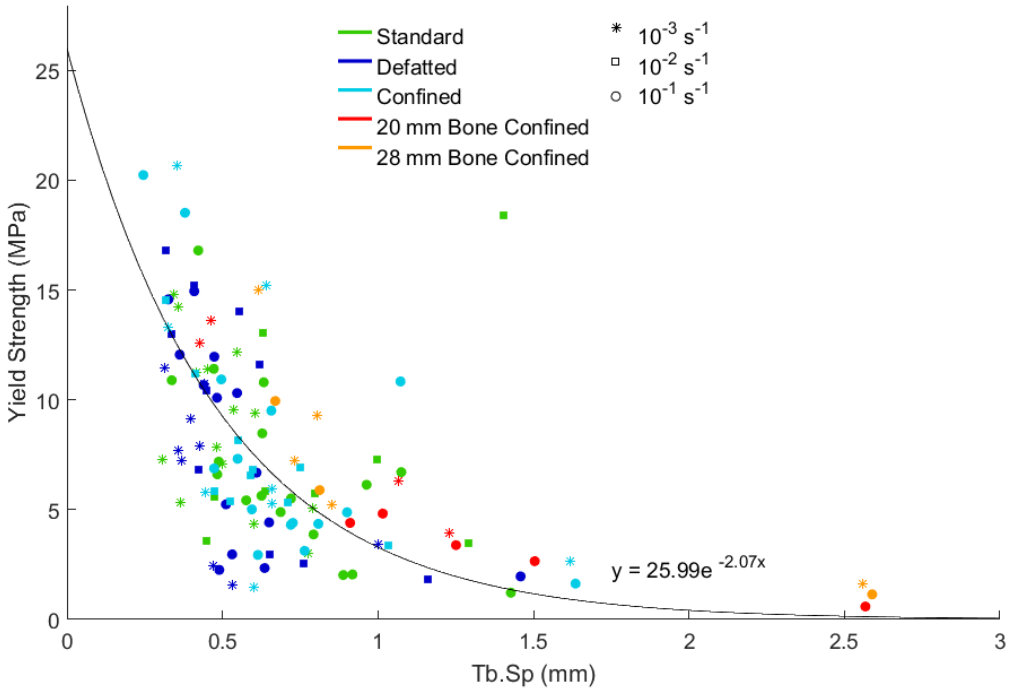

Figure 6.53: A graph of Yield Strength versus Tb.Sp for all test series performed in this study

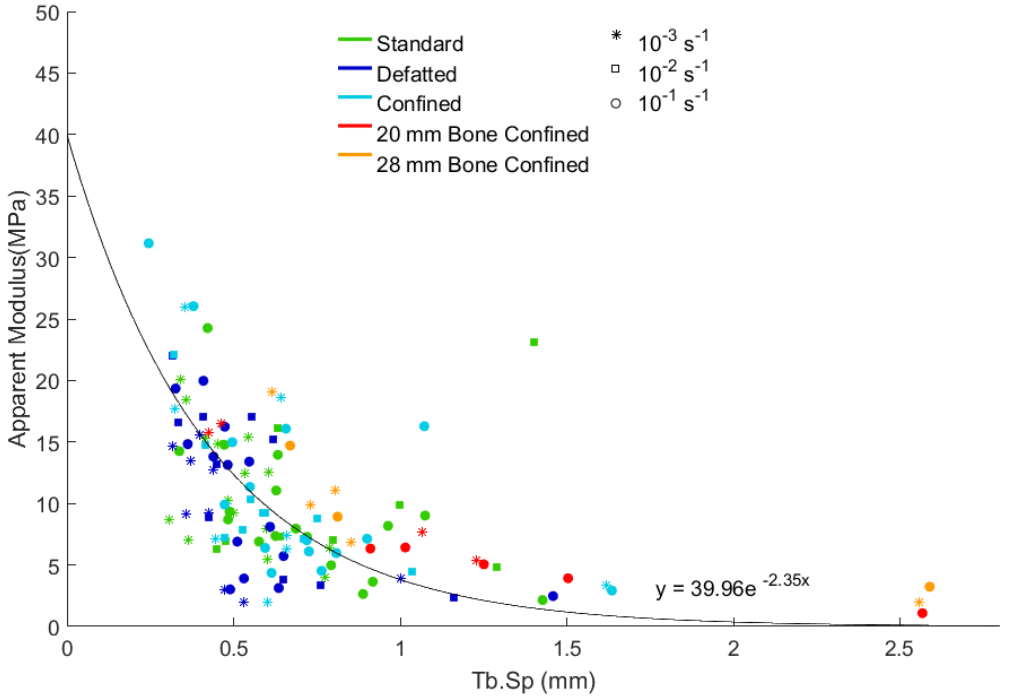

Figure 6.54: A graph of Ultimate Strength versus Tb.Sp for all test series performed in this study

6.5.4 Trabecular Thickness

Trabecular thickness is a measure of how thick individual trabeculae are within a sample. In theory, an increase in Tb.Th would result in an increase in mechanical strength, as thicker trabeculae suggest more total bone volume.

Figures 6.55-6.57 show graphs of apparent modulus, yield strength and ultimate strength versus Tb.Th. The graphs showed no obvious correlation for any of the mechanical properties, even when considering different test series. However, all the graphs exhibited a lower bound for the trabecular thickness of the samples tested of roughly 0.2 mm (200 μm), and an upper limit of roughly 0.58 mm (580 μm). This agrees with findings in the literature [3], further validating the results given by the developed architecture algorithms.

As no correlation was observed between the mechanical properties and Tb.Th, condition comparisons for this dataset were not plotted.

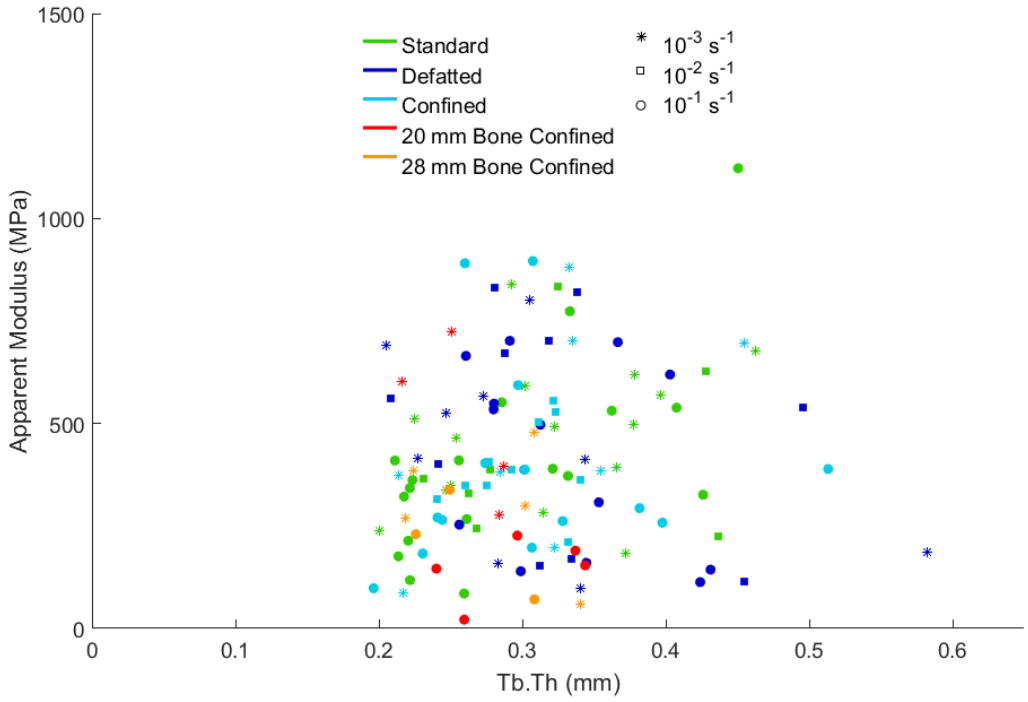

Figure 6.55: A graph of Apparent Modulus versus Tb.Th for all test series performed in this study

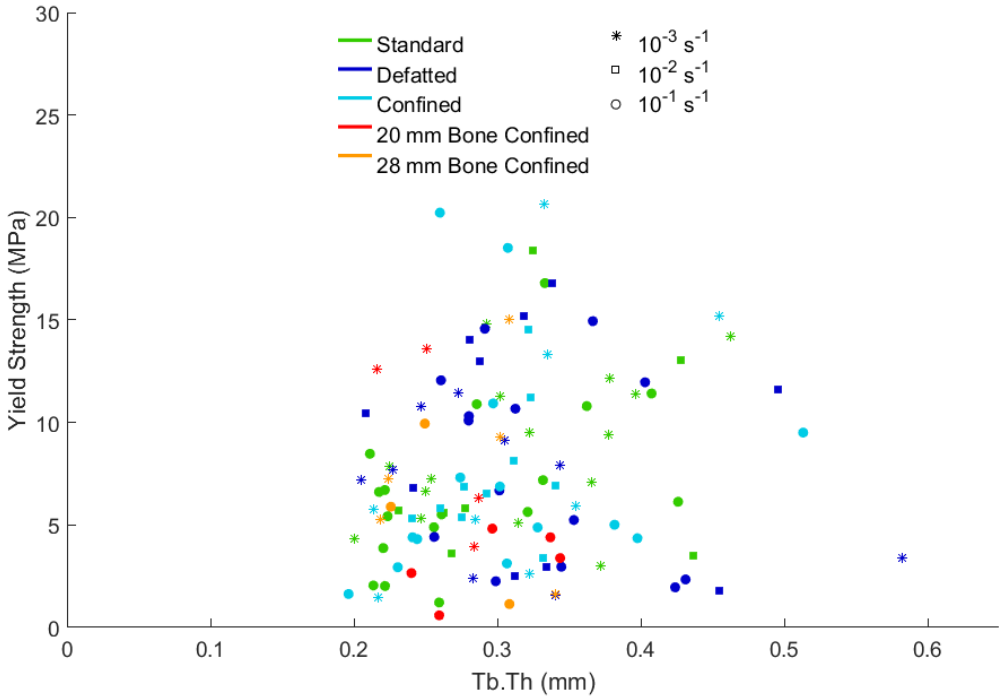

Figure 6.56: A graph of Yield Strength versus Tb.Th for all test series performed in this study

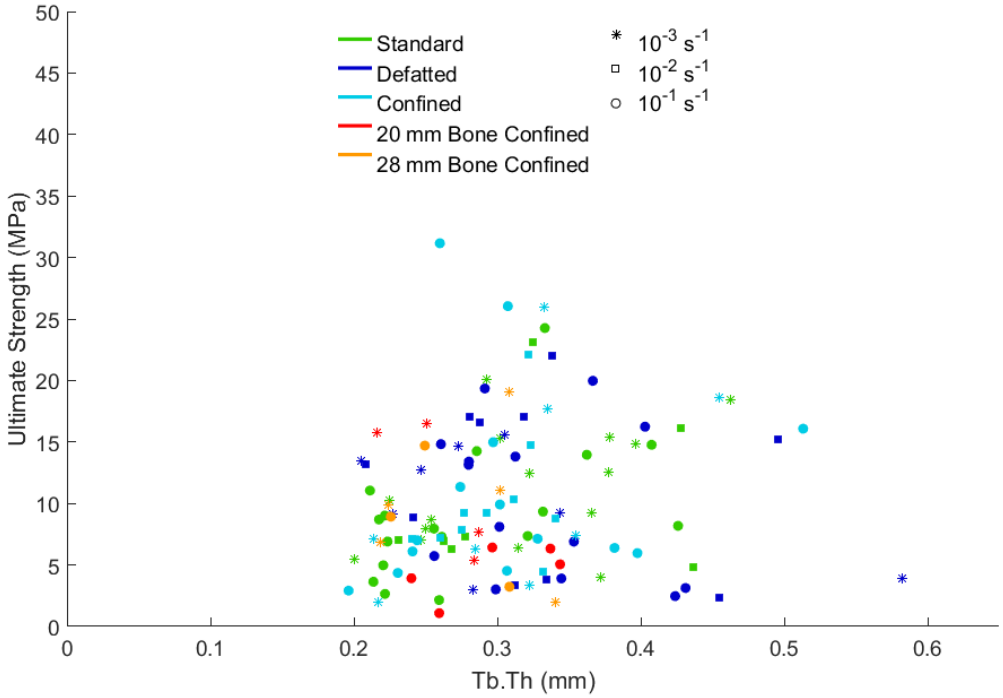

Figure 6.57: A graph of Ultimate Strength versus Tb.Th for all test series performed in this study

Chapter 7

Conclusions

This investigation aimed to assess the effect of strain rate, boundary conditions and architectural parameters on the mechanical response of bovine cancellous bone. Experimentation was performed at three quasi-static strain rates, namely 10^{-3}, 10^{-2} and 10^{-1} s^{-1}. Compression of the specimens at these strain rates yielded mechanical properties such as apparent modulus, yield strength and ultimate strength. The three main specimen conditions investigated were standard samples with marrow, defatted samples (without marrow) and confined samples. The confined samples were further divided into those confined structurally, using an aluminium collar, and those confined with a larger diameter of bone. These conditions were investigated to assess the effect of boundary conditions. Specimens were also individually scanned using a Phoenix μCT scanner (voxel size 80 μm, 70 kV, 350 μA, acquisition time of 500 ms per image) to obtain micro-structural architecture. The architectural parameters were coupled with the mechanical properties obtained during experimentation to assess the effect of architecture on the response of cancellous bone. The following sections present the conclusions drawn based on the outcomes of the aforementioned investigation.

7.1 Strain Rate

The effect of strain rate was considered for each specimen boundary condition tested. It was found that for quasi-static strain rates, there was little to no dependency of the overall mechanical properties on strain rate.

For the standard specimens, it was observed that an increase in strain rate caused a significant increase in the scatter of the experimental data. However, this was not the case for the defatted or confined specimens, which appeared to exhibit little correlation between both mechanical properties and scatter with varying strain rates. The response of

the inner 10 mm diameter of specimens confined by bone, both 20 mm and 28 mm overall diameter, showed a slight decrease in apparent modulus, yield and ultimate strength with an increase in strain rate. However, the sample sizes for the bone confined specimens were significantly smaller than those for the rest of the test series, and therefore no meaningful conclusions were drawn based on these results.

7.2 Boundary Condition

The effect of boundary condition was investigated by comparing the response of specimens tested using each boundary condition to the response of the standard specimens.

7.2.1 Presence of Marrow

Defatted specimens were found to have similar apparent modulus, yield strength and ultimate strength to standard specimens. It was concluded that at quasi-static strain rates, the presence of marrow does not significantly affect the strength of trabecular bone. It was also observed that the defatted sample sets exhibited less scatter in the data, suggesting that the flow of marrow may have a disruptive effect on the trabecular network. This finding was further validated by figure 6.23, which showed differing patterns and locations for marrow leaving the compressed standard specimen, as well as by the conclusions in presented section 7.2.2.1. It was concluded that the presence of marrow increases the apparent modulus by 8.76-51.69%, the yield strength by 0.16-37.50%, and the ultimate strength by 4.92-60.57%.

7.2.2 Confinement Condition

Confined tests were sub-divided into two main types of confinement, namely structural, and bone confinement. The structurally confined specimens were placed inside a 10 mm inner diameter aluminium collar, while the bone confined specimens relied on larger samples of machined bone to create a bone confinement surrounding the inner 10 mm diameter.

7.2.2.1 Structural Confinement

The structurally confined dataset yielded little difference in mechanical properties between themselves and those of the standard specimens. However, one particular group of confined samples appeared to exhibit far less scatter than the others. It was concluded that this dataset had larger diameters overall, which had a tighter fit within the aluminium collar confinement. This yielded the conclusion that undersized specimens would not be sufficiently confined by this confinement type. Therefore, in order to effectively confine specimens, the collar inner diameter should have a diameter the same size as or smaller than the outer diameter of the specimen. The decreased scatter within the tighter fitting dataset further validates the finding presented in section 7.2.1 that the movement of marrow within the trabecular bone at quasi-static strain rates disrupts the trabecular network.

7.2.2.2 Bone Confinement

The overall results for the bone confined specimens suggested a decrease in mechanical properties of confined specimens when compared to standard specimens. However, this result was attributed to both smaller sample sizes for the bone confined datasets, as well as longer storage times before experimentation of the specimens machined for bone confinement testing.

When comparing the response of the whole bone confined samples to the inner 10 mm of these samples, both 20 mm and 28 mm specimens showed a significant increase in mechanical properties. The apparent modulus of the inner 10 mm of the specimens was found to be 58% and 60% larger than the whole 20 mm and 28 mm specimens respectively. This suggests that the edge effects had been effectively removed by doubling the diameter of the specimen, and that further increasing the diameter would have no further effect on the apparent modulus of the inner 10 mm. Yield strength, however, showed increases for the inner 10 mm of 58% and 96% for 20 mm and 28 mm specimens respectively. This result suggests that further elimination of edge effects is required to accurately mimic *in vivo* mechanical properties post-yield.

No conclusions were drawn about the ultimate strength of the bone confined datasets as there were too few usable specimens in the 28 mm diameter dataset.

7.3 Architectural Parameters

The effects of architectural parameters, namely BV/TV, Tb.N, Tb.Sp and Tb.Th, on the mechanical properties of cancellous bone were investigated. Trends were observed in all architectural parameters except Tb.Th. The following sections detail the conclusions drawn for each architectural parameter.

7.3.1 Bone Volume versus Total Volume

BV/TV was found to have a positive linear relationship with the apparent modulus, yield strength and ultimate strength of cancellous bone. Apparent modulus, across all test types and strain rates, was found to be related to BV/TV by the equation $E_{app} = 1511.51\text{BV/TV} - 100.88$. Similarly, the yield and ultimate strength was found to be proportional to BV/TV according to equations $\sigma_y = 33.81\text{BV/TV} - 3.58$ and $\text{US} = 47.13\text{BV/TV} - 5.39$ respectively. These results suggested that the apparent modulus, yield strength and ultimate strength of a single trabecula - when BV/TV is equal to 1 - are 1410.63 MPa, 30.23 MPa and 41.74 MPa respectively.

7.3.2 Trabecular Number

The results for correlation between Tb.N and mechanical properties mirrored those for BV/TV. Apparent modulus was found to be related to Tb.N by the equation $E_{app} = 391.07\text{Tb.N} - 26.19$, while yield and ultimate strength was predicted using the equations $\sigma_y = 7.66\text{Tb.N} - 0.70$ and $\text{US} = 10.42\text{Tb.N} - 1.09$ respectively. While no inference was drawn about the mechanical properties of a singular trabecula using Tb.N, the similarity in trends to BV/TV suggested this result was valid.

7.3.3 Trabecular Separation

The results for Tb.Sp showed an exponential relationship between the mechanical properties and Tb.Sp. Apparent modulus, yield strength and ultimate strength were related to Tb.Sp by equations $E_{app} = 1105.67e^{-1.66Tb.Sp}$, $\sigma_y = 25.99e^{-2.07Tb.Sp}$ and $\text{US} = 39.96e^{-2.35Tb.Sp}$. Single trabecula properties were found to be predicted when Tb.Sp is zero (i.e. when there is no space between trabeculae). The apparent modulus, yield and ultimate strengths of a single trabecula were predicted to be 1105.67 MPa, 25.99 MPa and 39.96 MPa. The apparent modulus found using Tb.Sp was 21% lower than the value predicted by BV/TV. Yield and ultimate strengths predicted using

Tb.Sp were 14% and only 4% lower than those predicted using BV/TV. These results suggest that using both BV/TV and Tb.Sp in simulations involving cancellous bone would increase the accuracy of the results.

7.3.4 Trabecular Thickness

No obvious correlation was found between Tb.Th and the mechanical properties of cancellous bone. The results exhibited a minimum Tb.Th of 200 μm and a maximum of roughly 580 μm. This was found to agree with the literature and therefore further validated the archtiecture algorithms developed during the investigation.

7.3.5 General Influence of Architectural Parameters

Comparisons of each test type for all the architectural parameters yielded the result that test type influences the overall relationship between the mechanical property and the architectural parameter. This led to the conclusion that using a combination of the specimen condition and architectural parameters, preferably at least BV/TV and Tb.Sp, in simulation will yield the most accurate results for the response of cancellous bone.

7.4 General Conclusions

The investigation therefore determined the effect of strain rate, boundary conditions and architectural parameters on the mechanical response of bovine cancellous bone. Apparent modulus, yield strength and ultimate strength were analysed for each sample across five test types - standard, defatted, structurally confined, 20 mm bone confined and 28 mm bone confined - at three different quasi-static strain rates, namely 10^{-3}, 10^{-2} and 10^{-1} s^{-1}.

Each specimen was successfully μCT scanned and the images were used to determine the architectural parameters using algorithms developed during the investigation. The algorithms were validated using BoneJ, and the results of the validations showed good correlation between the developed technique and commercially available software.

An experimental confinement technique - bone confinement - was successfully used to reduce the edge effects of the boundary conditions on the tested specimens. This technique yielded positive results which suggest a significant increase in the strength of samples when confined by surrounding bone. This more accurately represents *in vivo* conditions.

Chapter 8

Recommendations

The objectives of this investigation were successfully met. However, the following recommendations for future work were identified:

- The study should be extended to intermediate and dynamic strain rate ranges to verify the effect of the presence of marrow.
- Further experimentation should be completed on larger diameter (20 mm and 28 mm) specimens to increase the sample sizes and therefore the statistical relevance of the data collected.
- A range of specimen conditions tests should be conducted using samples sourced from a single bone.
- Experimentation should be expanded to specimens with diameters larger than 28 mm, particularly for the post-yield properties of the specimens.
- Experiments should be conducted on lattices with carefully controlled architectural parameters to further investigate the effect of these parameters on mechanical response.
- Simulations should be run using models based on the μCT scanned images of the current specimens. This will give insight into the mechanics of the conducted experiments.
- Simulations should be extended to larger specimens, eventually being extended to whole bone samples rather than cored cylinders.
- Architectural parameters, especially BV/TV and Tb.Sp, should be included in simulations to better predict the response of cancellous bone.

References

[1] A. P. Singh, "Cortical and cancellous bone." Available at: `http://boneandspine.com/cortical-bone-and-cancellous-bone/`. Accessed: 2016-07-16.

[2] F. Chaari, E. Markiewicz, and P. Drazetic, "Identification of the spongy bone mechanical behavior under compression loads: numerical simulation versus experimental results," *International Journal of Crashworthiness*, vol. 12, no. 3, pp. 247–253, 2007.

[3] M. Charlebois, *Constitutive law for trabecular bone in large strain compression*. PhD thesis, Ph. D. thesis, 2008.

[4] N. Kelly and J. P. McGarry, "Experimental and numerical characterisation of the elasto-plastic properties of bovine trabecular bone and a trabecular bone analogue," *Journal of the Mechanical Behavior of Biomedical Materials*, vol. 9, pp. 184–197, 2012.

[5] N. M. Harrison and P. E. McHugh, "Comparison of trabecular bone behavior in core and whole bone samples using high-resolution modeling of a vertebral body," *Biomechanics and modeling in mechanobiology*, vol. 9, no. 4, pp. 469–480, 2010.

[6] Y. Chen, H. T. Ma, L. Liang, C. Zhang, J. F. Griffith, and P. C. Leung, "A simulation study on marrow fat effect on biomechanics of vertebra bone," in *2015 37th Annual International Conference of the IEEE Engineering in Medicine and Biology Society (EMBC)*, pp. 3921–3924, Aug 2015.

[7] H. T. Ma, R. Ren, Y. Chen, J. F. Griffith, P.-C. Leung, and P. Zhang, "A simulation study of marrow fat effect on bone biomechanics," in *2014 36th Annual International Conference of the IEEE Engineering in Medicine and Biology Society*, pp. 4030–4033, IEEE, 2014.

[8] T. A. Metzger, J. M. Shudick, R. Seekell, Y. Zhu, and G. L. Niebur, "Rheological behavior of fresh bone marrow and the effects of storage," *Journal of the mechanical behavior of biomedical materials*, vol. 40, pp. 307–313, 2014.

[9] D. R. Carter and W. C. Hayes, "The compressive behavior of bone as a two-phase porous structure," *The Journal of Bone & Joint Surgery*, vol. 59, no. 7, pp. 954–962, 1977.

[10] J. Halgrin, F. Chaari, and É. Markiewicz, "On the effect of marrow in the mechanical behavior and crush response of trabecular bone," *Journal of the mechanical behavior of biomedical materials*, vol. 5, no. 1, pp. 231–237, 2012.

[11] Asirt.org, "International travel, road crash, pedestrian safety, country road condition." [Online]. Available: http://www.asirt.org. [Accessed: 25- Apr- 2016], 2016.

[12] N. Reznikov, H. Chase, V. Brumfeld, R. Shahar, and S. Weiner, "The 3d structure of the collagen fibril network in human trabecular bone: relation to trabecular organization," *Bone*, vol. 71, pp. 189–195, 2015.

[13] T. F. Freddo and H. Gong, "Anatomy of the ciliary body and outflow pathways," *Duane's Clinical Ophthalmology, William Tasman, ed., Lipincott Williams and Wilkins*, vol. 3, pp. 1–18, 2007.

[14] M. L. Bouxsein, S. K. Boyd, B. A. Christiansen, R. E. Guldberg, K. J. Jepsen, and R. Müller, "Guidelines for assessment of bone microstructure in rodents using micro-computed tomography," *Journal of bone and mineral research*, vol. 25, no. 7, pp. 1468–1486, 2010.

[15] T. Hildebrand and P. Rüegsegger, "Quantification of bone microarchitecture with the structure model index," *Computer Methods in Biomechanics and Bio Medical Engineering*, vol. 1, no. 1, pp. 15–23, 1997.

[16] J. A. Hipp, A. Jansujwicz, C. A. Simmons, and B. D. Snyder, "Trabecular bone morphology from micro-magnetic resonance imaging," *Journal of Bone and Mineral Research*, vol. 11, no. 2, pp. 286–292, 1996.

[17] A. Odgaard, "Three-dimensional methods for quantification of cancellous bone architecture," *Bone*, vol. 20, no. 4, pp. 315–328, 1997.

[18] S. Majumdar, M. Kothari, P. Augat, D. Newitt, T. Link, J. Lin, T. Lang, Y. Lu, and H. Genant, "High-resolution magnetic resonance imaging: three-dimensional trabecular bone architecture and biomechanical properties," *Bone*, vol. 22, no. 5, pp. 445–454, 1998.

[19] A. da Silva, J. Alves, O. da Silva, N. da Silva Junior, M. Gazziro, J. Pereira, P. Lasso, C. Vaz, C. Pereira, T. Leiva, and R. Guarniero, "Microstructural assessment

of cancellous bone using 3d microtomography," in *Journal of Physics: Conference Series*, vol. 313, p. 012008, IOP Publishing, 2011.

[20] M. Prot, D. Saletti, S. Pattofatto, V. Bousson, and S. Laporte, "Links between mechanical behavior of cancellous bone and its microstructural properties under dynamic loading," *Journal of biomechanics*, vol. 48, no. 3, pp. 498–503, 2015.

[21] H. Follet, S. Viguet-Carrin, B. Burt-Pichat, B. Dépalle, Y. Bala, E. Gineyts, F. Munoz, M. Arlot, G. Boivin, R. D. Chapurlat, *et al.*, "Effects of preexisting microdamage, collagen cross-links, degree of mineralization, age, and architecture on compressive mechanical properties of elderly human vertebral trabecular bone," *Journal of Orthopaedic Research*, vol. 29, no. 4, pp. 481–488, 2011.

[22] A. Syahrom, M. R. A. Kadir, J. Abdullah, and A. Öchsner, "Mechanical and microarchitectural analyses of cancellous bone through experiment and computer simulation," *Medical & biological engineering & computing*, vol. 49, no. 12, pp. 1393–1403, 2011.

[23] Y. N. Yeni, M. J. Zinno, J. S. Yerramshetty, R. Zauel, and D. P. Fyhrie, "Variability of trabecular microstructure is age-, gender-, race-and anatomic site-dependent and affects stiffness and stress distribution properties of human vertebral cancellous bone," *Bone*, vol. 49, no. 4, pp. 886–894, 2011.

[24] A. Nazarian, F. J. A. Arroyo, C. Rosso, S. Aran, and B. D. Snyder, "Tensile properties of rat femoral bone as functions of bone volume fraction, apparent density and volumetric bone mineral density," *Journal of biomechanics*, vol. 44, no. 13, pp. 2482–2488, 2011.

[25] J. G. Garrison, J. A. Gargac, and G. L. Niebur, "Shear strength and toughness of trabecular bone are more sensitive to density than damage," *Journal of biomechanics*, vol. 44, no. 16, pp. 2747–2754, 2011.

[26] A. M. H. da Silva, J. M. Alves, O. L. da Silva, and N. F. da Silva Junior, "Two and three-dimensional morphometric analysis of trabecular bone using x-ray microtomography," *Revista Brasileira de Engenharia Biomedica*, 2014.

[27] T. Hildebrand, A. Laib, R. Müller, J. Dequeker, and P. Rüegsegger, "Direct three-dimensional morphometric analysis of human cancellous bone: Microstructural data from spine, femur, iliac crest, and calcaneus," *Journal of Bone and Mineral Research*, vol. 14, pp. 1167–1174, 7 1999.

[28] J. C. Teo, K. M. Si-Hoe, J. E. Keh, and S. H. Teoh, "Relationship between ct intensity, micro-architecture and mechanical properties of porcine vertebral cancellous bone," *Clinical Biomechanics*, vol. 21, no. 3, pp. 235–244, 2006.

[29] B. A. Christiansen, "Effect of micro-computed tomography voxel size and segmentation method on trabecular bone microstructure measures in mice," *Bone Reports*, vol. 5, pp. 136–140, 2016.

[30] K. Rathnayaka, T. Sahama, M. A. Schuetz, and B. Schmutz, "Effects of ct image segmentation methods on the accuracy of long bone 3d reconstructions," *Medical engineering & physics*, vol. 33, no. 2, pp. 226–233, 2011.

[31] B. S. Morse, "Lecture 4: Thresholding," Jan. 2000.

[32] Mathworks, "graythresh." Internet.

[33] E. Cendre, D. Mitton, J.-P. Roux, M. Arlot, F. Duboeuf, B. Burt-Pichat, C. Rumelhart, G. Peix, and P. Meunier, "High-resolution computed tomography for architectural characterization of human lumbar cancellous bone: relationships with histomorphometry and biomechanics," *Osteoporosis International*, vol. 10, no. 5, pp. 353–360, 1999.

[34] H. Follet, K. Bruyere-Garnier, F. Peyrin, J.-P. Roux, M. Arlot, B. Burt-Pichat, C. Rumelhart, and P. Meunier, "Relationship between compressive properties of human os calcis cancellous bone and microarchitecture assessed from 2d and 3d synchrotron microtomography," *Bone*, vol. 36, no. 2, pp. 340–351, 2005.

[35] J. G. Garrison, C. L. Slaboch, and G. L. Niebur, "Density and architecture have greater effects on the toughness of trabecular bone than damage," *Bone*, vol. 44, no. 5, pp. 924–929, 2009.

[36] C. Greenwood, J. Clement, A. Dicken, J. Evans, I. Lyburn, R. Martin, K. Rogers, N. Stone, G. Adams, and P. Zioupos, "The micro-architecture of human cancellous bone from fracture neck of femur patients in relation to the structural integrity and fracture toughness of the tissue," *Bone Reports*, vol. 3, pp. 67–75, 2015.

[37] S. Laporte, F. David, V. Bousson, and S. Pattofatto, "Dynamic behavior and microstructural properties of cancellous bone," *arXiv preprint arXiv:0911.5114*, 2009.

[38] M. Matsuura, F. Eckstein, E.-M. Lochmüller, and P. K. Zysset, "The role of fabric in the quasi-static compressive mechanical properties of human trabecular bone from various anatomical locations," *Biomechanics and Modeling in Mechanobiology*, vol. 7, no. 1, pp. 27–42, 2008.

[39] T. A. Metzger, T. C. Kreipke, T. J. Vaughan, L. M. McNamara, and G. L. Niebur, "The in situ mechanics of trabecular bone marrow: the potential for

mechanobiological response," *Journal of biomechanical engineering*, vol. 137, no. 1, p. 011006, 2015.

[40] E. Mittra, C. Rubin, and Y.-X. Qin, "Interrelationship of trabecular mechanical and microstructural properties in sheep trabecular bone," *Journal of biomechanics*, vol. 38, no. 6, pp. 1229–1237, 2005.

[41] E. Mittra, C. Rubin, B. Gruber, and Y.-X. Qin, "Evaluation of trabecular mechanical and microstructural properties in human calcaneal bone of advanced age using mechanical testing, μct, and dxa," *Journal of biomechanics*, vol. 41, no. 2, pp. 368–375, 2008.

[42] A. Nazarian, M. Stauber, D. Zurakowski, B. D. Snyder, and R. Müller, "The interaction of microstructure and volume fraction in predicting failure in cancellous bone," *Bone*, vol. 39, no. 6, pp. 1196–1202, 2006.

[43] M. Prot, D. Saletti, S. Laporte, S. Pattofatto, and V. Bousson, "Correlations between cancellous bone architecture and its dynamic behaviour," 2014.

[44] A. Sanyal, A. Gupta, H. H. Bayraktar, R. Y. Kwon, and T. M. Keaveny, "Shear strength behavior of human trabecular bone," *Journal of biomechanics*, vol. 45, no. 15, pp. 2513–2519, 2012.

[45] J. Wegrzyn, J.-P. Roux, M. E. Arlot, S. Boutroy, N. Vilayphiou, O. Guyen, P. D. Delmas, R. Chapurlat, and M. L. Bouxsein, "Determinants of the mechanical behavior of human lumbar vertebrae after simulated mild fracture," *Journal of Bone and Mineral Research*, vol. 26, no. 4, pp. 739–746, 2011.

[46] Y. Wu, S. Adeeb, and M. R. Doschak, "Using micro-ct derived bone microarchitecture to analyze bone stiffness–a case study on osteoporosis rat bone," *Frontiers in endocrinology*, vol. 6, 2015.

[47] L. Pryor McIntosh, D. S. Strait, J. A. Ledogar, A. L. Smith, C. F. Ross, Q. Wang, L. A. Opperman, and P. C. Dechow, "Internal bone architecture in the zygoma of human and pan," *The Anatomical Record*, vol. 299, no. 12, pp. 1704–1717, 2016.

[48] E. F. Morgan and T. M. Keaveny, "Dependence of yield strain of human trabecular bone on anatomic site," *Journal of biomechanics*, vol. 34, no. 5, pp. 569–577, 2001.

[49] N. A. Johanson, M. E. Charlson, L. Cutignola, M. Neves, E. F. DiCarlo, and P. G. Bullough, "Femoral neck bone density: Direct measurement and histomorphometric validation," *The Journal of arthroplasty*, vol. 8, no. 6, pp. 641–652, 1993.

[50] M. Kasra and M. D. Grynpas, "On shear properties of trabecular bone under torsional loading: effects of bone marrow and strain rate," *Journal of biomechanics*, vol. 40, no. 13, pp. 2898–2903, 2007.

[51] D. L. Kopperdahl and T. M. Keaveny, "Yield strain behavior of trabecular bone," *Journal of biomechanics*, vol. 31, no. 7, pp. 601–608, 1998.

[52] T. Keaveny, T. Pinilla, R. Crawford, D. Kopperdahl, and A. Lou, "Systematic and random errors in compression testing of trabecular bone," *Journal of Orthopaedic Research*, vol. 15, pp. 101–110, 1997.

[53] Z. Asgharpour, D. Fressmann, E. Schuller, and S. Peldschus, "Implementation of a strain rate dependent human bone model," in *8th European LS-DYNA Users Conference, Strasbourg*, 2011.

[54] M. Prot, T. Cloete, D. Saletti, and S. Laporte, "Intermediate strain rate behaviour of cancellous bone: from the lower to the higher strain rate," *Computer methods in biomechanics and biomedical engineering*, vol. 17, no. sup1, pp. 50–51, 2014.

[55] M. Prot, T. Cloete, D. Saletti, and S. Laporte, "The behavior of cancellous bone from quasi-static to dynamic strain rates with emphasis on the intermediate regime," *Journal of biomechanics*, vol. 49, no. 7, pp. 1050–1057, 2016.

[56] J. Ouyang, G. Yang, W. Wu, Q. Zhu, and S. Zhong, "Biomechanical characteristics of human trabecular bone," *Clinical Biomechanics*, vol. 12, no. 7, pp. 522–524, 1997.

[57] T. Cloete, G. Paul, and E. Ismail, "Hopkinson bar techniques for the intermediate strain rate testing of bovine cortical bone," *Philosophical Transactions of the Royal Society of London A: Mathematical, Physical and Engineering Sciences*, vol. 372, no. 2015, p. 20130210, 2014.

[58] R. R. Adharapurapu, F. Jiang, and K. S. Vecchio, "Dynamic fracture of bovine bone," *Materials Science and Engineering: C*, vol. 26, no. 8, pp. 1325–1332, 2006.

[59] T. Cloete, A. Van Der Westhuizen, S. Kok, and G. Nurick, "A tapered striker pulse shaping technique for uniform strain rate dynamic compression of bovine bone," *EDP Sciences*, vol. 1, pp. 901–907, 2009.

[60] A. Laouira, J. Rahmoun, H. Naceur, P. Drazetic, C. Fontaine, and G. Niebur, "On the influence of marrow on the mechanical behavior of porcine trabecular bone under dynamic loading: a numerical investigation," *Computer methods in biomechanics and biomedical engineering*, vol. 18, no. sup1, pp. 1974–1975, 2015.

[61] M. Charlebois, M. Pretterklieber, and P. K. Zysset, "The role of fabric in the large strain compressive behavior of human trabecular bone," *Journal of biomechanical engineering*, vol. 132, no. 12, p. 121006, 2010.

[62] P. Forquin, A. Arias, and R. Zaera, "An experimental method of measuring the confined compression strength of geomaterials," *International Journal of Solids and Structures*, vol. 44, no. 13, pp. 4291–4317, 2007.

[63] M. Stander, "Development of an intermediate strain rate compression testing machine," Master's thesis, University of Cape Town, February 2014.

[64] S. Mandal and M. J. Ali, "Log-normal distribution," 2015.

[65] G. Paul, "The strain rate dependent properties of bovine cortical bone," Master's thesis, University of Cape Town, 2014.

Appendices

Appendix A

Hoop Strain

A.1 Derivation

As discussed in Chapter 5, the hoop strain (ϵ_H) measured on the external surface of a thickwalled cylinder, as shown in figure A.1 is described in terms of the radii of the cylinder and by the applied internal pressure.

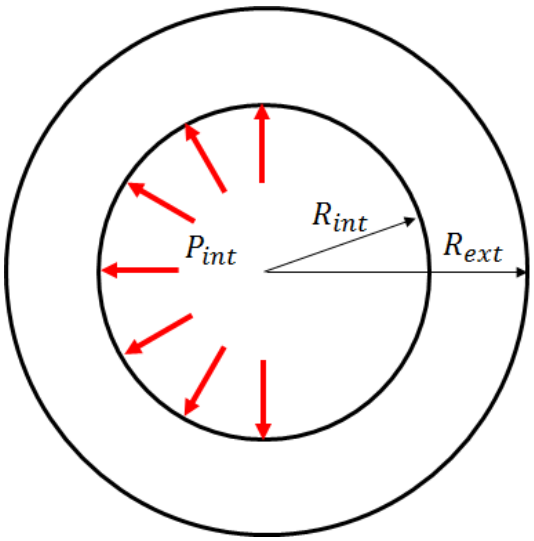

Figure A.1: A schematic of a thick-walled cylinder

Using thick-walled cylinder theory, the following equations apply:

$$\epsilon_H = \frac{\sigma_H}{E} - \nu\frac{\sigma_R}{E} \tag{A.1}$$

$$\sigma_R = A - \frac{B}{R^2} \tag{A.2}$$

$$\sigma_H = A + \frac{B}{R^2} \tag{A.3}$$

Where:

- ϵ_H is the hoop strain
- E is the Young's modulus of the cylinder material
- ν is the Poisson's ratio of the cylinder material
- σ_R is the radial stress
- σ_H is the hoop stress
- A and B are Lamé constants
- R is a radius of the cylinder within its thickness

In order to determine the hoop stress on the external surface of the cylinder, the following boundary conditions is applied.

$$\sigma_R|_{R=R_{ext}} = 0 \tag{A.4}$$

and

$$\sigma_R|_{R=R_{int}} = -P_{int} \tag{A.5}$$

Sub- and superscripts *int* and *ext* represent the internal and external surfaces of the cylinder respectively.

Substituting equations A.4 and A.5 into equation A.2, the following parameters are determined:

$$0 = A - \frac{B}{R_{ext}^2} \tag{A.6}$$

$$\therefore A = \frac{B}{R_{ext}^2} \tag{A.7}$$

$$-P_{int} = A - \frac{B}{R_{int}^2} \tag{A.8}$$

$$\therefore -P_{int} = B\left(\frac{1}{R_{ext}^2} - \frac{1}{R_{int}^2}\right) \tag{A.9}$$

$$\therefore B = \frac{P_{int}}{\frac{1}{R_{int}^2} - \frac{1}{R_{ext}^2}} \tag{A.10}$$

$$\therefore A = \frac{P_{int}}{R_{ext}^2} \times \frac{1}{\frac{1}{R_{int}^2} - \frac{1}{R_{ext}^2}} \tag{A.11}$$

Substituting the Lamé constants back into equation A.3 yields the following:

$$\sigma_H|_{R=R_{ext}} = \frac{P_{int}}{R_{ext}^2}\frac{1}{\frac{1}{R_{int}^2}-\frac{1}{R_{ext}^2}} + \frac{P_{int}}{R_{ext}^2}\frac{1}{\frac{1}{R_{int}^2}-\frac{1}{R_{ext}^2}} \tag{A.12}$$

$$\therefore \sigma_H^{ext} = \frac{2P_{int}}{R_{ext}2}\frac{R_{int}^2 R_{ext}^2}{R_{ext}^2 - R_{int}^2} \tag{A.13}$$

$$\therefore \epsilon_H^{ext} = \frac{2P_{int}}{E}\frac{R_{int}^2}{R_{ext}^2 - R_{int}^2} \tag{A.14}$$

Appendix B

Full Results

B.1 Standard Specimens, 10^{-3} s^{-1}

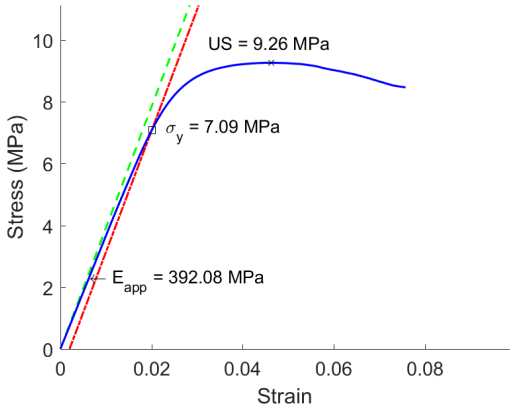

Figure B.1: Sample Number 23

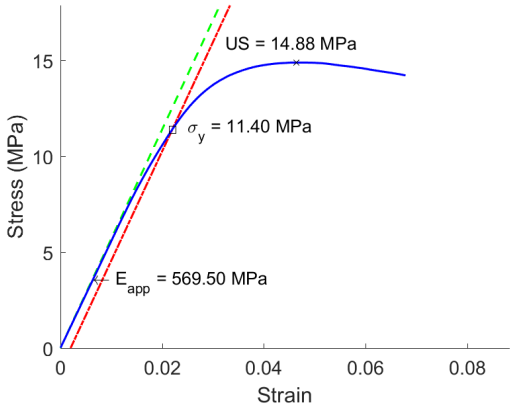

Figure B.2: Sample Number 26

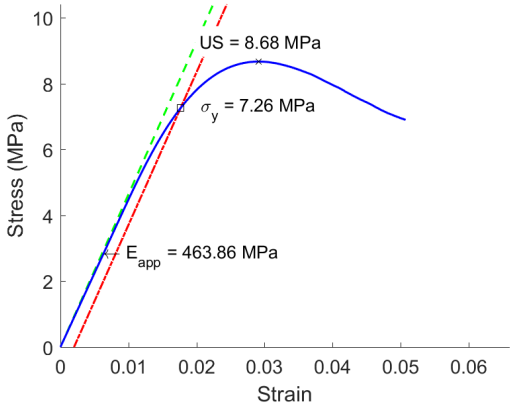

Figure B.3: Sample Number 136

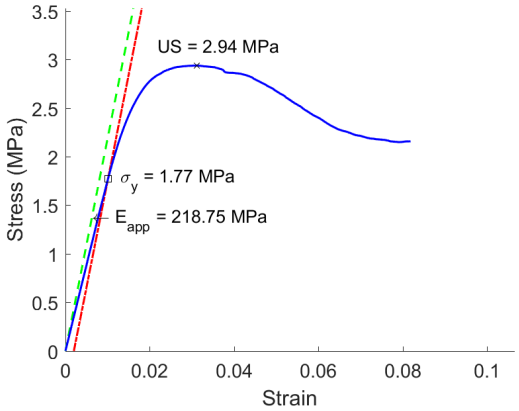

Figure B.4: Sample Number 220

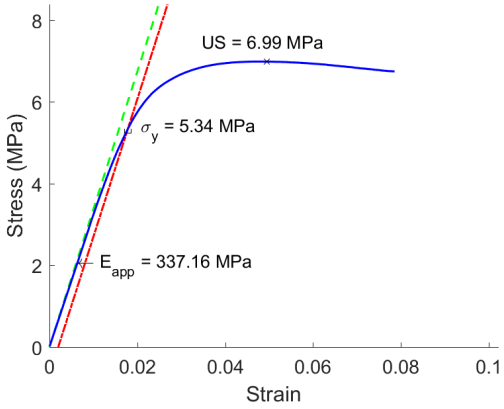

Figure B.5: Sample Number 230

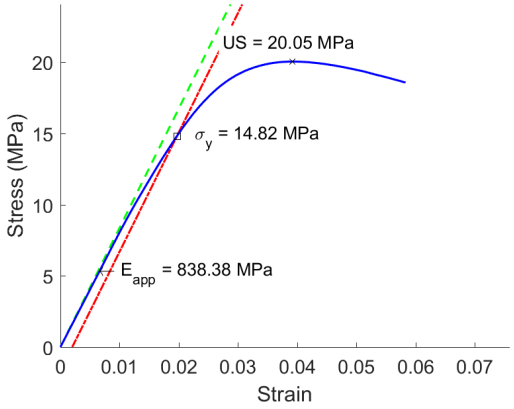

Figure B.6: Sample Number 280

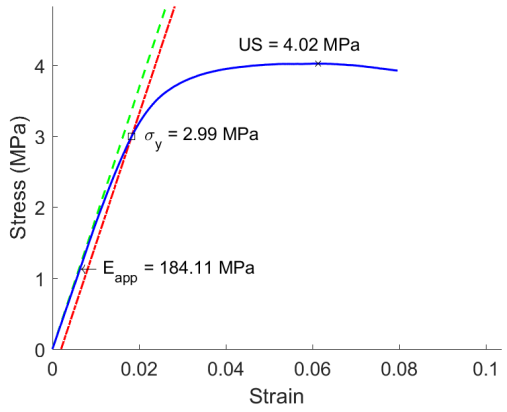

Figure B.7: Sample Number 319

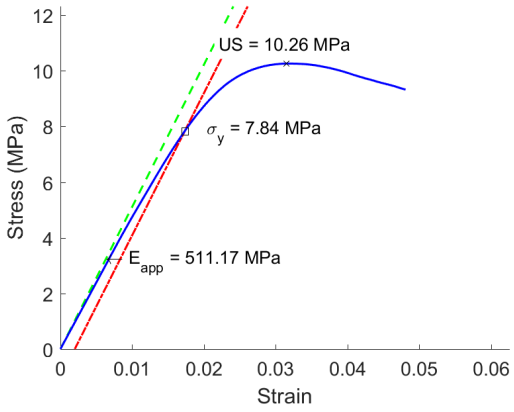

Figure B.8: Sample Number 402

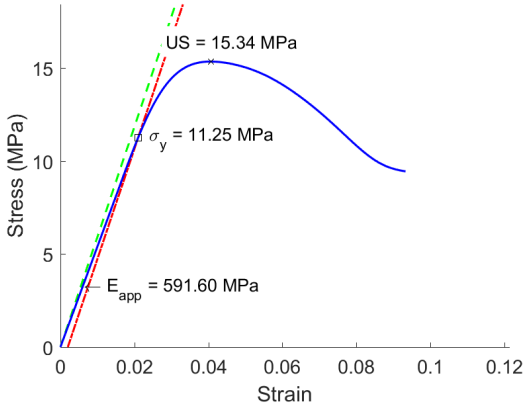

Figure B.9: Sample Number 451

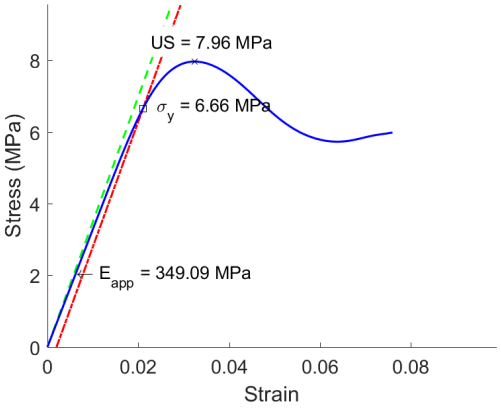

Figure B.10: Sample Number 452

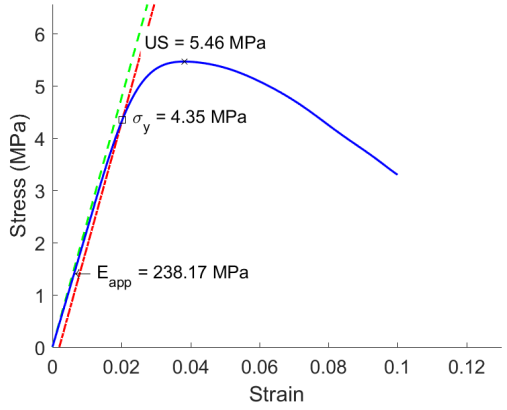

Figure B.11: Sample Number 453

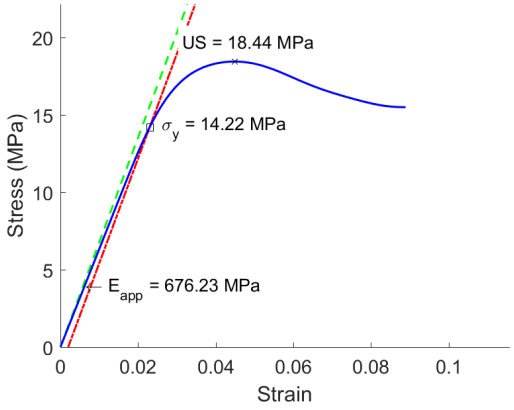

Figure B.12: Sample Number 454

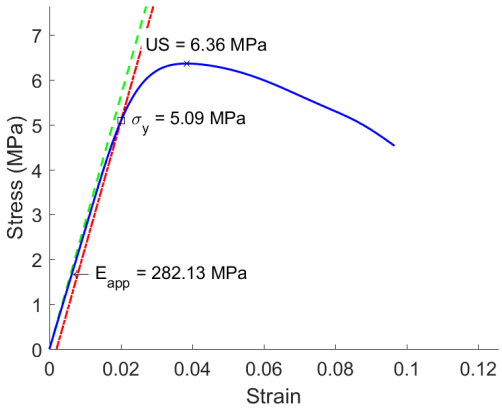

Figure B.13: Sample Number 455

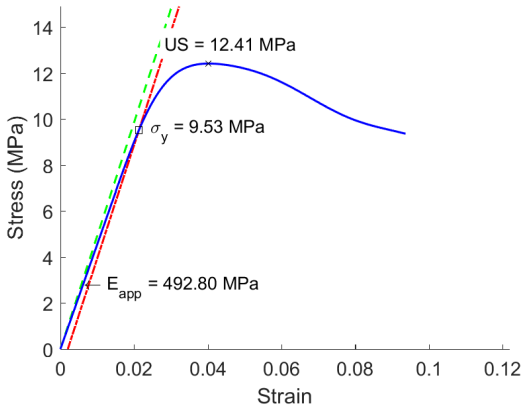

Figure B.14: Sample Number 456

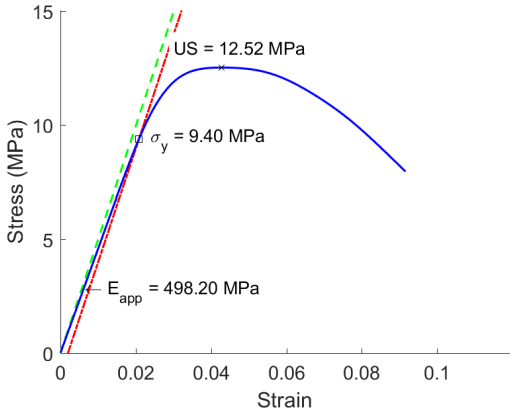

Figure B.15: Sample Number 457

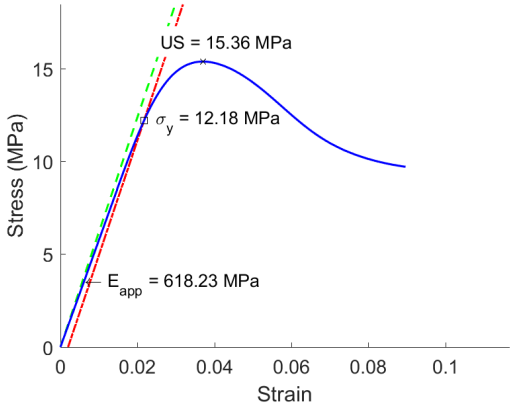

Figure B.16: Sample Number 458

B.2 Standard Specimens, 10^{-2} s^{-1}

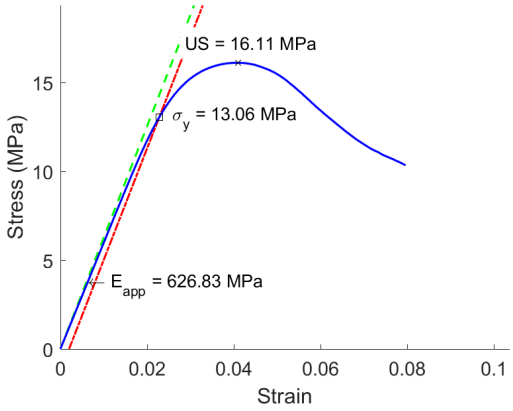

Figure B.17: Sample Number 105

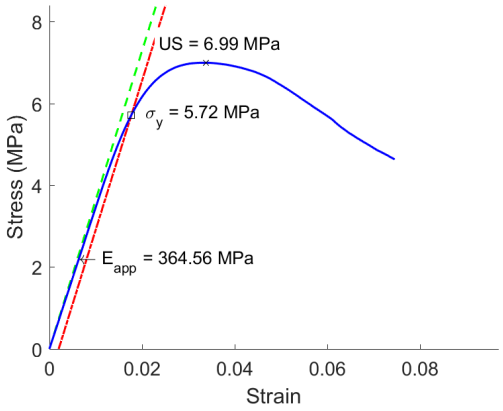

Figure B.18: Sample Number 124

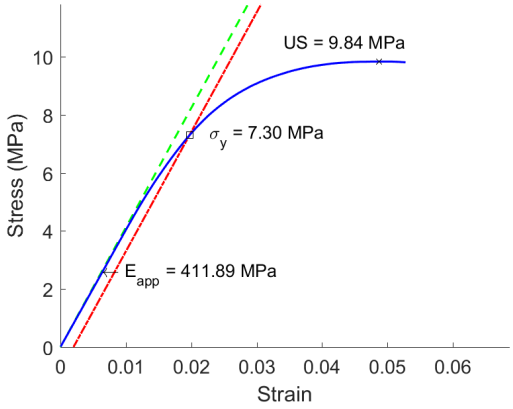

Figure B.19: Sample Number 228

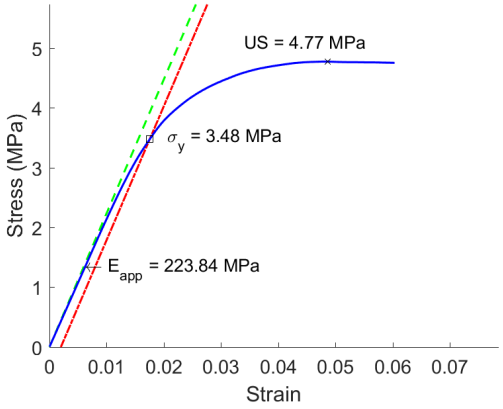

Figure B.20: Sample Number 251

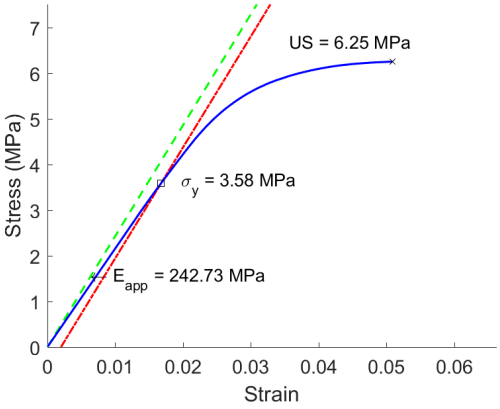

Figure B.21: Sample Number 270

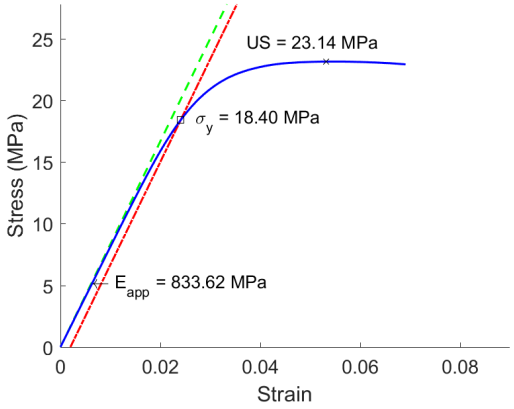

Figure B.22: Sample Number 332

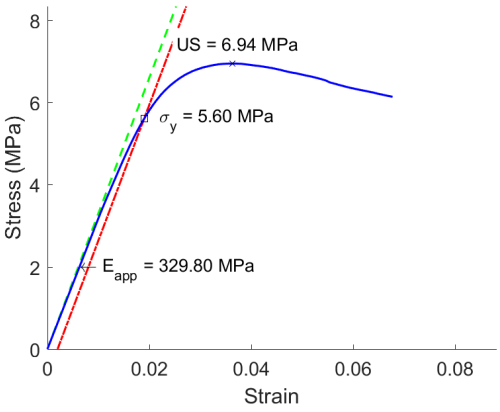

Figure B.23: Sample Number 384

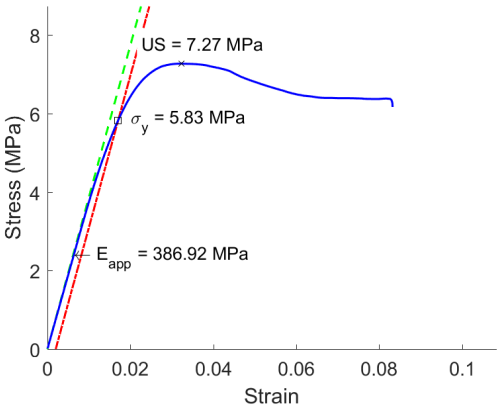

Figure B.24: Sample Number 424

B.3 Standard Specimens, 10^{-1} s^{-1}

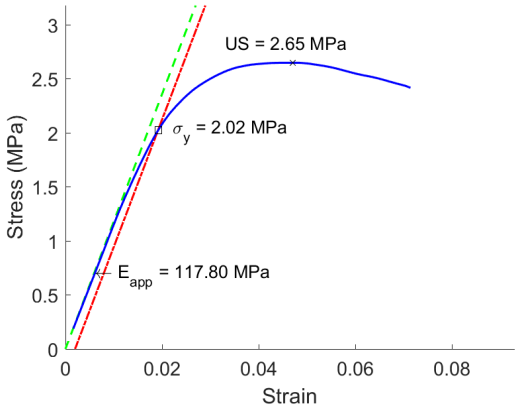

Figure B.25: Sample Number 119

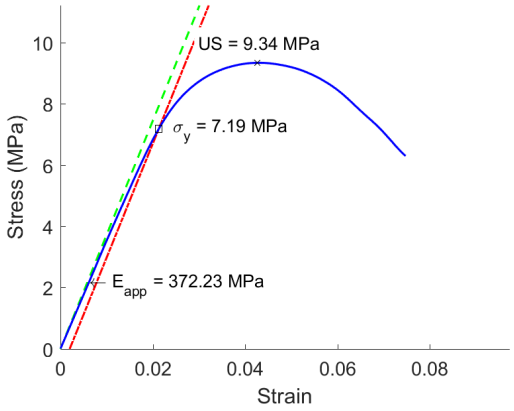

Figure B.26: Sample Number 171

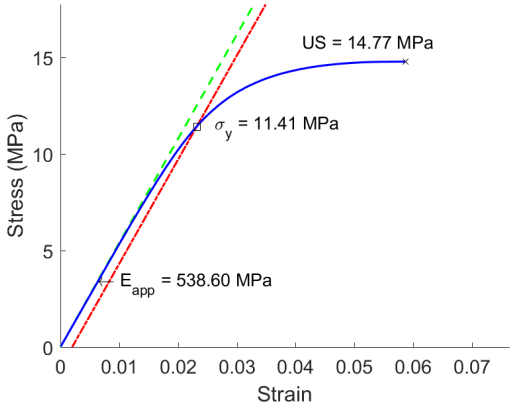

Figure B.27: Sample Number 247

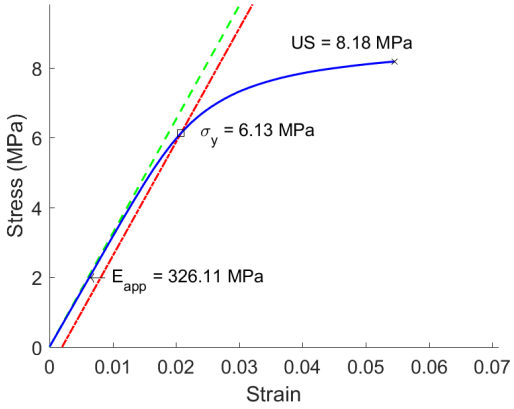

Figure B.28: Sample Number 248

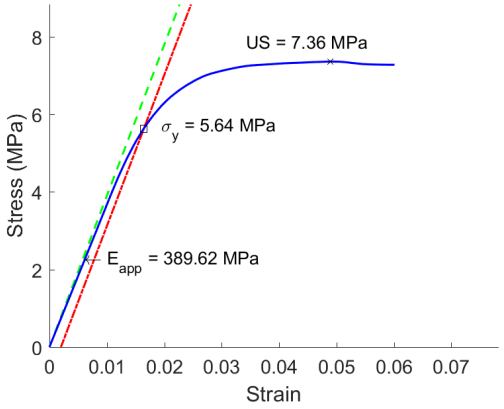

Figure B.29: Sample Number 309

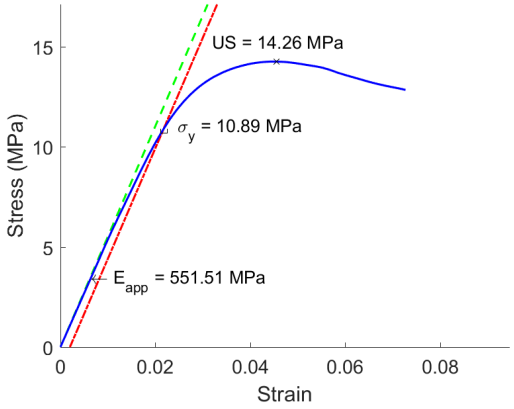

Figure B.30: Sample Number 410

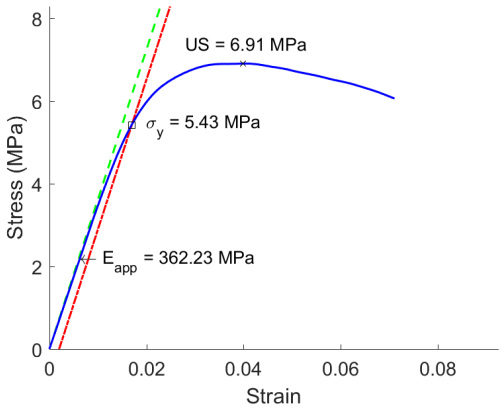

Figure B.31: Sample Number 427

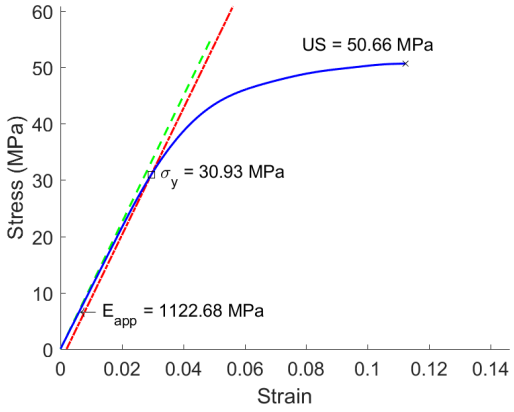

Figure B.32: Sample Number 461

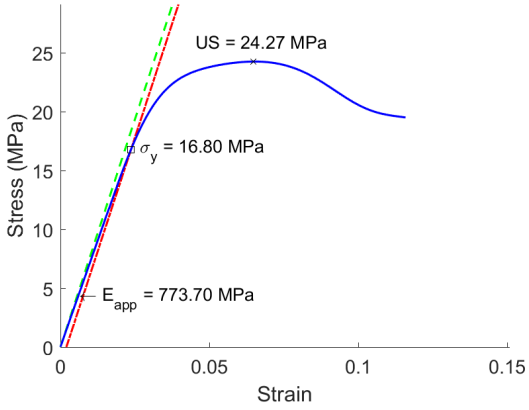

Figure B.33: Sample Number 462

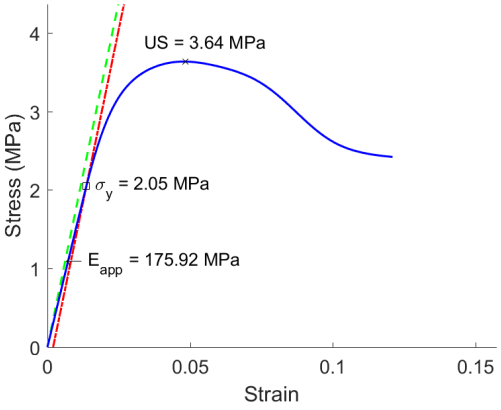

Figure B.34: Sample Number 464

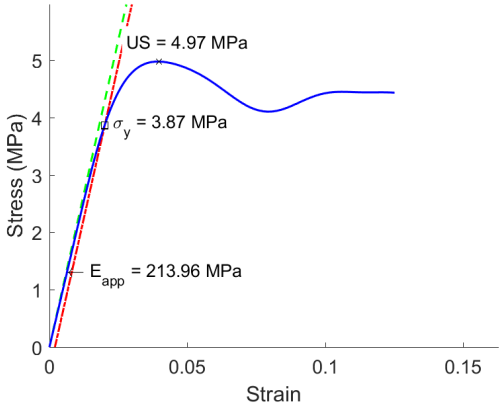

Figure B.35: Sample Number 465

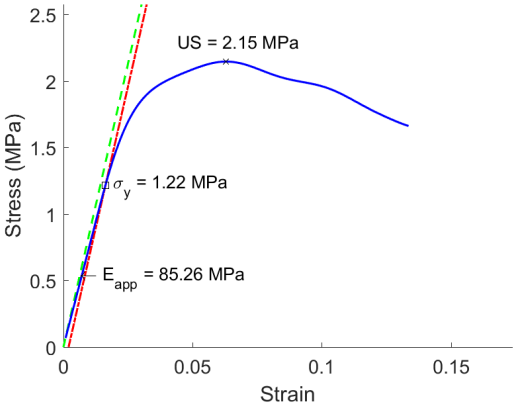

Figure B.36: Sample Number 466

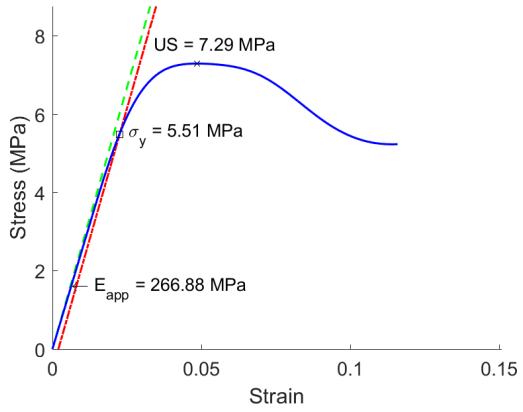

Figure B.37: Sample Number 467

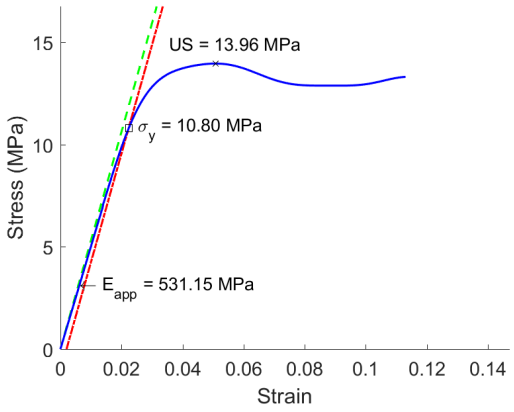

Figure B.38: Sample Number 469

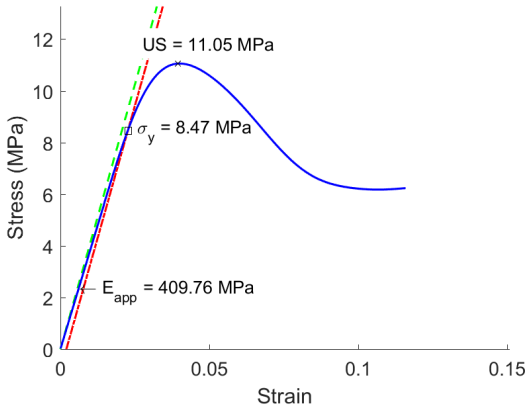

Figure B.39: Sample Number 493

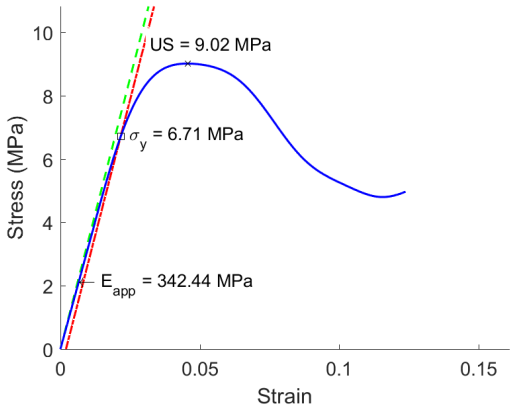

Figure B.40: Sample Number 494

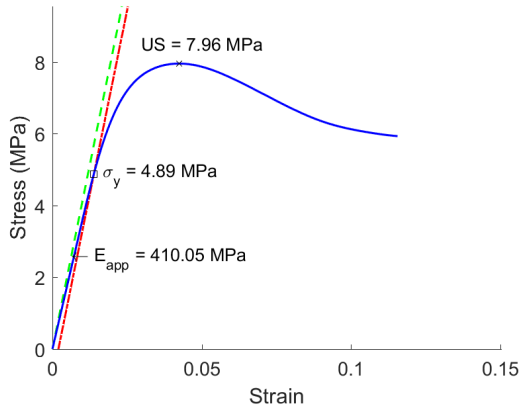

Figure B.41: Sample Number 496

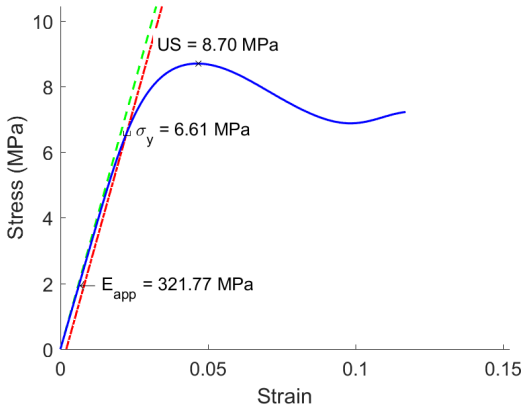

Figure B.42: Sample Number 502

B.4 Defatted Specimens, 10^{-3} s^{-1}

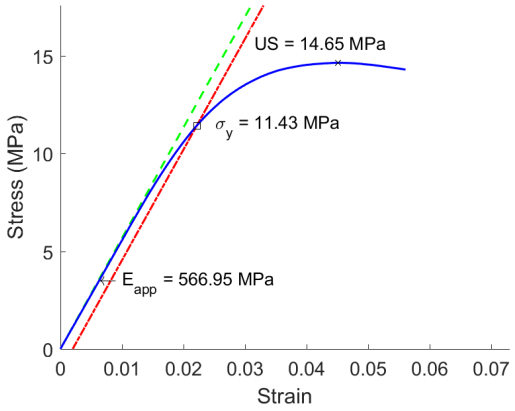

Figure B.43: Sample Number 13

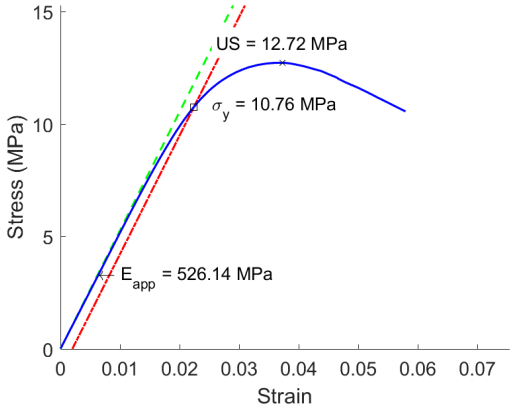

Figure B.44: Sample Number 131

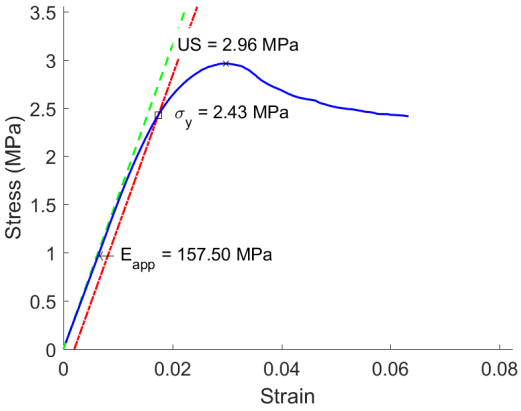

Figure B.45: Sample Number 135

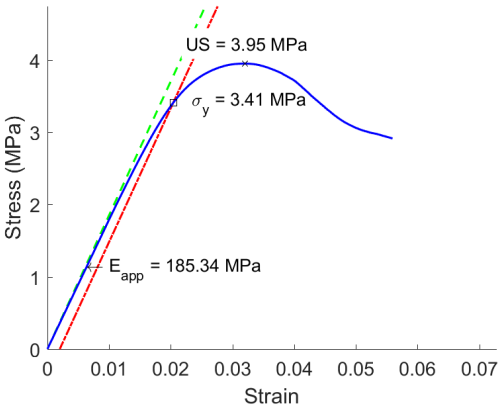

Figure B.46: Sample Number 138

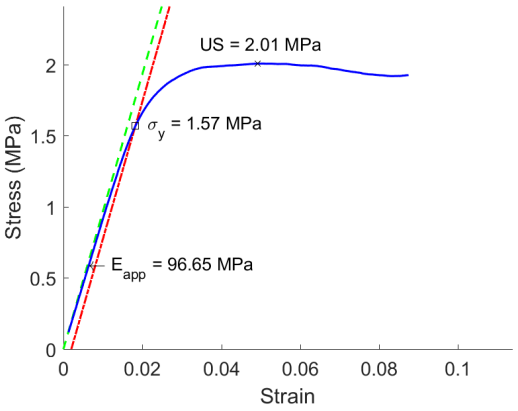

Figure B.47: Sample Number 165

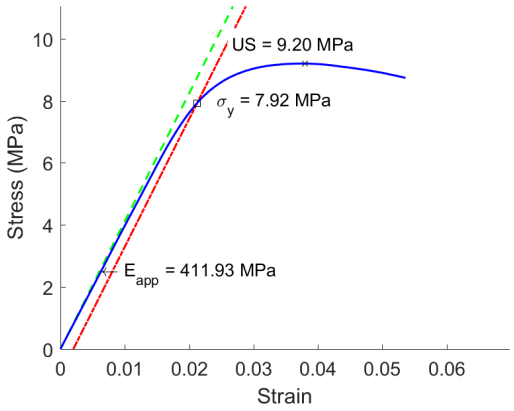

Figure B.48: Sample Number 229

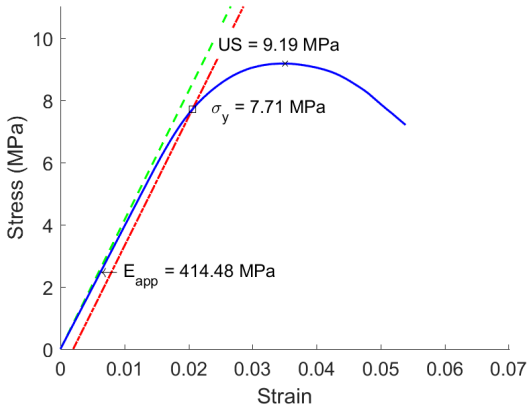

Figure B.49: Sample Number 314

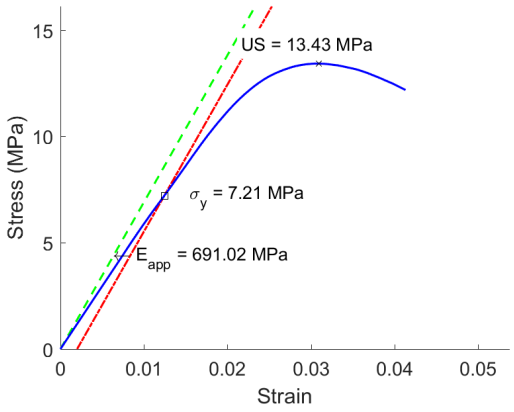

Figure B.50: Sample Number 404

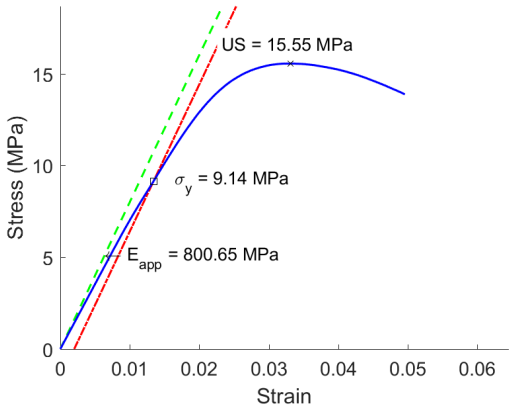

Figure B.51: Sample Number 433

B.5 Defatted Specimens, 10^{-2} s^{-1}

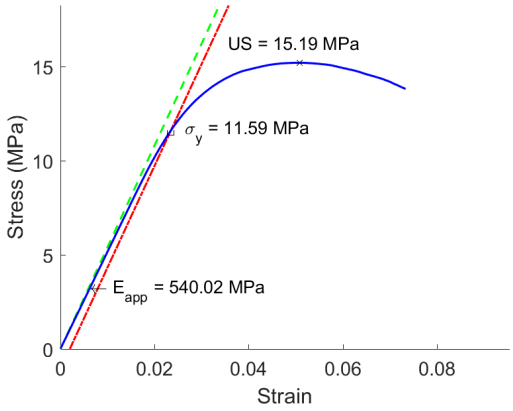

Figure B.52: Sample Number 17

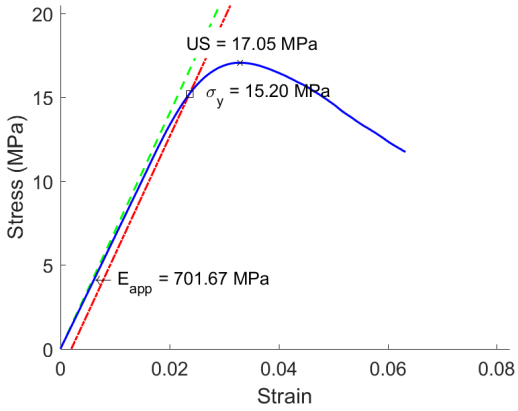

Figure B.53: Sample Number 79

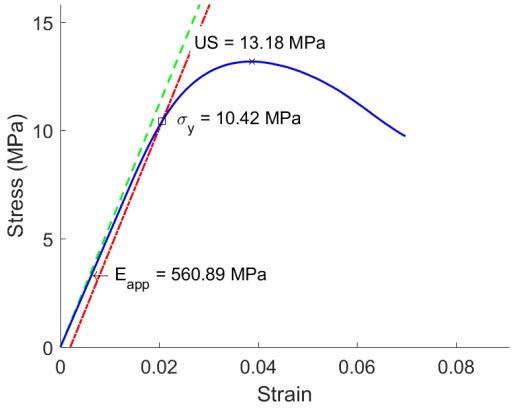

Figure B.54: Sample Number 114

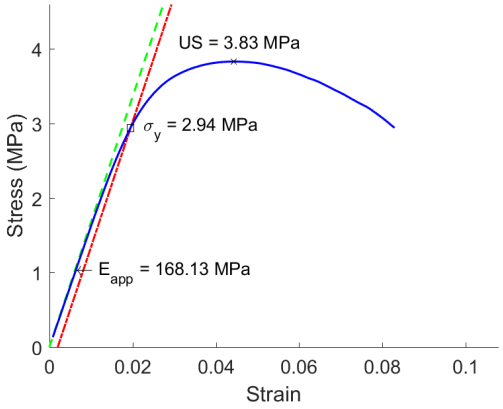

Figure B.55: Sample Number 198

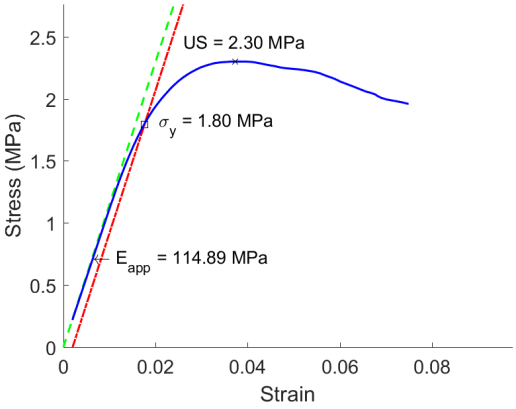

Figure B.56: Sample Number 208

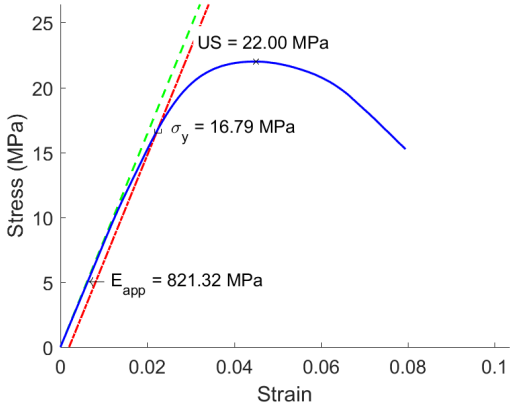

Figure B.57: Sample Number 255

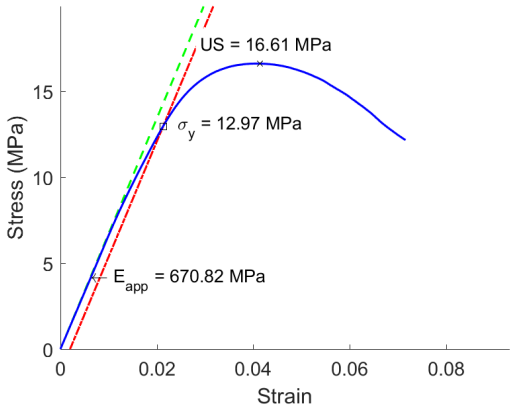

Figure B.58: Sample Number 277

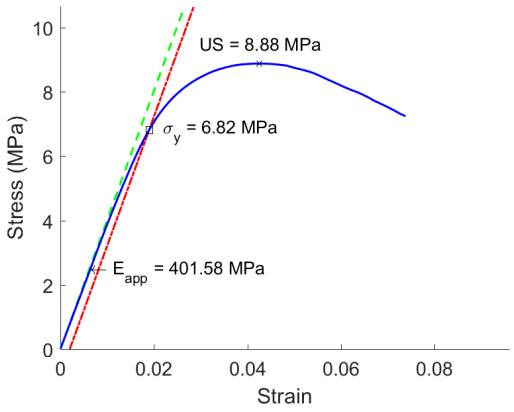

Figure B.59: Sample Number 326

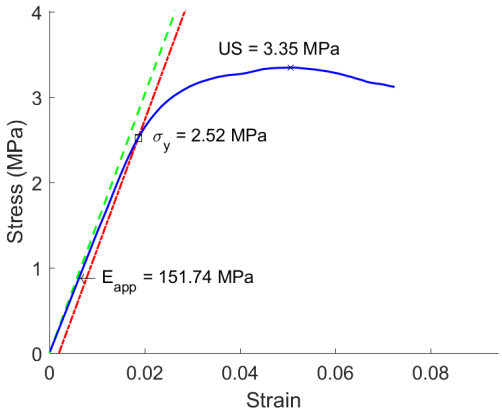

Figure B.60: Sample Number 366

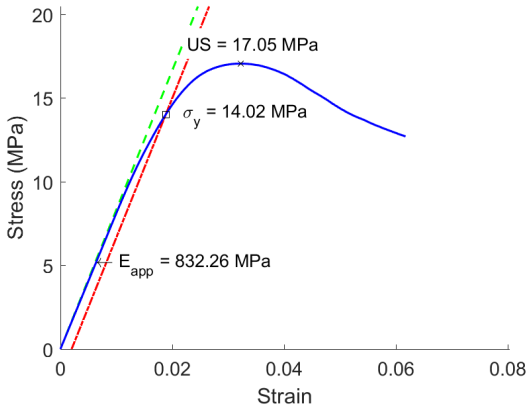

Figure B.61: Sample Number 438

B.6 Defatted Specimens, 10^{-1} s^{-1}

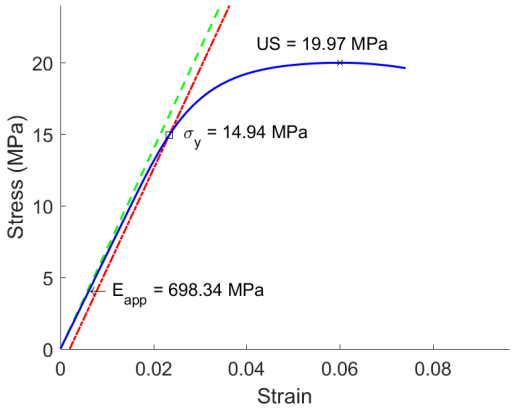

Figure B.62: Sample Number 15

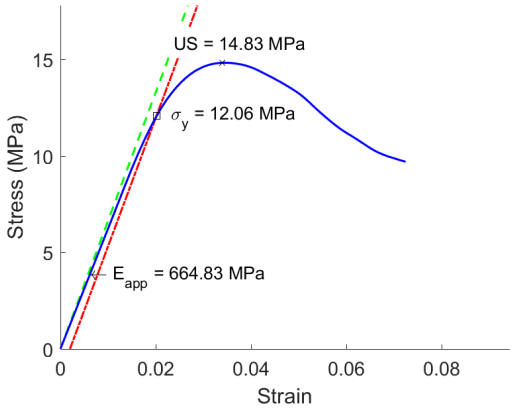

Figure B.63: Sample Number 25

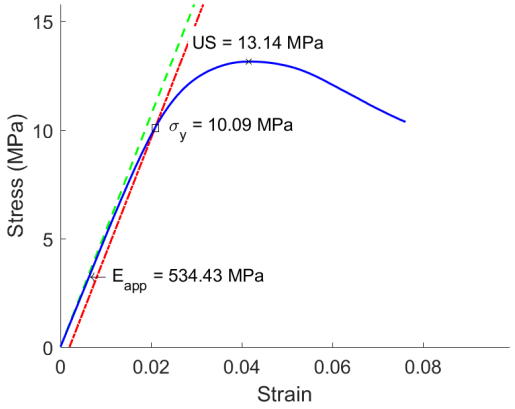

Figure B.64: Sample Number 94

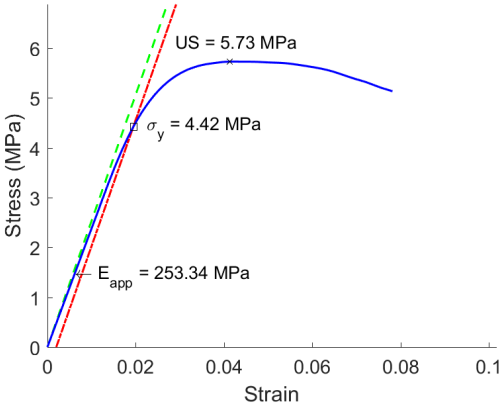

Figure B.65: Sample Number 129

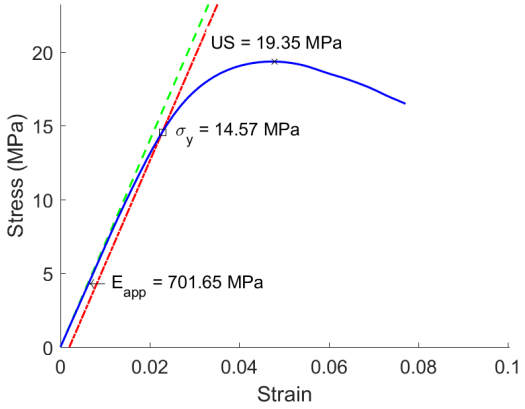

Figure B.66: Sample Number 152

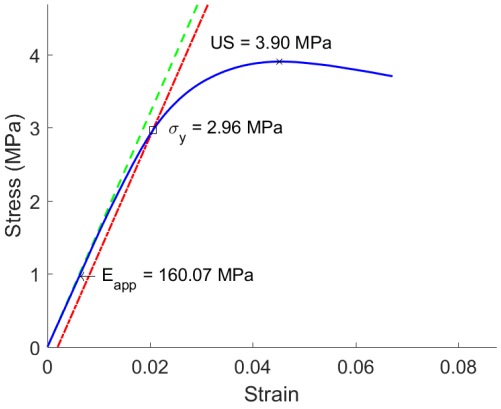

Figure B.67: Sample Number 163

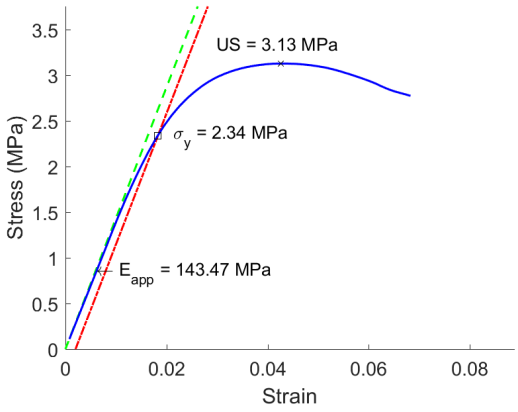

Figure B.68: Sample Number 184

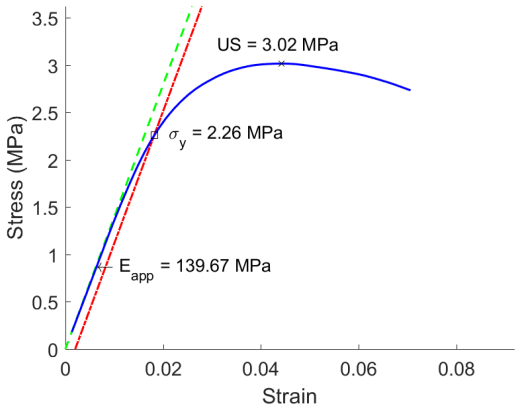

Figure B.69: Sample Number 204

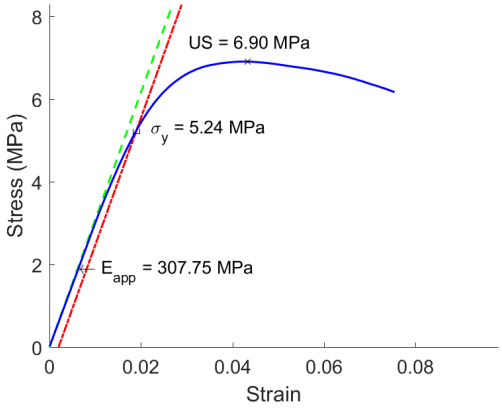

Figure B.70: Sample Number 273

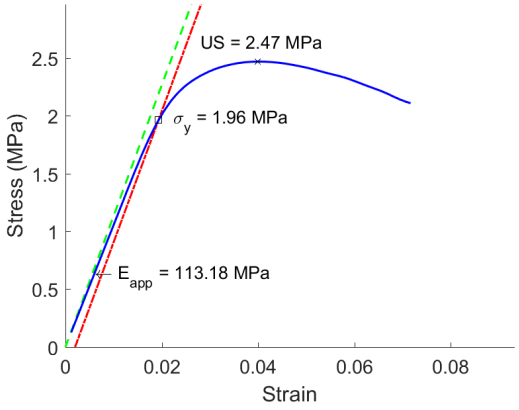

Figure B.71: Sample Number 274

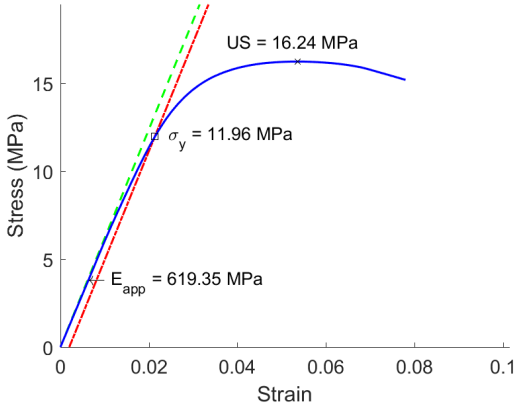

Figure B.72: Sample Number 371

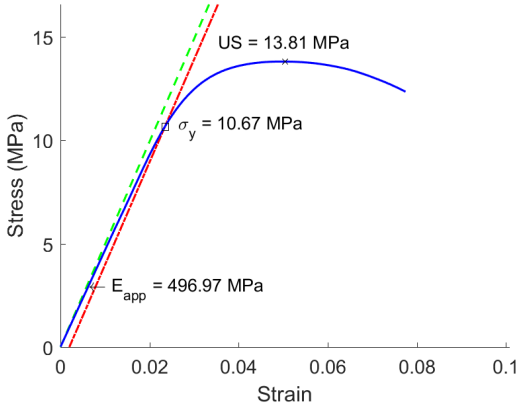

Figure B.73: Sample Number 390

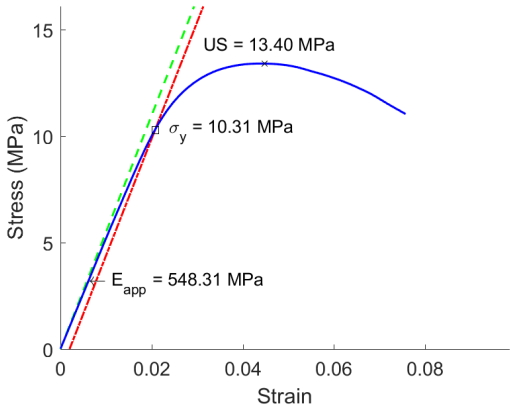

Figure B.74: Sample Number 400

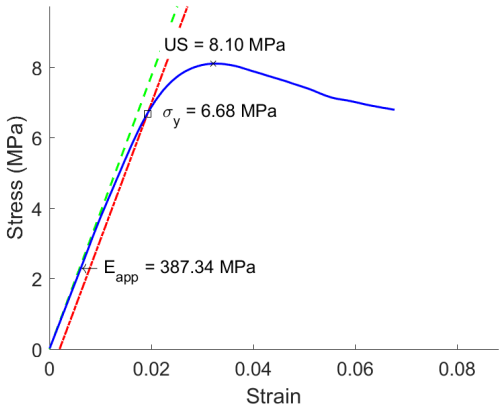

Figure B.75: Sample Number 439

B.7 Confined Specimens, 10^{-3} s^{-1}

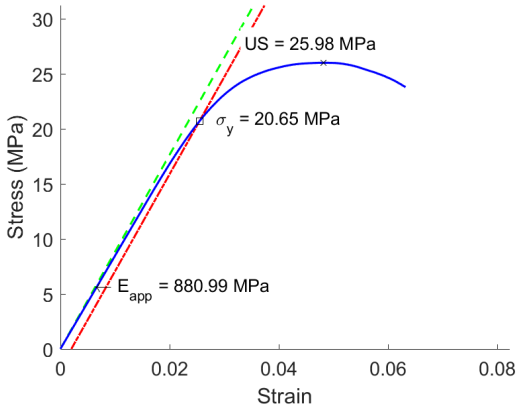

Figure B.76: Sample Number 77

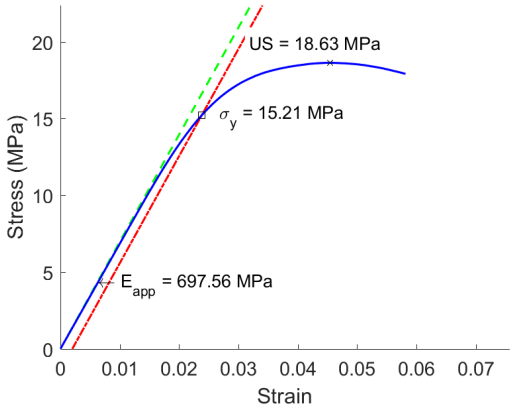

Figure B.77: Sample Number 90

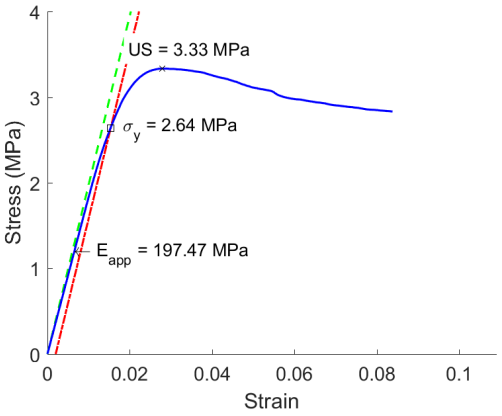

Figure B.78: Sample Number 150

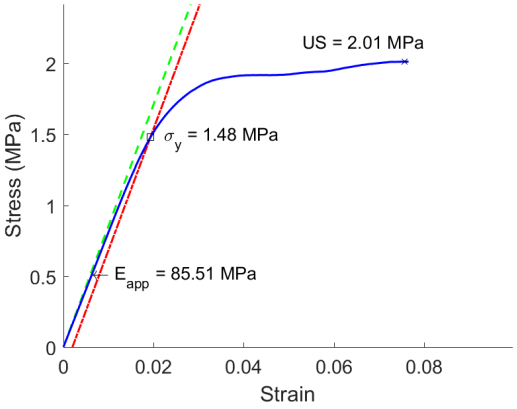

Figure B.79: Sample Number 161

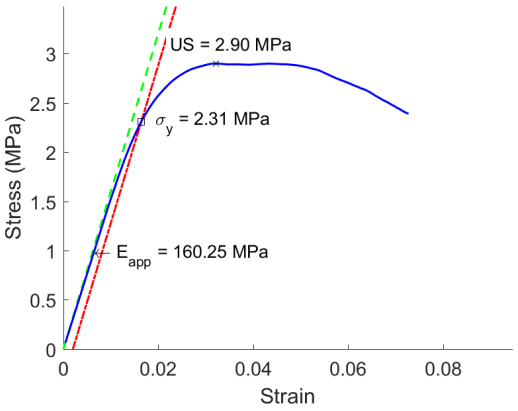

Figure B.80: Sample Number 214

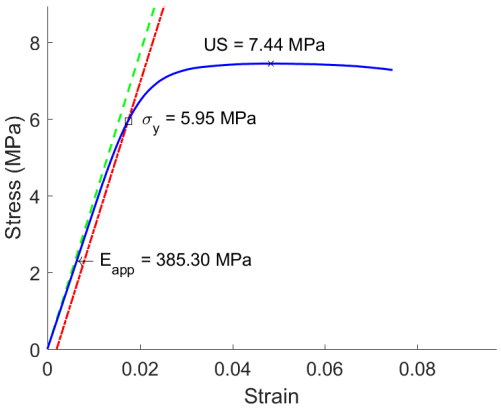

Figure B.81: Sample Number 264

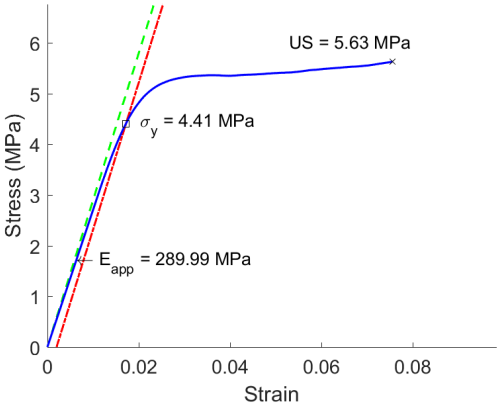

Figure B.82: Sample Number 299

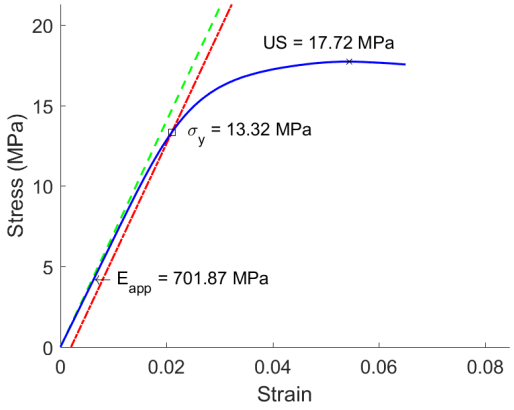

Figure B.83: Sample Number 324

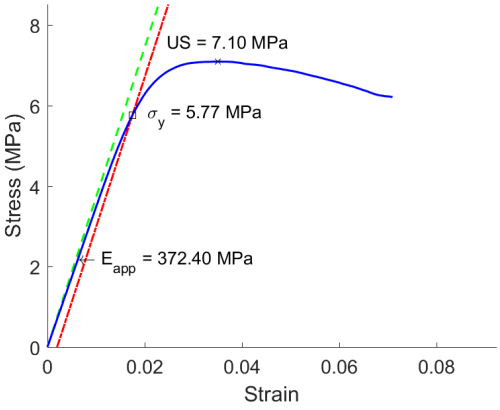

Figure B.84: Sample Number 361

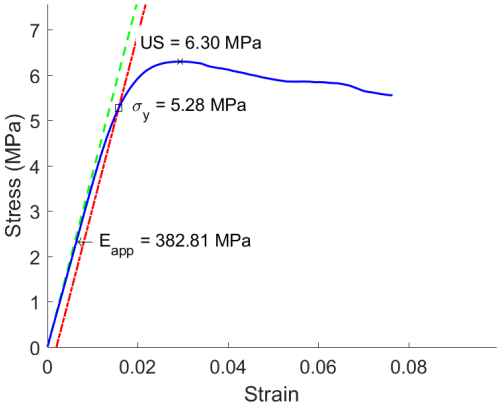

Figure B.85: Sample Number 434

B.8 Confined Specimens, 10^{-2} s^{-1}

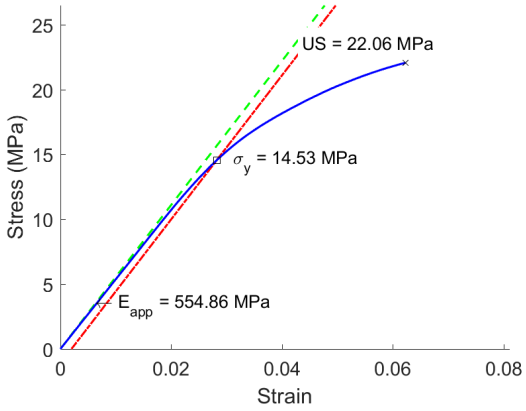

Figure B.86: Sample Number 19

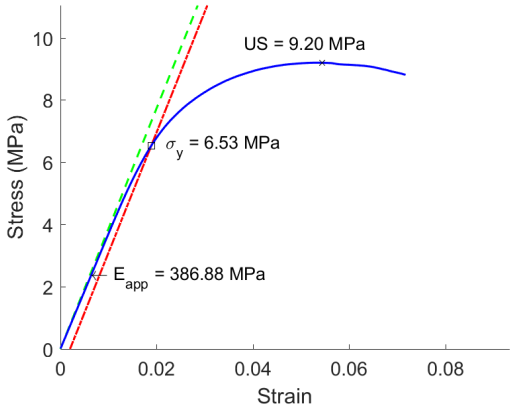

Figure B.87: Sample Number 31

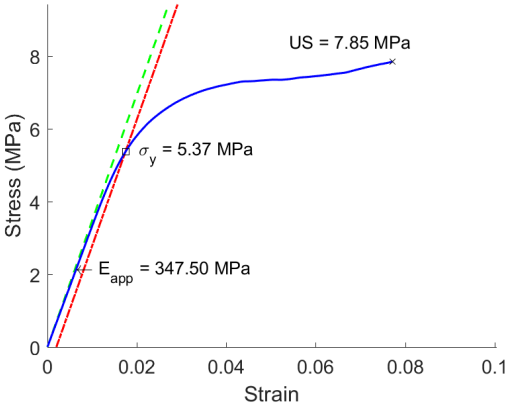

Figure B.88: Sample Number 33

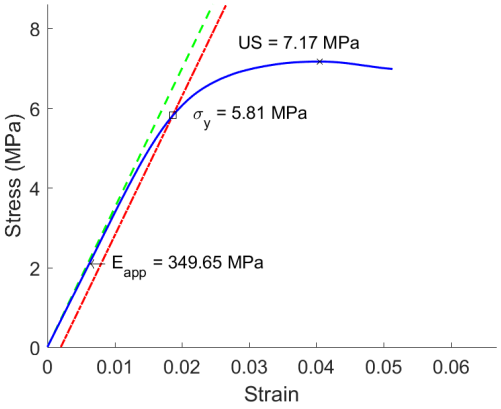

Figure B.89: Sample Number 137

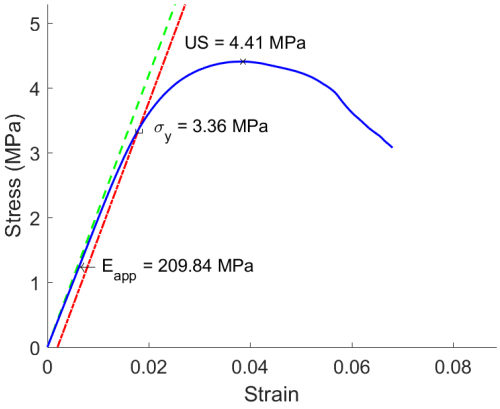

Figure B.90: Sample Number 182

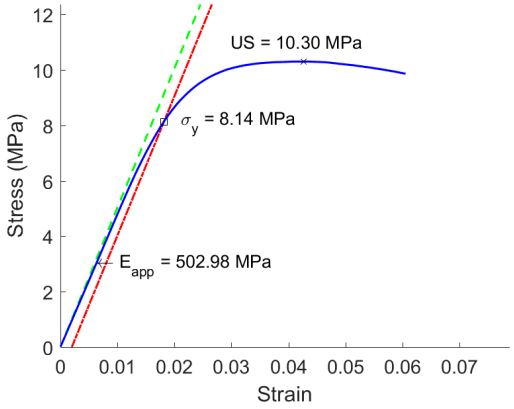

Figure B.91: Sample Number 205

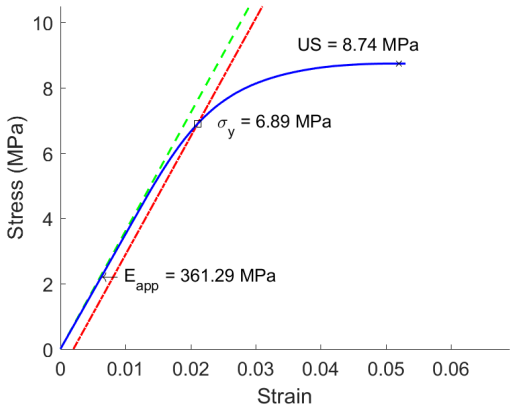

Figure B.92: Sample Number 285

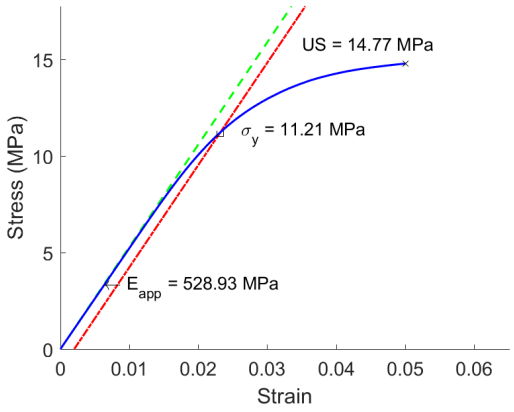

Figure B.93: Sample Number 358

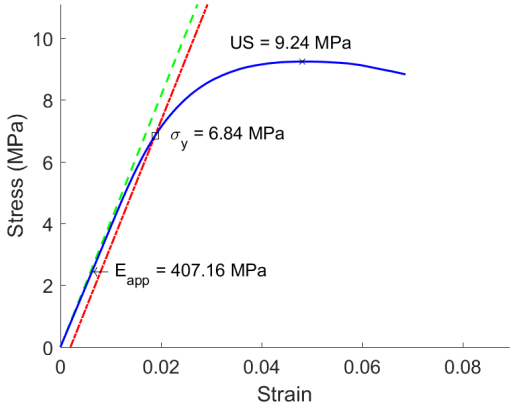

Figure B.94: Sample Number 379

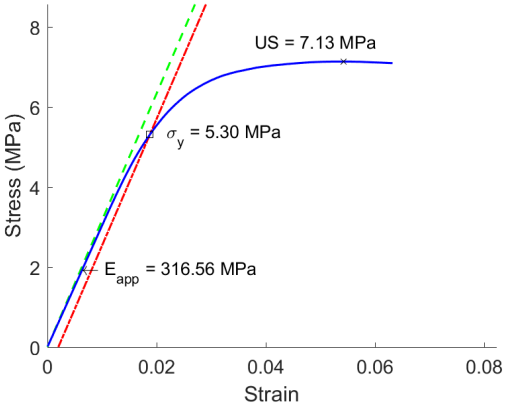

Figure B.95: Sample Number 399

B.9 Confined Specimens, 10^{-1} s^{-1}

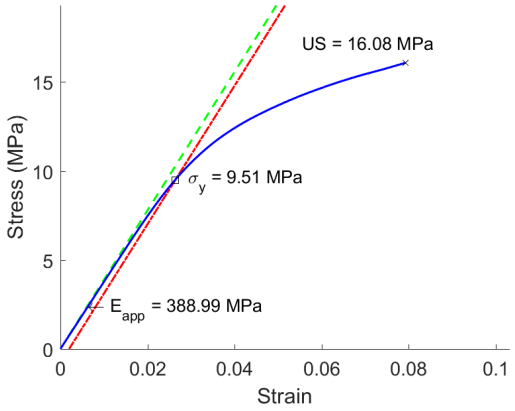

Figure B.96: Sample Number 38

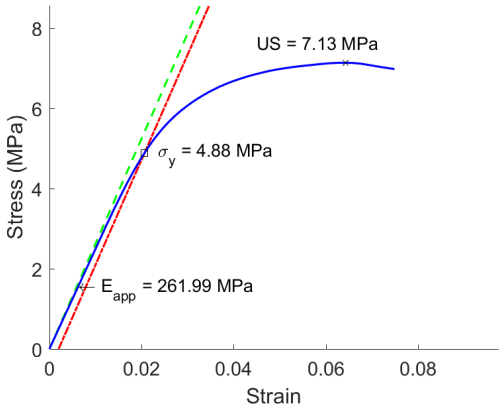

Figure B.97: Sample Number 59

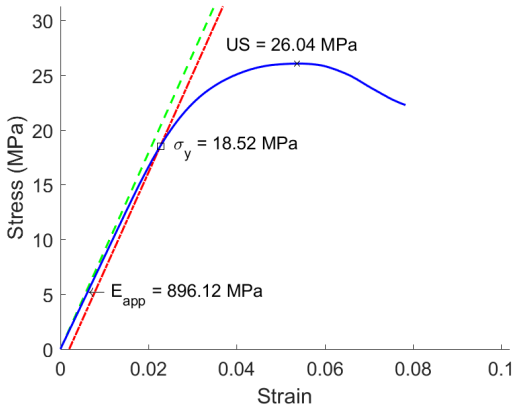

Figure B.98: Sample Number 82

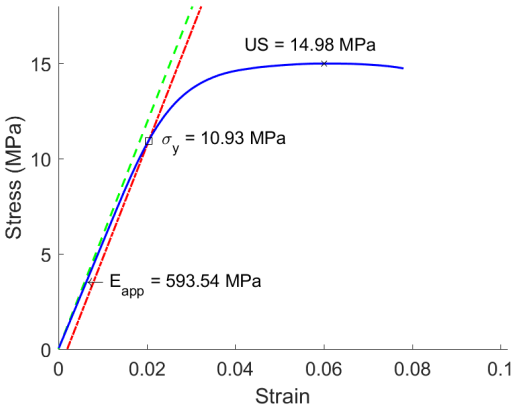

Figure B.99: Sample Number 97

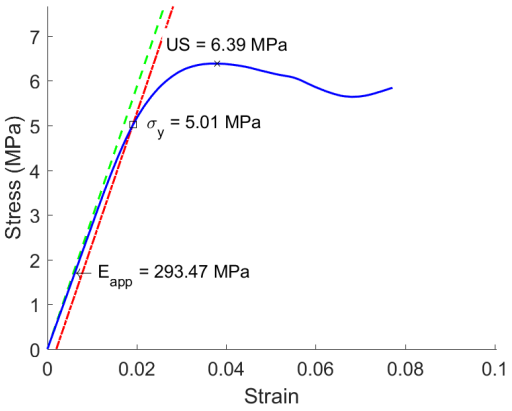

Figure B.100: Sample Number 140

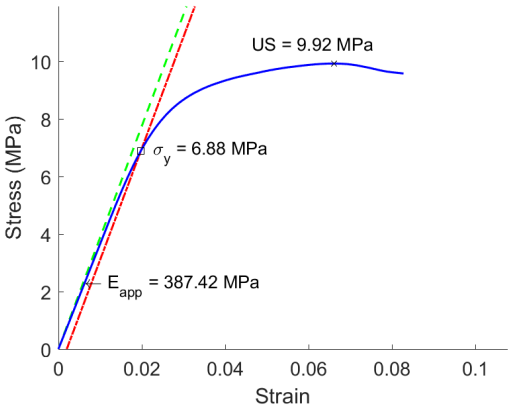

Figure B.101: Sample Number 177

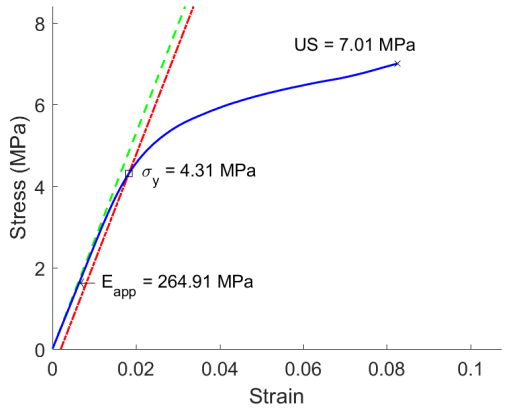

Figure B.102: Sample Number 260

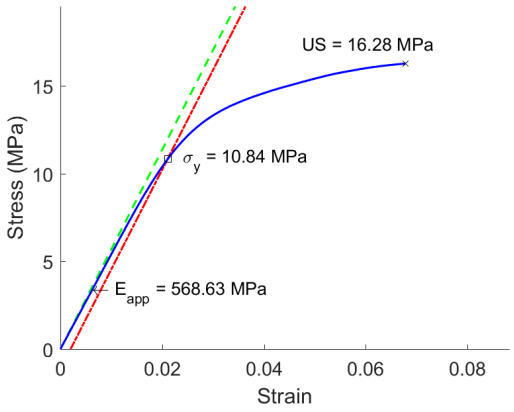

Figure B.103: Sample Number 261

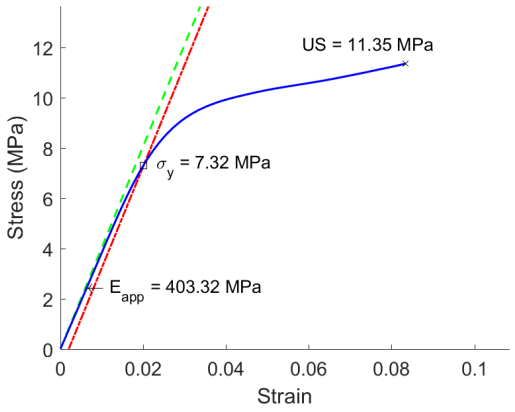

Figure B.104: Sample Number 283

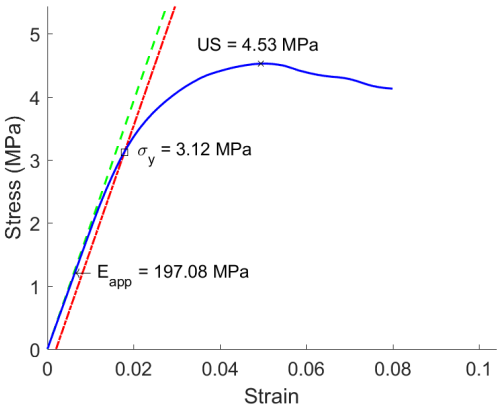

Figure B.105: Sample Number 345

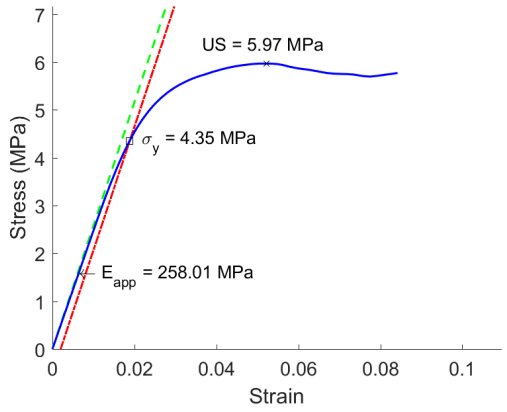

Figure B.106: Sample Number 365

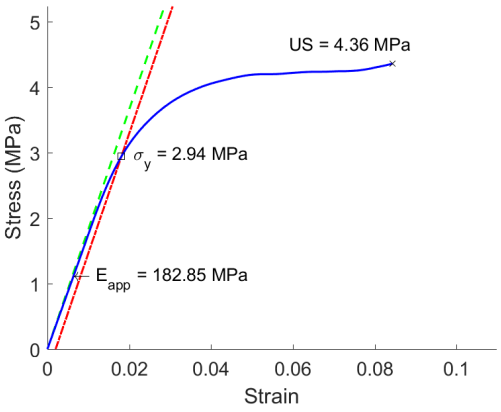

Figure B.107: Sample Number 385

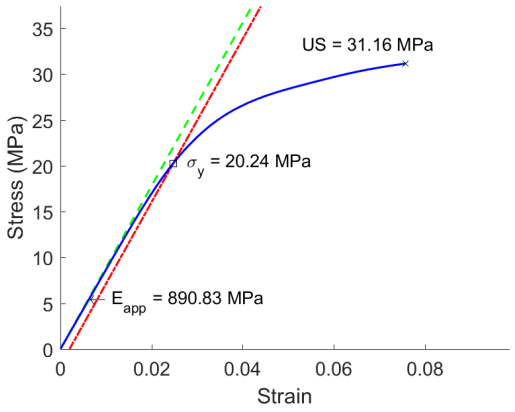

Figure B.108: Sample Number 394

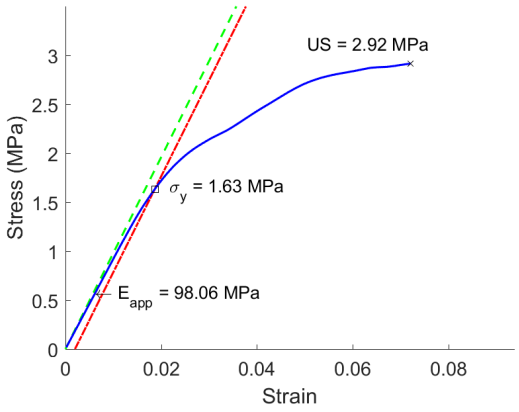

Figure B.109: Sample Number 435

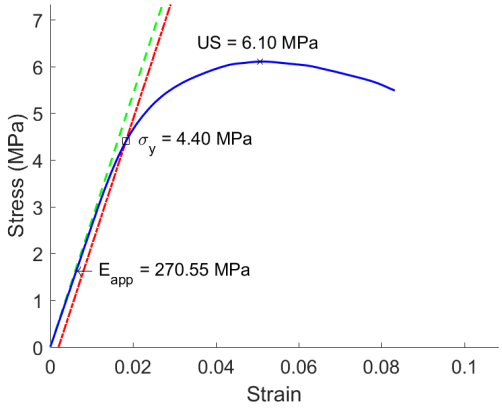

Figure B.110: Sample Number 440

B.10 20mm Bone Confined Specimens, 10^{-3} s^{-1}

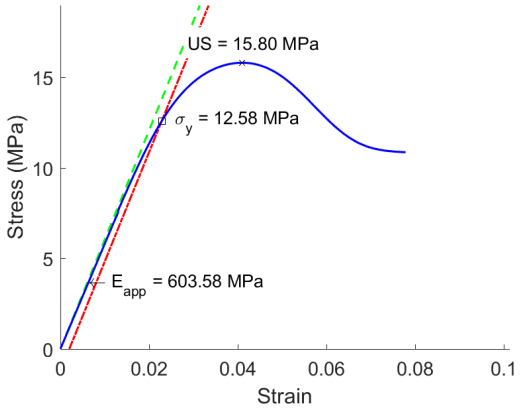

Figure B.111: Sample Number 498

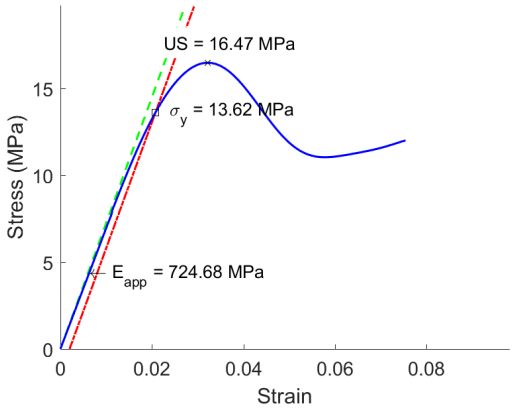

Figure B.112: Sample Number 503

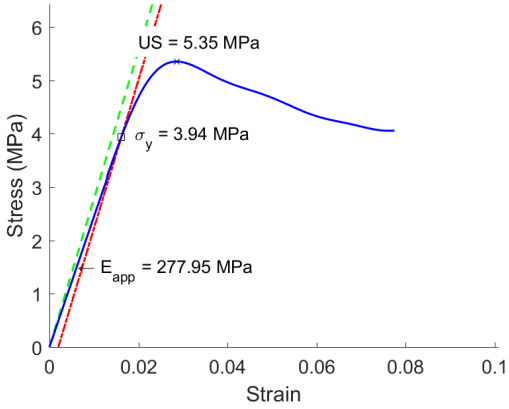

Figure B.113: Sample Number 504

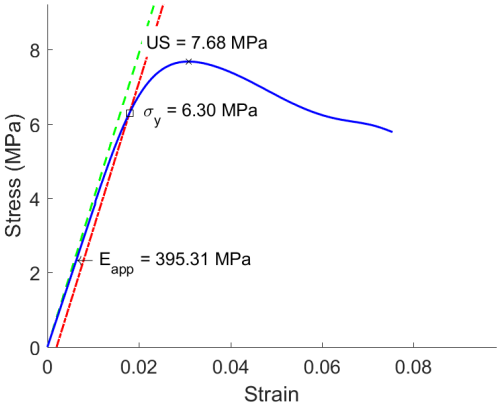

Figure B.114: Sample Number 506

B.11 20mm Bone Confined Specimens, 10^{-1} s^{-1}

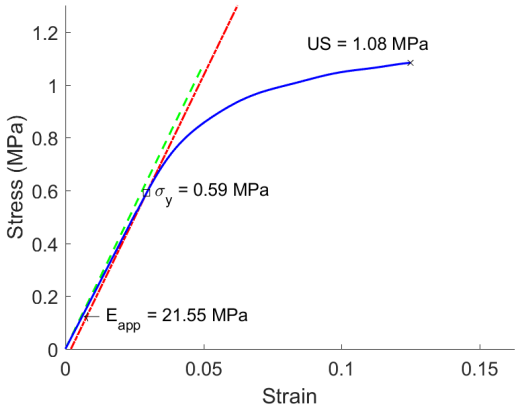

Figure B.115: Sample Number 508

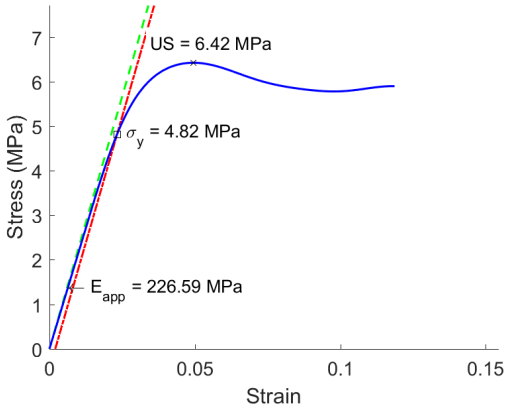

Figure B.116: Sample Number 510

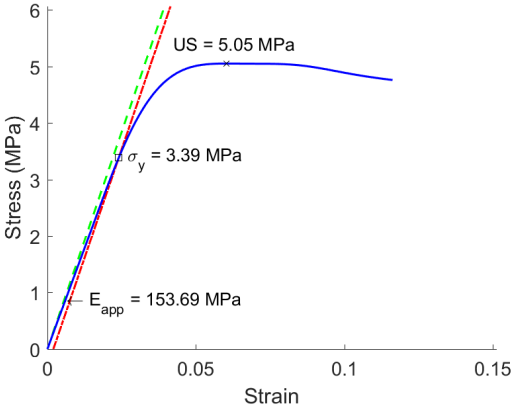

Figure B.117: Sample Number 512

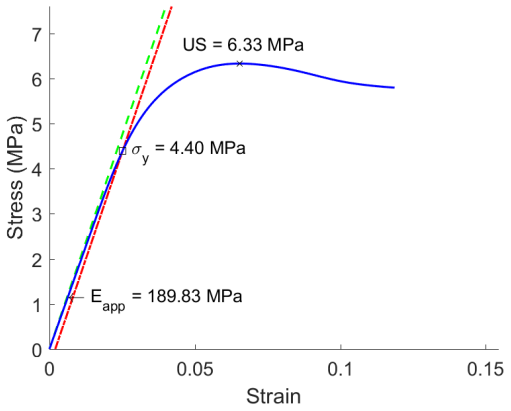

Figure B.118: Sample Number 513

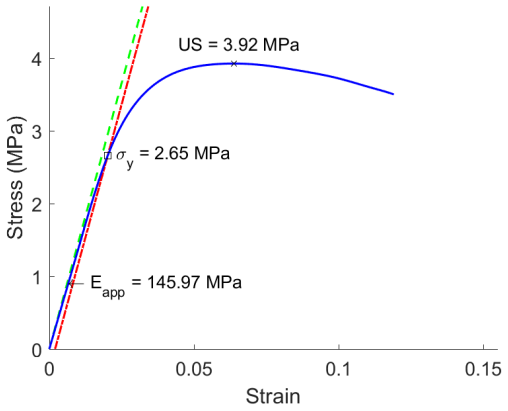

Figure B.119: Sample Number 514

B.12 28mm Bone Confined Specimens, 10^{-3} s^{-1}

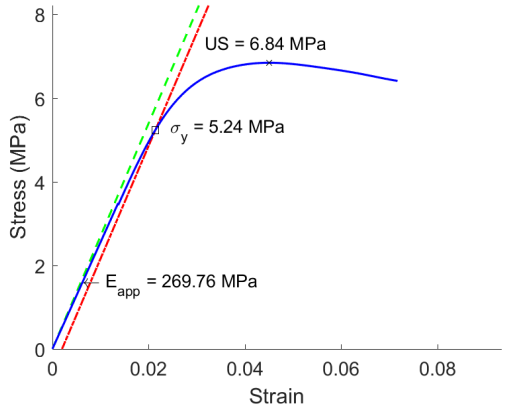

Figure B.120: Sample Number 529

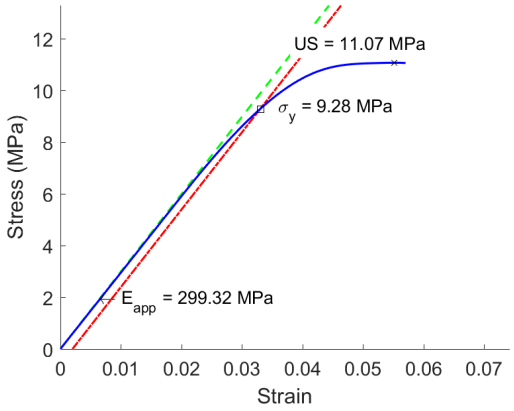

Figure B.121: Sample Number 530

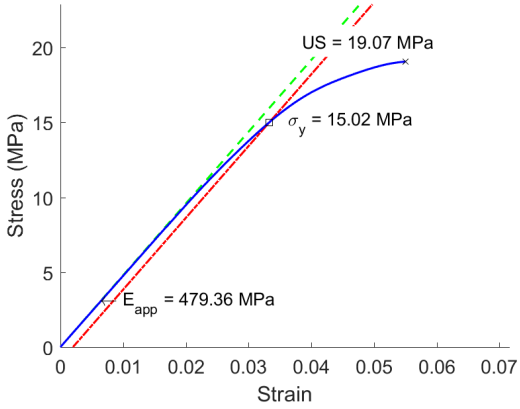

Figure B.122: Sample Number 532

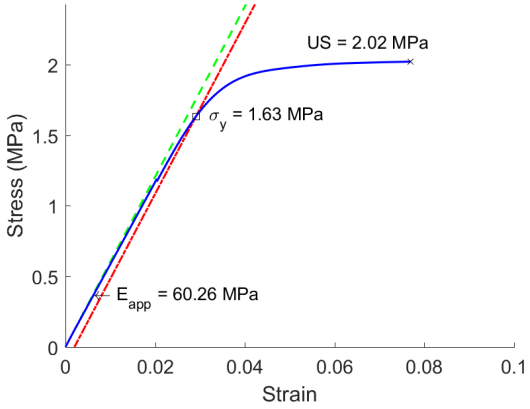

Figure B.123: Sample Number 533

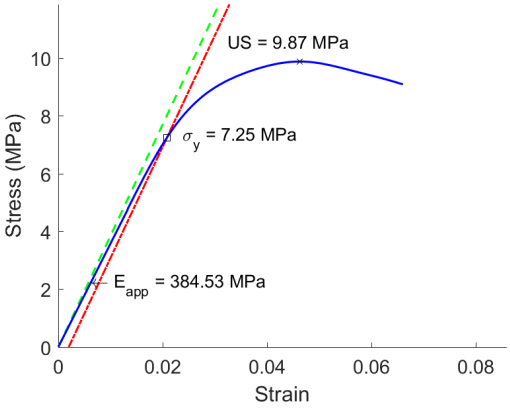

Figure B.124: Sample Number 534

B.13 28mm Bone Confined Specimens, 10^{-1} s^{-1}

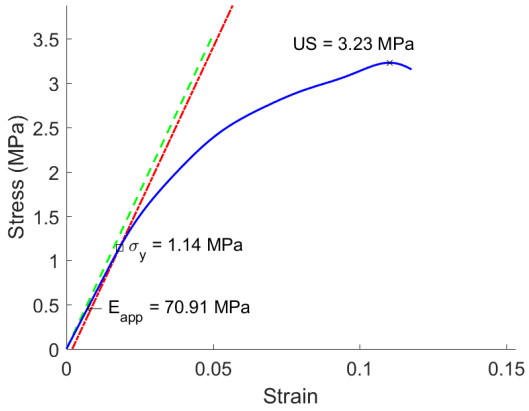

Figure B.125: Sample Number 535

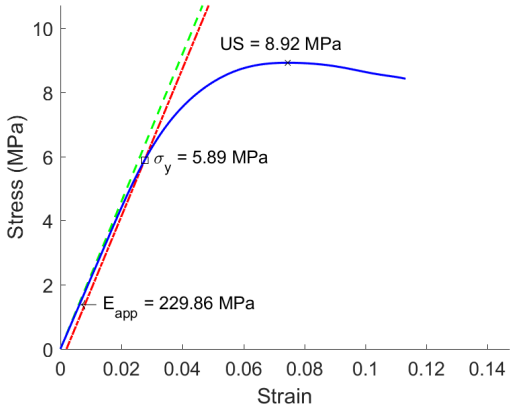

Figure B.126: Sample Number 537

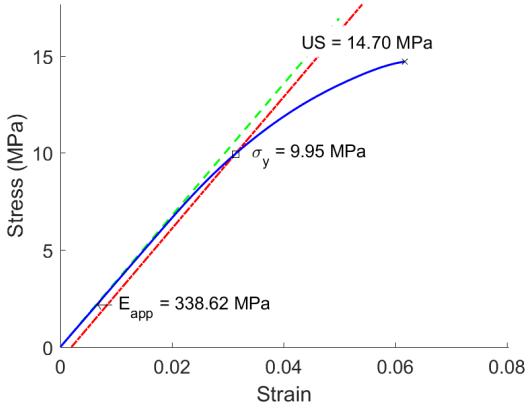

Figure B.127: Sample Number 538

B.14 Bone Confined Inner 10 mm versus Whole Specimen

B.14.1 20mm Specimens, 10^{-3} s^{-1}

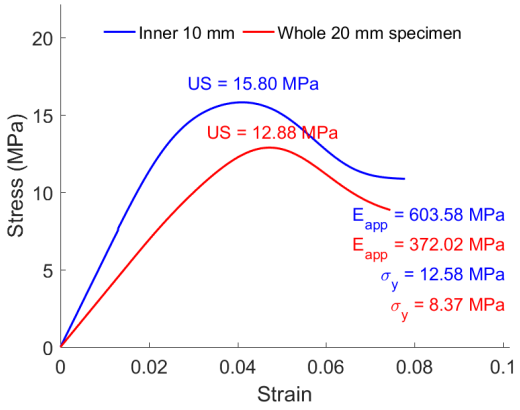

Figure B.128: Sample Number 498

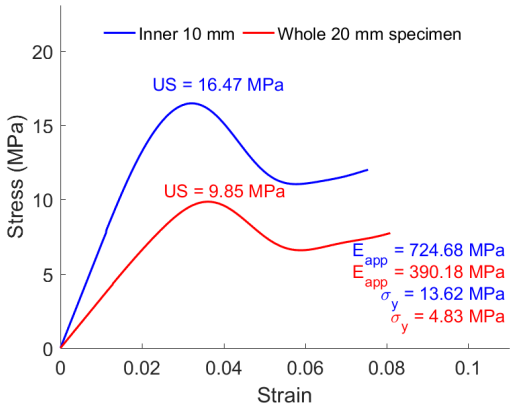

Figure B.129: Sample Number 503

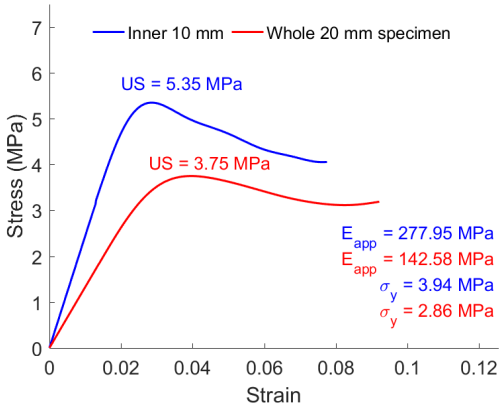

Figure B.130: Sample Number 504

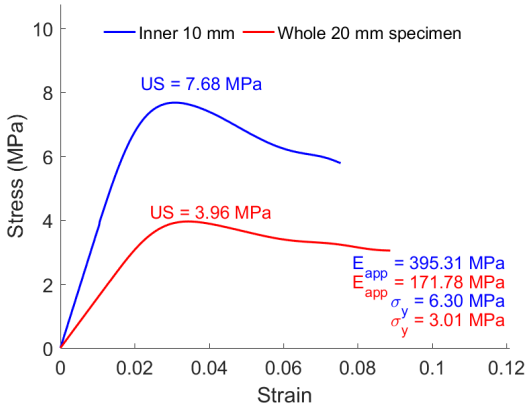

Figure B.131: Sample Number 506

B.14.2 20mm Specimens, 10^{-1} s^{-1}

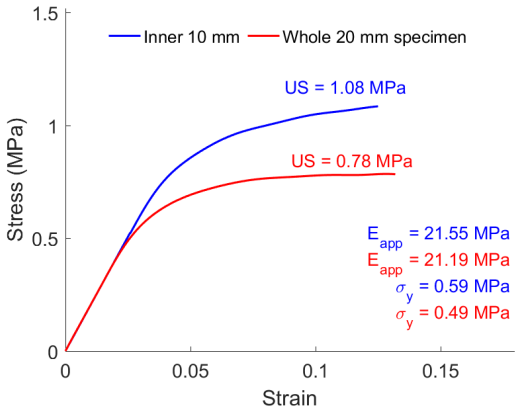

Figure B.132: Sample Number 508

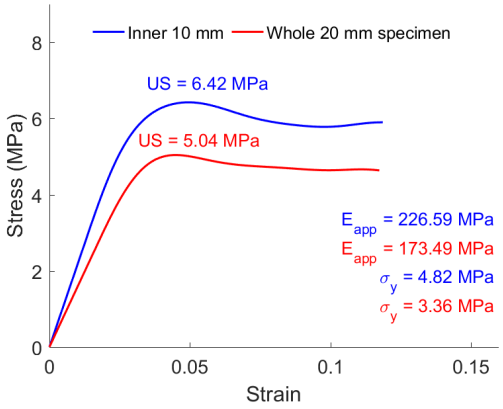

Figure B.133: Sample Number 510

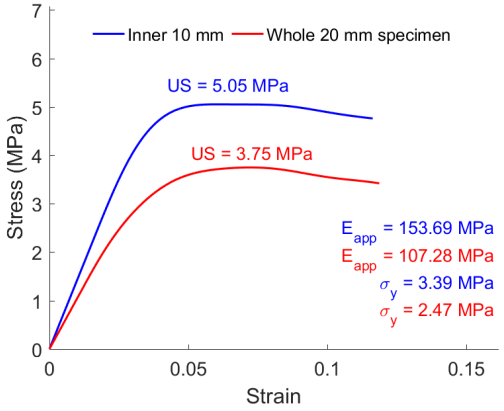

Figure B.134: Sample Number 512

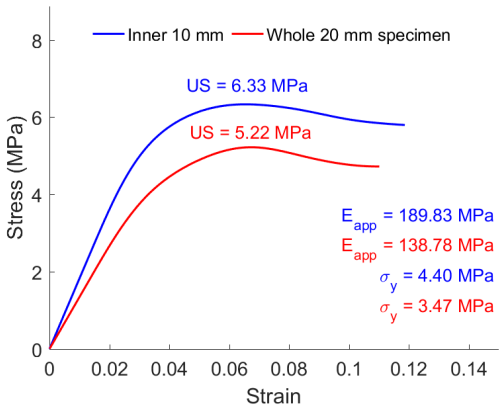

Figure B.135: Sample Number 513

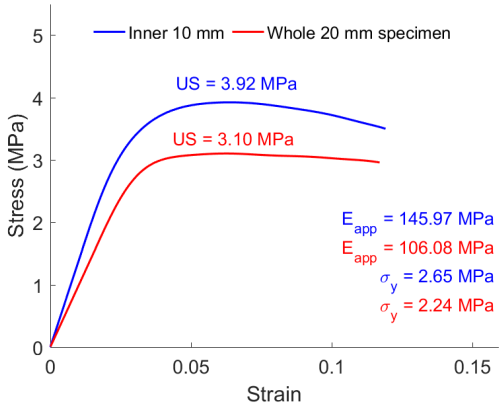

Figure B.136: Sample Number 514

B.14.3 28mm Specimens, 10^{-3} s^{-1}

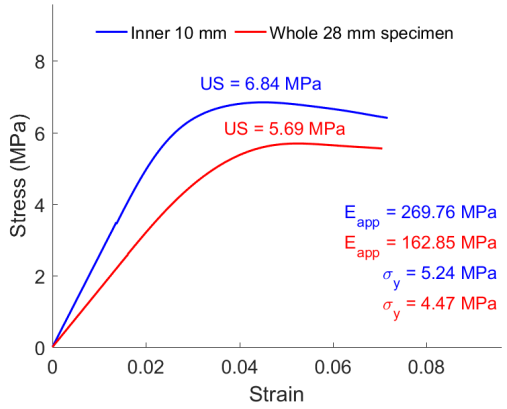

Figure B.137: Sample Number 529

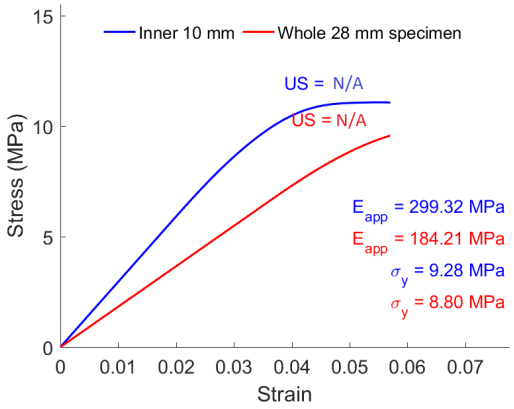

Figure B.138: Sample Number 530

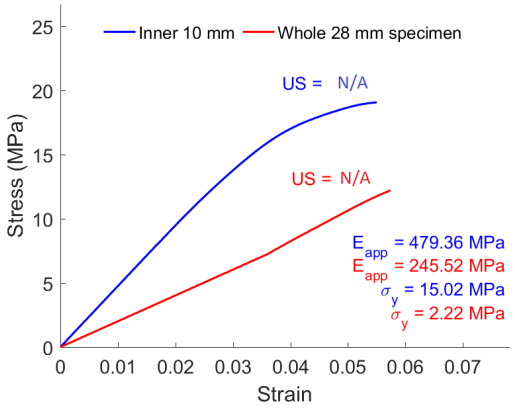

Figure B.139: Sample Number 532

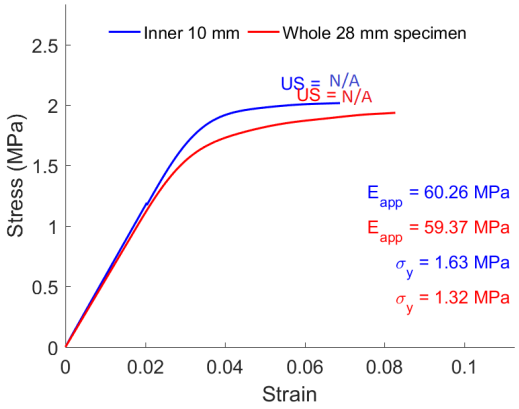

Figure B.140: Sample Number 533

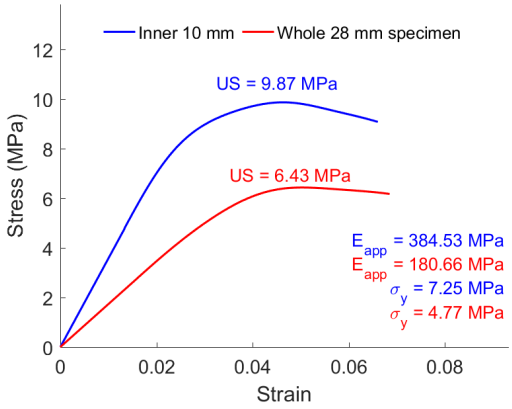

Figure B.141: Sample Number 534

B.14.4 28mm Specimens, 10^{-1} s^{-1}

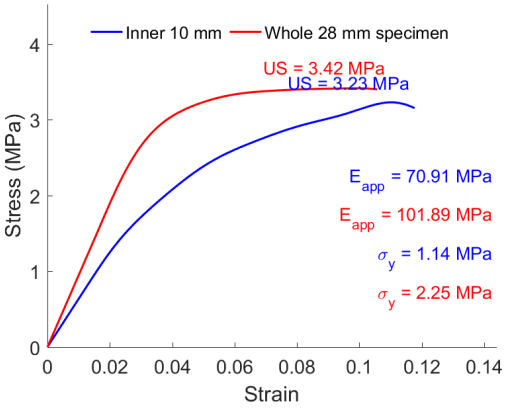

Figure B.142: Sample Number 535

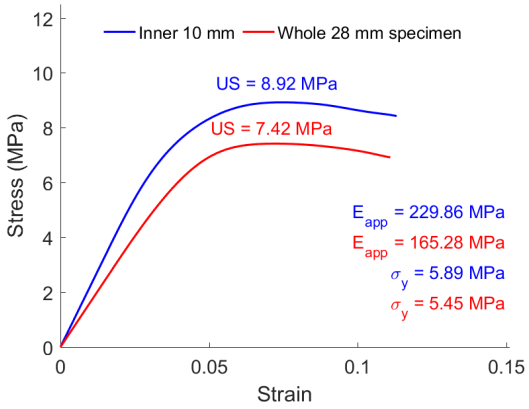

Figure B.143: Sample Number 537

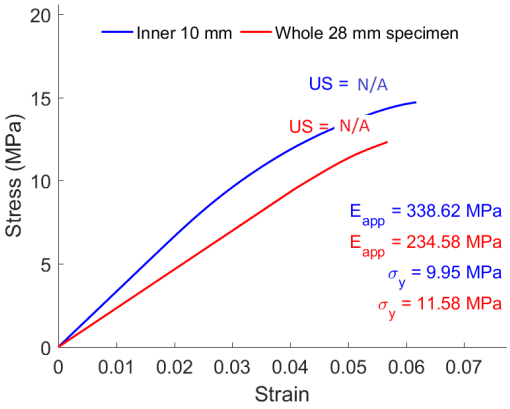

Figure B.144: Sample Number 538

B.15 Influence of Architectural Parameters

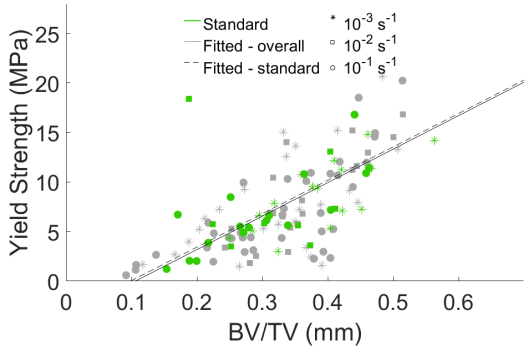

(a) Standard

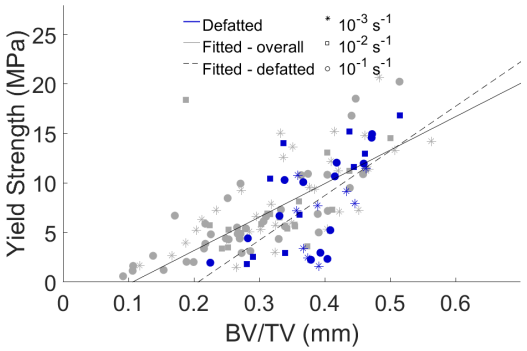

(b) Defatted

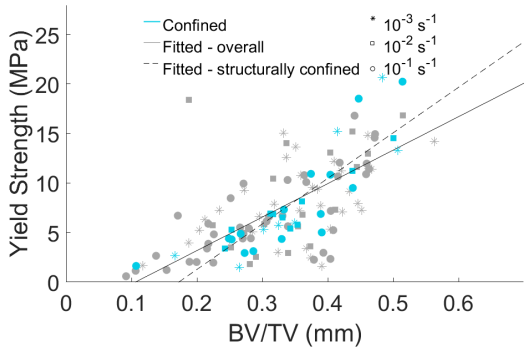

(c) Structurally Confined

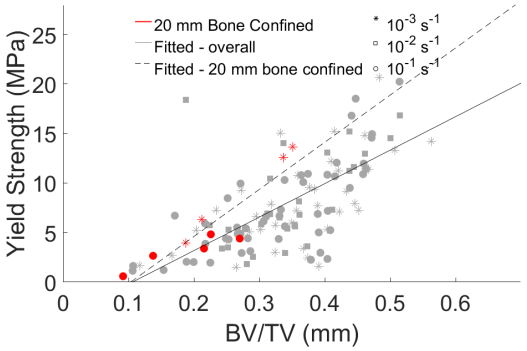

(d) 20 mm Bone Confined

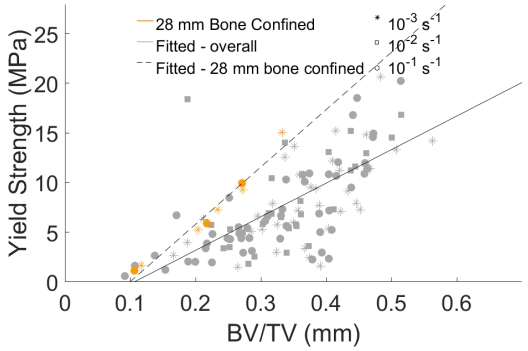

(e) 28 mm Bone Confined

Figure B.145: Graphs showing Yield Strength versus BV/TV for each specimen condition

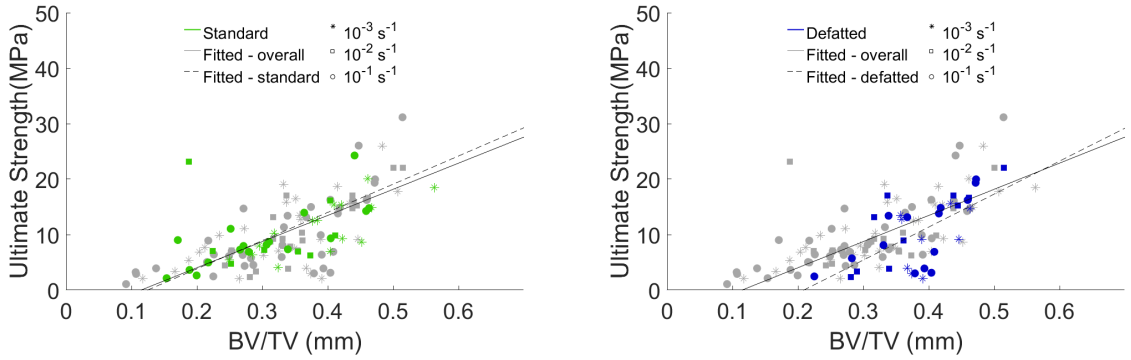

(a) Standard

(b) Defatted

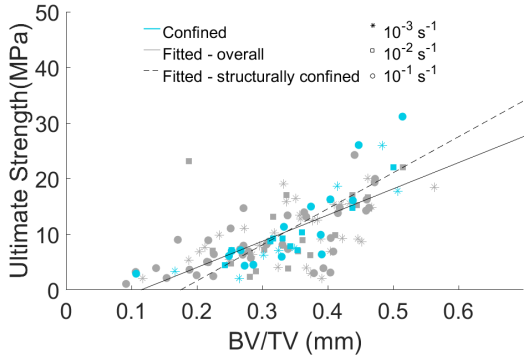

(c) Structurally Confined

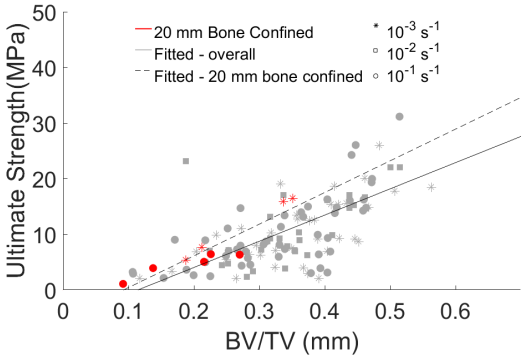

(d) 20 mm Bone Confined

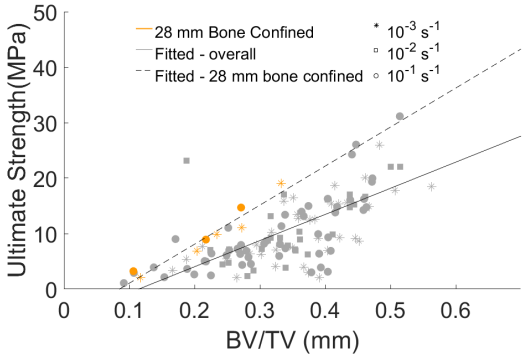

(e) 28 mm Bone Confined

Figure B.146: Graphs showing Ultimate Strength versus BV/TV for each specimen condition

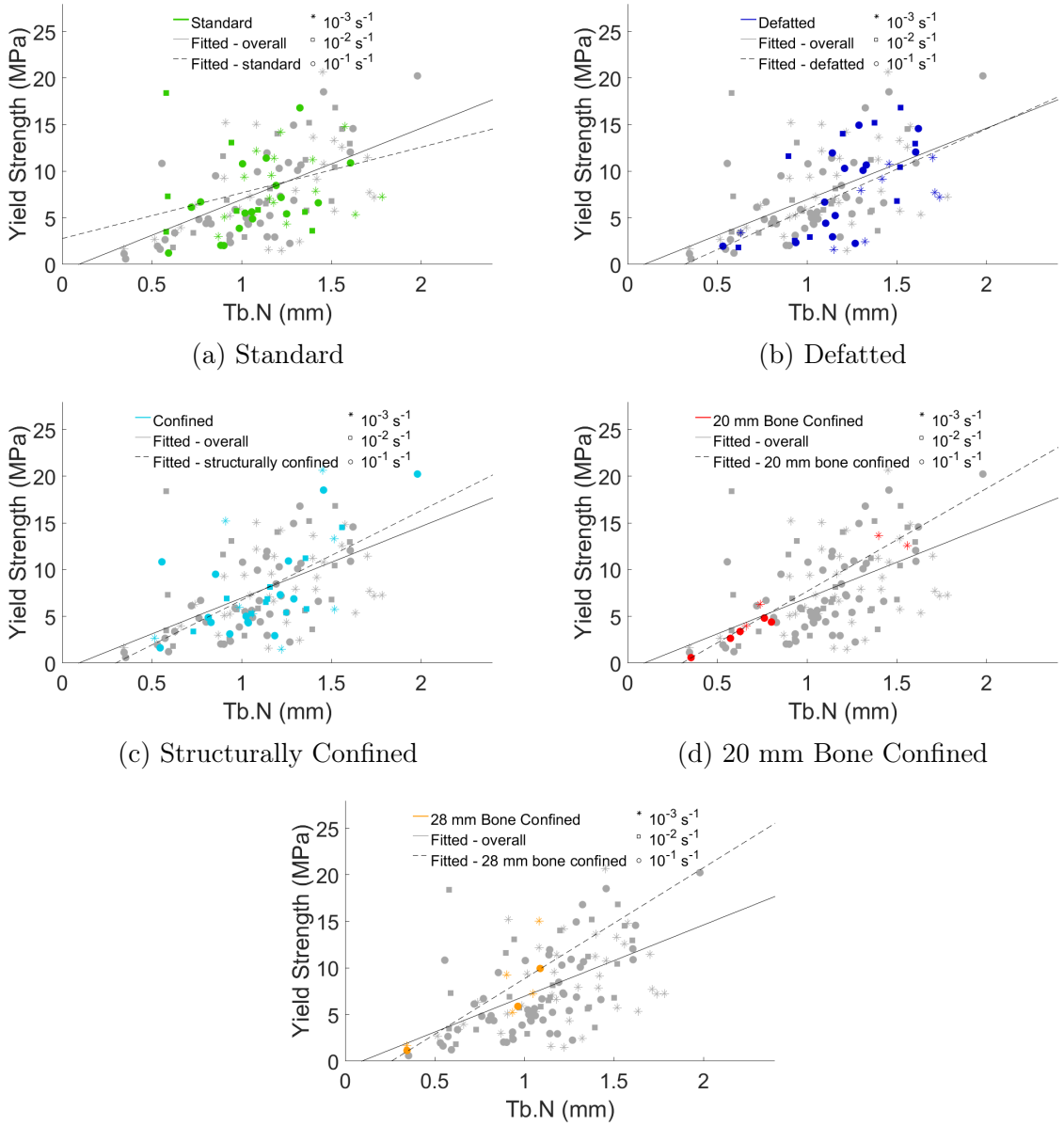

(a) Standard

(b) Defatted

(c) Structurally Confined

(d) 20 mm Bone Confined

(e) 28 mm Bone Confined

Figure B.147: Graphs showing Yield Strength versus Tb.N for each specimen condition

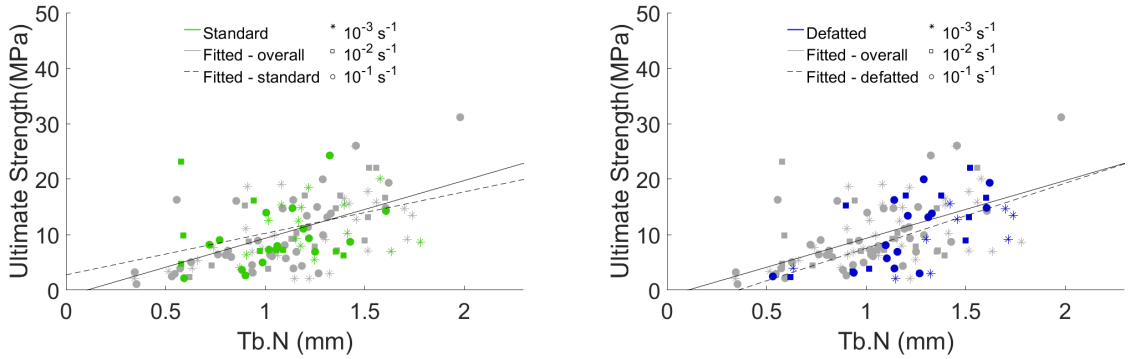

(a) Standard

(b) Defatted

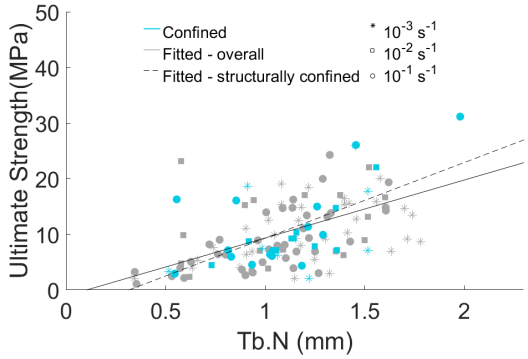

(c) Structurally Confined

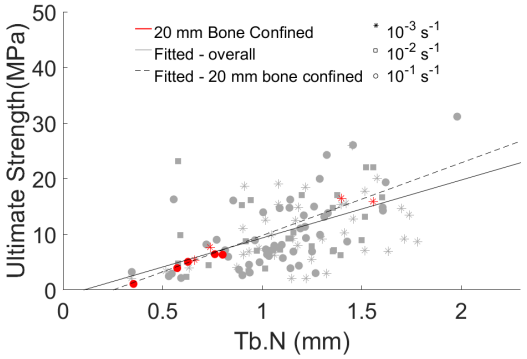

(d) 20 mm Bone Confined

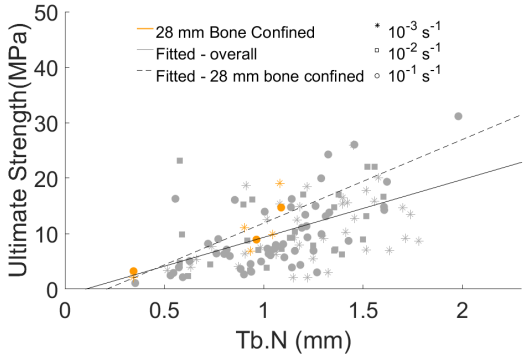

(e) 28 mm Bone Confined

Figure B.148: Graphs showing Ultimate Strength versus Tb.N for each specimen condition

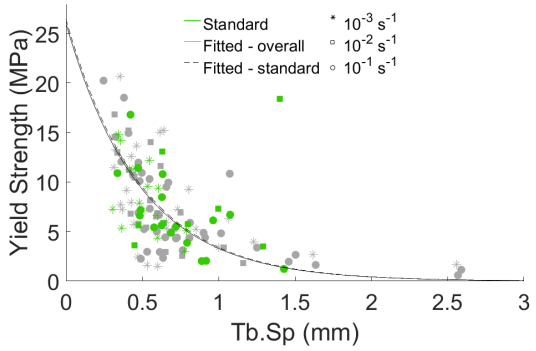

(a) Standard

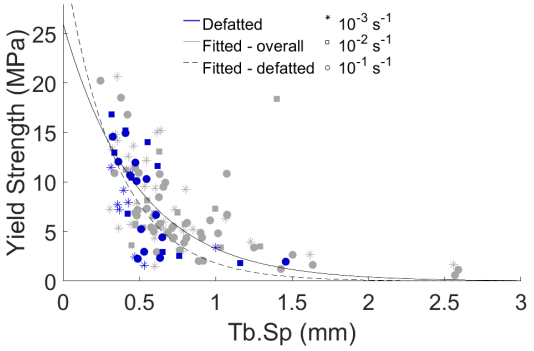

(b) Defatted

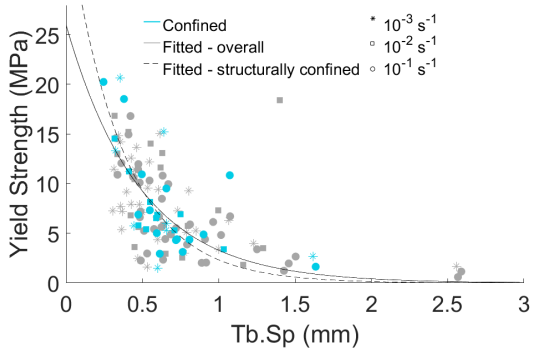

(c) Structurally Confined

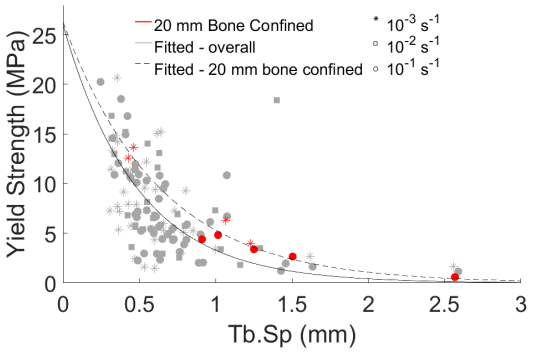

(d) 20 mm Bone Confined

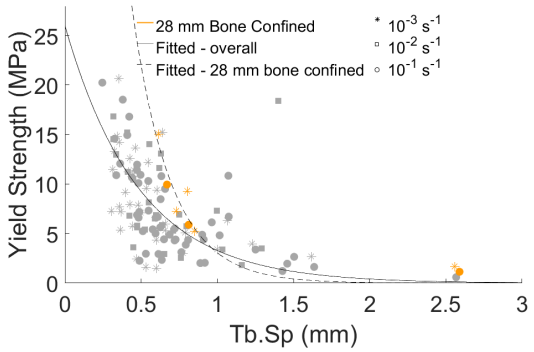

(e) 28 mm Bone Confined

Figure B.149: Graphs showing Yield Strength versus Tb.Sp for each specimen condition

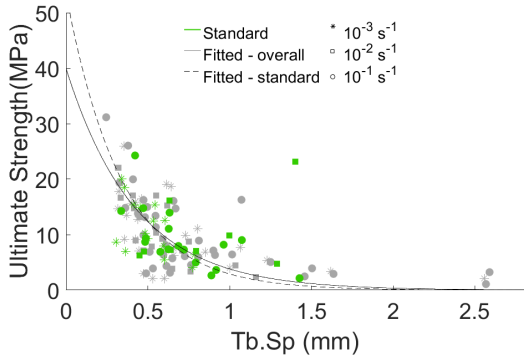

(a) Standard

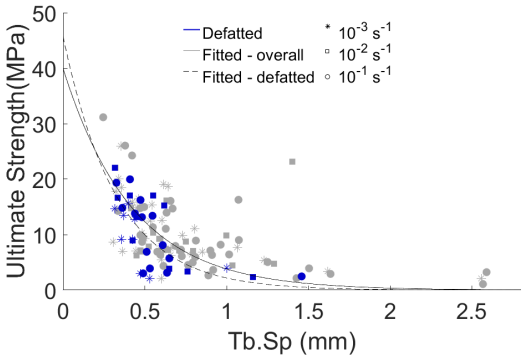

(b) Defatted

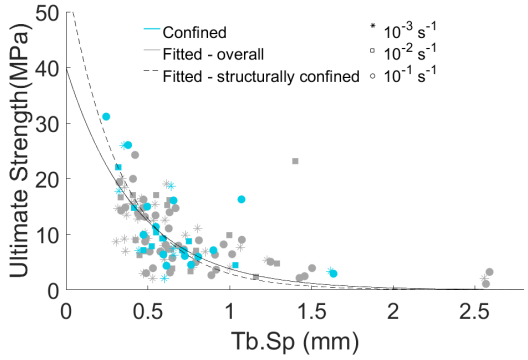

(c) Structurally Confined

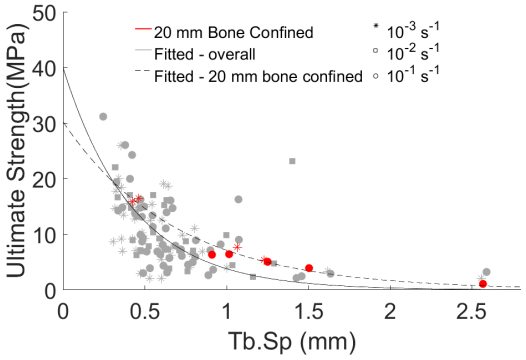

(d) 20 mm Bone Confined

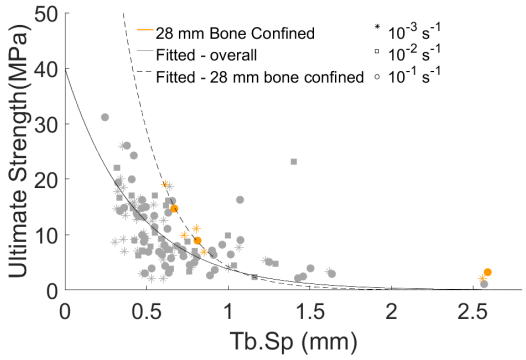

(e) 28 mm Bone Confined

Figure B.150: Graphs showing Ultimate Strength versus Tb.Sp for each specimen condition

Appendix C

Machine Drawings

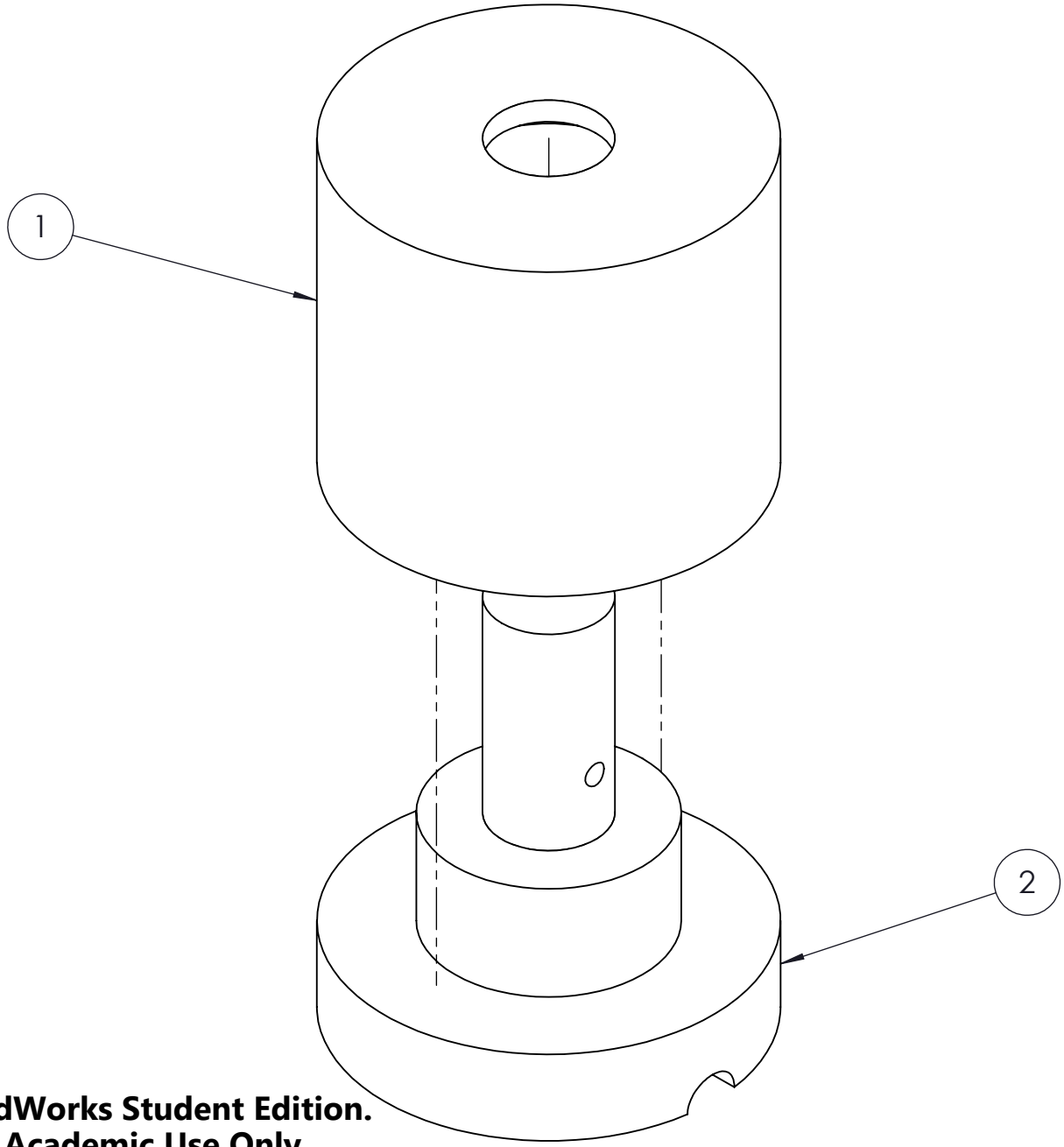

ITEM NO.	PART NAME	MATERIAL	QTY.
2	INNER PLATFORM	ALUMINIUM	1
1	OUTER PLATFORM	ALUMINIUM	1

A4 Landscape	University of Cape Town Department of Mechanical Engineering			
	Title: PLATFORM ASSEMBLY			
Assembly Drawing	Scale: 2:1	Date: 01-Dec-16	Sheet1	of 3
	Drawn By: Kelsey Hilton		Drawing Number 1	

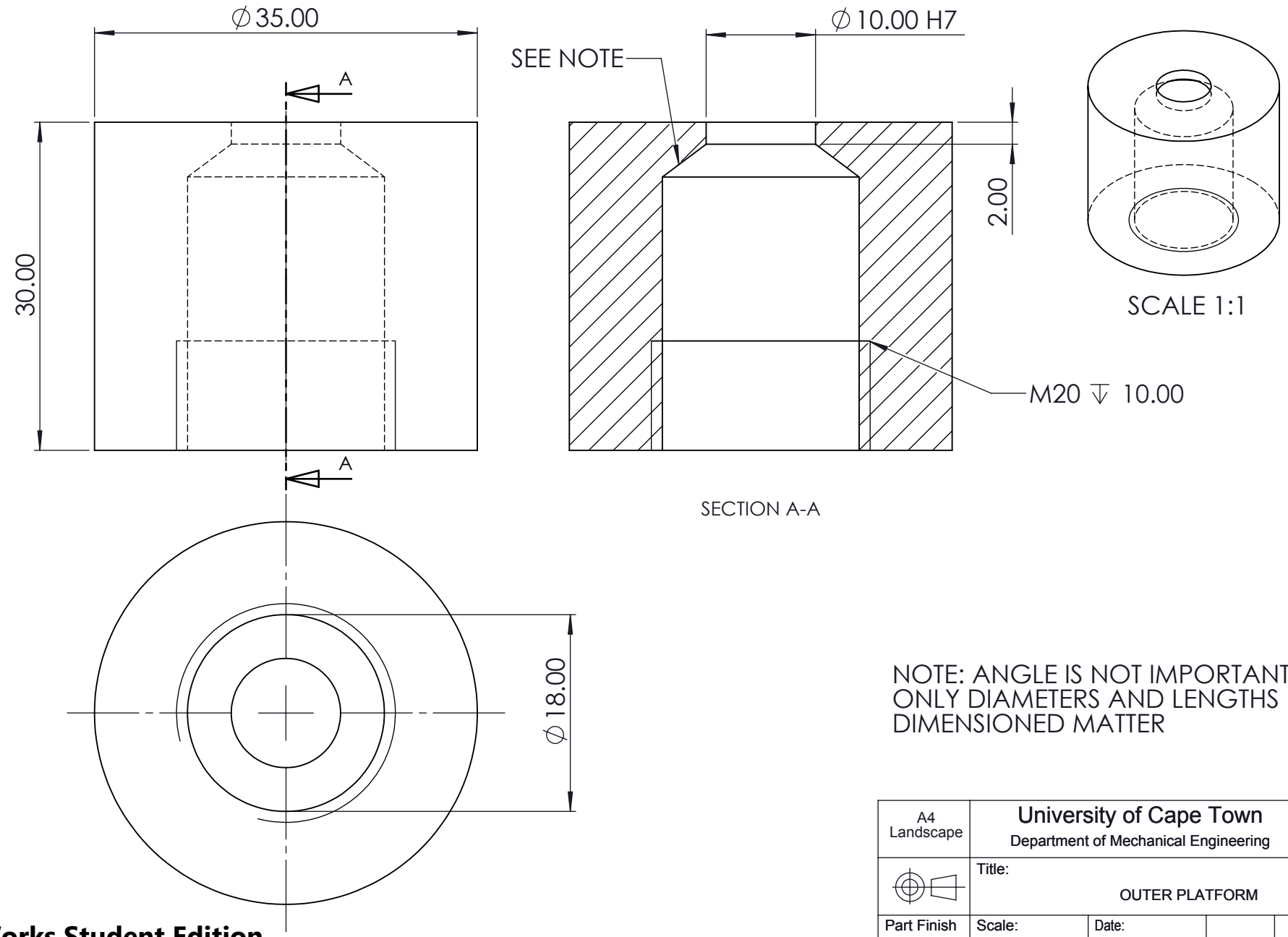

NOTE: ANGLE IS NOT IMPORTANT.
ONLY DIAMETERS AND LENGTHS
DIMENSIONED MATTER

SolidWorks Student Edition.
For Academic Use Only.

A4 Landscape	University of Cape Town Department of Mechanical Engineering			
	Title: OUTER PLATFORM			
Part Finish	Scale: 2:1	Date: 01-Dec-16	Sheet 3	of 3
Material: Aluminium	Drawn By: Kelsey Hilton		Drawing Number 3	

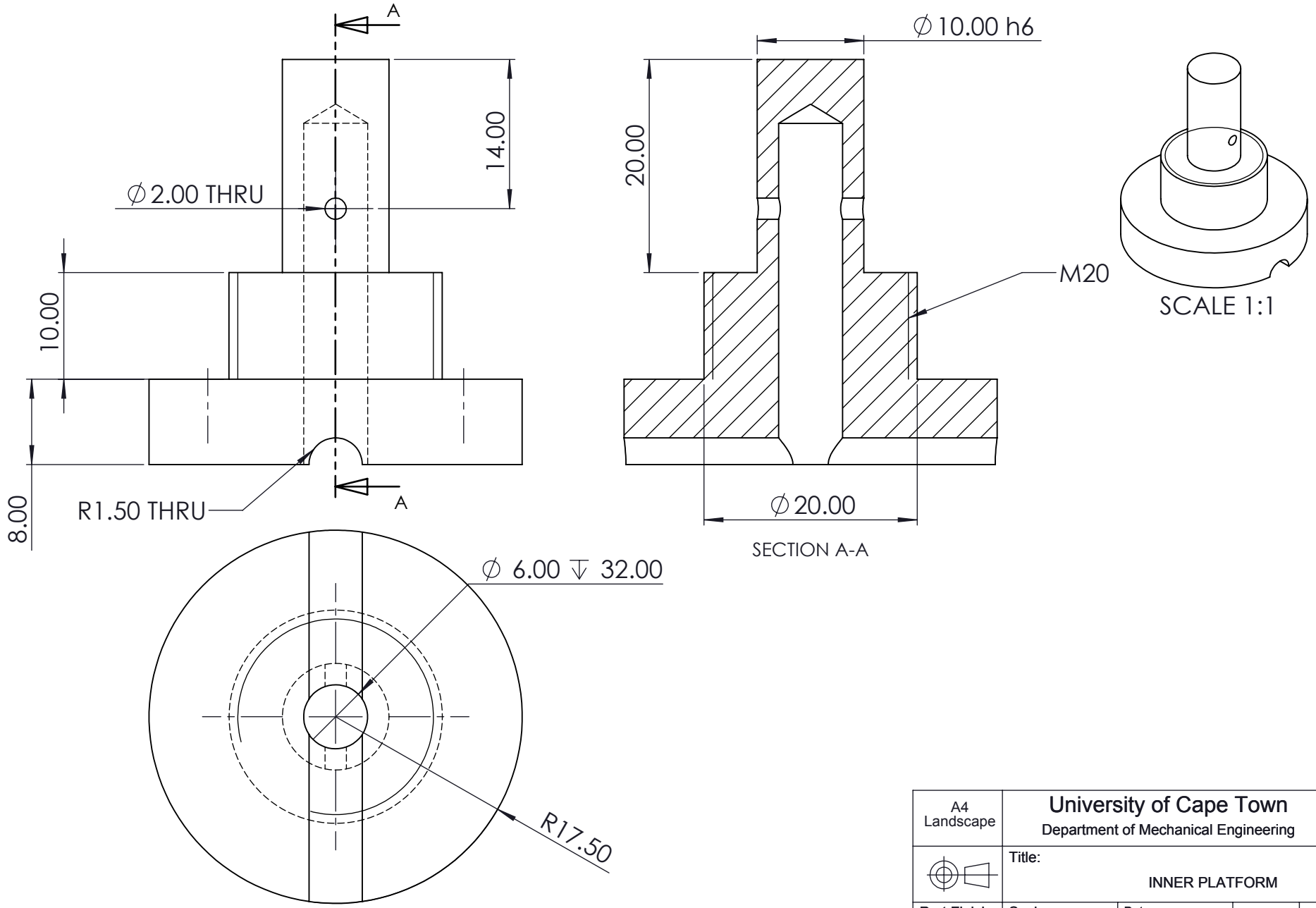

SolidWorks Student Edition.
For Academic Use Only.

A4 Landscape	University of Cape Town Department of Mechanical Engineering			
	Title: INNER PLATFORM			
Part Finish	Scale: 2:1	Date: 01-Dec-16	Sheet 2	of 3
Material: Aluminium	Drawn By: Kelsey Hilton		Drawing Number 2	

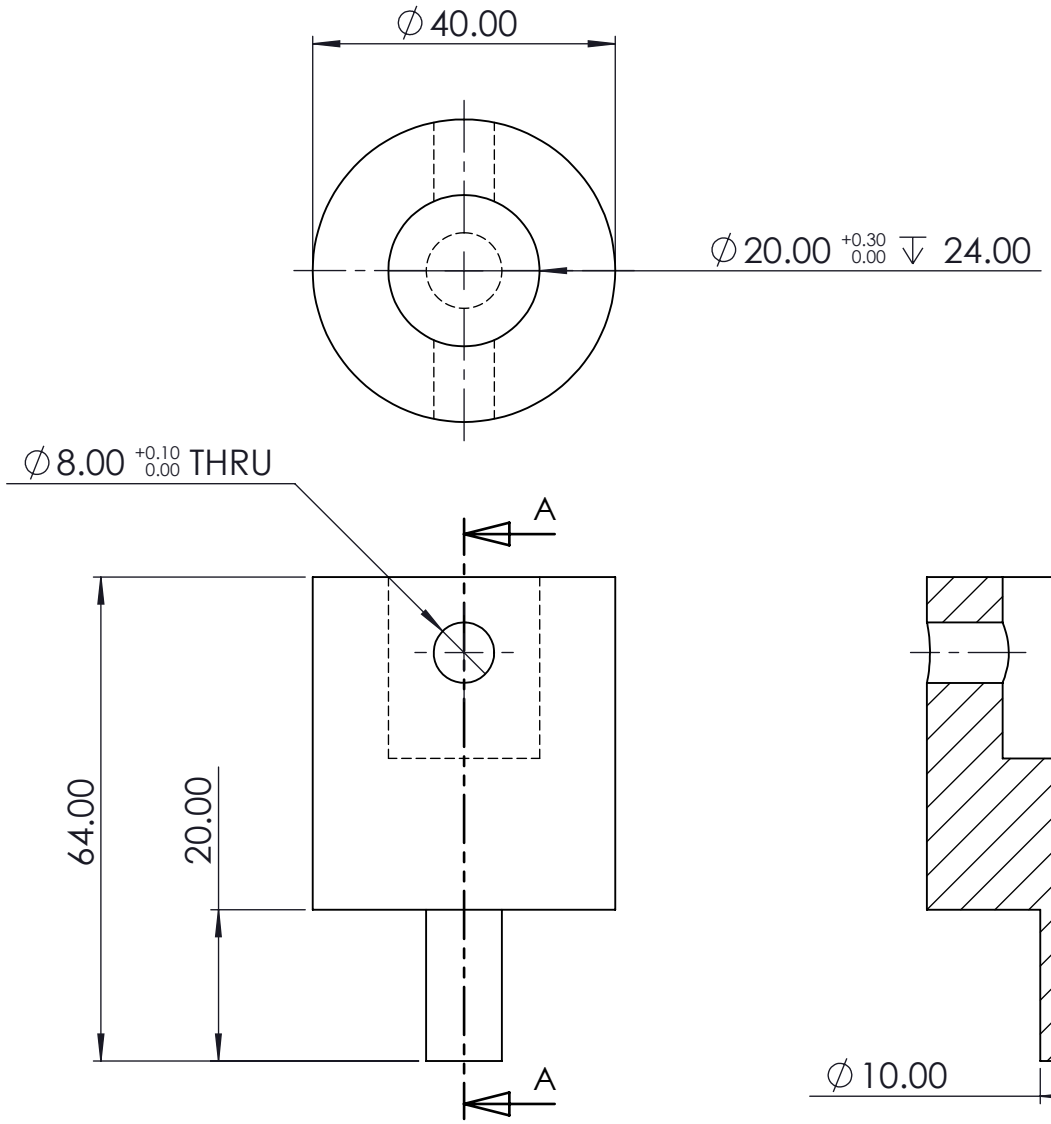

SECTION A-A

SolidWorks Student Edition.
For Academic Use Only.

A4 Landscape	University of Cape Town Department of Mechanical Engineering			
	Title: 10 MM PLUNGER			
Part Finish	Scale: 1:1	Date: 01-Dec-16	Sheet 4	of 6
Material: Steel	Drawn By: Kelsey Hilton		Drawing Number 4	

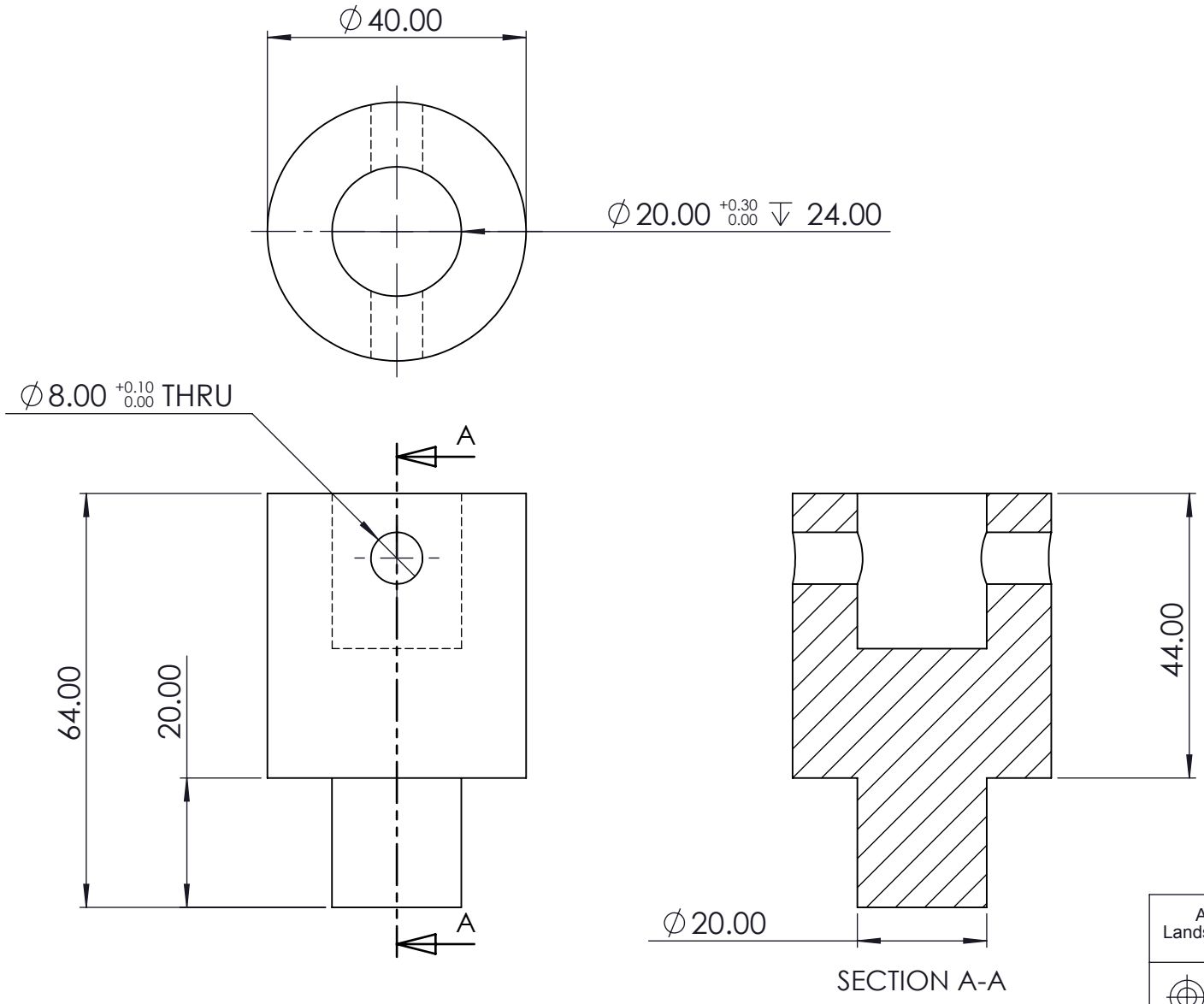

SolidWorks Student Edition.
For Academic Use Only.

A4 Landscape	University of Cape Town Department of Mechanical Engineering			
	Title: 20 MM PLUNGER			
Part Finish	Scale: 1:1	Date: 01-Dec-16	Sheet 5	of 6
Material: Steel	Drawn By: Kelsey Hilton		Drawing Number 5	

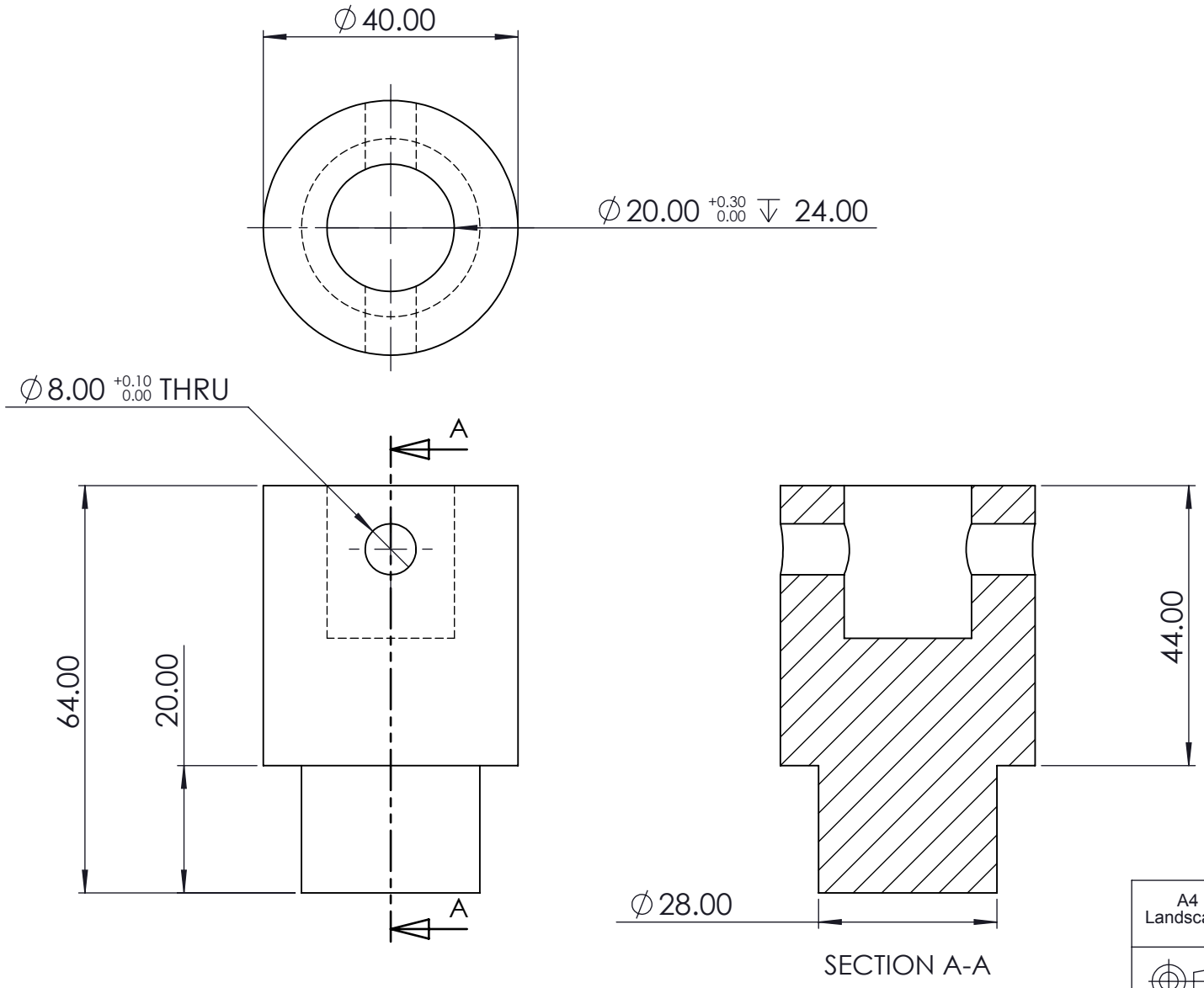

SolidWorks Student Edition.
For Academic Use Only.

A4 Landscape	University of Cape Town Department of Mechanical Engineering			
	Title: 28 MM PLUNGER			
Part Finish	Scale: 1:1	Date: 01-Dec-16	Sheet 6	of 6
Material: Steel	Drawn By: Kelsey Hilton		Drawing Number 6	

Appendix D

Ethics In Research

EBE Faculty: Assessment of Ethics in Research Projects

Any person planning to undertake research in the Faculty of Engineering and the Built Environment at the University of Cape Town is required to complete this form before collecting or analysing data. When completed it should be submitted to the supervisor (where applicable) and from there to the Head of Department. If any of the questions below have been answered YES, and the applicant is NOT a fourth year student, the Head should forward this form for approval by the Faculty EIR committee: submit to Ms Zulpha Geyer (Zulpha.Geyer@uct.ac.za; Chem Eng Building, Ph 021 650 4791). Students must include a copy of the completed form with the thesis when it is submitted for examination.

Name of Principal Researcher/Student: Kelsey Hilton Department: Mechanical Engineeri

If a Student: Degree: MScEng (Mech) Supervisor: Trevor Cloete

If a Research Contract indicate source of funding/sponsorship:

Research Project Title: Dynamic deformation fracture of bone.

Overview of ethics issues in your research project:

Question 1: Is there a possibility that your research could cause harm to a third party (i.e. a person not involved in your project)?	YES	(NO)
Question 2: Is your research making use of human subjects as sources of data? If your answer is YES, please complete Addendum 2.	YES	(NO)
Question 3: Does your research involve the participation of or provision of services to communities? If your answer is YES, please complete Addendum 3.	YES	(NO)
Question 4: If your research is sponsored, is there any potential for conflicts of interest? If your answer is YES, please complete Addendum 4.	YES	(NO)

If you have answered YES to any of the above questions, please append a copy of your research proposal, as well as any interview schedules or questionnaires (Addendum 1) and please complete further addenda as appropriate.

I hereby undertake to carry out my research in such a way that

- there is no apparent legal objection to the nature or the method of research; and
- the research will not compromise staff or students or the other responsibilities of the University;
- the stated objective will be achieved, and the findings will have a high degree of validity;
- limitations and alternative interpretations will be considered;
- the findings could be subject to peer review and publicly available; and
- I will comply with the conventions of copyright and avoid any practice that would constitute plagiarism.

Signed by:

	Full name and signature	Date
Principal Researcher/Student:	Kelsey Hilton KHilton	03/02/2015

This application is approved by:

Supervisor (if applicable):	T.J. Cloete	03/02/2015
HOD (or delegated nominee): Final authority for all assessments with NO to all questions and for all undergraduate research.	R.D. Knutsen	03/02/2015
Chair : Faculty EIR Committee For applicants other than undergraduate students who have answered YES to any of the above questions.		

ADDENDUM 1:
Please append a copy of the research proposal here, as well as any interview schedules or questionnaires:

ADDENDUM 2: To be completed if you answered YES to Question 2:

It is assumed that you have read the UCT Code for Research involving Human Subjects (available at http://web.uct.ac.za/depts/educate/download/uctcodeforresearchinvolvinghumansubjects.pdf) in order to be able to answer the questions in this addendum.

2.1 Does the research discriminate against participation by individuals, or differentiate between participants, on the grounds of gender, race or ethnic group, age range, religion, income, handicap, illness or any similar classification?	YES	NO
2.2 Does the research require the participation of socially or physically vulnerable people (children, aged, disabled, etc) or legally restricted groups?	YES	NO
2.3 Will you not be able to secure the informed consent of all participants in the research? (In the case of children, will you not be able to obtain the consent of their guardians or parents?)	YES	NO
2.4 Will any confidential data be collected or will identifiable records of individuals be kept?	YES	NO
2.5 In reporting on this research is there any possibility that you will not be able to keep the identities of the individuals involved anonymous?	YES	NO
2.6 Are there any foreseeable risks of physical, psychological or social harm to participants that might occur in the course of the research?	YES	NO
2.7 Does the research include making payments or giving gifts to any participants?	YES	NO

If you have answered YES to any of these questions, please describe how you plan to address these issues (append to form):

ADDENDUM 3: To be completed if you answered YES to Question 3:

3.1 Is the community expected to make decisions for, during or based on the research?	YES	NO
3.2 At the end of the research will any economic or social process be terminated or left unsupported, or equipment or facilities used in the research be recovered from the participants or community?	YES	NO
3.3 Will any service be provided at a level below the generally accepted standards?	YES	NO

If you have answered YES to any of these questions, please describe how you plan to address these issues (append to form)

ADDENDUM 4: To be completed if you answered YES to Question 4

4.1 Is there any existing or potential conflict of interest between a research sponsor, academic supervisor, other researchers or participants?	YES	NO
4.2 Will information that reveals the identity of participants be supplied to a research sponsor, other than with the permission of the individuals?	YES	NO
4.3 Does the proposed research potentially conflict with the research of any other individual or group within the University?	YES	NO

If you have answered YES to any of these questions, please describe how you plan to address these issues(append to form)